GEOTECHNICAL PROPERTIES OF COARSE-FINE MIXTURES AND THEIR INTERACTION WITH GEOGRIDS THROUGH LARGE DIRECT SHEAR TESTING

A THESIS SUBMITTED TO
THE GRADUATE SCHOOL OF NATURAL AND APPLIED SCIENCES
OF
MIDDLE EAST TECHNICAL UNIVERSITY

BY

ANIL EKİCİ

IN PARTIAL FULFILLMENT OF THE REQUIREMENTS
FOR
THE DEGREE OF DOCTOR OF PHILOSOPHY
IN
CIVIL ENGINEERING

JUNE 2022

Approval of the thesis:

GEOTECHNICAL PROPERTIES OF COARSE-FINE MIXTURES AND THEIR INTERACTION WITH GEOGRIDS THROUGH LARGE DIRECT SHEAR TESTING

submitted by **ANIL EKİCİ** in partial fulfillment of the requirements for the degree of **Doctor of Philosophy** i**n Civil Engineering, Middle East Technical University** by,

Prof. Dr. Halil Kalıpçılar
Dean, Graduate School of **Natural and Applied Sciences** _____

Prof. Dr. Erdem Canbay
Head of the Department, **Civil Engineering** _____

Assoc. Prof. Dr. Nejan Huvaj Sarıhan
Supervisor, **Civil Engineering, METU** _____

Assoc. Prof. Dr. Cem Akgüner
Co-Supervisor, **Civil Engineering, TED University** _____

Examining Committee Members:

Prof. Dr. Erdal Çokça
Civil Engineering, METU _____

Assoc. Prof. Dr. Nejan Huvaj Sarıhan
Civil Engineering, METU _____

Prof. Dr. Sami Oğuzhan Akbaş
Civil Engineering, Gazi University _____

Assoc. Prof. Dr. Nabi Kartal Toker
Civil Engineering, METU _____

Assoc. Prof. Dr. Özer Çinicioğlu
Civil Engineering, Boğaziçi University _____

Date: 29.06.2022

I hereby declare that all information in this document has been obtained and presented in accordance with academic rules and ethical conduct. I also declare that, as required by these rules and conduct, I have fully cited and referenced all material and results that are not original to this work.

Name Last name : Anıl Ekici

Signature :

ABSTRACT

GEOTECHNICAL PROPERTIES OF COARSE-FINE MIXTURES AND THEIR INTERACTION WITH GEOGRIDS THROUGH LARGE DIRECT SHEAR TESTING

Ekici, Anıl
Doctor of Philosophy, Civil Engineering
Supervisor: Assoc. Prof. Dr. Nejan Huvaj Sarıhan
Co-Supervisor: Assoc. Prof. Dr. Cem Akgüner

June 2022, 346 pages

Different proportions of gravel, sand, nonplastic silt, kaolin, and bentonite were mixed to obtain ten coarse-fine mixtures (CFM) having 0%, 12%, 20%, 30%, 40% fines content (FC) and 5% and 15% plasticity indices (PI). Mixtures were evaluated to identify behavioral thresholds and address backfill restrictions in commonly used guidelines to design reinforced earth walls. All CFM specimens were initially compacted to 95% of standard Proctor dry density at optimum moisture content. Index, hydraulic properties, and specific surface areas were investigated. FC=15% for PI=5% and FC=12% for PI=15% represented the transition between fine and coarse-grain domination according to particle packing.

Unconfined compressive strength, CU triaxial, and large-scale compression tests were conducted. FC=20% was the transitional boundary for CFM with PI=5%, reflected in shifting of the dilation tendency to contraction, while samples having PI=15% mainly had relatively high initial contraction followed by dilation. Consolidation data in triaxial tests indicated that FC of 30% to 40% for PI=15% was the transition at which normally-consolidated clay-like behavior began.

Strength of CFM and interaction with geogrids (with and without drainage property) were investigated through large direct shear tests (300x300 mm) under 55, 105, and 155 kPa normal stresses. Interface shear strength coefficients ranged between 0.65-1.05. Bond efficiencies increased with normal stress and decreased with PI. Geogrid's drainage component did not affect the interface strength for unsaturated specimens. In saturated mixtures, drainage was more critical for FC=40% than FC=20%, as strength reductions due to excess pore pressures were significant, especially for FC=40% and PI=15%.

Keywords: Fines Content, Plasticity Index, Coarse-Fine Mixtures, Reinforced Earth Fill Criteria, Geogrid Interaction

ÖZ

KABA-İNCE ZEMİN KARIŞIMLARININ GEOTEKNİK ÖZELLİKLERİ VE BÜYÜK DİREKT KESME DENEYLERİNDE GEOGRİD İLE ETKİLEŞİMLERİ

Ekici, Anıl
Doktora, İnşaat Mühendisliği
Tez Yöneticisi: Doç. Dr. Nejan Huvaj Sarıhan
Ortak Tez Yöneticisi: Doç. Dr. Cem Akgüner

Haziran 2022, 346 sayfa

Çakıl, kum, plastik olmayan silt, kaolin ve bentonitin farklı oranlarda karıştırılmasıyla ince dane oranı (FC) %0, %12, %20, %30, %40 ve plastisite indeksleri (PI) %5 ve %15 olacak şekilde on farklı kaba-ince zemin karışımı (CFM) hazırlanmıştır. Karışımlar, davranışsal eşikleri belirlemeye ve toprakarme dolgu duvarların tasarımı için yaygın olarak kullanılan tasarım kılavuzlarındaki kısıtlamaları ele almaya yönelik olarak değerlendirilmiştir. Tüm CFM numuneleri optimum su muhtevasında ve standart Proktor kuru yoğunluklarının %95'inde sıkıştırılarak hazırlanmıştır. Hazırlanan karışımların geoteknik indeks ve hidrolik iletkenlik özellikleri ile spesifik yüzey alanları incelenmiştir. Danelerin paketlenmesine bağlı olarak ince ve kaba danelerin baskınlıkları arasındaki geçiş PI=%5 için FC=%15 ve PI=%15 için FC=%12'de gerçekleşmiştir.

Serbest basınç, üç eksenli basınç (konsolidasyonlu drenajsız) ve büyük ölçekli oturma (sıkışma) testleri yapılmıştır. Genişleme eğiliminin sıkışmaya doğru değiştiği davranışsal geçiş sınırı, PI=%5 olan CFM için FC=%20 olurken; PI=%15 olan karışımların çoğu, başlangıçta nispeten yüksek bir sıkışma ve ardından genişleme

eğilimi göstermiştir. Üç eksenli testlerindeki konsolidasyon verileri, PI=%15 için %30 ila %40 FC'nin, normal-konsolide kil-benzeri davranışın başladığı sınır olduğunu göstermiştir.

CFM'nin mukavemet davranışı ve geogridlerle (drenaj özelliği olan ve olmayan) etkileşimi büyük direkt kesme testleri (300x300 mm) ile 55, 105 ve 155 kPa normal gerilmeler altında incelenmiştir. Ara yüz kayma dayanımı katsayıları 0,65-1,05 arasında değişmiştir. Zemin-geogrid etkileşim verimi normal gerilmeyle artmış, PI ile azalmıştır. Geogridin drenaj özelliği, doygun olmayan numunelerde ara yüz dayanımını etkilememiştir. Suya doygun numunelerde ise drenaj, FC=%20 olanlara kıyasla FC=%40 olan karışımlarda ilave boşluk suyu basınçlarındaki artışlara bağlı mukavemet düşüşleri önemli ölçüde olduğundan, özellikle de FC=%40 ve PI=%15 için daha kritiktir.

Anahtar Kelimeler: İnce Dane Oranı, Plastisite İndeksi, Kaba-İnce Karışımlar, Güçlendirilmiş Toprak Dolgu Kriterleri, Geogrid Etkileşimi

To my family

ACKNOWLEDGEMENTS

I would like to express my deepest gratitude to the following institutions and individuals who made this work possible with their help and support.

First, I would like to offer my special thanks to my supervisor, Dr. Nejan Huvaj, for her invaluable contributions, support, time, and encouragement throughout this research over the years. I am grateful for her ideas and guidance in making this study more efficient.

In addition to my advisor, I would like to extend my sincere thanks to my co-advisor, Dr. Cem Akgüner, for his insightful comments, contributions, and guidance at every stage of this research project.

My sincere thanks are directed to my thesis jury members, Dr. Kartal Toker, Dr. Sami Oğuzhan Akbaş, Dr. Erdal Çokça and, Dr. Özer Çinicioğlu for their valuable comments and feedback.

I would like to thank the Scientific and Technological Research Council of Turkey (TÜBİTAK) for providing financial support within the scope of the project issued as 117M145 during my doctoral study.

I would like to thank METU and METU Civil Engineering Department and Geotechnics Division members for allowing me to use all our laboratory facilities during my thesis work.

I would like to extend my sincere thanks to TEDU, where I worked as a research assistant, for allowing me to use all laboratory facilities and to all TEDU Civil Engineering Department members for their support.

I am incredibly grateful to my colleague at TEDU, Ömer Can Pamuk, for his helpful suggestions, continuous support, and valuable contributions during this long-term study.

I would like to express my gratitude to Ulaş Nacar and Kamber Bilgen, at the METU soil mechanics laboratory, and Saim Seloğlu, TEDU Civil Engineering Department soil mechanics laboratory former technician, for their support, friendly and helpful attitude throughout my laboratory studies.

I thank to my METU labmates Melih Birhan Kenanoğlu, Emre Duman, Berkan Söylemez, Yılmaz Emre Sarıçiçek and Elife Çakır for their friendship, help and contributions throughout my thesis.

I am grateful for having friends who constantly encouraged me with their motivation throughout my research. I wish to express my special thanks to Erdem İspir, Caner Uzun, Gamze Didem Öget, and Cavit Olcay Bingöl for always being there for me. Their invaluable friendship has been a great support to me all this time.

I wish to thank especially my beloved wife Ayşe Nur Yazgan Ekici, Pharm. PhD. who have stood by me all this time and given me strength at the most challenging moments. I am grateful for her support and love at every stage of my life.

Finally, I would like to express my sincere gratitude to my beloved parents, Nalan Ekici and Aygün Ekici. I will never forget their unconditional moral support and love throughout my life. They are the greatest reminders of the light at the end of the tunnel in every challenge I face. This work would not have happened without my family.

TABLE OF CONTENTS

ABSTRACT v

ÖZ vii

ACKNOWLEDGEMENTS x

TABLE OF CONTENTS xii

LIST OF TABLES xviii

LIST OF FIGURES xx

LIST OF ABBREVIATIONS xxxii

LIST OF SYMBOLS xxxiv

CHAPTERS

1 INTRODUCTION 1

1.1 Problem Statement 1

1.2 Objectives of the Study 6

1.3 Research Scope 7

1.4 Thesis Organization 8

2 LITERATURE REVIEW 11

2.1 Backfill Properties in Reinforced Soil Walls and Slopes 11

2.2 Soil Classification Systems 17

2.3 Properties of Coarse-Fine Mixtures 21

2.3.1 Index Properties 21

2.3.2 Hydraulic Properties 34

2.3.2.1 Specific Surface Area of Materials 43

2.3.3 Strength Properties 45

2.3.4 Compression Properties....58
2.4 Soil-Geosynthetic Interaction Studies....65
2.4.1 Large Direct Shear Tests....72
2.4.1.1 Tests on Cohesive Soils....78
3 TESTING MATERIALS AND METHODOLOGY....83
3.1 Soil Mixtures Used....83
3.1.1 Index Tests....83
3.1.2 Selection of Soil Products....84
3.1.2.1 Fine Gravel....85
3.1.2.2 Coarse, Medium, and Fine Sands....86
3.1.2.3 Non-Plastic Silt....87
3.1.2.4 Kaolin and Bentonite Clay....87
3.1.3 Preparation of Soil Mixtures....89
3.2 Geogrid Properties....94
3.3 Applied Tests....97
3.3.1 Methylene Blue Spot Test....97
3.3.1.1 Apparatus....97
3.3.1.2 Test Procedure....98
3.3.2 Hydraulic Conductivity Tests....99
3.3.2.1 Rigid Wall Hydraulic Conductivity Tests....99
3.3.2.1.1 Apparatus....99
3.3.2.1.2 Test Procedure....101
3.3.2.2 Flexible Wall Hydraulic Conductivity Tests....102
3.3.2.2.1 Apparatus....102

3.3.2.2.2 Specimen Preparation 104
3.3.2.2.3 Test Procedure 107
3.3.3 Unconfined Compressive Strength Tests 110
3.3.3.1 Apparatus 110
3.3.3.2 Specimen Preparation 111
3.3.3.3 Test Procedure 111
3.3.4 Isotropically Consolidated Undrained Triaxial Compression Tests 112
3.3.4.1 Apparatus 112
3.3.4.2 Specimen Preparation 114
3.3.4.3 Test Procedure 114
3.3.5 Static Large Compression Tests 116
3.3.5.1 Apparatus 116
3.3.5.2 Specimen Preparation 118
3.3.5.3 Test Program and Procedure 120
3.3.6 Large Direct Shear Tests 121
3.3.6.1 Apparatus 121
3.3.6.2 Specimen Preparation 130
3.3.6.2.1 Specimen Preparation Procedure for Unsaturated Tests 135
3.3.6.2.2 Specimen Preparation Procedure for Saturated Tests 140
3.3.6.3 Test Procedure 146
3.3.6.3.1 Settlement Stage 146
3.3.6.3.2 Shearing Stage 146
3.3.6.4 Test Program 147
4 INDEX AND HYDRAULIC CONDUCTIVITY TEST RESULTS 151

4.1 Classification of Soil Mixtures 151
4.2 Index Test Results 156
4.3 Methylene Blue Spot Test Results 160
4.4 Saturation of CFM Specimens 163
4.5 Hydraulic Conductivity Test Results 165
4.5.1 Rigid Wall Hydraulic Conductivity Test Results 165
4.5.2 Flexible Wall Hydraulic Conductivity Test Results 166
4.6 Discussion of Results 168
4.6.1 Index Properties 168
4.6.2 Specific Surface Area 170
4.6.3 Volume Change During Saturation 174
4.6.4 Threshold Fines Content Based on Particle Packing 175
4.6.5 Hydraulic Conductivity 177
4.6.5.1 Comparison of Measured Hydraulic Conductivities with Empirical Predictions in Literature 181
5 UNCONFINED COMPRESSION, TRIAXIAL COMPRESSION AND COMPRESSIBILITY TEST RESULTS 185
5.1 Unconfined Compressive Strength Test Results 185
5.2 Triaxial Compression Test Results 189
5.2.1 Consolidation of Saturated Specimens 189
5.2.2 Triaxial Compression Tests 192
5.3 Static Large Compression Tests 198
5.4 Discussion of Results 203
5.4.1 Discussion of Unconfined Compression Test Results 203

5.4.2 Discussion of Triaxial Compression Test Results 205
5.4.3 Discussion on Compressibility 228
5.4.3.1 Discussion of Consolidation of Saturated Specimens in Triaxial Test 228
5.4.3.2 Discussion of Static Large Compression Tests 233
6 LARGE DIRECT SHEAR TEST RESULTS 243
6.1 Test Results 243
6.1.1 Settlement Stage 245
6.1.2 Shearing Stage 248
6.2 Discussion of Results 250
6.2.1 Discussion of Shear Strength of Soil Mixtures 250
6.2.2 Discussion of Shear Strength of Soil Mixture-Geogrid Interface 258
6.2.2.1 Discussion of Direct Shear Tests on Saturated Specimens 274
6.2.2.2 Discussion of Direct Shear Tests with a Shear Rate of 0.01 mm/min 284
7 CONCLUSIONS 287
7.1 Conclusions on Index and Hydraulic Properties 288
7.2 Conclusions on Unconfined Compressive Strength, Shear Strength by Triaxial Tests, and Compressibility 291
7.3 Conclusions on Large Direct Shear Response 296
7.4 CFM usage in MSEW 300
7.5 Recommendations for Future Research 303
REFERENCES 305
APPENDICES

A. Large Direct Shear Test Results.....327
B. Equipment Specifications.....343
CURRICULUM VITAE.....345

LIST OF TABLES

TABLES

Table 2.1. Suitable backfill material criteria in different guidelines 12
Table 2.2. Hydraulic conductivity predictions in literature for coarse soils 36
Table 2.3. Hydraulic conductivity prediction equations in literature for fine, plastic soils 38
Table 2.4. Correlations for specific surface area (SSA) estimation 45
Table 2.5. Behavioral thresholds and regimes (Simpson and Evans, 2015) 46
Table 2.6. Interface shear strength coefficients for soil and geogrid interface 74
Table 3.1. Properties of commercially available soil products (Ekici et al., 2019) 88
Table 3.2. Percent fractions of soil products by weight to prepare soil mixtures ... 91
Table 3.3. Properties of the geogrid used in tests 95
Table 3.4. Properties, soil, and water masses of the prepared mixtures 134
Table 3.5. Direct shear test program (unsaturated specimens, R=0.25 mm/min) 149
Table 3.6. Direct shear test program (saturated specimens, R=0.25 mm/min) 150
Table 3.7. Direct shear test program (unsaturated specimens, R=0.01 mm/min) 150
Table 4.1. Classification of the prepared soil mixtures 152
Table 4.2. Classification of the prepared soil mixtures according to the Revised Soil Classification System (RSCS) suggested by Park and Santamarina (2017) .. 154
Table 4.3. Specific gravities of CFM and parameters related to the particle size distribution 157
Table 4.4. Maximum and minimum dry densities of SW and SP soil mixtures ... 157
Table 4.5. Standard Proctor test results of CFM 158
Table 4.6. Atterberg limits of CFM for portions passing No. 40 and No. 200 sieves 159

Table 4.7. Methylene Blue spot test results for CFM portions passing No. 40 and No. 200 sieves, kaolin, and bentonite 160
Table 4.8. Void ratios before and after saturation..... 164
Table 4.9. Hydraulic conductivity test results of SW and SP soil mixtures 165
Table 4.10. Hydraulic conductivity test results of CFM..... 167
Table 4.11. Results of specific surface area (SSA) and comparison with empirical predictions..... 171
Table 5.1. Unconfined compressive strength test results..... 187
Table 5.2. Repeated triaxial test results 196
Table 5.3. Phase parameters of the specimens in compression tests 199
Table 5.4. Summary of the triaxial compression test results 206
Table 5.5. Shear strength parameters of coarse-fine mixtures from consolidated undrained triaxial compression tests..... 208
Table 5.6. Critical state parameters of coarse-fine mixtures from triaxial tests ... 212
Table 5.7. Classification of coarse-fine mixtures according to contractive-dilative tendencies during undrained triaxial strength tests..... 218
Table 5.8. Consolidation parameters of saturated CFM specimens with PI=15% 229
Table 5.9. Cumulative percent axial strain observed at the end of each loading stage for CFM with PI=5% 233
Table 5.10. Cumulative percent axial strain observed at the end of each loading stage for CFM with PI=15%..... 234
Table 6.1. Shear strength properties of soil mixtures in direct shear tests..... 255
Table 6.2. Shear strength properties of soil mixture-geogrid interface 262
Table 6.3. Comparison of the shear strength parameters of soil mixtures with and without geogrid from direct shear tests..... 267
Table 6.4. Peak and ultimate (residual) interface shear strength coefficients of soil mixtures..... 270
Table 6.5. Phase parameters of the saturated specimens in direct shear tests..... 275
Table 6.6. Shear strength properties of saturated tests..... 275

LIST OF FIGURES

FIGURES

Figure 1.1. (a) Timber-faced geogrid reinforced wall constructed by using locally available soil as backfill (Keller, 1995), (b) geosynthetic reinforced MSEW constructed with locally available - marginal soil backfill in Bursa, Turkey (Guler and Ocbe, 2003)....4
Figure 1.2. Failure of (a) geogrid reinforced MSEW with a clayey soil backfill (Scarborough, 2005), (b) geosynthetic reinforced MSEW backfilled with low plasticity silty clay (Yang et al., 2018)....4
Figure 2.1. Definitions of reinforced fill from US transportation agency survey responses for (a) "high fines", (b) "high plasticity" (Marr and Stulgis, 2013)....14
Figure 2.2. Summary of the responses from U.S. transportation agencies for (a) compaction requirements, and (b) specified moisture content of reinforced fill (Marr and Stulgis, 2013)....15
Figure 2.3. Reinforcement utilized also as drainage (a) high strength (reinforced) nonwoven geotextile, (b) geogrid with in-plane drainage property (Zornberg and Kang, 2005)....17
Figure 2.4. Soil classification boundaries of RSCS (Park and Santamarina, 2017) 20
Figure 2.5. Different particle packing arrangements of coarse-fine soil matrices (Monkul and Ozden, 2007)....23
Figure 2.6. Particle diameter ratio, χ and transitional fines content (TFC) relationship (Rahman and Lo, 2008)....26
Figure 2.7. Schematic variation of active and inactive voids according to fines content (Chang et al., 2017)....27
Figure 2.8. (a) Liquid limit, (b) apparent liquid limit of clay matrix as a function of clay content (Kumar and Muir Wood, 1999)....29
Figure 2.9. Effect of (a) fines content, and (b) particle size ratio on the binary mixtures' minimum void ratio (Lade et al., 1998)....30

Figure 2.10. Comparison of different methods for the determination of transitional fines content (Zuo and Baudet, 2015) 32
Figure 2.11. Different compaction energy and fines content change according to (a) void ratio, (b) granular void ratio (Kim et al., 2016) 33
Figure 2.12. (a) Hydraulic conductivity prediction ranges of different correlations, (b) flow chart for the selection of the most reliable method (Chapuis, 2012) 40
Figure 2.13. Critical state friction angle variation and inferred trend according to clay fraction (Simpson and Evans, 2015) 47
Figure 2.14. Binary mixtures' peak shear strength as a function of mixing ratio and normal stress in direct shear testing (Vallejo, 2001) 48
Figure 2.15. (a) Normalized shear strength (as a function of the intergranular void ratio), and (b) state diagram for normalized mean effective stress at the onset of structural collapse (Ovando-Shelley and Pérez, 1997) 49
Figure 2.16. Effect of fines content on liquefaction resistance of silt-sand mixtures for constant global, intergranular, and interfine void ratio and cyclic stress ratio, CSR (Xenaki and Athanasopoulos, 2003) 51
Figure 2.17. Definition of SSL and state parameter (Been et al., 1991) 53
Figure 2.18. Effective stress paths for undrained triaxial tests (Pitman et al., 1994) 54
Figure 2.19. Critical state line, instability line, and instability zone defined by drained and undrained tests for loose sand (Chu and Leong, 2002) 55
Figure 2.20. Intergranular void ratio with fines content variation under different oedometer stresses (Monkul and Ozden, 2007) 60
Figure 2.21. Compression parameters with the variation of fines content (Monkul and Ozden, 2007) 60
Figure 2.22. Consolidation curves of sand and marine clay mixtures at different stress levels (a) 50 kPa, (b) 800 kPa (Shi and Yin, 2018) 62
Figure 2.23. Comparison of normal compression lines of BRS and results of Coop and Lee (1993) (Martins et al., 2001) 64

Figure 2.24. Collection of the particle size distribution of soils exhibiting transitional and non-convergent compression behavior (Shipton, 2010) 65
Figure 2.25. Interaction mechanisms in a geosynthetic reinforced soil wall (Palmeira, 2009) 66
Figure 2.26. Plan and cross views of the pullout apparatus (Zornberg and Kang, 2005) 69
Figure 2.27. Experimental pullout apparatus (Clancy and Naughton, 2011) 70
Figure 2.28. Reinforced soil wall displacements in centrifuge testing by using (a) weaker geogrid, (b) stronger geogrid (Balakrishnan and Viswanadham, 2016) 71
Figure 2.29. Natural and geogrid reinforced sand behavior for (a) shear strength, (b) dilatancy (Bauer and Zhao, 1993) 75
Figure 2.30. Different setups of the lower box (Liu et al., 2009a) 76
Figure 2.31. Cross-section of the direct shear box (Abdi et al., 2009) 79
Figure 2.32. Increase in bond coefficient with sandwich technique (Abdi et al., 2009) 79
Figure 2.33. Geogrid fixed to the aluminum plate (O'Kelly and Naughton, 2008) 80
Figure 3.1. Soil products stocked for the preparation of soil mixtures 85
Figure 3.2. The particle shape of fine gravel 86
Figure 3.3. View of the soil products 87
Figure 3.4. Particle size distribution curves of soil products 88
Figure 3.5. Particle size distribution curves of the prepared soil mixtures 90
Figure 3.6. Views from the geotechnical index test applications for CFM 93
Figure 3.7. (a) Geogrid with in-plane drainage property, (b) nonwoven geotextile bonded to the drainage channels along the reinforcement strips 94
Figure 3.8. Stress-strain curves of geogrid obtained from tensile tests 95
Figure 3.9. The view of the tensile test of the geogrid 95
Figure 3.10. (a, b) Removal of the geotextile from in-plane drainage channels in geocomposite, (c) geogrid prepared for testing 96

Figure 3.11. Methylene blue (MB) spot test apparatus 97
Figure 3.12. (a) Mixing of soil suspension after each addition of MB solution, (b) permanent blue halo around the soil suspension spot 98
Figure 3.13. (a) Apparatus, (b) test setup, and (c) permeameter cell for constant head hydraulic conductivity test of granular soils 100
Figure 3.14. Apparatus for flexible wall hydraulic conductivity testing of CFM 103
Figure 3.15. Test setup with integrated equipment for flexible wall hydraulic conductivity testing of CFM 103
Figure 3.16. Dynamic compaction apparatus: (a) compaction tools (b) split mold 104
Figure 3.17. Calculated layer thicknesses for cylindrical specimen preparation according to the undercompaction method 106
Figure 3.18. CFM specimens prepared in the split mold 107
Figure 3.19. Coating of the large gaps with a thin layer of moistened kaolin clay 107
Figure 3.20. Sealing the specimen between the top and bottom plates with O-rings 108
Figure 3.21. (a) Test setup with integrated measuring equipment, and (b) other apparatus for unconfined compressive strength tests 110
Figure 3.22. Placement of the specimen to the unconfined compressive strength equipment 111
Figure 3.23. Apparatus used for triaxial compression tests 113
Figure 3.24. Loading frame and the cell for triaxial compression tests 113
Figure 3.25. (a) Schematic, and (b) general view of the setup for compression tests 117
Figure 3.26. (a) Equipment for data acquisition, (b) steel mold, filter papers, loading plate, and the compaction apparatus 118
Figure 3.27. (a) Sample placement, and (b) dynamic tamping with the compaction apparatus 119

Figure 3.28. (a) Submersion in a water bath, and (b) submerged compression tests for coarse-fine mixtures 121
Figure 3.29. General view (side view) of the large direct shear testing equipment at METU Civil Engineering Department 122
Figure 3.30. Schematic diagram of the front view of the large direct shear testing equipment 123
Figure 3.31. Schematic diagram of the side view of the large direct shear testing equipment 124
Figure 3.32. The mechanism for the separation of the upper and lower boxes 127
Figure 3.33. The view of the geogrid clamping mechanism 129
Figure 3.34. (a) Dynamic compaction apparatus, (b) guiding frame, (c) porous plates, loading plate, and additional tools 129
Figure 3.35. Soil surface protruding from the lower box level on which the geogrid will be placed 131
Figure 3.36. Schematic view of the specimen preparation with dynamic compaction for (a) CFM without geogrid, (b) CFM with geogrid 133
Figure 3.37. Views of specimen preparation stages for the large direct shear test of SW and SP soil mixtures 136
Figure 3.38. Views of specimen preparation stages for the large direct shear test of CFM 138
Figure 3.39. Views of specimen preparation stages for the large direct shear test of all mixtures 139
Figure 3.40. Water reservoir placed to supply pressurized water 140
Figure 3.41. Pressurized water supply system for the direct shear specimens 141
Figure 3.42. Monitoring the water level with piezometer pipes 142
Figure 3.43. Positions of the piezometer pipes within the compacted specimen 143
Figure 3.44. Preparation of the pressure transducer to be placed in the specimen 144
Figure 3.45. Calibration of the pressure transducer 144

Figure 3.46. (a) Placement, and (b) vertical position of the pressure transducer within the compacted specimen 145
Figure 3.47. (a) The position of the rollers, and (b) the gap between the boxes just before the shear test..... 147
Figure 4.1. Classification charts for (a) S12-5, (b) S12-15, (c) S20-5, (d) S20-15 according to RSCS of Park and Santamarina (2017)..... 154
Figure 4.2. Classification charts for (a) S30-5, (b) S30-15, (c) S40-5, (d) S40-15 according to RSCS of Park and Santamarina (2017)..... 155
Figure 4.3. Methylene Blue spot test results for (a) kaolin, (b) bentonite 161
Figure 4.4. Methylene Blue spot test results for (a) S12-5 for sample finer than No. 40 sieve, (b) S40-15 for sample finer than No. 200 sieve..... 162
Figure 4.5. Standard Proctor compaction curves for CFM..... 168
Figure 4.6. Maximum dry unit weight with (a) optimum moisture contents, (b) fines contents..... 169
Figure 4.7. (a) LL and PL for PI=5% CFM (S12-5, S20-5, S30-5, S40-5), (b) LL and PL for PI=15% CFM (S12-15, S20-15, S30-15, S40-15), and (c) change in LL with fine sand for CFM samples passing No. 40 sieve..... 170
Figure 4.8. (a) SSA change with bentonite content for CFM with PI=15% and passing through No. 200 sieve, (b) SSA change with kaolin content for CFM with PI=5% and passing through No. 200 sieve 172
Figure 4.9. Relationship between initial void ratio (e_0) at the 95% Proctor compaction and the void ratio after saturation (e) 174
Figure 4.10. Relationship between FC with global void ratio after saturation (e), intergranular void ratio (e_s), and interfine void ratio (e_f)..... 175
Figure 4.11. Relationship between intergranular relative density and fines content of CFM..... 177
Figure 4.12. Hydraulic conductivity with fines content and plasticity index for saturated soil mixtures (*according to Casagrande and Fadum, 1940) 178
Figure 4.13. Changes in hydraulic conductivity (a) with d_{10}, d_{50} values of CFM, (b) with clay fractions of CFM 179

Figure 4.14. Hydraulic conductivity versus global void ratio (e), intergranular void ratio (e_s), and interfine void ratio (e_f) (*according to Casagrande and Fadum, 1940) for CFM specimens 180
Figure 4.15. Comparison of hydraulic conductivity results with the empirical predictions 182
Figure 5.1. Failure surfaces after unconfined compressive strength tests of CFM 188
Figure 5.2. Percent volumetric strain with time for CFM having PI=5% under consolidation pressures of (a) σ'_c=40 kPa, (b) σ'_c=150 kPa, and (c) σ'_c=300 kPa 190
Figure 5.3. Percent volumetric strain with time for CFM having PI=15% under consolidation pressures of (a) σ'_c=40 kPa, (b) σ'_c=150 kPa, and (c) σ'_c=300 kPa 191
Figure 5.4. (a) View of the specimen in the triaxial cell after a completed test, failure shapes of the specimens for (b) S20-15, (c) S30-15, and (d) failure shapes of the S40-5 (after oven-drying) for tests having different consolidation pressures 194
Figure 5.5. Repeated triaxial test results (a) deviatoric stress with axial strain, (b) pore pressure with axial strain 195
Figure 5.6. Deviatoric stress with axial strain for (a) σ'_c=40 kPa, (b) σ'_c=150 kPa, and (c) σ'_c=300 kPa; pore pressure with axial strain for (d) σ'_c=40 kPa, (e) σ'_c=150 kPa, and (f) σ'_c=300 kPa 197
Figure 5.7. Axial strain with time plots of the repeated compression tests on CFM for (a) unsubmerged tests of S40-5, (b) submerged tests of S20-15 200
Figure 5.8. (a) View of the specimen in the mold, (b) after the compression tests 201
Figure 5.9. Compression test results for (a) unsubmerged tests, (b) submerged tests 202
Figure 5.10. Compressive stress with axial strain plots of representative unconfined compression tests 203

Figure 5.11. Representative test results for (a) unconfined compressive strength with fines content, (b) axial strain at failure with fines content..... 204
Figure 5.12. Modified Mohr-Coulomb failure envelopes for total stress (a), (c), and effective stress (b), (d) 207
Figure 5.13. Variation of consolidated undrained and effective angle of internal friction with fines content 209
Figure 5.14. Stress paths during undrained triaxial tests for (a) PI=5%, (b) PI=15% 210
Figure 5.15. Mean effective stress change in e-p' space for (a) PI=5%, (b) PI=15% 211
Figure 5.16. Variation of stress ratio at critical state with fines content and plasticity index 212
Figure 5.17. Specimens having low initial contraction followed by dilation in undrained triaxial tests 214
Figure 5.18. Specimens having high initial contraction followed by dilation in undrained triaxial tests 214
Figure 5.19. Specimens having contraction in undrained triaxial tests 215
Figure 5.20. Quantification of initial contraction tendencies in undrained loading 217
Figure 5.21. Variation of axial strain at failure with fines content and plasticity index in undrained triaxial tests 220
Figure 5.22. Brittleness indices of CFM with PI=5%..... 220
Figure 5.23. Pore pressure parameter at failure (A_f) with fines content 221
Figure 5.24. Secant deformation modulus at 50% of the peak strength with fines content and plasticity index..... 223
Figure 5.25. Normalized secant deformation modulus at 50% of the peak strength with fines content and plasticity index..... 224
Figure 5.26. Secant deformation modulus with fines content for σ'_c=40 kPa..... 225
Figure 5.27. Secant deformation modulus with fines content for σ'_c=150 kPa..... 225
Figure 5.28. Secant deformation modulus with fines content for σ'_c=300 kPa..... 226

Figure 5.29. Secant deformation modulus at 0.5% axial strain with consolidation pressure 227
Figure 5.30. Deviatoric stress measurements in small strains for S40-5, S30-15, and S40-15 (a) σ'_c=150 kPa, (b) σ'_c=300 kPa 227
Figure 5.31. The final volumetric strain of all CFM at the end of the consolidation 230
Figure 5.32. Change in intergranular relative density with fines content for different consolidation pressures 231
Figure 5.33. Void ratio change with normal stress for unsubmerged and submerged compression tests of (a) S12-5 and S20-5, (b) S30-15 and S40-15 236
Figure 5.34. Void ratio change with normal stress for unsubmerged and submerged compression tests of S12-15, S20-15, S30-5 and S40-5 237
Figure 5.35. Compression index variation with fines content and plasticity index for unsubmerged and submerged tests 238
Figure 5.36. Rebound index variation with fines content and plasticity index for unsubmerged and submerged tests 238
Figure 5.37. Change in intergranular relative density with fines content for unsubmerged CFM in compression tests 239
Figure 5.38. Secant constrained modulus as a function of normal stress for CFM with (a) PI=5%, and (b) PI=15% 241
Figure 6.1. Settlement stage of large direct shear tests 245
Figure 6.2. Vertical displacement plots of specimens in the settlement stage 246
Figure 6.3. The position of the geogrids and the views of the failure surfaces after direct shear tests for saturated specimens 247
Figure 6.4. The position of the geogrids and the views of the failure surfaces after direct shear tests for specimens compacted at optimum moisture content 248
Figure 6.5. Corrected shear stress with horizontal displacement plots of the repeated direct shear tests 249
Figure 6.6. The shape of the failure surfaces after direct shear tests of CFM 251
Figure 6.7. Failure envelopes of SW and SP soil mixtures 252

Figure 6.8. Corrected shear stress with horizontal displacement plots of CFM having (a) PI=5%, and (b) PI=15%..... 253
Figure 6.9. Vertical displacement with horizontal displacement plots of CFM for (a) PI=5% and σ_n=105 kPa, (b) PI=15% and σ_n=105 kPa, (c) PI=5% and σ_n=155 kPa, and (d) PI=15% and σ_n=155 kPa..... 254
Figure 6.10. Cohesion intercept and angle of internal friction variation with fines content and plasticity index..... 256
Figure 6.11. Relative horizontal displacement variation with fines content, plasticity index, and normal stress..... 258
Figure 6.12. Failure surface views of soil mixture-geogrid interface in direct shear tests..... 260
Figure 6.13. Deformation of the transverse ribs in direct shear tests..... 261
Figure 6.14. Corrected shear stress with horizontal displacement plots of CFM having a slight stress increase after ultimate (residual) strength was reached for (a) σ_n=55 kPa, (b) σ_n=105 kPa, and (c) σ_n=155 kPa..... 264
Figure 6.15. Corrected shear stress with horizontal displacement plots of tests not reaching an ultimate (residual) strength..... 265
Figure 6.16. Failure envelopes for (a) SW and (b) SP soil mixtures for tests with and without geogrid..... 265
Figure 6.17. Failure envelopes for CFM having PI=5% (a, b, and c); and CFM having PI=15% (d, e, and f) for tests with and without geogrid..... 266
Figure 6.18. Variation of (a) efficiency on friction, and (b) efficiency on cohesion with fines content..... 269
Figure 6.19. Variation of the peak interface shear strength coefficient with fines content for tests with draining geogrid..... 271
Figure 6.20. Comparison of the peak and ultimate (residual) interface shear strength coefficients of soil mixtures..... 272
Figure 6.21. Vertical displacement with horizontal displacement plots of CFM with and without geogrid for PI=5% (a, b, c), and for PI=15% (d, e, f)..... 273

Figure 6.22. Comparison of the saturated tests' corrected shear stress with horizontal displacement plots for (a) S20-5, and (b) S20-15 276
Figure 6.23. Comparison of the saturated tests' corrected shear stress with horizontal displacement plots for (a) S40-5, and (b) S40-15 277
Figure 6.24. Excess pore water pressure with horizontal displacement during shear in saturated direct shear tests.....280
Figure 6.25. Views of the piezometer pipes during shear (a) initial level, (b) pore pressure increase, and (c) pore pressure decrease for S20-5 soil mixture. (d, e) Pore pressure increase in S40-15.....281
Figure 6.26. Comparison of the saturated tests' vertical displacement with horizontal displacement plots for (a) S20-5, (b) S20-15, (c) S40-5, and (d) S40-15 283
Figure 6.27. Comparison of the direct shear test results with 0.25 mm/min and 0.01 mm/min shear rates. (a) corrected shear stress-horizontal displacement plot, and (b) vertical displacement-horizontal displacement plot.....285
Figure A.1. SW (a, b) and SP (c, d) soil mixtures……328
Figure A.2. S12-5 (a, b) and S12-15 (c, d) soil mixtures……329
Figure A.3. S20-5 (a, b) and S20-15 (c, d) soil mixtures……330
Figure A.4. S30-5 (a, b) and S30-15 (c, d) soil mixtures……331
Figure A.5. S40-5 (a, b) and S40-15 (c, d) soil mixtures……332
Figure A.6. SW (a, b) and SP (c, d) soil mixtures with geogrid having draining property (DG)……333
Figure A.7. S12-5 (a, b) and S12-15 (c, d) soil mixtures with geogrid having draining property (DG)……334
Figure A.8. S20-5 (a, b) and S20-15 (c, d) soil mixtures with geogrid having draining property (DG)……335
Figure A.9. S30-5 (a, b) and S30-15 (c, d) soil mixtures with geogrid having draining property (DG)……336
Figure A.10. S40-5 (a, b) and S40-15 (c, d) soil mixtures with geogrid having draining property (DG)……337

Figure A.11. S20-5 (a, b) and S20-15 (c, d) soil mixtures and geogrid without draining property (G)……..……..……...…338
Figure A.12. S40-5 (a, b) and S40-15 (c, d) soil mixtures and geogrid without draining property (G)……..……..……...…339
Figure A.13. Saturated S20-5 (a, b) and S20-15 (c, d) soil mixtures with geogrids……..……..……..……...…340
Figure A.14. Saturated S40-5 (a, b) and S40-15 (c, d) soil mixtures with geogrids……..……..……..……...…341
Figure A.15. Soil mixtures tested with a shear rate of 0.01 mm/min……...…...342

LIST OF ABBREVIATIONS

ABBREVIATIONS

AASHTO	American Association of State Highway and Transportation Officials
ASTM	American Society for Testing and Materials
BS	British Standards
CF	Clay Fraction
CFM	Coarse - Fine Mixtures
COV	Coefficient of Variations
CSL	Critical State Line
CSSM	Critical State Soil Mechanics
CU	Consolidated Undrained
ESCS	European Soil Classification System
FC	Fines Content
FHWA	Federal Highway Administration
HDPE	High-Density Polyethylene
LL	Liquid Limit
MCHW	Manual of Contract Documents for Highway Works
MSEW	Mechanically Stabilized Earth Wall
NCL	Normal Compression Line
NCMA	National Concrete Masonry Association

OCR	Over-Consolidation Ratio
PET	Polyethylene Terephthalate
PI	Plasticity Index
PL	Plastic Limit
PP	Polypropylene
RSCS	Revised Soil Classification System
SSA	Specific Surface Area
TFC	Transitional Fines Content
UCS	Unconfined Compression Strength
USCS	Unified Soil Classification System

LIST OF SYMBOLS

SYMBOLS

A	Skempton's pore pressure parameter
A_0	Initial cross-sectional area of the specimen
A_c	Cross-sectional area of the specimen after consolidation in triaxial test
A_C	Corrected area in large direct shear tests
$A_{cor.}$	Corrected average cross-sectional area of the specimen
A_f	Skempton's pore pressure parameter at failure
A_{MB}	Area covered by one methylene blue molecule
A_v	Avogadro's number
a	Intercept of the modified Mohr-Coulomb envelope with the y-axis
b	Percentage of fines contributing force transfer in coarse-fine mixtures
C_C	Compression index
C_c	Coefficient of curvature
$C_{c\text{-}s}$	Granular compression index
C_F	Constant related to pore topology
C_H	Hazen's coefficient
C_k	Permeability change index
C_s	Rebound Index
C_u	Coefficient of uniformity

CF	Clay fraction
$CF_{No.40}$	Clay fraction measured from the soil passing through No. 40 sieve
$CF_{No.200}$	Clay fraction measured from the soil passing through No. 200 sieve
c'	Effective cohesion
c_a	Adhesion intercept
c_v	Coefficient of consolidation
D_c	Diameter of the specimen after consolidation
D_r	Relative density
D_{rs}	Intergranular relative density
d	Drainage distance
d_{10}	Particle size corresponding to 10% passing by mass
d_{50}	Particle size corresponding to 50% passing by mass
E_c	Efficiency on cohesion
E_m	Young's modulus for the membrane material for triaxial tests
E_s	Secant deformation modulus
E_{50}	Secant deformation modulus at 50% of the peak strength
E_ϕ	Efficiency on friction
e	Global void ratio
e_0	Initial void ratio
e_c	Void ratio after consolidation
e_{cs}	Critical state void ratio

e_f	Interfine void ratio
e_L	Void ratio at liquid limit
$e_{max,HS}$	Maximum void ratio of the host granular soil
$e_{min,HS}$	Minimum void ratio of the host granular soil
e_{max}	Maximum void ratio
e_{min}	Minimum void ratio
e_s	Intergranular void ratio
$(e_s)_{eq}$	Equivalent granular void ratio
FC	Fines content
f_{ds}	Coefficient of resistance to direct sliding
F_N	Normal load
F_S	Shear force
$G_{1@20°C}$	Measured specific gravity for part of the soil retained on 4.75 mm sieve at 20°C
$G_{2@20°C}$	Measured specific gravity for part of the soil passing the 4.75 mm sieve at 20°C
$G_{avg@20°C} = G_T$	Average specific gravity of a soil having particles both smaller and larger than 4.75 mm / Average specific gravity of total mixture
G_C	Specific gravity of coarse grains
G_F	Specific gravity of fine grains
G_S	Specific gravity of solid particles
H_0	Initial height of the specimen

H_c	Height of the specimen after consolidation
h_n	Height of the compacted material at the top of the layer being considered for undercompaction method
h_t	Final height of the specimen for undercompaction method
I_0	Intercept of the straight line with the x-axis in grain size distribution plot
I_B	Brittleness index
i	Hydraulic gradient
k	Hydraulic conductivity
k_{sat}	Saturated hydraulic conductivity
L_0	Initial length of the specimen
L	Length of the specimen
L	Length of the direct shear box
LL	Liquid limit
M	Slope of the critical state line (CSL) projected into p'-q space
M_s	Secant constrained modulus
m_{dry}	Dry soil mass
m_c	Mass of clay in a soil composite
m_v	Coefficient of volume compressibility
m_w	Mass of water
n_t	Total number of layers for undercompaction method
N	Number of increments in Methylene Blue Spot Test
P	Applied load to a specimen

P	Percent of soil passing the 4.75 mm sieve
PL	Plastic limit
PI	Plasticity index
p'	Mean effective stress
q	Deviatoric stress
q_u	Unconfined compressive strength
R	Percent of soil retained on 4.75 mm sieve
R	Rate of shear displacement in large direct shear tests
S_r	Degree of saturation
S_S	Specific surface area
SSA_{TOTAL}	Total specific surface area of a coarse-fine mixture
SSA_F	Specific surface area of sample passing through No. 200 sieve
SSA_C	Specific surface area of sample retained on No. 200 sieve
t_{90}	Time corresponding to completion of 90% of the primary consolidation
t_m	Thickness of the membrane
U_n	Percent undercompaction for layer n
U_{ni}	Percent undercompaction selected for the first layer
U_{nt}	Percent undercompaction selected for the final layer
u	Pore water pressure
u_{excess}	Excess pore water pressure
V_0	Initial volume of the specimen

V_{sat}	Saturated volume of the specimen
w	Moisture content of the specimen
w_c	Clay water content
w_L	Liquid limit
w_{opt}	Optimum moisture content obtained by standard Proctor test
α	Interface shear strength coefficient
α	Slope of the modified Mohr-Coulomb envelope
α_{ds}	Fraction of grid surface area that resists direct shear with soil
Γ	Intercept of the critical state line (CSL) projected into ν-lnp' space
$\gamma_{d,max}$	Maximum dry unit weight obtained by standard Proctor test
γ_w	Unit weight of water
Δd	Horizontal (shear) displacement in large direct shear tests
ΔH	Change in height of the specimen as determined from vertical deformation indicator
ΔH_0	Change in height of the specimen at the end of consolidation
ΔH_c	Change in height of the specimen during compression test
ΔH_s	Change in height of the specimen during saturation
Δh	Average head loss across the specimen
ΔL	Length change of specimen as read from the vertical displacement indicator
ΔQ	Quantity of flow for a given time interval
Δt	Time interval

ΔV_c	Change in volume of the specimen during consolidation
ΔV_{sat}	Change in volume of the specimen during saturation
$\Delta(\sigma_1 - \sigma_3)_m$	Membrane correction to be subtracted from the measured principal stress difference
δ	Angle of friction of the interface
ε_1	Axial strain for the given axial load for unconfined compressive and triaxial strength tests
ε_f	Axial strain at failure for the given axial load for unconfined compressive and triaxial strength tests
ε_a	Axial strain in laterally constrained state
λ	Slope of the critical state line (CSL) projected into ν-lnp' space
μ_w	Dynamic viscosity of water
ν	Specific volume
ρ	Percent open area
ρ_{dry}	Dry density of the soil specimen
ρ_{bulk}	Bulk density of the soil specimen
ρ_m	Mineral mass density of the soil
ρ_{min}	Minimum dry density of the soil
ρ_{max}	Maximum dry density of the soil
ρ_s	Density of the solid grains
ρ_w	Density of the water
σ'_1	Major principal effective stress
σ'_3	Minor principal effective stress

$\sigma_1 - \sigma_3$	Measured principal stress difference
σ'_c	Consolidation pressure
σ_{UCS}	Unconfined compressive stress for a given applied load
σ_n	Normal stress
τ	Shear stress
$\tau_{interface}$	Total shear resistance of the soil-geogrid interface
τ_p	Peak (yield) shear strength
τ_r	Ultimate (residual or critical state) shear strength
$\tau_{soil\text{-}geogrid}$	Shear resistance between soil and the surface of the geogrid
$\tau_{soil\text{-}soil}$	Internal shear strength of the soil itself
υ_f	Kinematic viscosity of the fluid
ϕ	Angle of internal friction
ϕ'	Effective angle of internal friction
ϕ_{CU}	Angle of internal friction in consolidated undrained triaxial tests
ϕ_{ds}	Angle of internal friction for soil in direct shear
Ψ	State parameter

CHAPTER 1

INTRODUCTION

1.1 Problem Statement

For decades, engineering properties of cohesive and cohesionless soils have been a research subject, both theoretically and experimentally. Most of the past research has focused on the properties and behavior of distinct groups of pure cohesive or cohesionless soils and the majority of design methods have been developed considering these two groups of soils. However, most soils found in nature are composed of relative percentages of cohesionless coarse and cohesive fine particles and may not fit into the distinct groups of "cohesive" and "cohesionless" soils in terms of their behavior or properties. These soils may also need to be used as embankment and earth dam fills, backfill soil in retaining walls, or seepage barriers according to the need and given requirements of a project. Coarse soil particles provide higher constructability, better shear strength and drainage properties, and lower compressibility potential, whereas fine particles are beneficial in lowering the hydraulic conductivity of the soil composite (Chung et al., 2018). The behavioral thresholds of fines content and plasticity after which the soil composite behaves as "cohesive" or "clayey" soil has been an important research question in the literature. In previous studies, these soils were defined differently as "clay/sand mixtures" (Kumar, 1996; Cabalar and Mustafa, 2015a), "composite soils" (Li, 2017; Al-Moadhen et al., 2018), "coarse-fine mixtures" (Park and Santamarina, 2017; Chung et al., 2018), "intermediate soils" (Tanaka et al., 2001; Lee et al., 2016), "marginal fills" (Christopher et al., 1998; Sandri, 2005), "poorly draining soils" (Zornberg and Mitchell, 1994; Lopez et al., 2006) or "transitional soils" (Ferreira and Bica, 2006; Shipton and Coop, 2012). In this study, the term coarse-fine mixtures

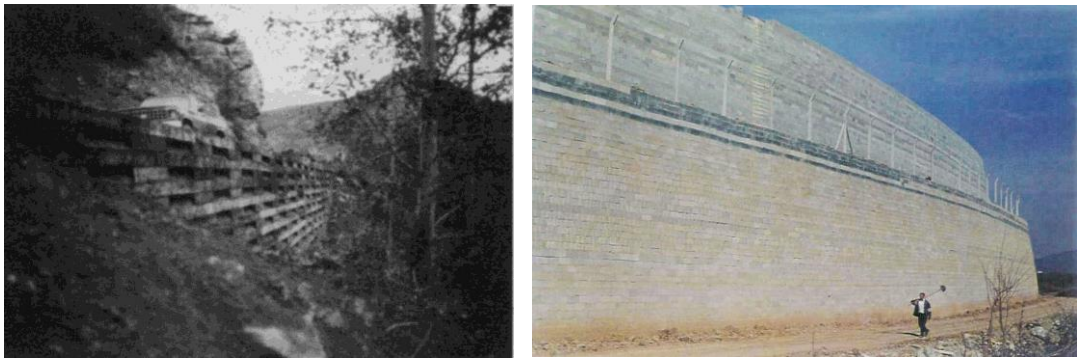
(CFM) will be used, and the percentage of particles passing No. 200 sieve (smaller than 75 microns) is defined as the fines content (FC).

There is an increasing tendency to use CFM instead of clean granular soils in geotechnical projects because of economical, environmental, and sustainability concerns. One of these applications is the mechanically stabilized earth walls (MSEW) and slopes, which are reinforced soil masses consisting of reinforcement elements (e.g., metal or geosynthetic), compacted backfill soil with or without wall facing elements. Most of the current technical manuals, codes, and design guidelines recommend using clean granular materials as backfill soils. Abu-Farsakh et al. (2004) listed their advantages as providing high shear strength, stable engineering properties with time and varying moisture contents, and free-drainage characteristics. However, some practical, economical, and environmental disadvantages are also associated with using clean granular fill materials recommended in guidelines (Christopher and Stulgis, 2005). Ekici et al. (2022) stated that these could be summarized as availability and accessibility problems associated with clean granular borrow materials and the negative effects of mining them on natural resources and ecosystems (UNEP GEAS, 2014). Raja et al. (2012) reported that clean granular fill materials have a larger carbon footprint than fill materials recovered on-site in a project life cycle. In addition, obtaining and transporting them to the construction site is generally quite expensive (Simons and Cameron, 2012). Durukan and Tezcan (1992) pointed out that the most expensive component of the MSEW is the supply of granular fill, which corresponds to 40% of the total construction cost. Christopher and Stulgis (2005) also indicated that fill material accounts for 30-40% of the total cost of an MSEW. In addition, they added that the cost difference between high-quality permeable fill and high fines-content soil can be as much as two to three times. Marr and Stulgis (2013) pointed out that MSEW costs can be reduced by 20 to 30% by replacing fill materials (as specified by AASHTO) with "higher fines" fill materials in the NCHRP 24-22 report. Because of the abovementioned reasons, there is an increasing demand to employ CFM in MSEW applications. Marr and Stulgis (2013) presented a survey of the responses of

49 U.S. state transportation agencies and National Concrete Masonry Association (NCMA) for the current design and construction practice of MSEW in NCHRP 24-22. The following important conclusions were drawn in this report:

- Both acceptable and unacceptable MSEW performances have been observed by the few transportation agencies that have allowed "high fines" soil usage in reinforced fills.
- "High fines" soil properties that satisfy acceptable performance criteria must be demonstrated for U.S. transportation agencies to adopt the usage of them as backfill soil.
- It is more common to use "high fines" and/or "high plasticity" soils as backfill in the private sector. Many successful applications have been reported, especially when water did not enter the reinforced backfill.

Case studies that successfully employ CFM as reinforced backfill was reported by researchers (Keller, 1995; Sandri et al., 2000; Guler and Ocbe, 2003; Yang et al., 2012) and some such examples are shown in Figure 1.1. On the other hand, various wall failures with CFM use have also been reported (Burwash and Frost, 1991; Gassner and James, 1998; Scarborough, 2005; Yang et al., 2018), as given in Figure 1.2.



(a) (b)

Figure 1.1. (a) Timber-faced geogrid reinforced wall constructed by using locally available soil as backfill (Keller, 1995), (b) geosynthetic reinforced MSEW constructed with locally available - marginal soil backfill in Bursa, Turkey (Guler and Ocbe, 2003)



(a) (b)

Figure 1.2. Failure of (a) geogrid reinforced MSEW with a clayey soil backfill (Scarborough, 2005), (b) geosynthetic reinforced MSEW backfilled with low plasticity silty clay (Yang et al., 2018)

Factors causing MSEW to fail have been investigated by researchers (Mitchell and Zornberg, 1995; Koerner and Koerner, 2013). Some concerns regarding the use of CFM as backfill soil in MSEW can be listed as:

- Pore water pressure generation in the fill during compaction, subsequent loading, and surcharging (Mitchell, 1981; Christopher et al., 1998).
- Lower shear strength and higher movements, and creep potential after construction (Zornberg and Mitchell, 1994).

- Compaction difficulties of poorly draining soils (Zornberg and Mitchell, 1994).
- Reduction of shear resistance between the geosynthetic - soil interface depending on the build-up of pore pressure (Naughton et al., 2001).
- Poorly draining cohesive soils being chemically more aggressive than cohesionless soils and increase the risk of corrosion of metallic reinforcements (Zornberg and Mitchell, 1994).
- Seepage development in the reinforced fill (Christopher et al., 1998).
- Loss of shear strength because of the backfill soil wetting, which is associated with the post-construction infiltration (Christopher et al., 1998).

Although there are problems and concerns associated with using CFM in MSEW as backfill soils, the problems listed above and wall failure case studies reveal that most of the problems involve the development of pore water pressure inside the backfill body, insufficient drainage measures, and poor backfill soil properties. It is well known that even a few percent of fines may result in a significant change in drainage characteristics (FHWA, 2009). Studies show that in case adequate and proper drainage is provided within the compacted backfill, soils involving fine and cohesive particles could also be used as fill materials (Kempton et al., 2000; Zornberg and Kang, 2005; O'Kelly and Naughton, 2008).

Because of the abovementioned reasons, technical design codes bring limitations for using fine, cohesive materials in reinforced soil walls. There is a lack of clarity in the design and analysis with soils containing fine-grained cohesive particles (Raja et al., 2012). Designating suitable backfill soil properties and the definition of "high fines" and "high plasticity" remain crucial and yet not clearly described points for the design of MSEW with CFM. Restrictions of the design guidelines differ because of the variances in the estimated behavior of these materials. Therefore, further research should be focused on the properties of CFM, their behavioral threshold fines content and plasticity, as well as their interaction with geosynthetics.

1.2 Objectives of the Study

This study aims to investigate the geotechnical properties of compacted CFM in terms of the effects of fines content and plasticity index on soil classification, index properties, compressibility, hydraulic conductivity, and shear strength, as well as CFM – geogrid interaction in direct shear failure mode by conducting large direct shear tests (300 mm x 300 mm cross-section).

Identifying the behavioral thresholds and investigating CFM characteristics require parameter-controlled experimentation. Collecting data from field and laboratory experimentation could help improve the allowable backfill soil properties database. As the soils having the potential to be included in the standards are clarified in the future, the criteria and procedures in design guidelines may eventually be reshaped. In addition, a more accurate prediction of the real soil-reinforcement interaction will be enabled with numerical modeling for a more reliable and precise design.

The main research questions in this study are:

- What are the threshold fines content and plasticity index values that would make the CFM behave similar to a "cohesive" or "clayey" soil in terms of hydraulic, compressibility, and mechanical properties?
- Are the existing soil classification systems able to accurately represent the different properties of CFM?
- Is the CFM-geogrid interface friction coefficient within acceptable ranges as reported in the literature? What are the effects of fines content and plasticity index on CFM-geogrid interaction? When the compacted CFM gets inundated with water (i.e., its degree of saturation increases), is the interface friction affected?
- Does CFM have the potential to be used as a backfill soil in MSEW, and if so, under what restrictions?

Target CFM properties were selected to identify behavioral thresholds and address the suitable backfill restrictions in commonly used design guidelines. Accordingly, the objectives of this study can be summarized as follows:

- To highlight the shortcomings of commonly used soil classification systems in representing the governing hydraulic and mechanical properties of transitional, mixed soils (CFM).
- Examining the relationship between specific surface area, Atterberg limits, and hydraulic properties of coarse-fine mixtures (CFM).
- Identification of the behavioral threshold fines content and plasticity index that governs hydraulic, mechanical, and compressibility properties of CFM.
- To investigate the effects of fines content and plasticity index on CFM-geogrid interaction via large direct shear tests for two different geogrids with and without in-plane drainage.

1.3 Research Scope

In the scope of this study, ten different soil mixtures having FC of 0%, 12%, 20%, 30%, 40%, and PI of 5% and 15% were prepared by mixing commercially available soil products in prescribed ratios. Soil products were crushed gravel, sands (coarse, medium, and fine-graded), non-plastic silt, kaolin, and bentonite. Mixing soil products in different proportions, with FC and PI being the variable parameters, allowed parameter-controlled experimentation and evaluation.

Firstly, index tests were conducted to identify CFM properties, such as particle size distribution and Atterberg limits of particles smaller than 0.425 mm (No. 40 sieve) and 0.075 mm (No. 200 sieve), compaction characteristics with the standard Proctor test, and maximum-minimum density relations. These results were used to classify prepared soil mixtures and investigate the particle packing properties.

CFM specimens having fines content were prepared by dynamic compaction at 95% of their standard Proctor dry densities at their optimum water contents because it is

the most common application in industrial practice for the compaction of the backfill soil. Rigid wall hydraulic conductivity tests for the mixtures without fines and flexible wall hydraulic conductivity tests for saturated CFM specimens were performed to determine the hydraulic conductivity. Specific surface area tests were also conducted, and results were evaluated together with the Atterberg limits.

Consolidated undrained (CU) triaxial compression tests were performed on saturated CFM specimens after isotropic consolidation of the specimens under 40, 150, and 300 kPa effective stresses. Additionally, unconfined compressive strength (UCS) tests were carried out, and the results were used to designate the strength parameters.

One-dimensional large static compression tests of partially saturated and water submerged CFM specimens were performed. Results were evaluated together with the consolidation tests to determine the compressibility properties of CFM. Consolidation data was obtained from CU triaxial compression tests conducted on saturated CFM specimens.

A large direct shear box (300 mm x 300 mm cross-section) was manufactured within the scope of this study to investigate CFM shear strength properties as well as their interaction with geogrids in direct shear failure mode. A total of 90 large direct shear tests were carried out in this study from which the strength parameters, soil-geogrid interface shear resistances, peak, and ultimate/residual strength relations, variation of interface bond strength with FC and PI, as well as the dilative/contractive response of the CFM were determined.

1.4 Thesis Organization

Following the introduction, which includes the problem statement, study's objectives, research scope, and thesis organization, Chapter 2 is dedicated to the presentation of the available literature review for the suitable backfill properties in MSEW, classification, index, hydraulic, compressibility, and strength properties of CFM.

In Chapter 3, all materials used in tests, including soil products to prepare soil mixtures, properties of the prepared soil mixtures, and geogrids; all test procedures and methodologies conducted in the study, including the description of the equipment, standards used, stages of the specimen preparation, and test programs are presented.

In Chapter 4, test results and discussion of the laboratory-prepared coarse-fine mixtures' index, specific surface area, and hydraulic conductivity properties and their classification according to different widely accepted classification systems are presented.

In Chapter 5, the compressive and shear strength of CFM is discussed within the scope of unconfined compressive and consolidated undrained triaxial compression tests, whereas compressibility properties are evaluated by consolidation data of saturated specimens in triaxial tests and one-dimensional static large compression tests.

In Chapter 6, the strength properties of CFM and their interaction with geogrids are discussed based on large direct shear tests (having a 300 mm x 300 mm cross-section).

In Chapter 7, a summary of the study, a brief presentation of the significant conclusions and highlights, usage of CFM in this study for the MSEW, and recommendations for future studies are presented.

CHAPTER 2

LITERATURE REVIEW

2.1 Backfill Properties in Reinforced Soil Walls and Slopes

Selection of the soil properties addressing the backfill material restrictions in different design guidelines and determining the geotechnical properties of these materials are among the primary motivations in this study, as stated in Section 1.2. Suitable backfill material criteria in different design guidelines are presented in Table 2.1. There are significant variances and a lack of consensus on the allowable backfill properties of international/national design codes. For instance, U.S. FHWA (2009) permits the use of soils having an FC (particles smaller than 75 μm) less than 15% and a PI less than 6%, whereas NCMA (2007) manual allows the use of soils with fines (particles smaller than 75 μm) up to 35% and PI up to 20% with the utilization of appropriate drainage system. Hong Kong's Geoguide 6 (2017) categorizes fill materials according to the height of the reinforced soil structure. Percent passing 63 μm BS sieve should be less than 10% for tall structures, whereas fines may be up to 45% and PI up to 20% for low to medium height structures and slopes. Germany's EBGEO (2011) categorizes fill materials according to whether soil structures are exposed to predominantly static or dynamic loads. The soil with the percent passing 63 μm less than 7% and friction angle more than 30° is recommended for dynamically loaded structures. AASHTO (2002), suggesting a material criteria as FHWA (2009), states that compacted fill material should exhibit an internal friction angle of not less than 34°.

Table 2.1. Suitable backfill material criteria in different guidelines

<table>
<tr><th>Code of practice</th><th>Material criteria</th></tr>
<tr><td>HA 68/94 (1994)
UK</td><td>Fill material is defined as either frictional or cohesive for highway slope design by reinforced soil</td></tr>
<tr><td>BS 8006 (1995)
UK</td><td>Frictional or cohesive frictional materials (classes 6I, 6J, 7C, and 7D as described in Specification for Highway Works) can be used as fill materials in reinforced walls and abutments</td></tr>
<tr><td>AASHTO (2002)
USA</td><td>Grading of the fill material to be used in MSEW should conform as follows:
<table><tr><th>US sieve size</th><th>Percent passing (%)</th></tr><tr><td>4 in (102 mm)</td><td>100</td></tr><tr><td>No. 40 (0.425 mm)</td><td>0-60</td></tr><tr><td>No. 200 (0.075 mm)</td><td>0-15</td></tr></table>Plasticity Index, PI≤6% (AASHTO T-90)
Compacted fill material should exhibit an internal friction angle not less than 34°</td></tr>
<tr><td>Geoguide 6 (2017)
Hong Kong</td><td>Although ideally well-graded granular materials are suggested as reinforced fill, Type I and Type II fill materials are also permitted. Type I fill, which has more stringent grading requirements, is preferred in tall retaining structures. Type II is appropriate for low to medium height structures and slopes.
<table><tr><th></th><th>Type I Fill</th><th>Type II Fill</th></tr><tr><td>% passing 63 microns BS sieve</td><td>0-10</td><td>0-45</td></tr><tr><td>Liquid limit (%)</td><td>Not applicable</td><td>≤ 45</td></tr><tr><td>Plasticity index (%)</td><td>Not applicable</td><td>≤ 20</td></tr></table></td></tr>
<tr><td>NORDIC (2005)</td><td>Although using substandard soil or recycling products in reinforced soil structures is allowed, purely cohesive soils are not generally accepted in permanent works.</td></tr>
<tr><td>NCMA (2007)
USA</td><td>Grading of the fill material to be used in MSEW:
<table><tr><th>U.S. Sieve size</th><th>Percent passing (%)</th></tr><tr><td>4 in (102 mm)</td><td>100-75</td></tr><tr><td>No. 4 (4.76 mm)</td><td>100-20</td></tr><tr><td>No. 40 (0.425 mm)</td><td>0-60</td></tr><tr><td>No. 200 (0.075 mm)</td><td>0-35</td></tr></table>The reinforced backfill soils could be one of GP, GW, GM, SW, SP, SM according to USCS. Soils having low plasticity may be used LL<40%, PI <20% provided that:
• Proper drainage is installed.
• Only soils with low to medium frost heave potential are utilized.
• Internal cohesion is ignored in stability analysis
• Unacceptable time-dependent movements are checked</td></tr>
</table>

Table 2.1 (continued).

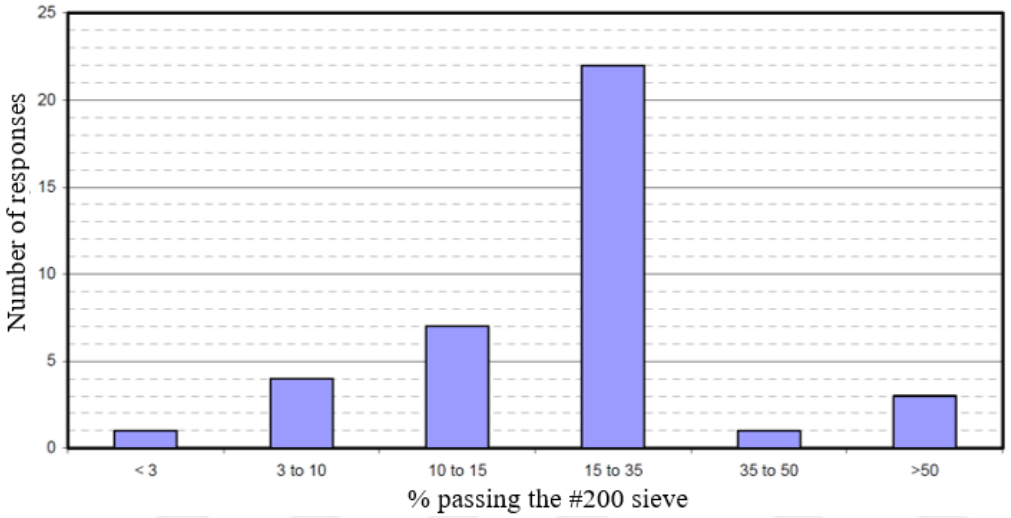
<table>
<tr><th>Code of practice</th><th>Material criteria</th></tr>
<tr><td>FHWA (2009)
USA</td><td>Material limitations for MSE wall backfills:
<table><tr><th>US Sieve size</th><th>Percent passing (%)</th></tr><tr><td>4 in (102 mm)</td><td>100</td></tr><tr><td>No. 40 (0.425 mm)</td><td>0-60</td></tr><tr><td>No. 200 (0.075 mm)</td><td>0-15</td></tr></table>PI≤6% (AASHTO T-90)
Water content at compaction should be ±2% of optimum moisture</td></tr>
<tr><td>BS 8006-1 (2010)
UK</td><td>As defined in Specification for Highway Works, the general cohesive fill should not be used in reinforced soil walls but may be used with caution in steep slopes.</td></tr>
<tr><td>EBGEO (2011)
Germany</td><td>Demands on fill material criteria are differentiated for predominantly statically and dynamically loaded structures. For dynamically loaded structures, % passing 63 µm BS sieve should be less than 7%.</td></tr>
<tr><td>KTS (2013)
Turkey

Specification of the General Directorate of Turkish Highways</td><td>Properties of backfill material for strip reinforced earth walls:
<table><tr><th>Sieve size (mm)</th><th>Percent passing (%)</th></tr><tr><td>125 (5")</td><td>100</td></tr><tr><td>75(3")</td><td>85-100</td></tr><tr><td>12,5 (1/2")</td><td>25-100</td></tr><tr><td>2 (No. 10)</td><td>15-100</td></tr><tr><td>0.60 (No. 30)</td><td>10-65</td></tr><tr><td>0,075 (No. 200)</td><td><15</td></tr></table>Coefficient of uniformity, C_u>5; PI <6%</td></tr>
<tr><td>Specification for Highway Works

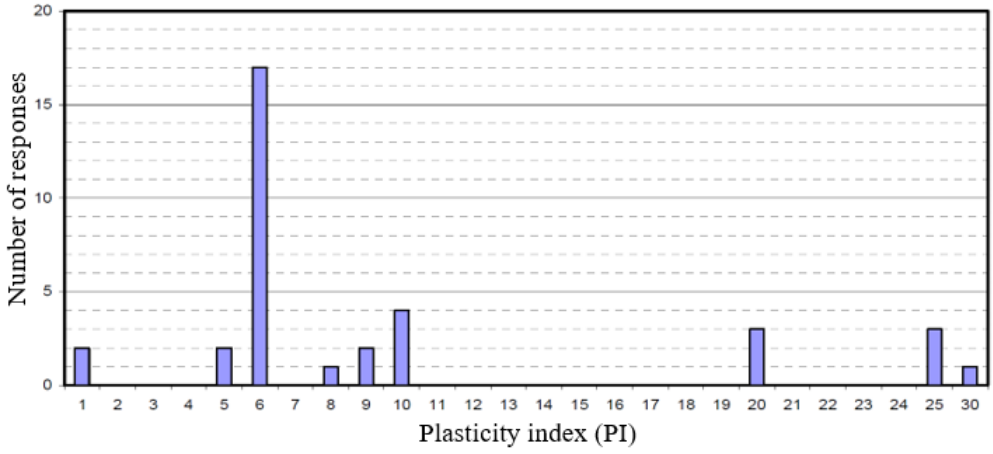
MCHW (2016)
UK</td><td>Material criteria of selected cohesive fills for reinforced soil structures are:
<table><tr><th>Soil class</th><th>Material definition</th><th>% passing 63 µm BS sieve</th><th>Liquid limit, LL %</th><th>Plastic index, PI %</th></tr><tr><td>7C</td><td>Selected wet cohesive material</td><td>15-45</td><td><45</td><td><25</td></tr><tr><td>7D</td><td>Selected stony cohesive material</td><td>15-45</td><td><45</td><td><25</td></tr></table></td></tr>
</table>

Survey questionnaire results of Marr and Stulgis (2013) in the NCHRP 24-22 report presented essential data to evaluate the tendencies of both US government transportation agencies and the private sector for the design and construction of MSEW (Figure 2.1 and Figure 2.2). Cristopher and Stulgis (2005) pointed out the

differences in the definition of "high fines". 3-10% of soil passing No. 200 US sieve was defined as "high fines" by some respondents, 15-35% by most of the respondents, and 35-55% by NCMA. The majority of the respondents specified the high plasticity index as 6%, following the recommendation of AASHTO (2002) and FHWA (2009) (Figure 2.1b).



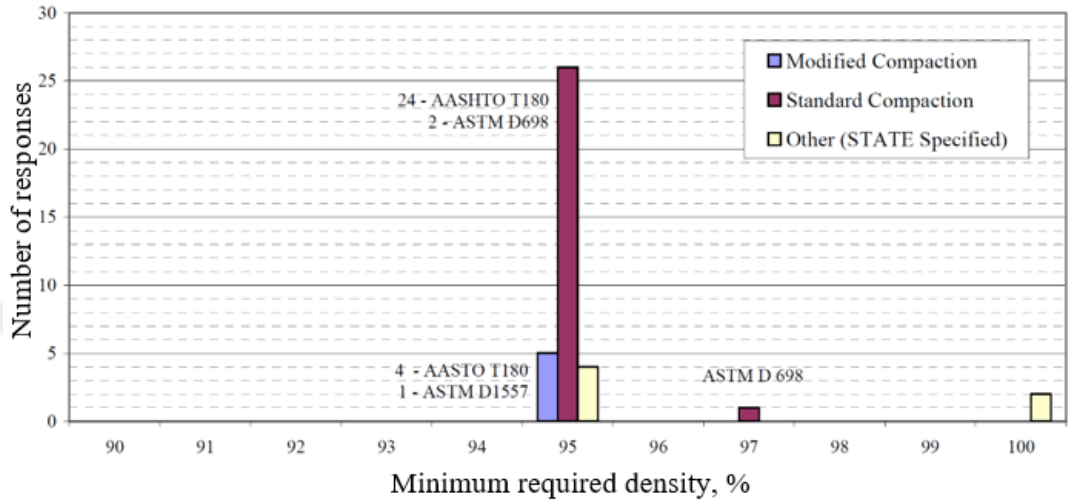
(a)



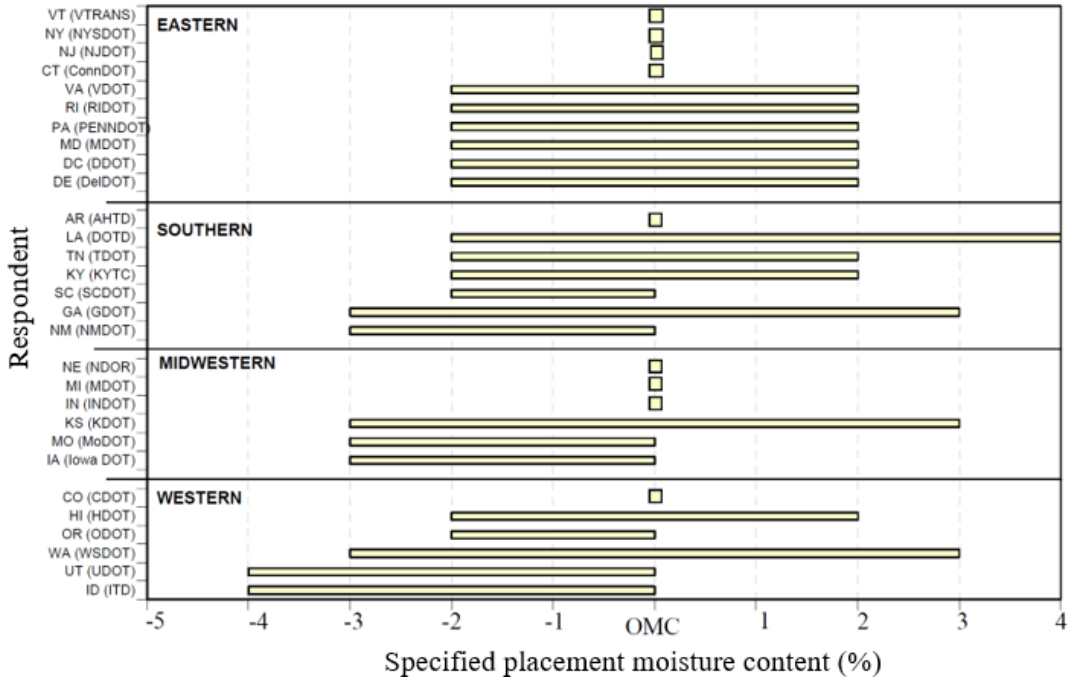
(b)

Figure 2.1. Definitions of reinforced fill from US transportation agency survey responses for (a) "high fines", (b) "high plasticity" (Marr and Stulgis, 2013)

The majority of the respondents require that soil must be compacted and placed at 95% of its maximum dry density and ±2% of optimum moisture content, as recommended in AASHTO (2002) and FHWA (2009) (Figure 2.2).



(a)



(b)

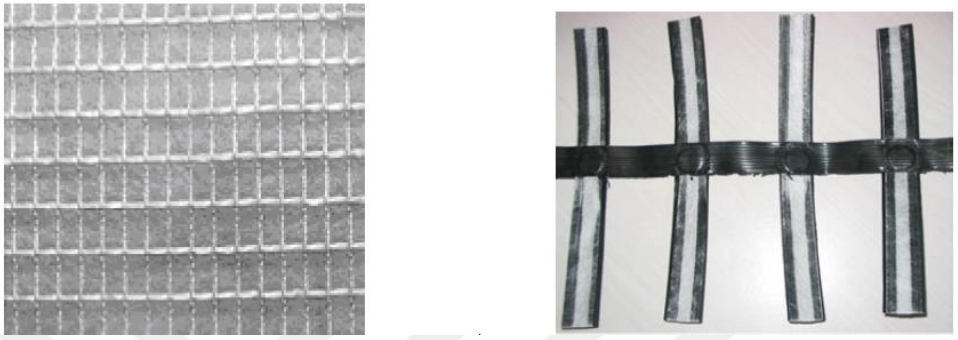
Figure 2.2. Summary of the responses from U.S. transportation agencies for (a) compaction requirements, and (b) specified moisture content of reinforced fill (Marr and Stulgis, 2013)

Design guidelines present precautionary expressions against the use of fine, cohesive backfills. Most of them recommend control of design and construction in addition to the monitoring of the post-construction movements in the compacted fill. FHWA (2009) requests the verification of the strength properties of soil-reinforcement bonds with short-term and long-term pullout and interface friction tests if backfill soil outside of the criteria will be used. Guidelines also specify the importance of taking proper drainage measurements if cohesive fills are being used. Koerner (2005) recommends backfill soil having no fines to avoid hydrostatic pressure build-up and excessive installation damage. If fines are used in the compacted fill, Koerner (2005) suggests water in front, behind, and beneath the reinforced zone be carefully collected and discharged. In addition, the top surface of the fill should be waterproofed to prevent water infiltration into the fill body.

Koerner and Koerner (2013) presented statistical data by evaluating 171 failed MSEW cases where 96% of the failed cases were privately financed walls. 91% of them were reinforced with geogrids, whereas the remaining 9% were reinforced with geotextiles. Silt and/or clayey fills in the compacted zone existed in 61% of the failed walls. 60% of the cases were water-related both internally and externally. Koerner and Koerner (2013) concluded that fine-grained silt and clay soil use in the MSEW without proper drainage measures are among the main problems associated with wall failures.

Several studies have investigated the water drainage from fine, cohesive fills. Horizontal drains may be placed into a slope/wall, or CFM can be reinforced with permeable geosynthetics. Fabian and Fourie (1986) stated that permeable reinforcement could improve the undrained shear strength of compacted clay by up to 40%, while low permeability reinforcement may decrease it to a similar degree. Cohesive soils reinforced with geogrids having an in-plane drainage capability (Figure 2.3b) were studied by Zornberg and Kang (2005) and O'Kelly and Naughton (2008). Zornberg and Kang (2005) reported a 30% increase in pullout resistance in the geogrid with drainage capability. Studies indicate that draining geogrid is effective for the dissipation of pore pressures. Another alternative is utilizing

granular soils' high strength and free drainage capabilities at the reinforcement-cohesive soil interface like a sandwich system. Abdi et al. (2009) encapsulated geogrids in thin sand layers within the clay and emphasized the efficiency of this technique in increasing shear strength.



(a) (b)

Figure 2.3. Reinforcement utilized also as drainage (a) high strength (reinforced) nonwoven geotextile, (b) geogrid with in-plane drainage property (Zornberg and Kang, 2005)

2.2 Soil Classification Systems

There are several classification systems to categorize and define soil materials. Material transition boundaries, similarities, and differences between the widely used classification systems are presented in this section. These systems were used for describing laboratory-prepared CFM in this study. Since the soil mixtures were prepared to be located near transition zones, material boundaries in classification systems have a significant effect on the definitions of the CFM in this study.

The USA system, also known as the Unified Soil Classification System (USCS - ASTM D2487-17), uses two-letter symbols to represent 15 main soil groups. It distinguishes coarse and fine particles by No. 200 US sieve (75 μm); sand and gravel particles by No. 4 US sieve (4.75 mm). If the soil has a fines content between 5%

and 12%, dual notation is used because the soil is both affected by particle size distribution and Atterberg limits.

European, CEN (Comité Européen de Normalisation) member countries implement European Soil Classification System (ESCS - EN ISO 14688-2:2018). This system distinguishes coarse and fine particles by sieve size of 63 μm; sand and gravel particles by 2 mm. Material is defined with symbols by the primary and secondary fractions composing the soil.

More than 50% of soil particles being fine- or coarse-grained determine the predominant grain size and primary definition of the soil in both USCS and ESCS. For instance, a coarse-grained soil, such as clayey sand, indicates that more than 50% of the dry soil by weight is sand. However, in terms of soil behavior, this clayey sand may behave like clay if it has a certain percentage of plastic fines. Therefore, it is not possible with these classification systems to clearly capture the transition zones between fine and coarse soils in terms of engineering behavior.

British Standard Soil Classification System (BS 1377:1990) uses the same boundaries with ESCS for coarse to fine and sand to gravel transitions. However, the soil's primary definition is named as fine soil if it consists of fine particles more than 35%, unlike USCS. Fine particles are divided into five groups according to their plasticity as low, intermediate, high, very high, and extremely high plastic soils instead of the dual classification of USCS as low and high plastic soils.

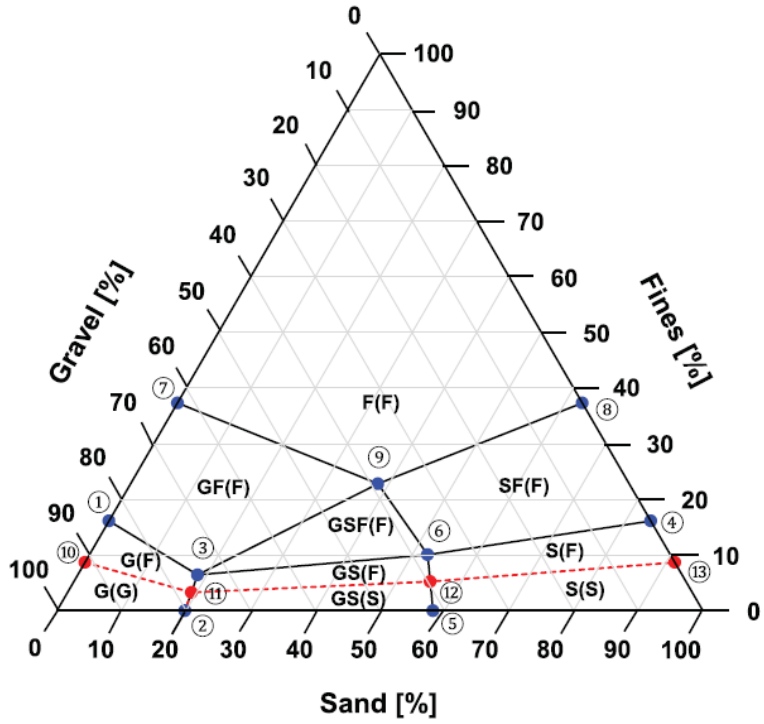
AASHTO M 145-91 (2017) is a classification system that categorizes soil and aggregate mixtures for highway construction. It separates coarse and fine particles by 75 μm; sand and gravel particles by 2 mm. General classification, whether the soil is a granular material or a silt-clay material, is made according to whether the fines content of the composite is more than 35% or not. Soils are classified into seven main groups, A-1 to A-7 (with further subdivisions), and the classification system provides an overall subgrade suitability rating rather than dividing soils such as sand, gravel, or clay.

BS 6031 (2009), a code of practice for earthworks, considers engineering fill material with a fines content of more than 15% as cohesive fill. It also states that soils with more than 35% of fines are typically evaluated as fine-grained for slope stability and settlement analysis.

There are differences in material transition boundaries and variations in the definition and symbolization of the soils in widely used soil classification systems such as USCS, ESCS, and AASHTO. Because there are sharp boundaries between the material transition zones, intermediate properties (where the characteristics of both fine and coarse-grained fractions are reflected) cannot ideally be represented with these classification systems in terms of engineering responses such as mechanical, compressional, or hydraulic behavior.

Park and Santamarina (2017) suggested a Revised Soil Classification System (RSCS) by considering the representation of transitional zones according to mechanical and hydraulic behavior (Figure 2.4). In this approach, soil classification is recommended according to particle packing. Classification groups are determined based on parameters such as roundness, particle angularity, coefficient of uniformity, Atterberg limits, and percent fractions of ingredients. The packing of soil particles in loose and dense states results in various threshold proportions. In Figure 2.4, blue points represent the mechanical control, and red points represent the flow properties. For instance, the zone encapsulated by the points marked with numbers 3, 6, and 9 is defined as GSF (F). It represents a soil whose mechanical behavior is governed by fine gravel-sand, and its hydraulic property is controlled by fines. Point 8 in Figure 2.4 indicates that for a soil having about 38% or more fines content, both mechanical and hydraulic properties are governed by fines, and the soil is classified as "fine-grained soil".

Needed Input			
Gravel G	Fraction F_G	e_G^{max} and e_G^{min}	or roundness R and uniformity C_u
Sand S	Fraction F_S	e_S^{max} and e_S^{min}	or roundness R and uniformity C_u
Fines F	Fraction F_F	$e_F\|^{10kPa}$, $e_F\|^{1MPa}$, and $e_F\|^{LL}$	or liquid limit LL



Group	Controlling Fraction		Description
	Mechanical Response	Fluid Flow	
F(F)	Fines	Fines	Fine-grained soil
GF(F)	Gravel & Fines	Fines	Transitional Mixture
SF(F)	Sand & Fines	Fines	Transitional Mixture
GS(F)	Gravel & Sand	Fines	Transitional Mixture
GSF(F)	Gravel-Sand-Fines	Fines	Transitional Mixture
G(F)	Gravel	Fines	Gravel with Fines
S(F)	Sand	Fines	Sand with Fines
G(G)*	Gravel	Gravel	Clean Gravel
S(S)*	Sand	Sand	Clean Sand
GS(S)	Gravel & Sand	Sand	Clean Gravel-Sand Mixture

Notes:

- (*) Specify well-graded or poorly-graded (Refer USCS). Well-graded G(G): $C_u \geq 4$ and $1 \leq C_c \leq 3$. Well-graded S(S): $C_u \geq 6$ and $1 \leq C_c \leq 3$.
- A soil group F or (F): Classify fines according to plasticity and sensitivity to pore-fluid chemistry.
- Recommendation: including triangular textural charts as part of standard reporting practice.

Figure 2.4. Soil classification boundaries of RSCS (Park and Santamarina, 2017)

2.3 Properties of Coarse-Fine Mixtures

Studies indicate that CFM exhibit intermediate behavior reflecting characteristics of both granular and fine-cohesive soils. Transition threshold affecting behavioral dominancy of coarse or fine fractions and evaluation criteria have been investigated in terms of index properties (Wasti and Alyanak, 1968; Cabalar and Mustafa, 2015a), hydraulic properties (Chapuis, 1990; Kumar, 1996), compressibility properties (Monkul and Ozden, 2007; Shipton and Coop, 2012) and strength properties (Georgiannou et al., 1990; Rahman and Lo, 2011) in the literature. Past studies about the properties of CFM have been reviewed in the following sections.

2.3.1 Index Properties

The behavior of the CFM previously was associated with parameters such as fines content (Novais-Ferreira, 1971; Kim et al., 2018), plasticity (Yin, 1999), particle size and shape characteristics (Kuerbis, 1989; Nagaraj, 2016), stress history (Revil et al., 2002; Ni et al., 2004), mineralogy, clay particle size distribution, and pore water chemistry (Georgiannou et al., 1990).

Some researchers investigated the behavioral thresholds in terms of particle packing of coarse and fine grains in composite soil matrix by evaluating density, porosity, and void ratio. Wasti and Alyanak (1968) have studied the effect of clay content on composite soil behavior. They stated that when the clay content decreased to fill only the spaces between the particles at maximum porosity, Atterberg limits and the clay content were no longer linearly related. In addition, the behavior changed from clayey to sandy soil.

Shakoor and Cook (1990) investigated the compaction characteristics of crushed limestone and silty-clay mixtures with varying proportions. 60-70% stone content led to the maximum dry density and the corresponding minimum void ratio resulting in the densest clay-aggregate mixture. More and more crushed stones contacted each other for higher stone contents, which caused a decrease in maximum dry density

and an increase in void ratio. The dry density of the mixtures was independent of the stone size, whereas round particles tended to give higher densities than angular particles at each stone content tested.

Variation between liquid limit and undrained shear strength at various sand contents and different particle gradations on clay-sand mixtures were investigated by Cabalar and Mustafa (2015a) with fall cone tests. A linear decrease in the liquid limit of mixtures was observed with the increase of sand content having the same gradation. Sands having finer gradation but the same shape as well as sands with relatively angular grains but having the same size fraction resulted in a slightly higher liquid limit of mixtures. More rounded sand grains having the same size caused an increase in undrained shear strength of the mixtures, where the gradation of the sand grains did not have an apparent effect.

Approaches have been improved for CFM evaluation to avoid misleading conclusions of the terms, void space, and relative density. The void ratio implies the space not occupied by the solid particles of the soil matrix. However, when a soil sample includes coarse-grained and fine-grained particles together, overall behavior is considered a function of the volumes occupied by these two groups. Therefore, it has led to the definitions of the coarse soil matrix and fine soil matrix. Their percent contribution to the force transfer is related to the particle packing of the soil composite and their interactions in between. For these reasons, Mitchell (1976) and Kenney (1977) identified the concept of intergranular void ratio, which considers the fine particles as part of the void space if they do not contribute to the force transfer mechanism. Several different names were used in the literature as the intergranular, granular, or skeleton void ratios, which, more or less, all refer to the same idea. When fines content is lower than a transitional value, clay particles only occupy the void space between the granular particles. This leads to coarse particles dominating the overall behavior (Figure 2.5). The ratio of the sums of voids and clay volume to granular particle volume was defined as the intergranular void ratio (e_s) in this case, as a representative parameter.

Thevanayagam and Mohan (2000) pointed out that fine grain matrix will be highly compressible in the coarse-grained dominated case unless fine particles are trapped between the contact points of coarse particles or coat the coarse particle surfaces. When the fines content exceeds the transitional threshold value, fines dominate the behavior with the coarse particles suspended in the fine matrix without contacting each other (e.g., Figure 2.5a). Voids of such a soil can be characterized by defining separate void ratios for the fine and coarse fractions. Interfine void ratio (e_f) is defined as the ratio of void volume to clay volume. Equations 2.1 and 2.2 give the mathematical formulations for the interfine void ratio (e_f) and intergranular void ratio (e_s).

$$e_f = \frac{e}{\frac{G_T}{G_F}\left(\frac{FC}{100}\right)} \tag{2.1}$$

$$e_s = \frac{e + \frac{G_T}{G_F}\left(\frac{FC}{100}\right)}{\frac{G_T}{G_C}\left(1 - \frac{FC}{100}\right)} \tag{2.2}$$

Where e is the global void ratio; FC is fines content (by mass); G_T, G_F, and G_C are the specific gravity of the total mixture, fine and coarse particles, respectively.

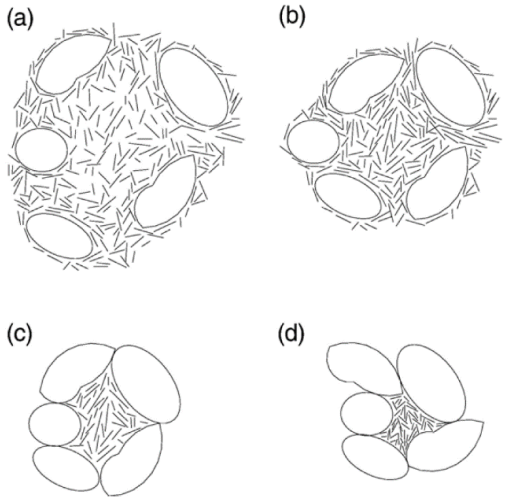


Figure 2.5. Different particle packing arrangements of coarse-fine soil matrices (Monkul and Ozden, 2007)

The intergranular void ratio was used in the past studies for the evaluation of strength (Ovando-Shelley and Pérez, 1997; Thevanayagam, 1998; Ni et al., 2004), liquefaction potential (Polito and Martin, 2001; Xenaki and Athanasopoulos, 2003; Papadopoulou and Tika, 2016) and compressibility (Cabalar, 2011; Shi and Zhao, 2020) of CFM. Monkul and Ozden (2005) investigated transitional fines contents (TFC) of different sand-clay mixtures by comparing the intergranular void ratio of the mixture with the maximum void ratio of the granular fraction. They stated that when the intergranular void ratio of the CFM exceeds the maximum void ratio of the host granular fraction, coarse particles are no longer in contact with each other. Instead, they are suspended in the clay matrix (Figure 2.5a,b).

Equation 2.2 becomes Equation 2.3 if the specific gravities of fine and coarse fractions are assumed to be equal.

$$e_s = \frac{e + \frac{FC}{100}}{1 - \frac{FC}{100}} \tag{2.3}$$

Thevanayagam et al. (2000) stated that the intergranular void ratio may not be adequate to distinguish coarse and fine dominancy in terms of mechanical response, especially for higher fines content. Although fine particles only occupy the voids between coarse particles without completely filling them, they may partially contribute to the load transfer. Therefore, equivalent intergranular contact index void ratio or equivalent granular void ratio was defined as shown in Equation 2.4. In this equation, b indicates the percent of fines being active in the force chain together with the coarse particles. For lower fines contents, the b value is considered as zero giving the same formulation with Equation 2.3. A gradual increase in the contribution of fines in the force structure can be reflected by larger b values, in the range of 0–1 (Rahman et al., 2008).

$$(e_s)_{eq} = \frac{e + (1-b)\frac{FC}{100}}{1-(1-b)\frac{FC}{100}} \tag{2.4}$$

Several studies investigated the proper values for the b value. Although there are reported constant b values for a given coarse-fine mixture in the literature (e.g., b=0.25 in Thevanayagam et al., 2002; b = 0.25 for fines contents less than transitional fines content and b = 0.40 at the transitional fines content of 30% in Yang et al., 2006b), Rahman and Lo (2008) listed the factors affecting the b value as transitional fines content (TFC, for delineating the regime of "fines in sand" from "sand in fines"), fines content (f_c), and size ratio of coarse to fine particles (D/d). If the coarse particles and fines are not single size, (D/d), in general, is used as D_{10}/d_{50}, D_{10} for defining the size of the host granular soil and d_{50} for that of fines (Rahman and Lo, 2008 and Ni et al., 2004). Rahman and Lo (2008) proposed Equation 2.5 for the prediction of the b value, where r=d/D, $k=(1-r^{0.25})$.

$$b = \left[1 - exp\left(-0.3\frac{(f_c/TFC)}{k}\right)\right].\left(r\frac{f_c}{TFC}\right)^r \tag{2.5}$$

Rahman and Lo (2008) also noted that transitional fines content (TFC) values reported in the literature are in the range of 30% to 41% according to their definition of TFC, and an average value of 35% may be selected as a first approximation. A method for predicting TFC and the relation between TFC and size ratio of coarse to fine particles (D/d) is presented by Rahman and Lo (2008) (Equation 2.6 and Figure 2.6).

$$TFC = A\left(\frac{1}{1+e^{\alpha-\beta\chi}} + \frac{1}{\chi}\right) \tag{2.6}$$

The χ term is the size ratio of coarse to fine particles (D/d). Independent from the values of α and β, the coefficient of A is 0.40 which is the asymptotic value. The α

and β parameters are determined to yield a minimum TFC around $(D/d)_{crit}$ and the maximum TFC data point corresponding to the smallest χ of ~2.0. Rahman et al. (2011) indicated α = 0.50 and β = 0.13 for the data in Figure 2.6, for χ between 2–42 from eight different databases.

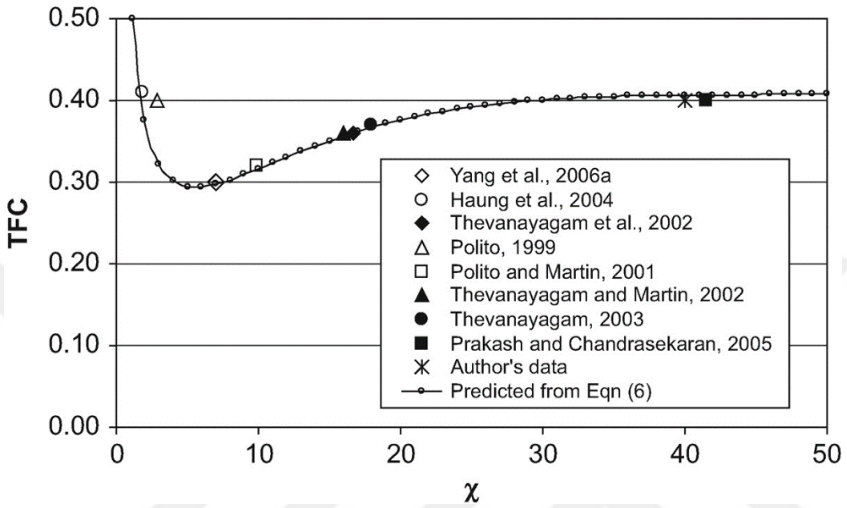


Figure 2.6. Particle diameter ratio, χ and transitional fines content (TFC) relationship (Rahman and Lo, 2008)

Instead of relative density, which is generally considered valid for cohesionless soils, intergranular relative density (D_{rs}) was introduced and used by Thevanayagam (1998) to quantify the compactness of CFM. It can be calculated by Equation 2.7.

$$D_{rs} = \frac{e_{max,HS} - e_s}{e_{max,HS} - e_{min,HS}} \tag{2.7}$$

Where e_s is the intergranular void ratio, $e_{max,HS}$ and $e_{min,HS}$ are maximum and minimum void ratios of the host granular soil, respectively. An increase in intergranular void ratio up to the maximum void ratio of the coarse fraction decreases the intergranular relative density, implying looser packing of coarse particles. Intergranular relative density being zero indicates the transition between fine and coarse-grained dominated soils. Thevanayagam (1998) reported that e_s, D_{rs}, and confinement stress affect the shear strength of silty sands, whereas the density of

silty sand could be a misleading parameter. Kim et al. (2016) stated that e_s and D_{rs} are more effective parameters than void ratio (e) and relative density (D_r) to evaluate cyclic shear strength for clay-sand mixtures.

Mitchell and Soga (2005) related the amount of clay required to fill the voids of the granular particles and the water content for a saturated clay-granular mixture. The amount of clay and water that completely fills the voids of the granular phase was given as in Equation 2.8. In this equation, w is the water content, C is the percent clay by weight, e_g is the void ratio of the granular phase, and G_{SC} and G_{SG} are specific gravities of the clay particles and granular particles, respectively.

$$\frac{w}{100}+\frac{C}{100(G_{SC})}=\left(1-\frac{C}{100}\right)\frac{e_g}{G_{SG}} \tag{2.8}$$

Chang et al. (2017) developed a compression model for sand and silt mixtures, including fines content in its formulation by introducing the parameters of active and inactive voids according to the kinematic availability of voids to compression process (Figure 2.7).

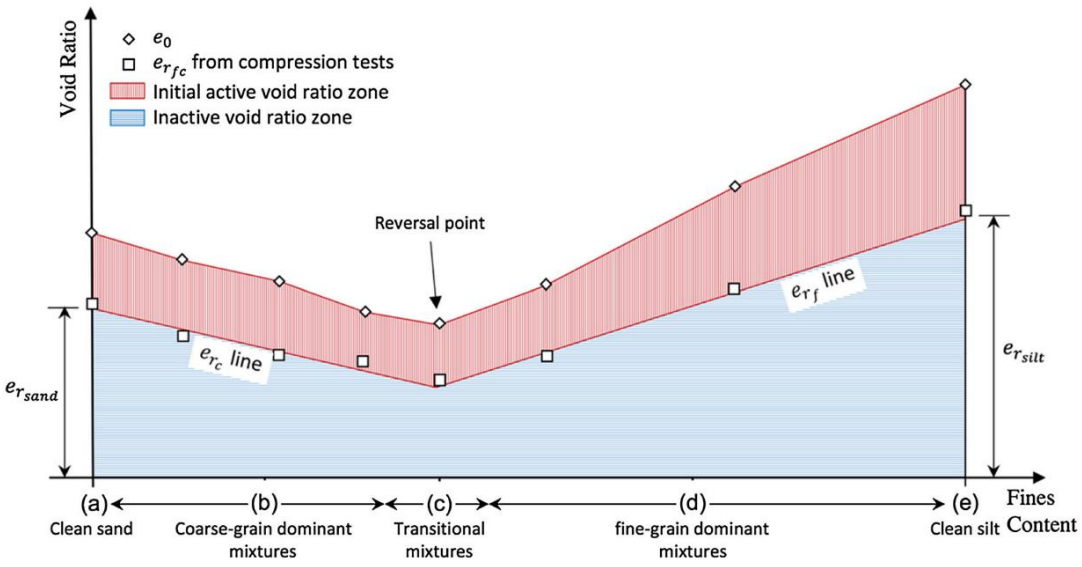


Figure 2.7. Schematic variation of active and inactive voids according to fines content (Chang et al., 2017)

According to Chang et al. (2017), the identified active void ratio depends on initial density and stress level, whereas the inactive void ratio depends on particle size and shape, and also fines content. The authors verified their proposed model for six different silt-sand mixtures having different fines content.

Kumar and Muir Wood (1999) conducted fall cone tests on kaolin and fine gravel mixtures to evaluate the link between the change of liquid limit, clay content, and undrained shear strength. It was observed that the liquid limits of the composite matrix increased almost linearly with the increasing clay content. The term apparent liquid limit (Equation 2.9) was also used, which calculates the moisture content according to the clay mass instead of the total mass. Results concluded that the apparent liquid limit of the clay matrix was not changed until clay content fell below about 30% (Figure 2.8).

$$w_c = \frac{m_w}{m_c} \tag{2.9}$$

where w_c is the clay water content, m_w is the mass of water, and m_c is the mass of clay in soil composite.

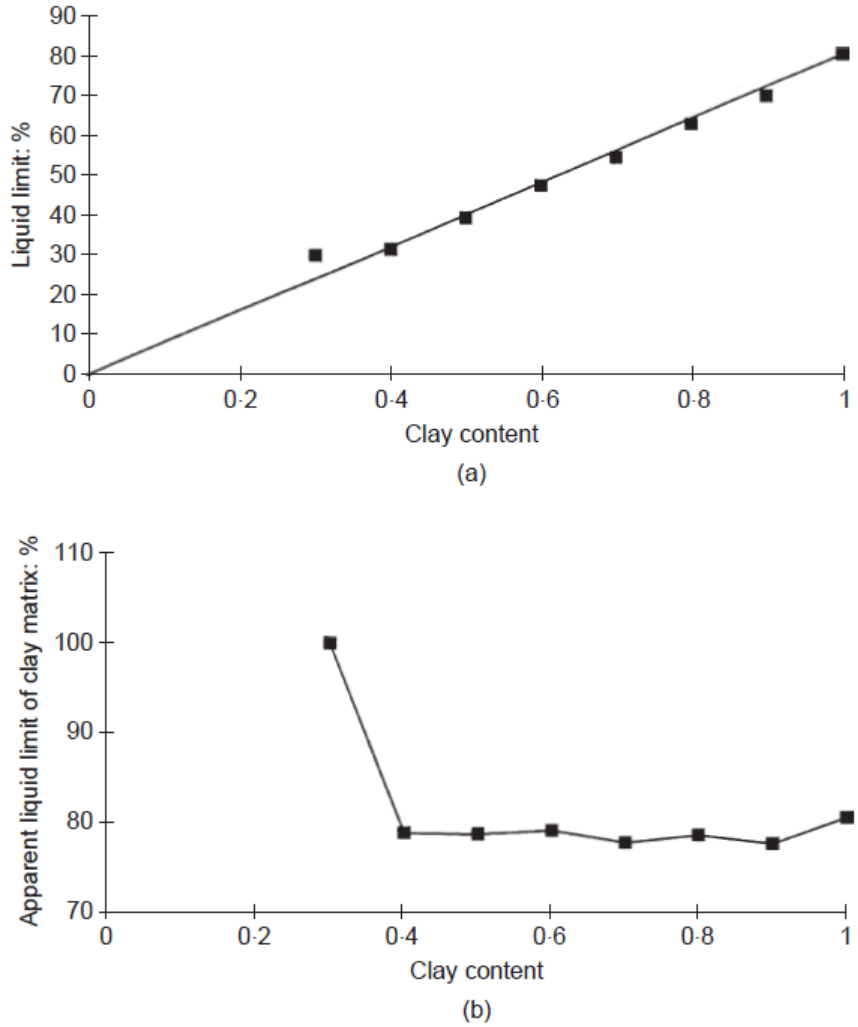
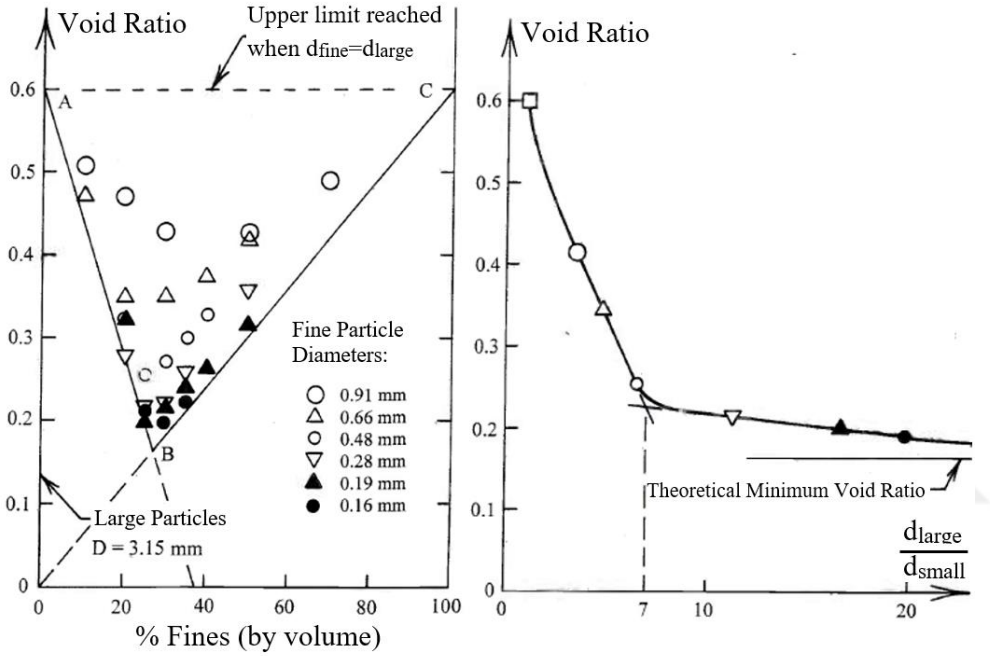


Figure 2.8. (a) Liquid limit, (b) apparent liquid limit of clay matrix as a function of clay content (Kumar and Muir Wood, 1999)

Lade et al. (1998) studied the particle packing properties of binary mixtures. They investigated the effect of coarse to fine particle size ratio and amount of fines on the minimum void ratio of the mixtures. The authors re-analyzed the experimental data obtained by McGeary (1961), who conducted tests on binary packings of steel spheres having different sizes. In Figure 2.9(a), a smaller sphere diameter refers to fines content. It was shown that the minimum void ratio of the mixture decreased up to a certain fines content and increased after that, giving a V-shaped curve. As the diameter of the smaller spheres decreased, the minimum void ratio achieved approached the theoretically possible densest packing configuration. When the small

and large particle diameters were equal in magnitude, the upper limit of the minimum void ratio was obtained. The mixture's minimum void ratio decreased sharply until the particle size ratio of 7. The rate of decrease was significantly reduced for larger particle size ratios, as seen in Figure 2.9(b). Shire et al. (2016) verified the conclusions of Lade et al. (1998) by using discrete element method simulations on homogeneous, isotropic collections of binary mixtures.



(a) (b)

Figure 2.9. Effect of (a) fines content, and (b) particle size ratio on the binary mixtures' minimum void ratio (Lade et al., 1998)

Zuo and Baudet (2015) compiled the analytical and experimental methods to identify transitional fines content (FC_t) of sand and nonplastic fine mixtures. Results of the experimental (Method 1-3), analytical (Method 4-6), and semi-analytical (Method 7) methods used in the past studies are presented in Figure 2.10. Zuo and Baudet (2015) summarized these methods as:

- "Method 1: FC_t=fines content when e_{min} and e_{max} reach a minimum value (index properties)

- Method 2: FC_t=fines content when the intercepts of normal compression line (NCL) or critical state line (CSL) reach a minimum value (monotonic loading)
- Method 3: FC_t=fines content when the number of cycles to liquefaction reaches a minimum (cyclic loading)
- Method 4: FC_t=fines content when e_f (void ratio of fines) falls below $e_{max(fines)}$ (max. void ratio of fines) and e_s (void ratio of sand) falls below $e_{max(sand)}$ (max. void ratio of sand)
- Method 5: FC_t=fines content when the packing density is maximum, determined with $e_{min(fines)}$ and $e_{min(sand)}$
- Method 6: FC_t=fines content when the packing density corresponds to the intercept in an e-lnp' plot of the critical state line extrapolated from large stress critical state values, determined with $e_{\Gamma(fines)}$ and $e_{\Gamma(sand)}$
- Method 7: FC_t=fines content determined as a function of the particle diameter ratio based on back-analysis."

The experimental evaluation gave a larger range (between 20% and 50%) than analytical and semi-analytical methods. Methods 4 and 5, which are analytical assessments based on intergranular void ratio and binary packing densities of the mixtures, respectively, tended to give lower transitional fines content. Zuo and Baudet (2015) pointed out that experimental and analytical values were in better agreement when the particle size ratio of large to small grains was higher.

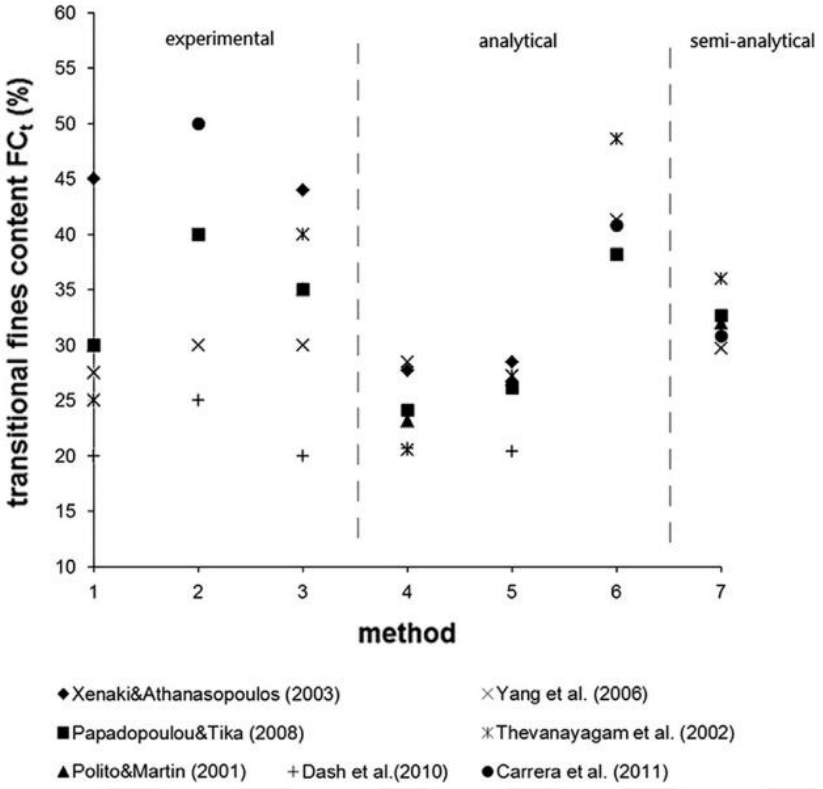


Figure 2.10. Comparison of different methods for the determination of transitional fines content (Zuo and Baudet, 2015)

Kim et al. (2016) investigated the global and intergranular void ratio relationship according to fines content and different compaction energies applied to sand and clay mixtures. The authors divided their samples into nonplastic (FC smaller than 16.7%) and plastic (FC higher than 19.6%) mixtures. Undercompaction and pre-consolidation methods were implemented for nonplastic and plastic specimens, respectively. In Figure 2.11a, an increase in fines content decreased the void ratio linearly for low compaction energy. However, the initial decrease of 10-15%, accompanied by an increase in the void ratio, was observed for high compaction energies. Void ratios converged with the increase of fines, and a less significant void ratio difference can be seen at a fines content of 16.7% for different compaction energies. In Figure 2.11(b), the intergranular void ratio of the specimens exceeded the maximum void ratio of the silica sands (0.850) for fines content greater than 15%.

This result indicated that sand particles were not in contact with each other anymore, and fine particles started to govern overall behavior.

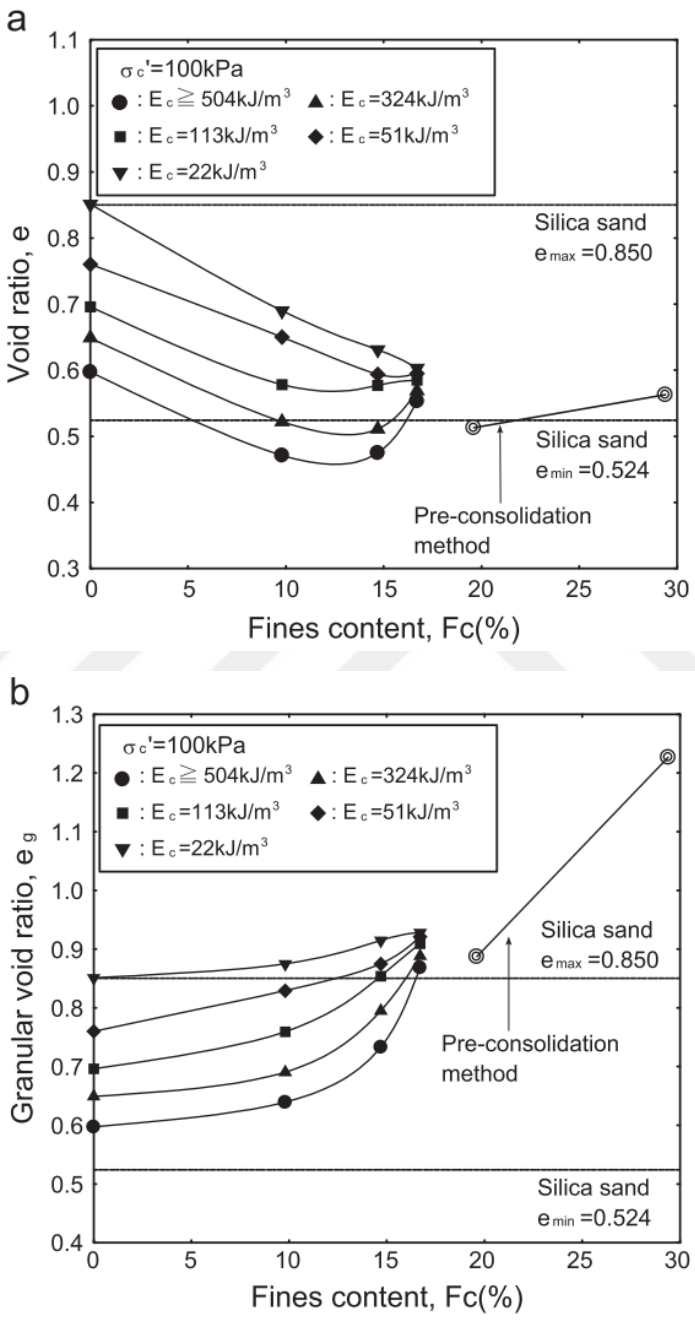


Figure 2.11. Different compaction energy and fines content change according to (a) void ratio, (b) granular void ratio (Kim et al., 2016)

2.3.2 Hydraulic Properties

Several theoretical and empirical formulations were developed for the hydraulic conductivity estimations of soils. Most of the previous studies have focused on fine-grained plastic soils or coarse-grained cohesionless soils, and hydraulic conductivities of these groups were evaluated separately as fluid transport was affected by different mechanisms. Because hydraulic properties of CFM include the characteristics of both portions, approaches for coarse-grained and plastic materials and some predictive correlations are reviewed in this chapter.

In suggested formulations for hydraulic conductivities of coarse soils (Hazen, 1892, 1911; Kozeny, 1927; Carman, 1956; Chapuis, 2004), variables are mainly associated with the void ratio, size, shape properties as well as relative sizes of particles, particle size distribution, pore topography, and tortuosity. Ren and Santamarina (2018) pointed out that estimated hydraulic conductivity values might differ more than one order of magnitude from the measured value because of the grain size variability and particle shape difference.

Hazen (1892, 1911) developed a correlation by relating the hydraulic conductivity of sands with the particle size corresponding to 10% passing by mass, d_{10} (Equation 2.10). It is a popularly used empirical correlation because of its simplicity. Compressibility, particle shape, void ratio, and permeant properties are not considered in this formula. In the past studies, reported Hazen's coefficient values (C_H) mainly range between 40 and 150, although it is usually assumed to be 100. The application of the formula is valid for uniform sand having a coefficient of uniformity less than five ($C_u \leq 5$) and meeting the grain size criteria of 0.01 cm < d_{10} < 0.30 cm. Chapuis (2012) also stated that the formula gives accurate predictions for loose sands in which the void ratio is close to the maximum void ratio of the soil sample.

A correlation for hydraulic conductivity by considering the specific surface area and the void ratio was developed by Kozeny (1927) and later modified by Carman (1956), popularly known as the Kozeny-Carman formula. Although the correlation

has several forms by including different parameters, the formulation presented in Equation 2.11 is one of the most widely used. Several researchers have investigated the prediction capability and validity of the equation (Hansen, 2004; Aubertin et al., 2005; Chapuis, 2012). Carrier (2003) stated that electrochemical particle forces and reactions between water and soil are not considered in the Kozeny-Carman formula. Therefore, it can be used for sandy soils and nonplastic silts, but it is not suitable for clayey soils. Carrier (2003) also indicated that the Kozeny-Carman formula gives more accurate predictions than Hazen's formulation for sandy soils.

Chapuis (2004) investigated the hydraulic conductivity of saturated sand and gravel with the effective diameter (d_{10}) and void ratio. Because the Hazen formula is valid for loosely compacted soils where porosity is near its maximum value, Chapuis (2004) proposed a modified version of the Hazen (1911) equation by extending the formula to any porosity value as presented in Table 2.2, Equation 2.12. An empirical equation for natural nonplastic silty soils using the compound parameter, $d_{10}^2\ e^3/(1 + e)$ was also proposed as presented in Equation 2.13. This correlation was developed using fully saturated hydraulic conductivity data of soils meeting the criteria of 0.003 mm < d_{10} < 3 mm and 0.3 < e < 1.0. The poor prediction capability of Equation 2.13 was reported for crushed materials. The angularity of particles increases tortuosity and internal resistance, consequently causing different pore void geometry compared to natural soils. However, recent studies by Toumpanou et al. (2021) indicated that the compound parameter, $d_{10}^2\ e^3/(1 + e)$, gave a reliable prediction of hydraulic conductivity for sand-sized crushed limestone.

Alyamani and Sen (1993) proposed a correlation by associating the hydraulic conductivity with the initial slope and intercept of the particle size distribution graph (Equation 2.14).

Table 2.2. Hydraulic conductivity predictions in literature for coarse soils

Reference	Formulations	Notes	Equation No
Hazen (1892, 1911)	$k = C_H . {d_{10}}^2$	C_H: Hazen's coefficient d_{10} (cm): particle diameter corresponding to 10% passing k (cm/s): hydraulic conductivity	(2.10)
Kozeny (1927) – Carman (1956)	$k = \frac{C_F g}{{\upsilon_f \rho_m}^2} {S_S}^{-2} \frac{e^3}{1+e}$	C_F (≈0.2): pore topology constant υ_f (m^2/s): kinematic viscosity of the fluid ρ_m (kg/m^3): mineral mass density S_S (m^2/kg): specific surface area e: void ratio k (m/s): hydraulic conductivity	(2.11)
Chapuis (2004)	$k = 1.5 {d_{10}}^2 \frac{e^3 (1+e_{max})}{{e_{max}}^3 (1+e)}$	d_{10} (mm): effective diameter, particle diameter corresponding to 10% passing e_{max}: maximum void ratio e: void ratio k (cm/s) : hydraulic conductivity at 20°C	(2.12)
	$k = 2.4622 \left[\frac{{d_{10}}^2 e^3}{(1+e)}\right]^{0.7825}$	d_{10} (mm): effective diameter, particle diameter corresponding to 10% passing e: void ratio k (cm/s): hydraulic conductivity	(2.13)
Alyamani and Sen (1993)	$k = 1300[I_0 + 0.025(d_{50} - d_{10})]^2$	d_{10} and d_{50} (mm): particle diameters corresponding to 10% and 50% passing, respectively I_0 (mm): intercept of the straight line with the x-axis in grain size distribution plot k (m/day): hydraulic conductivity	(2.14)

Hydraulic conductivity of cohesive soils is associated with their stress state, compressibility, consistency limits, and pore void characteristics (Lambe, 1955; Nagaraj et al., 1994). Mesri and Olson (1971) distinguished the factors affecting the

hydraulic conductivity of clays into two parts as mechanical and physico-chemical variables. Mechanical variables are related to the shape, size, and geometrical arrangement of clay particles, whereas physico-chemical variables are related to clay's tendency to disperse or form aggregates. Other parameters affecting the hydraulic conductivity can be listed as anisotropy, permeant characteristics, and changes in pore fluid chemistry (Ren and Santamarina, 2018).

Nagaraj et al. (1993) and Nagaraj et al. (1994) proposed Equation 2.15 and Equation 2.16 in Table 2.3, respectively, for the saturated hydraulic conductivity estimation of normally consolidated uncemented clays. The authors related the hydraulic conductivity of clays with a generalized state parameter (e/e_L).

Sivapullaiah et al. (2000) proposed an equation to predict the hydraulic conductivity of bentonite-sand mixtures (Equation 2.17). Hydraulic conductivity was related to the void ratio (e) and liquid limit (w_L) of the composite. The authors stated that the validity of the proposed equation is for soils with a LL higher than 50%.

Mbonimpa et al. (2002) categorized the factors affecting the hydraulic conductivity of soils as fluent properties, solid surface characteristics, and pore size distribution. The authors proposed Equation 2.18 (Table 2.3) for the saturated hydraulic conductivity of plastic and clayey materials.

Dolinar (2009) proposed Equation 2.19 to estimate the hydraulic conductivity of soils having non-swelling or limited swelling clay minerals. Because the equation was derived for artificially prepared soil samples, it is valid for 20°C, remolded, saturated clay without organic matter.

Table 2.3. Hydraulic conductivity prediction equations in literature for fine, plastic soils

Reference	Formulations	Notes	Equation No
Nagaraj et al. (1993)	$\frac{e}{e_L} = 2.38 + 0.233 \log k$	e: void ratio e_L: void ratio at liquid limit k (cm/s): hydraulic conductivity	(2.15)
Nagaraj et al. (1994)	$\frac{e}{e_L} = 2.162 + 0.195 \log k$		(2.16)
Sivapullaiah et al. (2000)	$log_{10}k = \frac{e - 0.0535w_L - 5.286}{0.0063w_L + 0.2516}$	e: void ratio w_L(%): liquid limit k (m/s): hydraulic conductivity	(2.17)
Mbonimpa et al. (2002)	$k = C_P \frac{\gamma_w}{\mu_w} \frac{e^{3+x}}{1+e} \frac{1}{\rho_s{}^2 w_L{}^2 \chi}$	C_P (=5.6 g^2/m^4), constant γ_w (≈9.8 kN/m^3): unit weight of water μ_w (≈ 10^{-3} Pa.s): dynamic viscosity of water e: void ratio ρ_s (kg/m^3): density of solid grains w_L(%): liquid limit χ (=1.5, unitless): parameter relating w_L and specific surface x (=7.7$w_L^{-0.15}$-3): parameter representing tortuosity k (cm/s): hydraulic conductivity	(2.18)
Dolinar (2009)	$k = \frac{6.31.10^{-7}}{(I_p - 8.74p)^{3.03}} e^{2.66(I_P - 8.74p)^{0.234}}$	e: void ratio I_p(%): plasticity index p (0 < p ≤1): portion of clay minerals in the soil k (m/s): hydraulic conductivity	(2.19)

Consolidation time for saturated clays is related to the permeability of soils, among many other parameters. Hydraulic conductivity of saturated clays can be estimated indirectly by the parameters obtained from consolidation testing and the equations of Terzaghi (1925, 1943). In Equation 2.20, k_{sat} (m/s) is saturated hydraulic conductivity, c_v (m^2/s) is the coefficient of consolidation, m_v (m^2/kN) is the

coefficient of volume compressibility and γ_w (kN/m^3) is the unit weight of water. The coefficient of volume compressibility can be calculated with Equation 2.21, where Δe is the change in void ratio, and $\Delta\sigma'$ (kN/m^2) is the effective stress increase. The square root of time method proposed by Taylor (1948) can be used to calculate the coefficient of consolidation (Equation 2.22). In this equation, d (m) is the maximum drainage distance, and t_{90} (s) is the time corresponding to 90% completion of the primary consolidation according to the square root time method.

$$k_{sat} = c_v . m_v . \gamma_w \tag{2.20}$$

$$m_v = \left(\frac{\Delta e}{1 + e_0}\right) \frac{1}{\Delta \sigma'} \tag{2.21}$$

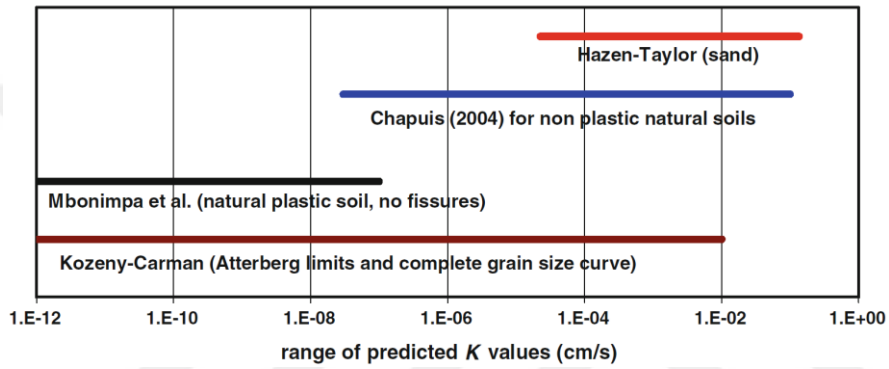
$$c_v = \left(\frac{0.848 d^2}{t_{90}}\right) \tag{2.22}$$

Fewer predictive equations are available to cover hydraulic properties of intermediate geomaterials or CFM. Kacprzak et al. (2010) pointed out that formulations proposed for sand-clay mixtures are less developed compared to those for pure sands or clays.

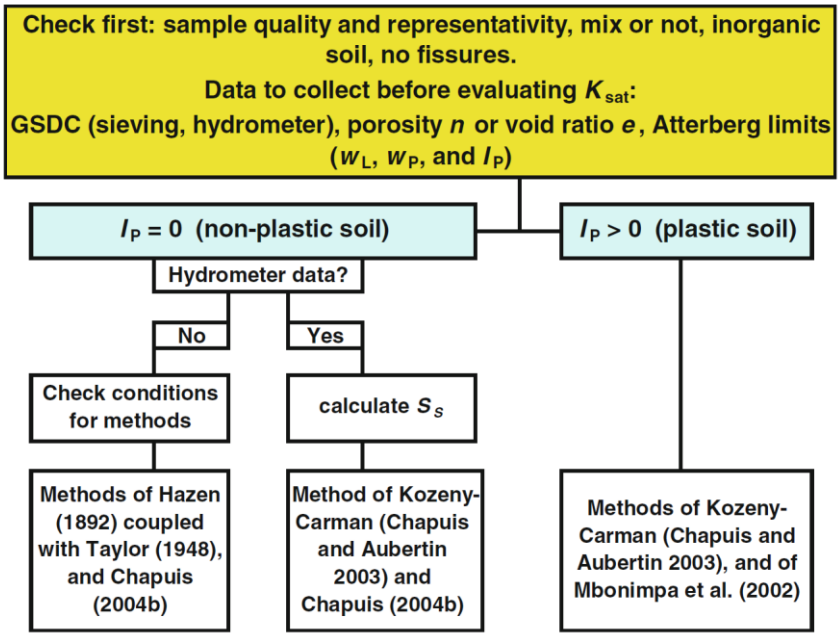
Some studies have attempted to generalize previously proposed equations for a particular soil type to more variable soil types. For instance, Chapuis and Aubertin (2003) suggested a modified version of the Kozeny – Carman equation, which is originally developed for cohesionless sands. The authors stated that the proposed version in Equation 2.23 could estimate the hydraulic conductivity of most soils, including clays. In this formulation, k_{sat} (m/s) is the saturated hydraulic conductivity, S_s (m^2/kg) is the specific surface, G_s is the specific gravity of solid particles, and e is the void ratio.

$$\log\ (k_{sat}) = 0.5 + log\ \left(\frac{e^3}{{G_S}^2 {S_S}^2 (1 + e)}\right) \tag{2.23}$$

Chapuis (2012) presented an extensive review of the saturated hydraulic conductivity prediction of soils. The author pointed out the most reliable predictive correlations for different soils and suggested that Hazen (1892) equation coupled with Taylor (1948) and Chapuis (2004) can be used for nonplastic soils. On the other hand, the equation of Mbonimpa et al. (2002) can be used for plastic soils. Prediction ranges and flow chart to select the most reliable correlation according to Chapuis (2012) can be seen in Figure 2.12.



(a)



(b)

Figure 2.12. (a) Hydraulic conductivity prediction ranges of different correlations, (b) flow chart for the selection of the most reliable method (Chapuis, 2012)

Hydraulic conductivity of kaolin or bentonite mixtures with sand, which is used for seepage barriers (Abeele, 1986; Chapuis, 1990; Mollins et al., 1996), was investigated in most of the CFM studies. As Benson et al. (1994) mentioned, an effective liner should have a hydraulic conductivity value less than $1x10^{-7}$ cm/s. According to Gleason et al. (1997), a bentonite content of 15% in a bentonite-sand mixture is appropriate to be used as a hydraulic liner. Kenney et al. (1992) pointed out that the hydraulic conductivity of bentonite-sand mixtures significantly increased for bentonite ratios less than 8%, and no significant variation was observed for bentonite contents higher than 12%. The authors also indicated that sand-bentonite mixtures of up to 20% bentonite content behaved as a two-component mixture. The sand skeleton provided structural support and stability, and bentonite occupied the space between sand grains and acted as a seepage barrier. Acar and Olivieri (1989) stated that water content and dry density control are essential in constructing low-permeability earth barriers. A decrease in the dry density might result in a hydraulic conductivity increase of more than one order of magnitude.

Abeele (1986) pointed out that using clay mixtures instead of pure clays as liners in moisture barriers or waste disposal facilities may be desirable not only for economic reasons but also for the mechanical benefits they have. It was stated that the empirical relation given in Equation 2.24 (also proposed by Taylor, 1948; Tavenas et al., 1983) can be used for determining the hydraulic conductivity of sand-bentonite mixtures. The author also reported that the hydraulic conductivity of mixtures having a bentonite content of 6% or more was equal to pure bentonite.

$$logk = logk_0 - \frac{e_0 - e}{C_k} \tag{2.24}$$

where e_0 and k_0 are remolded, or known pre-consolidation void ratio and hydraulic conductivity, respectively. C_k is the permeability change index which can also be defined as the slope of the void ratio vs. log k curve [$C_k = \Delta e/\log(k/k_0)$].

Shakoor and Cook (1990) reported that hydraulic conductivities of compacted limestone aggregate and clay mixtures were not significantly affected up to an aggregate content of 50%, and four to five orders of magnitude increase were observed for aggregate contents between 50% and 70%.

Shelley and Daniel (1993) reported that hydraulic conductivities of compacted gravel-kaolinite-mine spoil mixtures were less than 1×10^{-7} cm/s for gravel contents up to 60%. For higher percentages of gravel, clay particles could not fill the voids, and hydraulic conductivity increased significantly. The authors emphasized that gravel segregation during construction and molding water content may further influence hydraulic conductivity.

Lower hydraulic conductivity may be a significant disadvantage in using CFM as backfills in MSEW. FHWA (2009) states that a few percent of fines may create a significant reduction in hydraulic conductivity, resulting in drainage restriction. Alakayleh et al. (2018) stated that hydraulic conductivity decrease is less significant when fines content is higher than 15%.

Al-Moadhen et al. (2018) investigated the hydraulic properties of composite soils. They suggested that hydraulic conductivity was the function of the clay void ratio for fines contents higher than 35%. Intergranular void ratio and particle gradation were the governing parameters when fines content was lower than 20%. A transitional behavior was observed for soils having fines content between 20% and 35%, depending on confining pressure and density. As a result of the experimental analysis on clay-sand mixtures, they proposed two different empirical equations (Equations 2.25 and 2.26) for the hydraulic conductivity prediction of coarse-dominated and fine-dominated soils. Where k_h (m/s) is hydraulic conductivity, d_{10} is particle diameter corresponding to 10% passing by mass, e_i and e_m are intergranular and matrix void ratios, respectively. A is the activity (PI/clay fraction) of the soil.

Clast-dominated soils (fines content less than 20%):

$$k_h = 2\ x\ 10^{-4}\left[\frac{1}{{d_{10}}^2}\frac{{e_i}^3}{(1+e_i)}\right]^{0.885} \quad (2.25)$$

Matrix-dominated soils (fines content more than 30-40%):

$$k_h = 10^{-10}\left[\frac{1}{A^2}\frac{{e_m}^3}{(1+e_m)}\right]^{1.531} \quad (2.26)$$

2.3.2.1 Specific Surface Area of Materials

The specific surface area (SSA) of a material is defined as the total surface area per unit of its mass. Hydraulic conductivity of soil mediums has been associated with the specific surface area since Kozeny, 1927 and Carman, 1956. Although several experimental methods exist, such as the methylene blue (MB) spot test method or N_2 adsorption method to determine the specific surface area of soils, empirical correlations were also developed to predict SSA from basic soil properties. Some of them are presented in Table 2.4. These empirical formulas can be distinguished into two parts, formulations for fine and coarse-grained soils. Correlations for fine-grained soils mainly were associated with the plasticity properties, whereas correlations for coarse particles were related to the particle size distribution of soils.

Farrar and Coleman (1967) proposed Equation 2.27 in Table 2.4 for British Clays having a liquid limit between 28% and 121%. However, most of the soils' liquid limits were in the range of 40% and 80%. Therefore, it can be said that the prediction accuracy of the correlation is valid within the specified liquid limit ranges.

Chapuis and Aubertin (2003) proposed Equation 2.28 by gathering past experimental data with soils having a liquid limit (LL) lower than 110%. Chapuis and Aubertin (2003) stated that the correlation estimates SSA of soils within ±25% of the measured value when LL<60%. Poorer accuracy is obtained for soils having LL>60%, especially for soils having bentonite.

Chapuis and Légaré (1992) proposed Equation 2.30 for the surface area determination of fine aggregates in bituminous mixtures. Correlation assumes that the surface area is formed by a collection of spherical or cube-shaped particles. Chapuis and Légaré (1992) stated that the correlation gives a reasonable estimate of the specific surface area, although there are studies considering the shape factors for irregular particles.

Equation 2.31 was proposed by Santamarina et al. (2002) by considering the soil made of spherical or cubic particles having a cumulative particle size distribution represented by a straight line. Santamarina et al. (2002) stated that the contribution of the finer particles on the total specific surface area increases with the increase of the coefficient of uniformity. The authors also extended their correlation for platy particles by assuming grains in soil medium to have a similar slenderness ratio.

Ren and Santamarina (2018) pointed out that the specific surface area of mixtures can be calculated by summing the contributions of different particle size fractions based on their percent ratios by mass in mixtures. Sanzeni et al. (2013) suggested Equation 2.29, which calculates the total SSA of fine-grained soils as the weighted average of SSA values for portions finer and coarser than 2 microns. SSA estimations of these fractions were suggested to be calculated by appropriate methods for plastic and nonplastic soils. Sanzeni et al. (2013) indicated that the method has two assumptions. Firstly, finer and coarser portions are assumed to have the same specific gravity. Secondly, the plastic nature of the soil is due to the clay particles smaller than 0.002 mm in the soil sample passing by the No. 40 ASTM sieve.

Table 2.4. Correlations for specific surface area (SSA) estimation

Reference	Formulations	Notes	Equation No
Farrar and Coleman (1967)	$S_S = 1.8w_L - 34$	w_L: liquid limit (%) S_S (m^2/g): Specific surface area	(2.27)
Chapuis and Aubertin (2003)	$\frac{1}{S_S} = \frac{1.3513}{w_L} - 0.0089$	w_L: liquid limit (%) S_S (m^2/g)	(2.28)
Sanzeni et al. (2013)	$S_0 = \frac{F.S_{0,F} + f.S_{0,f}}{100}\%$ $S_S = \frac{S_0}{\rho_s}$	S_0 (1/m): specific surface area per unit volume of particles F,f: % fraction coarser and finer than 0.002 mm, respectively ρ_s (kg/m^3): density of the solids S_S (m^2/kg)	(2.29)
Chapuis and Légaré (1992)	$S_S = \frac{6}{\rho_s}\sum\left[\frac{P_{No\ D} - P_{No\ d}}{d}\right]$	$P_{NO\ D}$ - $P_{NO\ d}$: percentage by mass smaller than D and larger than d sieve sizes ρ_s (kg/m^3): density of the solids	(2.30)
Santamarina et al. (2002)	$S_S = \frac{3}{4}\frac{C_u + 7}{\rho_W G_S d_{50}}$	C_u (unitless): coefficient of uniformity ρ_w (kg/m^3): density of water G_S (unitless): specific gravity d_{50} (m): particle diameter corresponding to 50% passing	(2.31)

2.3.3 Strength Properties

The effect of variables such as mixing ratio, plasticity, initial density, particle shape, gradation, and relative sizes on the mechanical response of CFM has been investigated in the literature. Mechanical response evaluation includes peak and residual strength characteristics and parameters, volumetric behavior (dilative/contractive), brittle/ductile response, and liquefaction resistance.

Several behavioral threshold fines content values have been reported for CFM. Georgiannou et al. (1990) studied the undrained stress-strain response of clayey sands in triaxial compression and extension tests. Clay inclusion did not considerably

reduce the friction angle of the granular component for FC up to 20%. However, they observed that mixtures were no longer dilative and behaved similarly to sedimented clays at 30% clay content.

Simpson and Evans (2015) investigated the behavioral thresholds of clay and sand mixtures with varying mixing ratios. As a result of consistency and strength tests in fall cone apparatus, thermal conductivity tests with a thermal needle probe, compressibility tests in oedometer cell, and undrained triaxial strength testing, they identified three behavioral thresholds governed by four different behavior regimes (Table 2.5).

Table 2.5. Behavioral thresholds and regimes (Simpson and Evans, 2015)

Threshold	Approximate fines content	Applicable behaviors
t^{*1}	0.2	Consistency, compressibility
t^{*2}	0.4-0.6	Critical state strength, conductivity
t^{*3}	0.9	Compressibility

Behavior regime	Applicable fines content, f
Coarse percolated	$0 \leq f \leq t^{*1}$
Coarse and fines percolated	$t^{*1} < f \leq t^{*2}$
Fines percolated	$t^{*2} < f \leq t^{*3}$
Dilute suspension	$t^{*3} < f \leq t^{*4}$

Simpson and Evans (2015) stated that consistency and compressibility behavior depend on the availability of either coarse particles or active fine particles to interact. Critical state strength parameters and conductivity were significantly affected by t^{*2}, where the transition from coarse to fine percolation to only fine percolation occurred. The authors attributed this to coarse-particle clusters creating a force chain and interconnected pores, which resulted in an increase in strength and conductivity at lower fines contents (Figure 2.13).

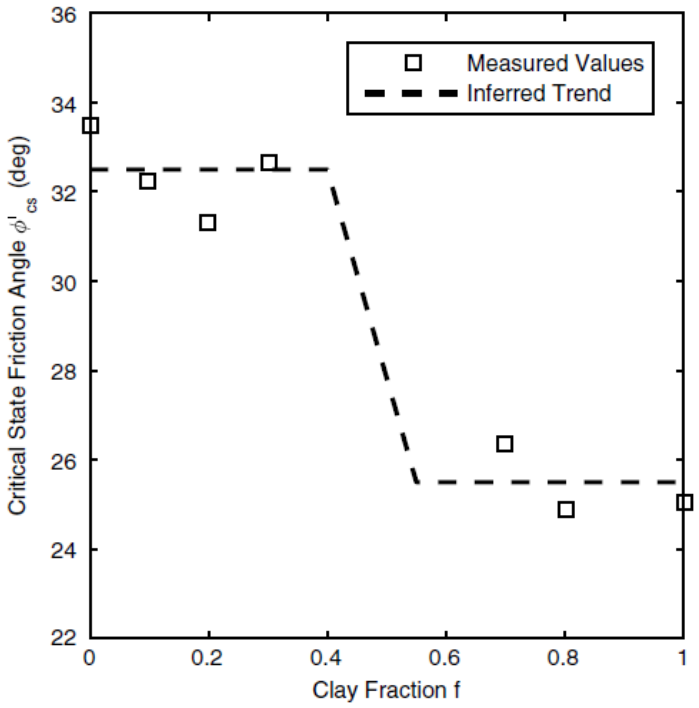


Figure 2.13. Critical state friction angle variation and inferred trend according to clay fraction (Simpson and Evans, 2015)

Bayoglu (1995) conducted undrained triaxial testing on clay-sand mixtures and stated that the drained angle of friction of the sand significantly decreased with the excess of 15% fines. In addition, the undrained friction angle did not seem to be affected by the sand for more than 35% of fines content. Olmez and Ergun (2008) stated that 20% fines content was a threshold value where undrained and drained strength properties changed remarkably. Cabalar and Mustafa (2015b) performed a series of Proctor compaction, California bearing ratio (CBR), and unconfined compression strength (UCS) tests on sand-clay mixtures. They stated that 30% of fines content in sand-clay mixtures was an optimum mixing ratio for pavement design.

Vallejo (2001) investigated the strength properties of binary mixtures by conducting laboratory experiments on mixtures of glass beads having two different sizes, 5 mm and 0.4 mm. Static compaction tests indicated that minimum porosity values were obtained, and coarse particles dominated the structural contact up to fine beads

ratio of 30%. Vallejo (2001) validated this conclusion with the direct shear test results, where the peak shear strength values reflected the strength response of glass beads (Figure 2.14). Behavior was controlled by the coarse and fine beads' partial contribution for fines content between 30% and 60%. Fine beads entirely governed the mechanical response for further increase in fines.

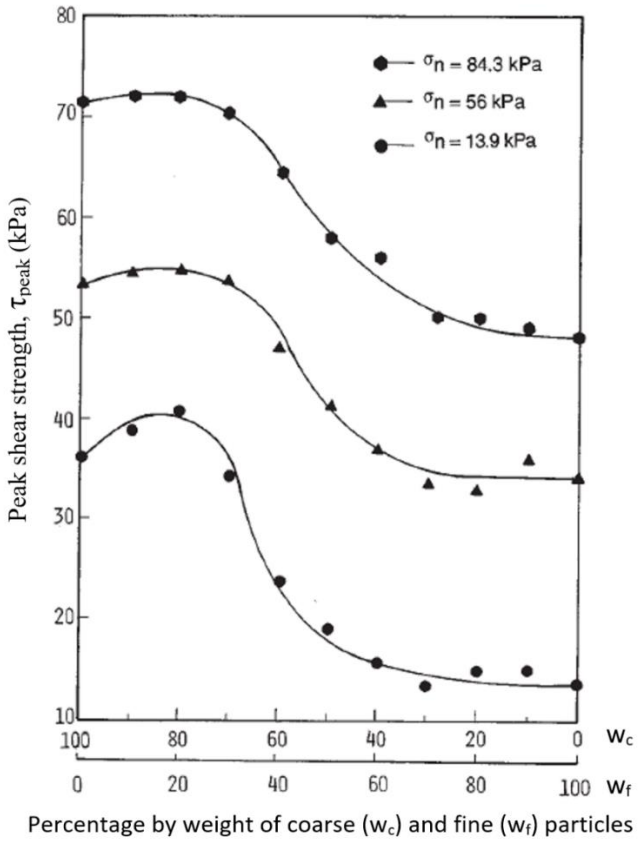
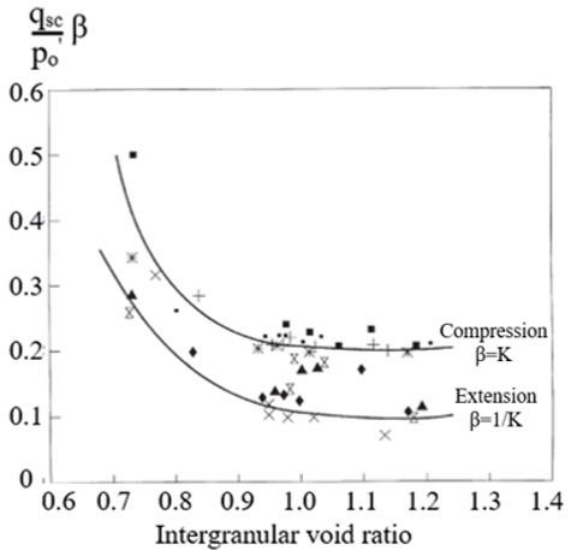


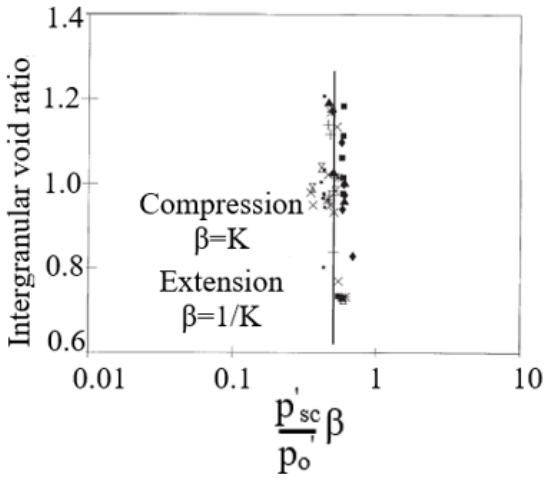
Figure 2.14. Binary mixtures' peak shear strength as a function of mixing ratio and normal stress in direct shear testing (Vallejo, 2001)

Ovando-Shelley and Pérez (1997) investigated the undrained behavior of sands mixed with 3%, 5%, and 7% kaolin contents prepared by wet tamping. Compression and extension triaxial tests were performed for both isotropically and anisotropically normally consolidated specimens up to 100 kPa, and 200 kPa mean effective stresses. They used normalized stress parameters to compare the results of different variables in experimentation. Results indicated that normalized stress at the onset of the

structural collapse depended on the intergranular void ratio for medium-dense specimens. However, it was independent for loose and very loose specimens when $e_s > 0.95$ (Figure 2.15). In the figure, q_{sc} and p'_{sc} are deviatoric stress and mean effective stress at the onset of structural collapse, respectively. p'_0 is the mean effective stress at the end of consolidation, β is the modifying factor for stress parameters, and K is the stress ratio (ratio of radial and vertical stresses).



(a)



(b)

Figure 2.15. (a) Normalized shear strength (as a function of the intergranular void ratio), and (b) state diagram for normalized mean effective stress at the onset of structural collapse (Ovando-Shelley and Pérez, 1997)

Muir Wood and Kumar (2000) conducted undrained and drained triaxial tests on normally consolidated and overconsolidated (OCR: 1.33 and 4) kaolin clay and uniform sand mixtures. Results concluded that the clay matrix controlled the mechanical behavior until fines content fell below 40% and granular volume fraction reached about 0.45 in all specimens. Observed pore pressures and volumetric strains were unaffected by the presence of sand.

Several conclusions were also reported in the literature about the shear strength properties of coarse-fine mixtures in which the coarse fraction contains gravel. Holtz and Gibbs (1956) investigated gravel-clay mixture properties in triaxial compression tests up to 230 mm in diameter. The authors observed a shear strength increase in mixtures having gravel content up to 50-60% and no further increase for higher gravel contents. They emphasized the effect of gravel shape on mechanical response and reported that angular particles resulted in higher shear strength than subangular to rounded particles. Cabalar et al. (2020) indicated a similar conclusion about the effect of particle angularity. Cho et al. (2006) and Shin and Santamarina (2013) pointed out that higher particle irregularity causes an increase in the void ratio, compressibility, and critical state friction angle.

Santucci De Magistris et al. (1998) investigated the effect of compaction on the mechanical characteristics of silty sands. They concluded that the dynamic compaction of materials caused a particular structural arrangement so that it resulted in lower initial stiffness, reduced ductility, and higher dilatancy compared to the soil having the same resultant density but prepared with static overconsolidation. Yamamuro and Wood (2004) also emphasized the effect of depositional methods on the undrained shear strength of sand and silt mixtures. They reconstituted sand with 20% nonplastic silt according to slurry deposition, water sedimentation, air pluviation, mixed dry deposition, and dry funnel deposition methods. They observed a significant difference in strength response even for the identical samples having the same density and stress conditions. They stated that variation in strength behavior was more noticeable in samples with lower densities than higher densities. They attributed the decrease in the effect of the depositional method to the generation of

similar soil fabrics in high densities, which required the application of a high amount of energy.

Liquefaction resistance of CFM has been investigated by several researchers (Georgiannou et al., 1991; Polito and Martin, 2001; Cubrinovski and Rees, 2008). Xenaki and Athanasopoulos (2003) investigated the liquefaction resistance of sand-silt mixtures via stress-controlled cyclic triaxial tests. Results obtained from sixty-one specimens having a global void ratio ranging between 0.55 and 0.95 and normally consolidated to the effective stress of 200 kPa indicated that liquefaction resistance might increase or decrease with the increase of nonplastic fines. A threshold FC of approximately 44% was observed for the specimens having the same global void ratio (Figure 2.16).

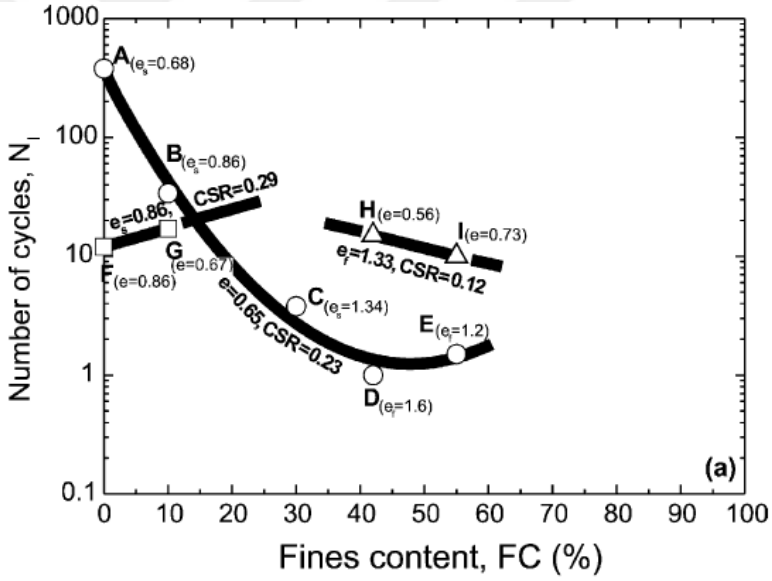


Figure 2.16. Effect of fines content on liquefaction resistance of silt-sand mixtures for constant global, intergranular, and interfine void ratio and cyclic stress ratio, CSR (Xenaki and Athanasopoulos, 2003)

In addition, an increase in fines caused an increase in liquefaction resistance for the same intergranular void ratio for FC lower than the threshold value. On the other hand, increase in fines content decreased the liquefaction resistance for FC higher than the threshold value by keeping the interfine void ratio constant (Figure 2.16).

The authors pointed out that the reported threshold value was not unique but depended on the coarse and fine grain properties and global void ratio.

Polito and Martin (2001) also studied sand and nonplastic silt mixtures' liquefaction resistance. They observed two distinct behavioral patterns according to the particle packing characteristics of mixtures. They stated that threshold fines content would be within the range of 25-45% associated with the largest amount of silt content placed in the voids of the sand skeleton and the relative density of the mixture.

Papadopoulou and Tika (2016) investigated monotonic and cyclic shear resistance of sands (e_{max}=0.841, e_{min}=0.582, d_{50}=0.30 mm, C_u=1.3) mixed with nonplastic silt (e_{max}=1.663, e_{min}=0.658, d_{50}=0.02 mm, C_u=7.5) and kaolin clay (LL= 65%, PL=30%, PI=35%, 90% of particles < 5 μm) in varying fines content (0-15%) and plasticity (0-35%) in triaxial testing. Results indicated that strength response weakened until a threshold plasticity index, PI_{th}, and improved after that with a further increase in plasticity. PI_{th} were 6% and 22% for fines content 5% and 15%, respectively. Excess pore water pressure generation occurred in cyclic triaxial testing, and it approached the initial confining stress ($\Delta u/p'_0 \geq 0.90$) when the state of liquefaction was reached.

Strength properties of CFM have also been investigated with the critical state soil mechanics (CSSM) framework after Roscoe et al. (1958). This approach considers the strength response of soil based on its current stress state. Poulos (1981) defined the steady-state condition as the deformation of a soil mass at constant volume, constant shear stress, and constant velocity. Line combining steady states of soil in void ratio and mean effective stress (p') space is called the critical state line (CSL) (Figure 2.17). Mean effective stress (p'), deviatoric stress (q), and the projection of the CSL into the p'-q diagram are defined in Equations 2.32, 2.33, and 2.34.

Been and Jefferies (1985) pointed out that the unique structure of the CSL is independent of the initial conditions of the sand. The mathematical formulation defining this line in ν-lnp' space is presented in Equation 2.35. The current state of the soil is defined with the state parameter (ψ), the difference between the initial and critical state void ratios (Equation 2.36). The volumetric response of soils can be

determined with the state parameter. Soils show contractive behavior during shearing if they have state points above the CSL, positive state parameters. On the other hand, negative state parameters indicate a dilative response.

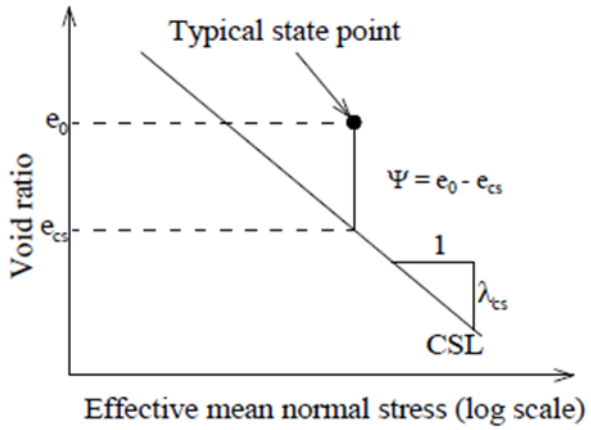


Figure 2.17. Definition of SSL and state parameter (Been et al., 1991)

$$p' = \frac{\sigma_1' + 2\sigma_3'}{3} \tag{2.32}$$

$$q = \sigma_1' - \sigma_3' \tag{2.33}$$

$$M = \frac{q}{p'} \tag{2.34}$$

$$\nu = \Gamma - \lambda ln p' \tag{2.35}$$

$$\psi = e_0 - e_{cs} \tag{2.36}$$

where, σ_1' and σ_3' are the major and minor effective stresses, respectively. q is the deviatoric stress, p' is the mean effective stress, and ν is the specific volume. λ and Γ are the slope and intercept of the CSL in ν-lnp' space, respectively. ψ is the state parameter; e_0 and e_{cs} are the initial and critical state void ratios, respectively. M is the slope of the critical state line projected into p'-q space.

Effective stress paths for undrained triaxial tests of sandy soils are categorized in Figure 2.18 after Pitman et al. (1994). Type 1 behavior is specific to loosely packed soils, and they exhibit a strain-softening behavior after a peak shear strength is reached. Shear stress stabilizes at ultimate steady-state or residual strength in large

strains while contractive volumetric behavior is observed. Bishop (1967) proposed Equation 2.37 to quantify the degree of strain-softening by defining the Brittleness Index, I_B. In this equation, τ_p and τ_r are the peak and residual shear strengths, respectively.

$$I_B = \frac{\tau_p - \tau_r}{\tau_P} \tag{2.37}$$

Type 2 behavior represents the transition associated with the medium-dense soils. Limited strain-softening and contractive behavior, followed by a strain-hardening at ultimate state, creating an "elbow" in effective stress path, is observed in these soils. Ishihara et al. (1975) defined the phase transformation line, and it has been widely used after that to identify the transition between the contractive and dilative soil responses. Type 3 is an undrained strength behavior of dense sand, which exhibits strain-hardening and dilative soil response. Because strain-softening behavior is associated with the deformation flow, Type 1, Type 2, and Type 3 behavior are also defined as flow, limited flow, and no-flow conditions, respectively (Pitman et al., 1994; Cubrinovski and Rees, 2008).

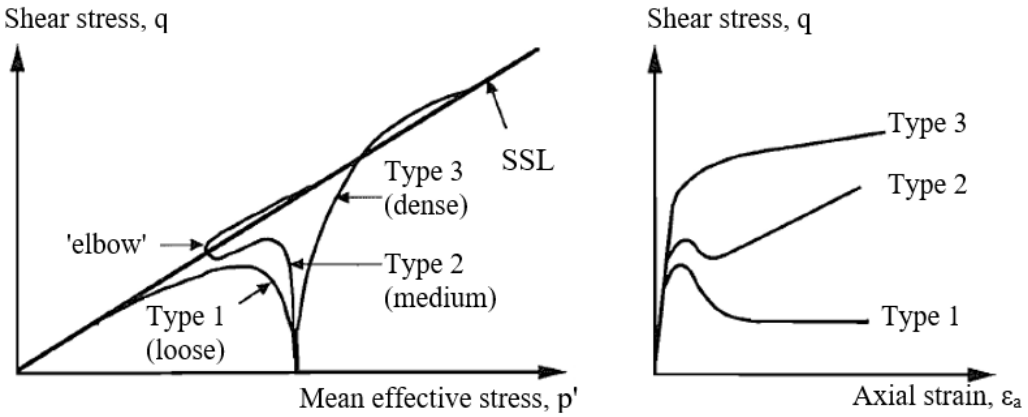


Figure 2.18. Effective stress paths for undrained triaxial tests (Pitman et al., 1994)

After a peak strength is reached, a reduction in strength is observed in the undrained behavior of loose soils (Type 1). Therefore, the soil becomes unstable far before the

steady-state or failure condition is achieved. Chu and Leong (2002) defined the term instability as the condition in which large plastic strains rapidly occur due to soils' inability to sustain a given load or stress (Figure 2.19). The zone between the CSL and instability line is defined as the zone of instability.

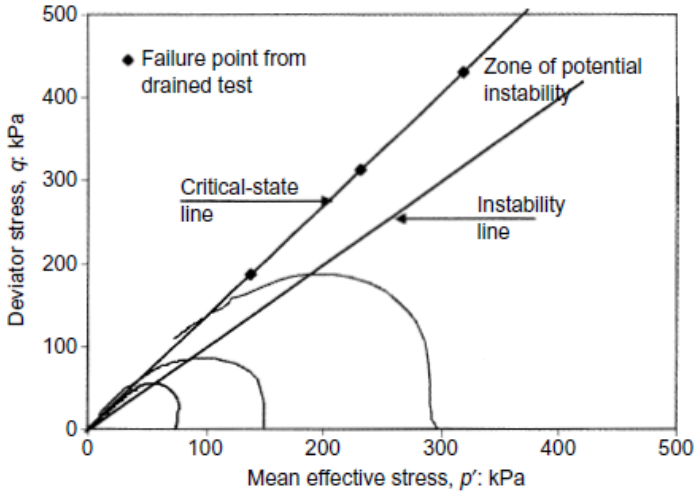


Figure 2.19. Critical state line, instability line, and instability zone defined by drained and undrained tests for loose sand (Chu and Leong, 2002)

Abedi and Yasrobi (2010) investigated the effect of plastic fines on sands' strength and stability response. The sand used in tests was classified as SP and had angular particles, whereas the fine portion consisted of bentonite and natural fine mixture (LL=51%, PL=21%, PI=30%, G_s=2.72). Undrained triaxial strength tests were performed using mixtures with fines content up to 30% and two different initial dry densities (1.45 g/cm^3 and 1.50 g/cm^3). Specimens were isotropically consolidated to two different confining pressures (100 kPa and 140 kPa). Results revealed that a small amount of fines inclusion increased the susceptibility of the sand to instability. However, the instability potential of the sand increased for fines content above 10-15%. A decrease in the peak shear strength was observed up to fines content of 10% and remained constant for further fines increases.

Georgiannou et al. (1990) reported that sand with a clay content of 7.6% gave deviatoric stress 1.7 times lower than the sand with a clay content of 4.6% at phase

transformation. Twice as high strain values were recorded at the end of the contractive phase in 7.6% clayey sand than 4.6% clayey sand. After the phase transformation, effective stress paths followed the same line until failure for at least 20% axial strain. Undrained brittleness, as well as strains observed at phase transformation, increased for clay contents of 4.6% to 10%, even though mixtures had the same intergranular void ratio. In addition, they stated that overconsolidation of the sedimented clay-sand mixtures resulted in a decrease in undrained brittleness and increased the axial strain at failure.

Pitman et al. (1994) investigated the effect of plastic and nonplastic fines on the collapse of loose sands. They concluded that undrained brittleness decreased as both plastic and nonplastic fines content increased. No brittleness, only strain hardening response was observed in mixtures having 40% fines. They stated that undrained brittleness might be a function of fine particle amount in the mixture but not the plasticity, at least for fines content higher than 10%. They indicated that 20% fines content to be a marked threshold fines content between the sand dominated to fine dominated soils.

Thevanayagam and Mohan (2000) conducted undrained triaxial tests to investigate the stress-strain behavior of silty-sands by considering the intergranular state variables. Single host sand was mixed with two different types of nonplastic silts as ground silica fines and kaolin silt fines, as the resultant fines content of the mixtures would be 2%, 12%, and 27%. They introduced intergranular and interfine state variables as ψ_s and ψ_f, respectively, using intergranular and interfine void ratios instead of the global void ratio. They concluded that an increase in fines resulted in smaller undrained shear strength and more contractive volumetric response up to a threshold fines content of 30% at the same void ratio and confining stress. Further increase in fines content might result in a less contractive and stronger soil response.

Several researchers reported the tendency of the downward shift of the CSL for CFM as fines content increases. Naeini and Baziar (2004), who investigated the steady-state strength properties of sand-silt mixtures, reported that CSL moved downward

up to 35% silt content inside the sand matrix. Above 35% silt content, CSL moved upward again. Zlatović and Ishihara (1995) and Yang et al. (2006a) reported similar behavior in sand-silt mixtures as CSL moved downward in e-p' space until 30% silt content and moved upward for further fines content increase.

Yamamuro and Lade (1998) conducted drained and undrained triaxial tests on loose silty sands and stated that undrained test results with samples having different initial void ratios did not converge into a single unique steady-state line. They attributed this conclusion to the "reverse" behavioral properties of silty sand, a more dilative response with increasing confining pressure under undrained shearing.

Ferreira and Bica (2006) investigated the CSL of natural and reconstituted transitional soils with intermediate sand and clay properties. The mean values of the void ratio of the samples taken from three different areas were 0.60, 0.66, and 0.70. The mean values of the Atterberg limits for each sample were LL=20% and PL=14%. Drained triaxial tests were conducted on isotropically consolidated specimens. They concluded that other than natural soils, reconstituted soils (prepared by static compaction of wet samples in three layers) did not show a unique CSL and normal compression line (NCL) because the shape of the CSL depended on the sample's initial void ratio. Therefore, Ferreira and Bica (2006) suggested that the non-uniqueness of the CSL and NCL should be considered if the CSSM framework is applied to transitional soils.

Shipton and Coop (2015) investigated the transitional characteristics of sand, including plastic and nonplastic fines, with drained and undrained triaxial strength testing. The authors confirmed the results of previous studies reporting non-convergent CSL for transitional soils. Series of parallel CSL was observed depending on the initial specific volume of the soil at medium strain levels. Other conclusions of Shipton and Coop (2015) were:

- The similarity between the patterns of sand with plastic fines and sand with nonplastic fines implied that transitional behavior need not be related to the plasticity of the fines.

- A linear correlation was observed between the initial specific volume and the intercept of the critical state line, Γ giving gradients of 0.52 and 0.97 for sand with plastic and sand with nonplastic fines, respectively. In this correlation, a family of parallel CSL hypothesis was assumed to be correct for each transitional soil.
- Different sample preparation techniques did not affect the relationship between the initial specific volume and the intercept of the CSL, Γ.

2.3.4 Compression Properties

Compressibility properties of CFM have been investigated both experimentally and analytically in several studies (Kumar and Muir Wood, 1999; Thevanayagam and Mohan, 2000; Monkul and Ozden, 2005; Shi and Zhao, 2020). Varying threshold fines content was reported in the literature where compressibility characteristics remarkably differ. Bayoglu (1995) stated that the compressibility behavior of sand-clay mixtures changed from coarse-grained to cohesive soil dominancy at percent fines of about 25-30%. Simpson and Evans (2015) stated that when fines content exceeded 20%, the compressibility of the clay-sand mixture increased significantly. This increase can be observed up to 90% fines content. Any fines increment beyond this ratio did not increase compressibility because coarse particles became so dilute inside the fine matrix.

Monkul and Ozden (2005) emphasized the non-uniqueness of the transitional fines content for the compression behavior of sand and kaolinite mixtures. They stated that it mainly depends on initial conditions, effective stress, global void ratio, and maximum void ratio of the host granular soil. Granular compression index, $C_{c\text{-}s}$ was used for the clear observation of the influence of coarse grain matrix on mixtures' compression behavior (Equation 2.38). In this equation, the intergranular void ratio is used instead of the global void ratio. Granular compression index is defined as the decrease of intergranular void ratio (Δe_s) with the effective stress increment ($\Delta \log \sigma'$).

$$C_{c-s} = \frac{\Delta e_s}{\Delta log\ \sigma'} \tag{2.38}$$

Monkul and Ozden (2007) performed oedometer tests on sand (C_u=2.67, C_c=0.81, e_{max}=1.12, d_{50}=0.190 mm, classified as SP) and kaolin (LL=38.2%, PL=19.2%, d_{50}=1.9 μm, classified as CL) mixtures having kaolinite content of 0%, 10%, 15%, 20%, 25%, 30%, and 40%. The authors identified the transitional fines content (TFC) according to the intergranular void ratio of the mixture being equal to the host granular soil's maximum void ratio. They reported that TFC varied between 19% and 34% in their study. They also stated coarse-grain particles mainly governed compression behavior for lower FC, whereas clay matrix dominated the compression when fines content exceeded the TFC. They emphasized that the value of TFC increased with the increase of effective stress on mixtures (Figure 2.20). Denser particle packing and a lower intergranular void ratio were observed for the mixtures having the same FC but higher effective stress values. The effect of the coarse-grain matrix on transitional behavior could be better captured by evaluating the granular compression index, $C_{c\text{-}s}$ (Figure 2.21). The difference between the global and granular compression indices increased with FC. Cabalar (2010) verified the conclusions of Monkul and Ozden (2007).

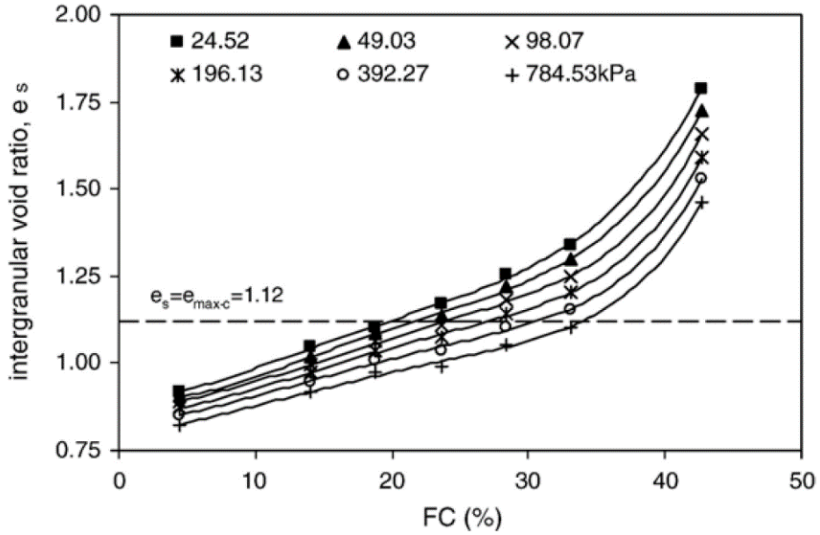


Figure 2.20. Intergranular void ratio with fines content variation under different oedometer stresses (Monkul and Ozden, 2007)

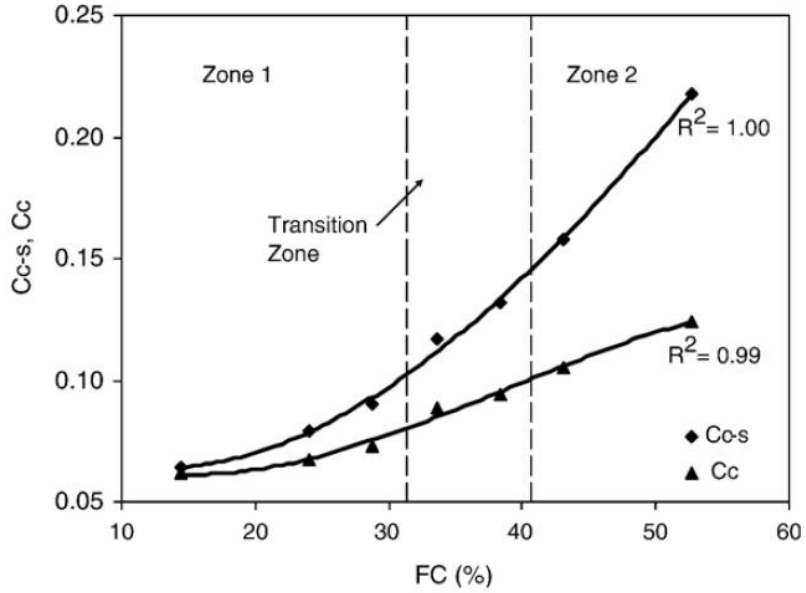


Figure 2.21. Compression parameters with the variation of fines content (Monkul and Ozden, 2007)

Kumar and Muir Wood (1999) performed compression tests on saturated kaolinite clay (G_s=2.62, LL=80%, PL=39%, PI=41%, and 95% of particles < 2 μm) and fine gravel (G_s=2.65, e_{max}=0.99, e_{min}=0.58, uniform particle grading between 2.0 mm and 3.35 mm) mixtures. Compression tests consisted of two sets as hydraulic oedometer

(Rowe cell) and consolidation tube by applying dead weight. Test results of the mixtures having clay contents range between 10% and 100%, with 10% increments, showed that a remarkable behavioral change was observed for clay contents lower than 40%. The authors stated that clay matrix alone controlled the mechanical behavior of the mixtures for clay contents higher than 35%. Fine gravel began to influence the mechanical behavior when the granular volume fraction reached 0.45.

Phanikumar et al. (2010) studied the swell-consolidation characteristics of artificially prepared sand and expansive clay mixtures. They reported that the increment of sand content up to 30% decreased swelling potential (swell thickness/original height) by 71% and 50%, and swelling pressure by 67% and 57%, respectively, for soil portions passing 425 μm and 75μm sieve. In addition, it caused a decrease in coefficient of volume compressibility and compression index by 30% and 50%, respectively, for soil fractions passing 425 μm.

Shi and Yin (2018) investigated the consolidation behavior of saturated sand (e_{max}=0.945, e_{min}=0.601) and marine clay (LL=62.4%, PL=27.5%) mixtures. After marine clay having a moisture content of 86.9% was prepared, it was mixed with sand homogenously at fractions of 0%, 20%, 40%, and 60%. Specimens were consolidated with stepwise increments from 2.5 kPa to 800 kPa. Shi and Yin (2018) reported that mixtures with a 20% sand fraction had a consolidation curve very close to pure clay (Figure 2.22). An increase in sand content for more than 20% resulted in the acceleration of the consolidation process.

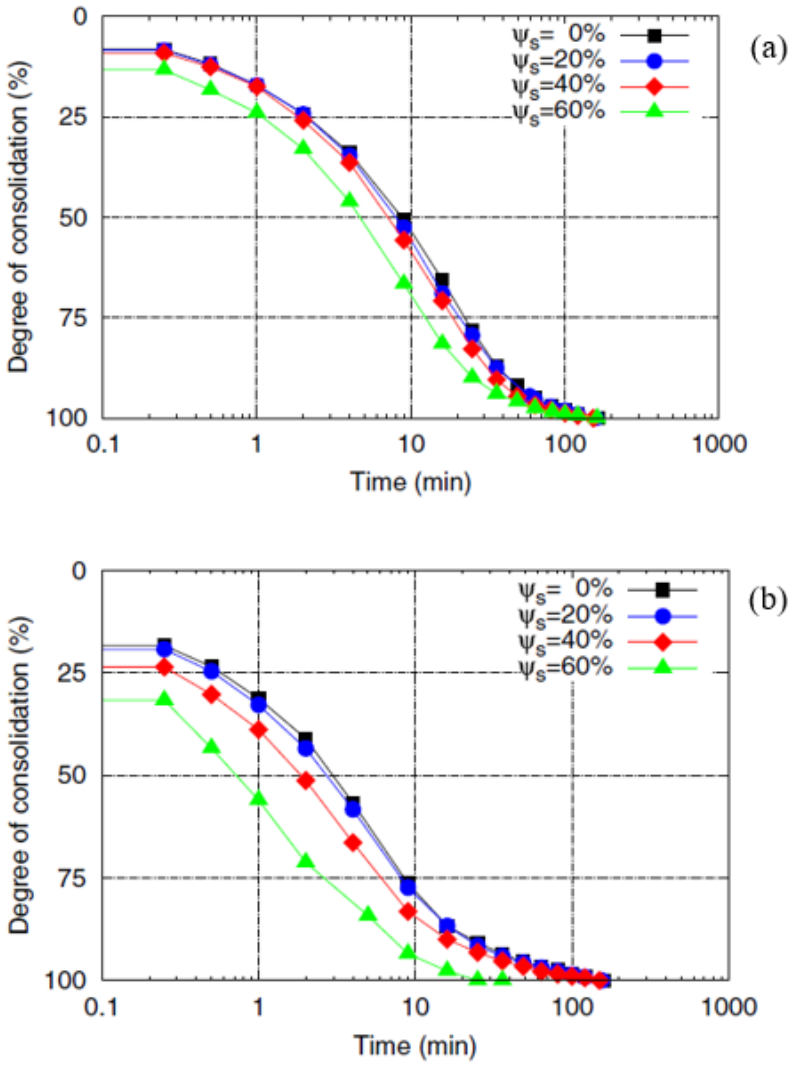


Figure 2.22. Consolidation curves of sand and marine clay mixtures at different stress levels (a) 50 kPa, (b) 800 kPa (Shi and Yin, 2018)

Shi and Zhao (2020) proposed a compression model for clayey/silty sands having fines content lower than the TFC by using the equivalent intergranular void ratio concept of Thevanayagam et al. (2000) (Equation 2.4). The proposed compression model, presented in Equation 2.39, contains three model parameters: α, compression parameter, related to the decreasing rate of void ratio with increasing loading rate; e_r is the inactive void ratio of coarse granular materials; b is a structure parameter, representing the contribution of fines to the force transfer mechanism. A minimum of two compression tests were recommended to calibrate these parameters: one test

on pure coarse material from which α and e_r can be determined. The other test on gap-graded mixture having predefined fine fraction, which b parameter can be calibrated from its compression curve. The authors verified the performance of the proposed model by reporting good agreement with experimental results. In Equations 2.39, 2.40, and 2.41, e_0 is the initial void ratio, ${e_0}^{eq}$ is the equivalent initial void ratio (calculated from Equation 2.4), and ${e_r}^{eq}$ is the equivalent inactive void ratio. α^{eq} is the equivalent compression parameter, σ' is the effective stress, σ_r=1 kPa is the unit reference stress, and f_c denotes the fine fraction.

$$e = (e_0 - {e_r}^{eq})\exp\left(-\alpha^{eq}\frac{{e_0}^{eq}(1+{e_0}^{eq})}{(1+e_0)\sigma_r}\sigma'\right) + {e_r}^{eq} \quad (2.39)$$

$$\alpha^{eq} = \frac{\alpha}{1-(1-b)f_c} \quad (2.40)$$

$${e_r}^{eq} = e_r - (1-b)f_c(1+e_r) \quad (2.41)$$

Past research showed that clean sands, as well as clays, could be described within the scope and parameters of critical state soil mechanics, CSSM (Been and Jefferies, 1985; Coop and Lee, 1993). Therefore, it is possible to define a unique normal compression line, NCL, being parallel to the CSL, which ultimately different initial conditions of the same soil converge. However, recent research indicates that there are transitional soils that do not fit this trend. For these soils, a unique CSL and NCL could not be identified, implying that the concept of CSSM is not valid (Martins et al., 2001; Nocilla et al., 2006).

Martins et al. (2001) studied the compressibility behavior of clayey sands. Reconstituted soil derived from Botucatu sandstone, BRS (weathered, consists of 30% fines, plastic properties of fine fraction: LL=49%, PL=34%) in addition to an artificial mixture, KS (d_{50}=0.55 mm, plastic properties of fine fraction LL=39%, PL=30%), which consisted of 75% clean quartzitic medium sand and 25% kaolin were used in tests. Oedometer and K_0-triaxial tests were carried out on the samples. The authors reported that as a typical behavior in gap-graded sandy clays, no unique

NCL could be identified up to stress levels of 6 MPa; instead, observed behavior was a function of the initial void ratio (Figure 2.23). The authors suggested that this behavior was seen in intermediate soils having a fines content in the range of 20-30%, in which exact values depending on the plasticity and nature of the sand grains. Ferreira and Bica (2006) reported similar conclusions and confirmed the non-convergence of NCL and CSL of transitional soils up to stress levels of 25 MPa.

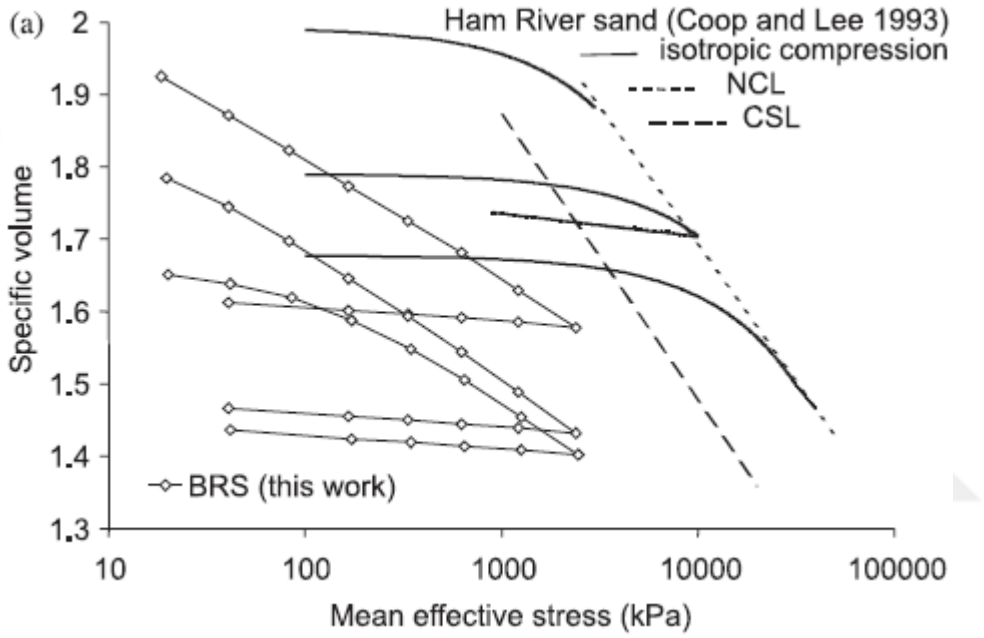


Figure 2.23. Comparison of normal compression lines of BRS and results of Coop and Lee (1993) (Martins et al., 2001)

Shipton and Coop (2012) investigated the compression behavior of transitional soils with artificial mixtures having varying sand and nonplastic or plastic fine ratios. Series of oedometer tests were performed with mixtures prepared from three different types of sand, crushed quartz silt, and kaolin clay (LL=62%, PL=32%). The authors investigated the conditions under which non-convergence of NCL can be expected in transition soils. They stated that the factors affecting compression behavior are rather complex. Therefore, they suggested that each soil encountered must be evaluated individually. Particle size distribution of soils exhibiting

transitional and non-convergent compression behavior compiled by Shipton (2010) is presented in Figure 2.24. Shipton and Coop (2012) also concluded that mixed grading soils with mixed mineralogy and particle types tended to give non-convergent NCL. In addition, they stated that particle breakage could be observed in these soils, although it is not a prerequisite.

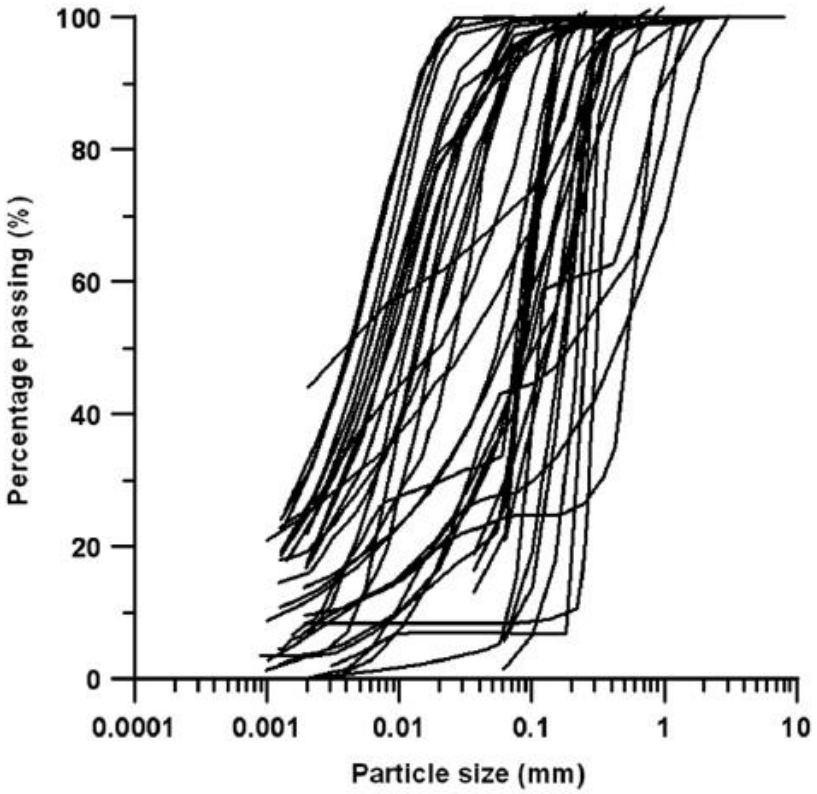


Figure 2.24. Collection of the particle size distribution of soils exhibiting transitional and non-convergent compression behavior (Shipton, 2010)

2.4 Soil-Geosynthetic Interaction Studies

Understanding soil – geosynthetic reinforcement interaction mechanisms has extreme importance in the design of MSEW for predicting their long-term performance and stability. Different types of tests and theoretical analyses were developed with particular reference to the usage of geosynthetic materials.

Palmeira (2009) summarized the possible failure mechanisms of a reinforced soil wall in regions based on the geosynthetic's active loading conditions and position (Figure 2.25). The author also pointed out the most suitable experimentation methodologies simulating the field conditions for each region, although they have some limitations in representing the actual site response. The soil mass may slide on the reinforcement surface in Region A; therefore, the soil-reinforcement bond can be quantified with direct shear tests. In region C, direct shear tests in which the reinforcement inclined to the shear plane can be employed. In region B, lateral deformation of both soil and the reinforcement might occur; therefore, testing similar to a soil tensile test could be employed. Lastly, pullout tests could be adapted to simulate the failure mechanism in Region D.

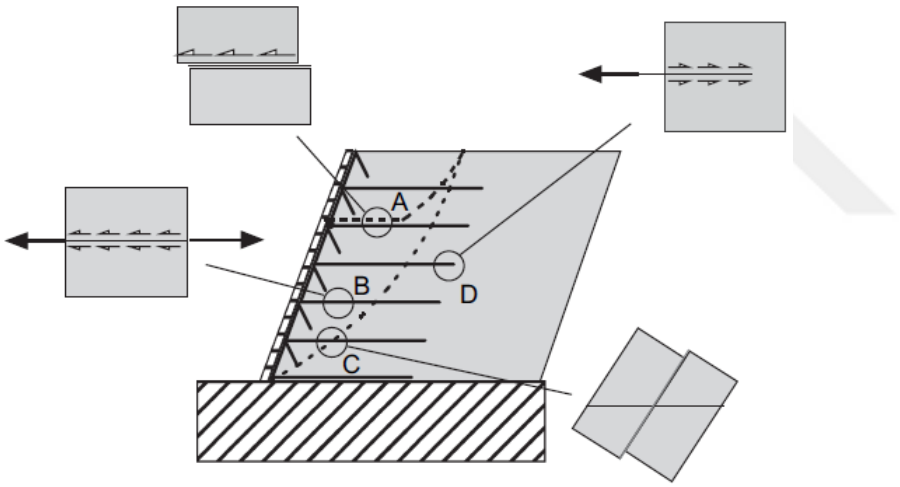


Figure 2.25. Interaction mechanisms in a geosynthetic reinforced soil wall (Palmeira, 2009)

Although the scope of this study is the investigation of geogrid and CFM interaction mechanism in direct shear testing, studies on other test setups (such as pullout apparatus, centrifuge testing) and other materials (granular soils, geotextile, e.g.) were briefly mentioned in this section to review the common approaches and investigated parameters.

Ferreira et al. (2015a) investigated the influence of soil moisture and density on the soil-geogrid interaction in pullout conditions. Large scale pull-out tests were conducted on granite residual soil (classified as SW-SM, d_{50}=1.0 mm, C_u=16.9, C_c=1.0, $\gamma_{d,min}$=13.4 kN/m^3, $\gamma_{d,max}$=18.9 kN/m^3 and w_{opt}=11.5%) and uniaxial extruded geogrid. Results concluded that frontal displacements, at which the maximum resistance achieved, decreased and the pullout resistance substantially increased with the soil dry unit weight increment regardless of moisture content. Failure mode was observed to be strictly dependent on the soil density. Failure was due to the lack of sufficient tensile strength of the geogrid in denser soils, whereas it was because of the sliding at the interface for lower density soils. Geogrid deformation was more pronounced at the point of pullout force application and decreased progressively with the distance from the front end. Non-uniform shear stress mobilization through geogrid length was far more significant for denser soils. The pullout resistance obtained at half of the optimum moisture content for loose soils was higher than the other moisture conditions. On the other hand, the effect of moisture content on the pullout resistance and deformation was almost negligible for denser soils. Pullout interaction coefficients within the scope of the experiments ranged from 0.33 to 0.58.

The increasing tendency to use CFM as backfill material in reinforced soil structures (as mentioned in Section 2.1) has necessitated comprehensive evaluations for the geosynthetic and CFM interaction in different initial specimen placement and loading conditions. Most studies have focused on examining the interface shear strength response with moisture content, pore pressure, soil density, and the effect of draining the water from the composite reinforced system. Many researchers (Zornberg and Mitchell, 1994; Christopher et al., 1998; Koerner, 2005; Naughton et al., 2015) emphasized the vital importance of draining the water from reinforced fill and preventing water infiltration into the body when using cohesive, marginal fill materials. Tatsuoka and Yamauchi (1986) pointed out the efficiency of permeable geosynthetics by investigating the reinforcement of steep clay slopes by using non-woven geotextile in test embankments. The authors stated that usage of non-woven

geotextile not only provides drainage of pore water but also allows better compaction operation and gives tensile reinforcement to the soil.

Abu-Farsakh et al. (2004) conducted a series of reduced-scale laboratory and field pullout test programs on different geosynthetic reinforcements in marginal cohesive fills.

In laboratory setup:

- Apparatus dimensions were 91 x 152 x 91 cm.
- Four types of geogrids and a woven geotextile were used.
- Soil material was low plasticity clay (PI=%15, c=14 kPa, ϕ=24°)
- Confining stress range was 20.7-103 kPa

In field pullout test:

- 6 m high, 47 m long geosynthetic reinforced soil wall
- The normal stress range was 22-89.6 kPa

Displacements and pullout force were measured in the experiments. Results concluded that cohesive soils showed adequate pullout resistance to be used in reinforced soil walls. The authors also stated that the suitability of marginal backfill was strongly related to the structure's height. Laboratory and field test results were in good agreement, especially with softer (extensible) geosynthetics. However, in stiffer reinforcements, differences became larger. The authors attributed this to the difference between the length of the specimens, material stiffness, and reinforcement geometry of laboratory and field tests.

Zornberg and Kang (2005) studied the reinforcement of poorly draining silty soils (LL=29%, PL=12%, w_{opt}=12.9%, $\gamma_{d,max}$=18.67 kN/m^3) with geogrids in large pullout apparatus (1520 x 610 x 280 mm). Two different geogrids having similar tensile strength (strength in the machine and cross-machine directions: 100 and 15 kN/m) but with and without in-plane drainage properties were used in tests. The normal pressure of 41 kPa and 2 mm/min displacement rate was applied. The apparatus was

instrumented with four LVDT, pore water pressure transducers, and a load cell (Figure 2.26). Results concluded that the majority of the pullout resistance mobilized within 0.2 in (5.1 mm) displacement. Geogrid having a drainage property resulted in an approximately 30% increase in pull-out resistance. Lopez et al. (2006), using the same equipment and testing materials, stated that geogrid with in-plane drainage was more efficient when the initial pore water pressure was higher.

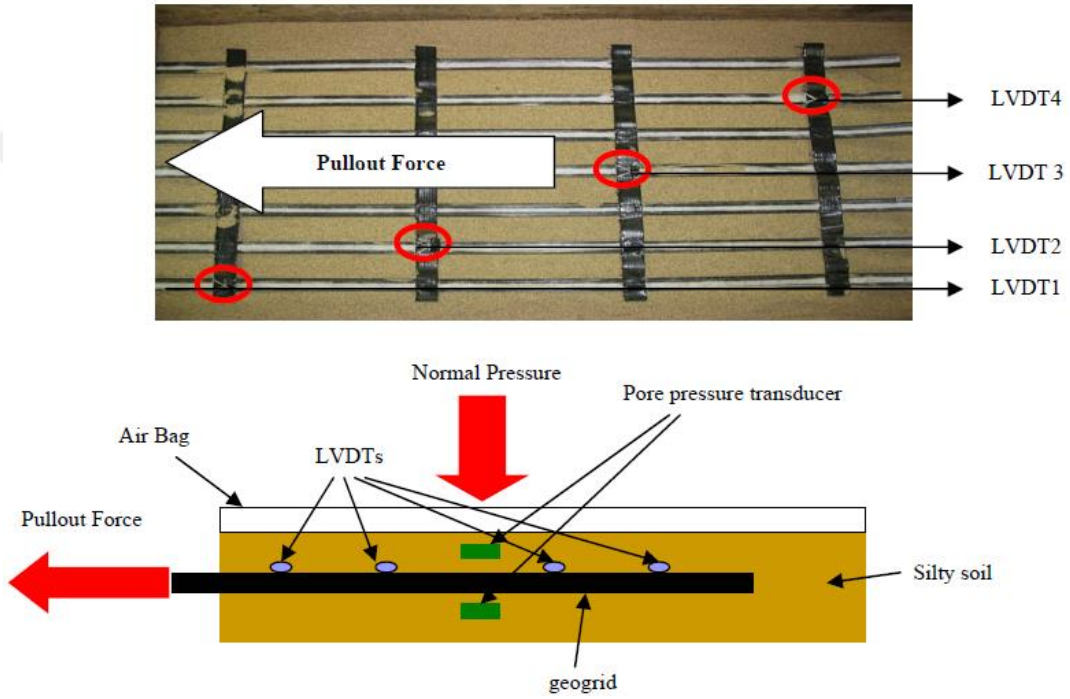


Figure 2.26. Plan and cross views of the pullout apparatus (Zornberg and Kang, 2005)

Clancy and Naughton (2011) investigated the pullout resistance of a fine-grained cohesive soil (LL=52.5%, PI=26.8%, c=21.5 kPa, ϕ=18.6°, percent passing 63 μm= 58%) reinforced with geogrids. Conventional geogrid and a geogrid having drainage capability with in-plane drainage channels and triaxial apparatus were used (Figure 2.27). Confining stresses of 25, 50, and 90 kPa, different pullout rates of 0.2, 2, and 10 mm/min, and moisture contents ranging between 35 to 60% were evaluated as varying parameters.

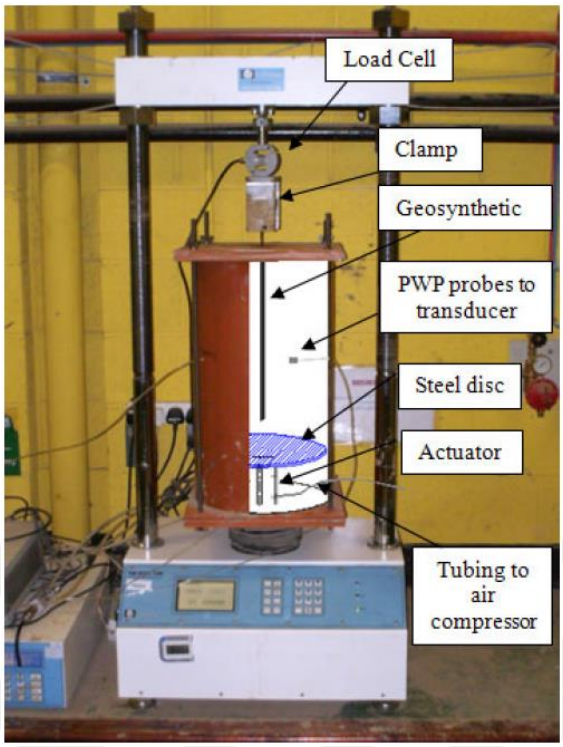


Figure 2.27. Experimental pullout apparatus (Clancy and Naughton, 2011)

Results indicated that pullout resistance was inversely proportional to the moisture content and confining pressure for conventional geogrid. Higher pullout rates resulted in stronger pullout resistances for both conventional and draining geogrids. The draining geogrid produced a higher pullout response than conventional geogrid for all drainage conditions, including zero, partial and full excess pore water pressure dissipation. Generated pore water pressures during pullout at the drainage location of the geogrid reached 47.6, 24.6, and 17.4% of the 25, 50, 90 kPa confining stresses, respectively. These results concluded that the drainage element works more efficiently under higher confining stresses.

Balakrishnan and Viswanadham (2016) evaluated the geogrid reinforced soil wall performance via centrifuge model testing. Marginal backfill soil (SM, percent passing 75 μm=21%, d_{50}=0.16 mm, LL=23%, PL=Non-plastic) was tested with two geogrids (PET, PVC) having different stiffness properties. Centrifuge testing apparatus applied 40 g to the reinforced soil wall models with wrap-around facings.

Results indicated that soils reinforced with weaker geogrids experienced excessive deformations very rapidly. The shift of the wall facing and the highest strains being in the uppermost reinforcements indicated that pullout failure was observed in the reinforcements in the upper half. On the other hand, using the stronger geogrid in marginal backfill significantly limited wall face movements, surface settlements, tension cracks, and peak strains in geogrid layers (Figure 2.28).

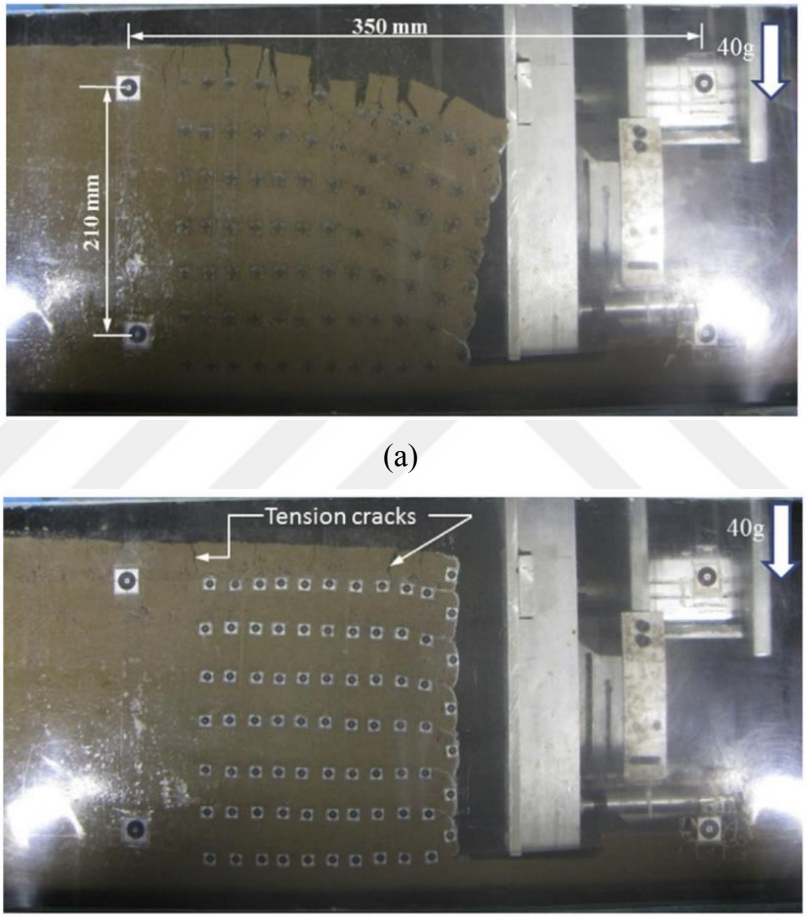


Figure 2.28. Reinforced soil wall displacements in centrifuge testing by using (a) weaker geogrid, (b) stronger geogrid (Balakrishnan and Viswanadham, 2016)

2.4.1 Large Direct Shear Tests

Sliding along the soil-geosynthetic interface is one of the failure mechanisms that may compromise the internal stability of an MSEW and should be evaluated in direct shear failure mode. In addition to the failure assessment, it is also essential in evaluating the deformation response of the system. Hatami and Bathurst (2005) showed that the interface stiffness of a reinforced soil wall significantly affects the amount of lateral wall displacement according to the numerical studies conducted.

Theoretical expressions have been developed to quantify the interface direct shear resistance between the geogrid and soil. Jewell et al. (1985) suggested that the total interface resistance could be considered as the summation of the contributions of soil shearing over itself in grid openings and shear between soil and geogrid surface. They proposed Equation 2.42 to describe direct sliding resistance in a generalized expression.

$$f_{ds}\ tan\phi_{ds} = \alpha_{ds}\ tan\delta + (1 - \alpha_{ds})\ tan\phi_{ds} \quad (2.42)$$

Where f_{ds} is the coefficient of resistance to direct sliding, ϕ_{ds} is the internal friction angle for soil in direct shear, δ is the skin friction angle for the soil on plane reinforcement surfaces, α_{ds} is the fraction of grid surface area that resists direct shear with soil. In this equation, α_{ds} is dependent on the relative size between the soil and grid openings (aperture size/soil particle size). A reduction in the value of α_{ds} results in the increase of direct shear resistance. For coarser soils, having a similar particle size as the grid apertures, $\alpha_{ds}=0$ and $f_{ds}=1$ indicating the rupture zone is forced away from the grid surface and entirely located in the soil. For finer soils or higher values of aperture size/soil particle size, the value of α_{ds} can be expressed as the fraction of the solid surface of geogrid in the shear zone (1-percent open area/100).

Alfaro et al. (1995) stated that linear-elastic perfectly-plastic Mohr-Coulomb failure criteria could represent the mobilized direct shear resistance of the interface in

Equation 2.43. In this equation, τ is the shear strength, c_a is the adhesion, σ_n is the normal pressure on the direct shear surface, and δ is the friction angle of the interface.

$$\tau = c_a + \sigma_n \tan\delta \tag{2.43}$$

Bergado et al. (1993) also defined the total shear resistance of the soil-geogrid interface as the summation of the percent contributions of soil-soil and soil-geogrid shear resistances. Bergado et al. (1993) defined the bond coefficient as the ratio of resistances between soil and reinforcement to soil and soil.

A generalized formulation, including cohesive soils, can be expressed as in Equation 2.44. In this equation, $\tau_{interface}$ is the total shear resistance of the soil-geogrid interface. $\tau_{soil\text{-}geogrid}$ is the shear resistance between soil and the surface of the geogrid. $\tau_{soil\text{-}soil}$ is the internal shear strength of the soil itself. ρ is the percent open area (soil to soil contact area divided by the total shear surface area).

$$\tau_{interface} = (1-\rho)\tau_{soil-geogrid} + \rho\,\tau_{soil-soil} \tag{2.44}$$

Many researchers (Abu-Farsakh et al., 2007; Liu et al., 2009a; Xu et al., 2018) have used the bond coefficient, which can also be named as the interface shear strength coefficient (α) in Equation 2.45. Interface shear strength coefficients for soil-geogrid interface obtained by large direct shear testing reported in several studies are presented in Table 2.6.

$$\alpha = \frac{c_a + \sigma_n \tan\delta}{c + \sigma_n \tan\phi_{ds}} \tag{2.45}$$

Table 2.6. Interface shear strength coefficients for soil and geogrid interface

Geogrid properties	Soil properties	Interface shear strength coefficient (α)	Reference
6 different PET geogrids. Percent open area ranges: 49%-73%. Aperture size ranges (mm): 7x7 – 57.8x18.5 – 436x7. Utimate tensile strength ranges (kN/m): 50x50- 100x100 – 200x20 - 100x0	Sand (SP, d_{50}=0.36 mm, C_u=1.52 and C_c=0.95)	0.93–1.01	Liu et al. (2009a)
	Gravel (GP, d_{50}=3.2 mm, C_u=1.38 and C_c=0.90; GP, d_{50}=7.4 mm, C_u=1.49 and C_c=0.92)	0.89–1.01	
	Clay (CH, LL=53% and PL=29%)	0.92–0.99	
Polypropylene geogrid Aperture size (mm): 33x33. Percent open area: 77.4%. Tensile strength: 40 kN/m.	Gravel - Sand (6 different crusher run aggregates scalped to pass 75, 37.5, 19, 9.5, 4.75, and 2.36 mm. C_u ranges: 4.79-10.53)	0.767–0.94	Xu et al. (2018)
3 different geogrids: - Polyster, 25.4x25.4 mm aperture size. 29.2x29.2 kN/m tensile strength. - Polyster, 22x22 mm aperture size. 102.1 kN/m machine direction tensile strength. - Polypropylene, 30.2x36.5 mm aperture size. 12.8x13.5 kN/m tensile strength	Sand (SP, w_{opt}= 4.8%, $\rho_{d,max}$=1.62 kg/m^3)	0.94-0.95	Abu-Farsakh et al. (2007)
	Clay (3 different types LL values: 27, 41, 83%; PL values: 6, 25, 49%)	0.66-1.05	
7 different geogrids having equivalent aperture sizes range between 20.8 to 88 mm. Square, rectangular, triangular aperture patterns and extruded, welded, and knitted geogrid types. Tensile strength ranges (kN/m): 55x30-20x14	Gravel (Angular shaped, fresh latite ballast. d_{max}=50 mm, d_{50}=35 mm, C_u=1.87, C_c=1.12)	0.8-1.16	Indraratna et al. (2012)

Bauer and Zhao (1993) investigated the mechanical behavior and the volumetric response of geogrid reinforced granular soil (coarse sand and crushed limestone aggregate) in large direct shear device (1000 x 1000 x 940 mm). Woven polyester geogrid with openings of 27 by 25 mm and an extruded uniaxial polyethylene

geogrid having apertures of 152 by 16 mm were used in experiments. The authors stated that the shear strength of granular soil significantly increased with the geogrid depending on the orientation of the reinforcement. A maximum shear strength increase was observed when the reinforcement was 60° inclined to the shear plane (Figure 2.29). Granular soils dilated in shearing in an amount directly related to the orientation and mobilized tensile strain in geogrids.

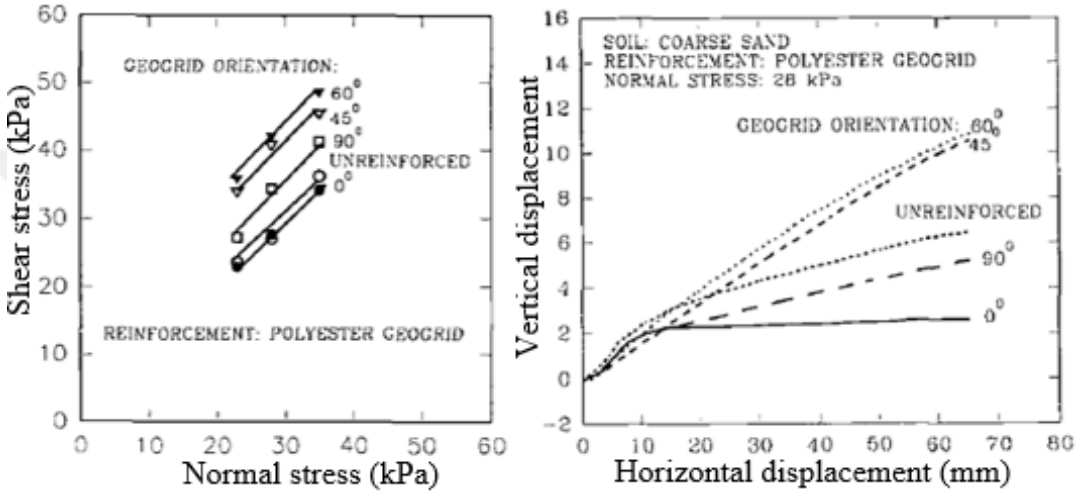


Figure 2.29. Natural and geogrid reinforced sand behavior for (a) shear strength, (b) dilatancy (Bauer and Zhao, 1993)

Liu et al. (2009a) studied the interface strength of different soil and PET-yarn geogrids with different tensile strengths, aperture sizes, and patterns via large direct shear testing. Ottowa sand, fine gravel, coarse gravel, and laterite were used as testing soil (Table 2.6). While the length, width, and thickness of the upper box were 450 x 450 x 130 mm, the effect of various lower boxes on strength response was evaluated. For the lower box alternatives, having (a) the same size and (b) larger size with the upper box, both filled with the desired soil, and (c) a larger box with a rigid block were studied (Figure 2.30). Liu et al. (2009a) concluded that a lower box filled with soil and having the same size as the upper box (Figure 2.30a) was the most appropriate alternative for simulating the soil-geogrid interaction behavior. The use of a rigid surface as the lower box prevented the soil interlocking, which occurs in

the actual field behavior. The authors also concluded that the direct shear resistance of the soil/geogrid interface was higher than the soil-geotextile interfaces. Geogrids having a smaller percent open area and larger transverse strength were observed to increase the direct shear resistance of soil-geogrid interfaces.

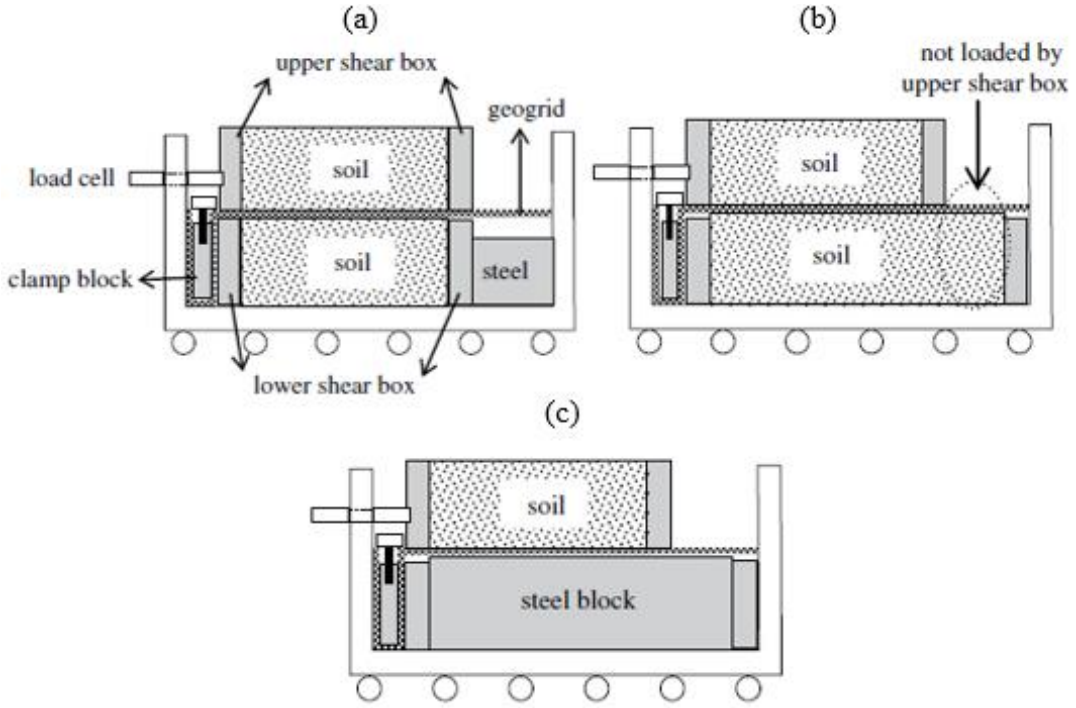


Figure 2.30. Different setups of the lower box (Liu et al., 2009a)

Kim and Ha (2014) investigated the effect of particle size on the shear behavior of geogrid (soft and stiff) reinforced soils in large direct shear testing (300 x 300 mm). Three different well-graded sand samples having parallel particle size distribution curves and maximum particle sizes of 4.5 mm, 7.9 mm, and 15.9 mm were compacted with a relative density of 70% and tested under normal pressures of 98 kPa, 196 kPa, and 294 kPa. Results indicated that a higher shear strength response was obtained with sands having larger particle sizes in all tests, including no reinforcement, stiff and soft geogrids. The increase in adhesion was directly proportional to the particle size, and the adhesion of the soil reinforced with stiff geogrid was higher than the soil reinforced with soft geogrid. The degree of particle

crushing significantly increased with normal stress and particle size in the unreinforced case.

Pullout resistance of soil-geogrid is governed by the friction between the soil-geogrid and bearing resistance of the transverse ribs. Studies indicate that contribution of the bearing resistance of the ribs could be higher than the frictional resistance in pullout conditions (Bergado et al., 1993). In the case of direct shear failure mode, Liu et al. (2009b) stated that the interaction involves three components as (1) shear resistance between soil and the surface of the geosynthetic, (2) internal shear resistance of the soil in the grid openings (3) passive resistance of the transverse ribs. Liu et al. (2009b) studied the contribution of the passive resistance of the geogrids' transverse ribs to the overall resistance in direct shear failure mode. The authors concluded that transverse ribs provided approximately 10% of the internal shear resistance. Passive resistance increased with the tensile strength and stiffness of the ribs whereas decreased with the percent open area of the geogrid.

Ferreira et al. (2015b) investigated the effect of moisture content, density, and geosynthetic type on the residual soil-geosynthetic interface response via large direct shear testing. Four different geosynthetics, including uniaxial extruded geogrid (HDPE), biaxial woven geogrid (PET), a uniaxial geocomposite (PET/PP) and a nonwoven geotextile (PP) were tested with granite residual soil (classified as SW-SM, d_{50}=1.0 mm, C_u=16.9, C_c=1.0, $\gamma_{d,min}$=13.4 kN/m^3, $\gamma_{d,max}$=18.9 kN/m^3, and w_{opt}=11.5%) under normal stresses of 50, 100, 150 kPa. Results indicated a positive correlation between the interface shear strength and density, although the effect of the density was more pronounced in soil-geogrid interfaces than the soil-geotextile interfaces. A reduction of up to 20% in the interface shear strength was observed due to the increase in moisture content between the dry sample and the sample with $w=0.5w_{opt}$. For the mobilization of shear stresses, geogrids were found to be more efficient compared to geotextiles. The most effective reinforcement was determined to be the biaxial geogrid for this particular soil. In all test conditions, the strength of the interface was lower than the soil's internal shear strength. Interaction coefficients

ranged between 0.71 and 0.99 for soil-geogrid interfaces and 0.54 and 0.85 for soil-geotextile interfaces.

2.4.1.1 Tests on Cohesive Soils

Mitchell et al. (1990) performed direct shear tests to characterize the interface shear strength properties and examine the causes of a waste landfill slope failure. Dry and submerged conditions were tested for various interface combinations, including HDPE membrane – compacted clay liner and geotextile – compacted clay liner. Tests conducted under normal pressures of 158, 316, and 479 kPa revealed that HDPE liner and clay interface in which the specimen compacted at field density and water content gave 13.6° peak and 12.4° residual friction angles. However, when the specimens were submerged and pre-soaked after the compaction, results could be represented with unconsolidated-undrained (UU) testing conditions in which the shear response was independent of the normal pressure applied. Residual shear resistance of the interface decreased to 43.5 kPa when the clay was in near-saturated condition.

Strength improvement on reinforced clays was studied by Abdi et al. (2009) when the geogrids were encapsulated within thin sand layers (with thicknesses of 4, 6, 8, 10, 12, and 14 mm) (Figure 2.31). Kaolinite clay (LL=53%, PL=33%, w_{opt}=23%, $\rho_{d,max}$=1550 kg/m^3, c=23.2 kPa, ϕ=10°) and sand (C_u=6.25, C_c=1.69, w_{opt}=4%, $\rho_{d,max}$=1600 kg/m^3, ϕ=33.7°) materials were tested in large direct shear device (300 x 300 x 200 mm) with 1 mm/min shear rate under normal pressures of 25, 50, and 75 kPa. The authors stated that the sandwich technique significantly improved the strength response (Figure 2.32). The optimum sand layer thickness of 10 mm provided the highest strength increase for the reinforced composite system independent of the normal pressure applied. It was also stated that transverse members of geogrids contributed at most 10% to the total shear strength of the composite system.

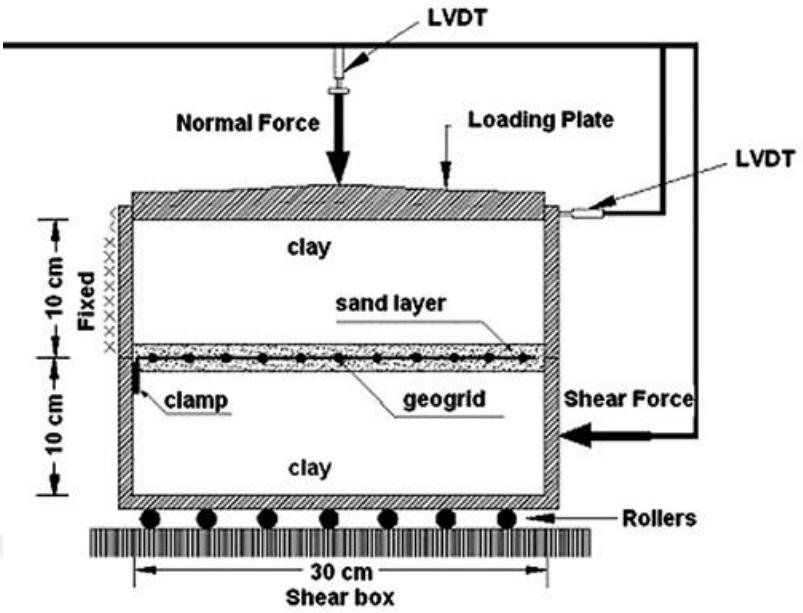


Figure 2.31. Cross-section of the direct shear box (Abdi et al., 2009)

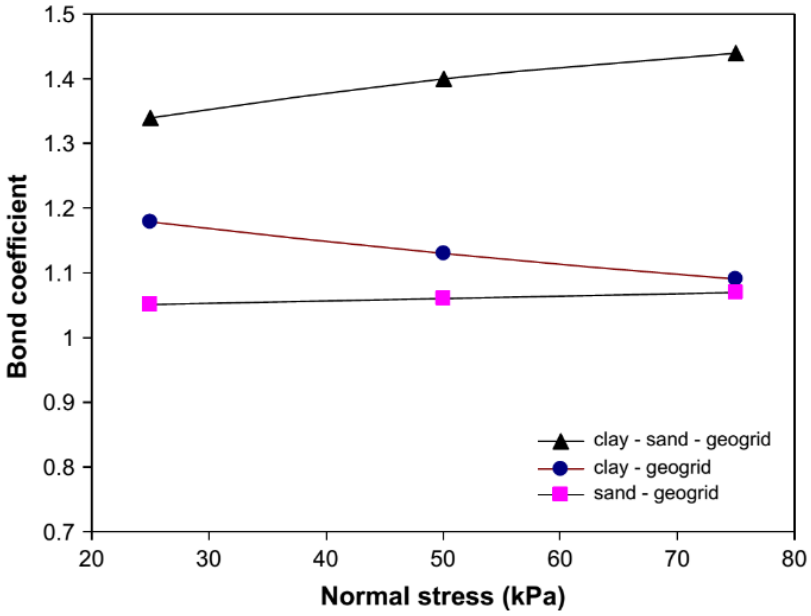


Figure 2.32. Increase in bond coefficient with sandwich technique (Abdi et al., 2009)

Abu-Farsakh et al. (2007) investigated moisture content and density effect on the cohesive soil-geosynthetic interaction with 300 x 300 mm large direct shear tests.

Sand and three different clays were tested with three geogrids and one geotextile (Table 2.6). 0.85 mm/min shear rate was used in all tests. 25, 50, 75 kPa, and 15, 30, 45 kPa normal stresses were applied for clay and sand specimens, respectively. Results indicated good bonding between cohesive soils and geosynthetics (interface coefficients greater than 0.7 in most cases); however, stronger bond strength was observed for sand specimens. Molding moisture content had a significant influence on reinforcement efficiency. An increase in the moisture content caused a reduction of suction forces and increased the potential of excess pore water pressure development as in the saturated clays. Therefore, the authors suggested that soils with 95% of the maximum dry density and 2% above the optimum moisture content should be considered in the design of soil-geosynthetic structures. In addition, the factors affecting the cohesive soil bond efficiency were remarked as soil characteristics, geosynthetic type, and the level of normal stress.

O'Kelly and Naughton (2008) investigated the interface shear strength improvement of cohesive materials reinforced with geogrid having in-plane drainage capability (Figure 2.33). Marginal fill material (Brown Dublin wet gravelly boulder clay,

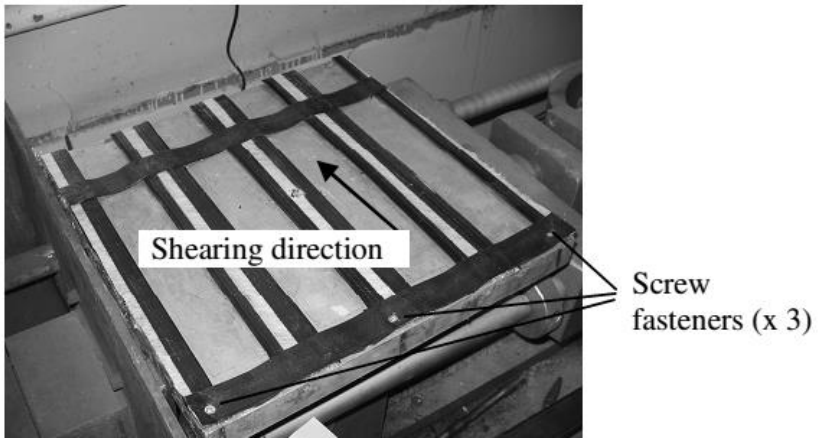


Figure 2.33. Geogrid fixed to the aluminum plate (O'Kelly and Naughton, 2008)

LL= 31%, PL=16%) was compacted to 92% of its maximum dry density and tested with the shear rate of 0.25 mm/min under consolidated-undrained (CU) conditions in a large shear box (300 x 300 x 150 mm). Instead of using a lower box filled with

soil, a rigid aluminum plate was placed at the shear zone and geogrid fully fixed to this plate. The upper box filled with soil was provided to slide on the plate and the geogrid. Shear resistance in soil – geosynthetic interface was analyzed using different test series (soil alone, soil over aluminum, soil over geogrid). Results indicated that the shear strength mobilized along the draining geogrid-soil interface was similar to the soil's undrained shear strength. However, interface strength was only 82% and 85% of the soil's undrained shear strength by using geogrid without drainage capability but with similar tensile strength properties.

CHAPTER 3

TESTING MATERIALS AND METHODOLOGY

Investigation of the geotechnical properties of coarse-fine mixtures (CFM) and interaction of these intermediate, transitional soils with geogrid in direct shear testing requires parameter-controlled experimentation. Mixtures were prepared having certain gradation, fines content and plasticity index values that relate to the sand-gravel, silt-clay boundaries of the commonly used soil classification systems, and the upper and lower limits of soil index properties defined in different design codes for appropriate backfill material criteria. Seven different commercially available soil products were used to obtain ten different soil mixtures for this purpose. In this section, the selection and geotechnical properties of the soil products and soil mixture preparation methodology are discussed in detail. In addition to the soil materials to be tested, the physical and mechanical characteristics of the geogrids used and all specimen preparation and test procedures in the scope of the study are described.

3.1 Soil Mixtures Used

3.1.1 Index Tests

Properties of the commercially available soil products and laboratory-prepared soil mixtures were determined with geotechnical index tests. Tests were performed in accordance with the commonly accepted international standards. All index tests were repeated at least three times, and the standard deviations of the results were within the acceptable limits of the relevant standard. In the scope of this study, the averages of the measured test values are presented as representative results.

Particle size distributions of soils were determined with the dry, mechanical sieve analysis (ASTM D6913-17), wet sieving by washing (ASTM D1140-17), and hydrometer tests (ASTM D7928-21). The vibratory table method (ASTM D4253-16) was used to identify the minimum and maximum dry densities and the minimum and maximum void ratios of the cohesionless-granular soils. Standard Proctor tests (ASTM D698-12) were carried out to determine the maximum dry unit weights and optimum moisture contents of the prepared soil mixtures. Liquid limit tests were performed with the Casagrande cup, while plastic limit tests were carried out by the thread-rolling method according to ASTM D4318-17. Specific gravity tests were carried out in accordance with the ASTM D854-14 and ASTM C127-15 standards. ASTM D854-14 suggests the pycnometer method for soils having particles smaller than 4.75 mm, whereas ASTM C127-15 uses the water immersion method for particles larger than 4.75 mm. Some commercially available soil products and all prepared soil mixtures had particles smaller and larger than 4.75 mm. For these soils, specific gravities of the relevant fractions were measured, and the average specific gravity of each soil was calculated using Equation 3.1, as indicated in ASTM D854-14.

$$G_{avg@20^0C} = \frac{1}{\frac{R}{100.\,G_{1@20^0C}} + \frac{P}{100.\,G_{2@20^0C}}} \tag{3.1}$$

$G_{1@20^oC}$ and $G_{2@20^oC}$ are the specific gravities measured for the soil retained on and passing through a 4.75 mm sieve, respectively. R and P are the percentages of soil retained on and passing through a 4.75 mm sieve, respectively.

3.1.2 Selection of Soil Products

CFM in this study were prepared by mixing different ratios of cohesionless/coarse and cohesive/fine commercially available soils ranging from fine gravel to clay-sized particles. Instead of a gap-graded binary mixture (as gravel-clay or sand-clay

mixtures having a large coarse to fine particle size ratio), preparing CFM in which the coarse fraction was based on well-graded sand with gravel was aimed. As a result of trials on many soil products, seven different soils were selected to constitute soil mixtures with pre-targeted properties. These soils were fine gravel, sands (coarse, medium, and fine-grained), non-plastic silt, kaolin, and bentonite. They were purchased and stocked in large quantities (Figure 3.1) because a prepared (mixed and compacted) and tested soil mixture has never been used again in other tests. This also required standardization of the procedures of mixture preparation and repeatable test results.

Water contents of each soil product were measured according to ASTM D2216-10. Results indicated that soils had less than 0.5% water moisture in their stored states.



Figure 3.1. Soil products stocked for the preparation of soil mixtures

3.1.2.1 Fine Gravel

Crushed limestone aggregate having an angular shape (according to ASTM D2488-09a) was used as the fine gravel fraction in soil mixtures (Figure 3.2). Particle sizes of the fine gravel ranged between 2 mm and 10 mm. The absorption capacity of the

particles was measured as 0.4% according to ASTM C127-15. The abrasion of the particles was determined following the ASTM C131-20 by using the Los Angeles testing machine, and the percent material loss was observed as 17.8%.



Figure 3.2. The particle shape of fine gravel

3.1.2.2 Coarse, Medium, and Fine Sands

Three types of clean sands with different gradations were used as coarse-graded, medium-graded, and fine-graded. SiO_2 constituted 99% of all sands, according to the manufacturers. They had been washed and oven-dried during the production stages before purchase, and they were free of particles smaller than 75 μm. Particle sizes of coarse-graded, medium-graded, and fine-graded sands ranged between 1 and 4.75 mm, 0.15 and 4.75 mm, and 0.075 and 0.425 mm, respectively. Coarse and medium-graded sands had subrounded particle shapes according to ASTM D2488-09a.

3.1.2.3 Non-Plastic Silt

Particles of non-plastic silt, 99% of its mineralogy constituted by SiO_2, ranged between 1 and 150 μm, although 98% of the material passed through 75 μm. Particle size corresponding to 50% passing by mass, d_{50}, was 20 μm.

3.1.2.4 Kaolin and Bentonite Clay

Two types of clay, kaolin and bentonite, were used to prepare soil mixtures. Both had particles smaller than 0.075 mm, and clay-size fractions (CF, percent of fines smaller than 0.002 mm) were 40% and 89% for kaolin and bentonite, respectively.

View of the soil products used for the preparation of soil mixtures is presented in Figure 3.3. Index test results of soil products, including specific gravity, minimum-maximum density and void ratios, Atterberg limits for kaolin and bentonite, are summarized in Table 3.1. Particle size distributions of soil products are presented in Figure 3.4.

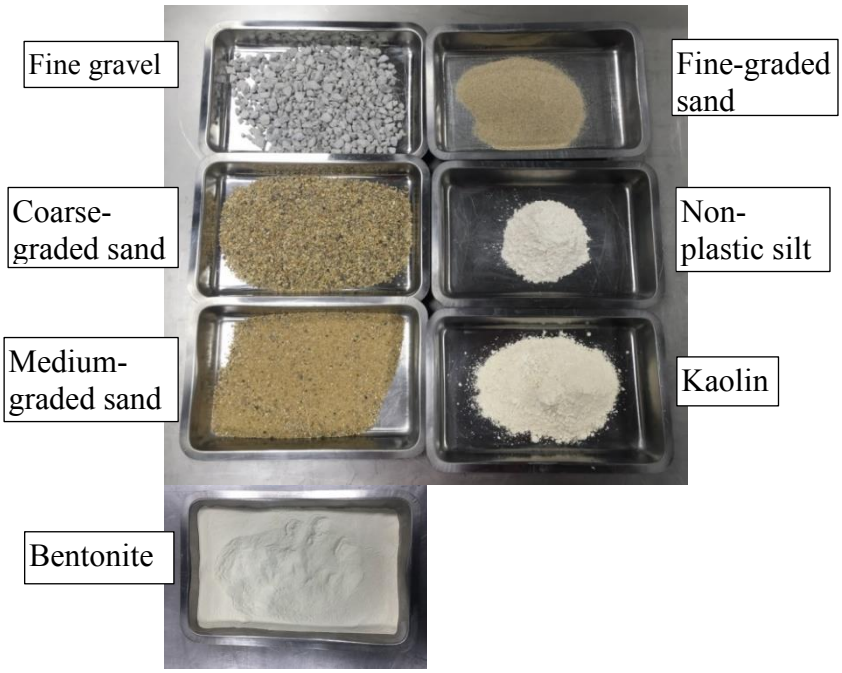


Figure 3.3. View of the soil products

Table 3.1. Properties of commercially available soil products (Ekici et al., 2019)

Soil products	Properties	Specific gravity, G_s	Min. dry density, ρ_{min} (g/cm^3)	Max. dry density, ρ_{max} (g/cm^3)	Min. void ratio, e_{min}	Max. void ratio, e_{max}
Fine gravel	Crushed limestone, Angular shaped, (Absorption Capacity: 0.4%, Los Angeles test material loss:17.8%)	2.69	1.42	1.65	0.63	0.90
Coarse sand	~ %99 SiO_2 (washed and dried)	2.64	1.55	1.78	0.48	0.70
Medium sand		2.66	1.63	1.89	0.41	0.63
Fine sand		2.65	1.32	1.64	0.62	1.01
Non-plastic silt		2.65	0.97	1.51	0.75	1.72
Kaolin	LL=48%, PL=34%, PI=14%	2.60		-		
Bentonite	LL=499%, PL=40%, PI=459%	2.72		-		

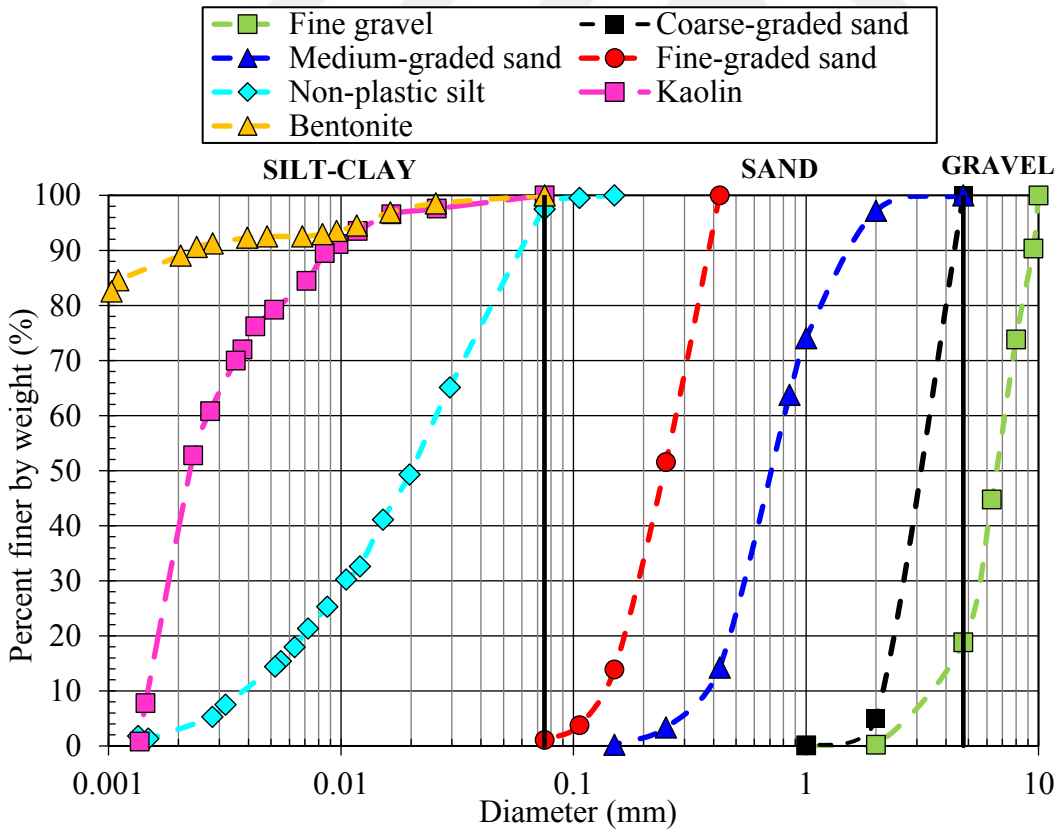


Figure 3.4. Particle size distribution curves of soil products

The soil products were classified based on ASTM D2487-17 (Unified Soil Classification System) soil boundaries. Therefore, of the seven soil products in this study, non-plastic silt, kaolin, and bentonite were grouped as fine-graded soils (particles smaller than 0.075 mm), whereas others as coarse materials (all of their particles greater than 0.075 mm) (Figure 3.4).

3.1.3 Preparation of Soil Mixtures

Ten different soil mixtures were prepared by mixing varying proportions of seven soil products, the properties of which are specified in Section 3.1.2. In the scope of the study, properties of intermediate or transitional soils and the evaluation of their interaction with the geogrid in direct shear failure mode were investigated by these ten soil mixtures. Two of them were prepared as well-graded and poorly-graded granular soils without fines. Gravel and sand percentages by weight were selected to be at the boundary of the gravel and sand transition zone according to USCS. Therefore, the mixtures were defined as SW and SP, which were well-graded sand with gravel and poorly-graded sand with gravel, respectively. While creating the SW and SP soil mixtures with targeted particle size distributions, the preliminary mixing ratios were determined analytically based on individual particle gradations of soil products. Afterwards, the mixtures were prepared in the laboratory, and the particle gradations were confirmed by a series of mechanical sieve analyses. The soil product mixing ratios required to obtain SW and SP soil mixtures and particle size distribution curves are presented in Table 3.2 and Figure 3.5, respectively.

The remaining eight soil mixtures were designed to be coarse-fine mixtures (CFM), predominantly gravelly-sandy soil mixtures with a PI of 5% and 15%, and having FC of 12%, 20%, 30%, and 40%. These values were selected to address the suitable backfill material criteria in different design guidelines (Table 2.1). In addition, according to past studies, soil mixtures having these PI and FC values have the potential to be at the boundaries of behavioral transition zones.

The prepared SP soil mixture was not used in the coarse-fine mixtures (CFM). The coarse fraction and granular skeleton of eight CFM were based on well-graded sand with gravel (SW) mixture. In other words, to prepare a coarse-fine mixture with 20% fines content, 80% coarse fraction was obtained from the soil product mixing ratios to prepare the SW soil mixture. On the other hand, 20% fine fraction was obtained by mixing different proportions of non-plastic silt, kaolin, and bentonite. Therefore, the shape of the particle size distributions for coarse fractions was identical for the mixtures having the same fines content and similar for all other mixtures (Figure 3.5). This provided fines content and plasticity index-controlled experimentation and evaluation.

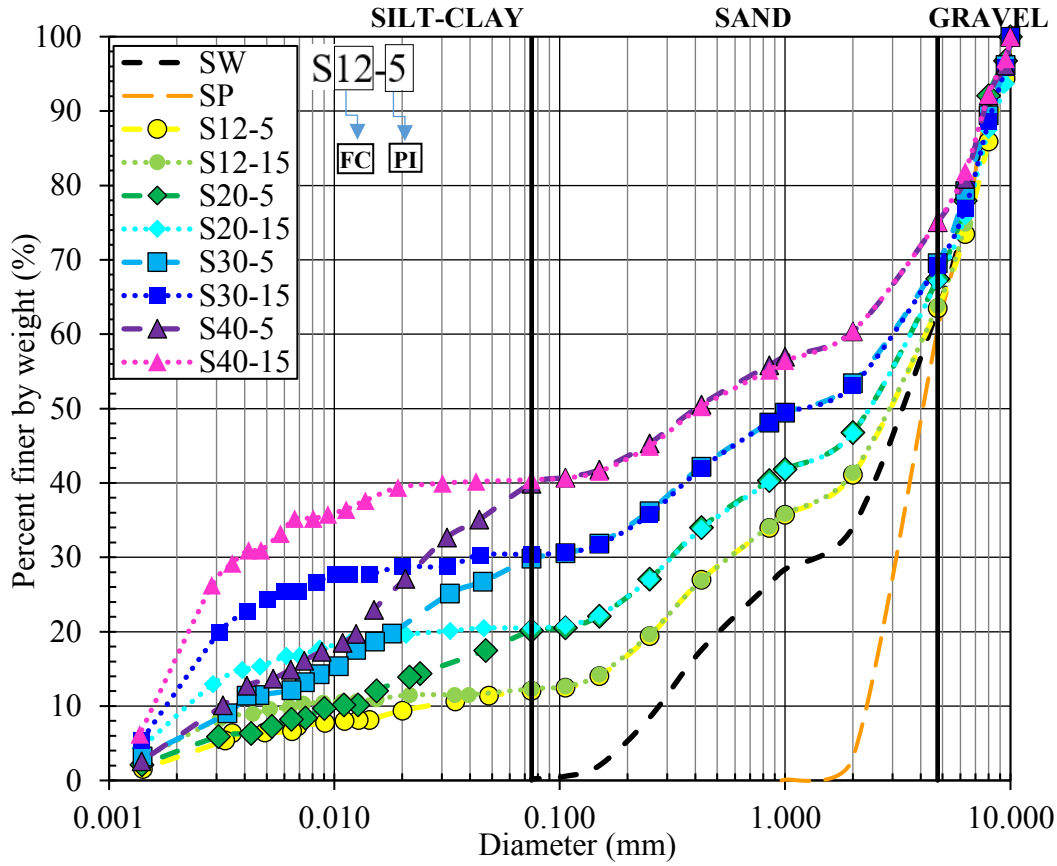


Figure 3.5. Particle size distribution curves of the prepared soil mixtures

Table 3.2. Percent fractions of soil products by weight to prepare soil mixtures

Soil code	Fines content (%)	Atterberg limits of mixtures for samples passing No. 40 sieve	Mixture compositions (%)						
			Fine gravel	Coarse-graded sand	Medium-graded sand	Fine-graded sand	Non-plastic silt	Kaolin	Bentonite
SW	0	-	50.0	17.0	18.0	15.0	0.0	0.0	0.0
SP	0	-	50.0	50.0	0.0	0.0	0.0	0.0	0.0
S12-5	12	LL=19%,PL=14%, PI=5%	44.0	15.0	15.8	13.2	4.5	7.5	0.0
S12-15	12	LL=31%,PL=16%, PI=15%	44.0	15.0	15.8	13.2	0.0	11.02	0.98
S20-5	20	LL=19%,PL=14%, PI=5%	40.0	13.6	14.4	12.0	12.6	7.4	0.0
S20-15	20	LL=34%,PL=19%, PI=15%	40.0	13.6	14.4	12.0	0.0	18.94	1.06
S30-5	30	LL=22%,PL=17%, PI=5%	35.0	11.9	12.6	10.5	19.0	11.0	0.0
S30-15	30	LL=40%,PL=25%, PI=15%	35.0	11.9	12.6	10.5	0.0	28.75	1.25
S40-5	40	LL=22%,PL=17%, PI=5%	30.0	10.2	10.8	9.0	29.2	10.8	0.0
S40-15	40	LL=42%,PL=27%, PI=15%	30.0	10.2	10.8	9.0	0.0	38.65	1.35

For the fine fraction of the CFM, the proportions of non-plastic silt, kaolin, and bentonite were adjusted to match the pre-targeted plasticity index of the total mixture. The target plasticity indices (5% and 15%) of the CFM were measured according to ASTM D4318-17, which recommends testing the soil sample passing through No. 40 sieve (0.425 mm), which is also widely used in geotechnical practice.

In the first stage, SW soil mixture was sieved through the No. 40 sieve, and the fine sand fraction between 0.075 mm and 0.425 mm was collected. This fine sand portion was mixed with different proportions of non-plastic silt, kaolin, and bentonite so that the plasticity indices of the total mixtures would be 5% and 15%, and total fines

contents would be 12%, 20%, 30%, and 40%. Atterberg limits of the CFM passing through the No. 40 sieve and the mixing ratios of the soil products by weight forming the CFM were determined this way (Table 3.2). The fine portions of CFM with PI=5% included non-plastic silt and kaolin, whereas the fine portions of CFM with PI=15% included kaolin and bentonite, as can be seen in Table 3.2.

Even though plasticity indices of CFM were designed for soil portion passing through No. 40 sieve and Atterberg limits were measured accordingly, liquid and plastic limits of the CFM passing through No. 200 sieve were also measured to provide additional data. Fine fractions of CFM were constituted by non-plastic silt and kaolin (for PI=5%) or kaolin and bentonite (for PI=15%), all of which are smaller than 0.075 mm.

CFM were defined by the notation: 'S - fines content - plasticity index value' throughout this study (Table 3.2). In this notation, for example, 'S12-5' represents a soil mixture having 12% fines content and 5% plasticity index value.

After the proportions of each soil product to generate CFM with the desired properties were determined, index tests were repeated to identify the geotechnical properties of CFM, as shown in Figure 3.6. The particle size distributions of all mixtures are presented in Figure 3.5.



(a) Specific gravity test by water immersion method



(b) Specific gravity test with pycnometer



(c) Dry, mechanical sieve analysis



(d) Wet sieve analysis by washing



(e) Liquid limit test with Casagrande cup



(f) Plastic limit test by thread-rolling



(g) Hydrometer test

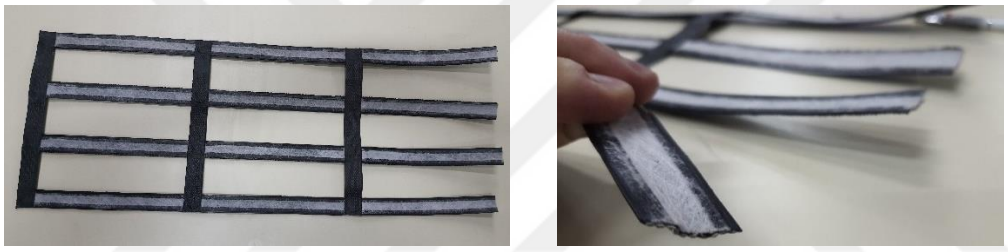


(h) Standard Proctor test

Figure 3.6. Views from the geotechnical index test applications for CFM

3.2 Geogrid Properties

Geogrid used in direct shear tests was a geocomposite product having both reinforcement and in-plane drainage properties (sometimes referred to as "draining geogrid" or "geogrid-geotextile composite" in practice). Reinforcement strips were manufactured from polyester fibers that were coated with a polyethylene sheath and then bonded. Reinforcement strips were profiled to have in-plane drainage channels along their length. Nonwoven geotextile was placed into these drainage channels and bonded to the reinforcement strips by the manufacturer (Figure 3.7). Uniaxial geogrid is chosen in this study since it is the more commonly employed geogrid type in MSEW, as compared to biaxial or triaxial type geogrids (Koerner, 2012).



(a) (b)

Figure 3.7. (a) Geogrid with in-plane drainage property, (b) nonwoven geotextile bonded to the drainage channels along the reinforcement strips

Tensile properties of geogrids' strips in machine direction were determined with a constant rate extension testing machine (Figure 3.9) at METU Central Laboratories. ASTM D6637M-15 (Method A - Testing a single geogrid rib in tension) was considered in the tests. Extensometers were placed on two sides of the transverse rib with a total gauge length of 100 mm. A strain rate of 10 mm/min was applied to three different specimens. Stress-strain curves as a result of tensile tests are presented in Figure 3.8. Strain values measured from both the cross head movement and gauge length were plotted together with the tension values. The strain values between cross head and gauge length differed in all tests as significant elongation occurred outside

of the gauge length. In Table 3.3, the physical and mechanical properties of the geogrid used in direct shear tests are summarized.

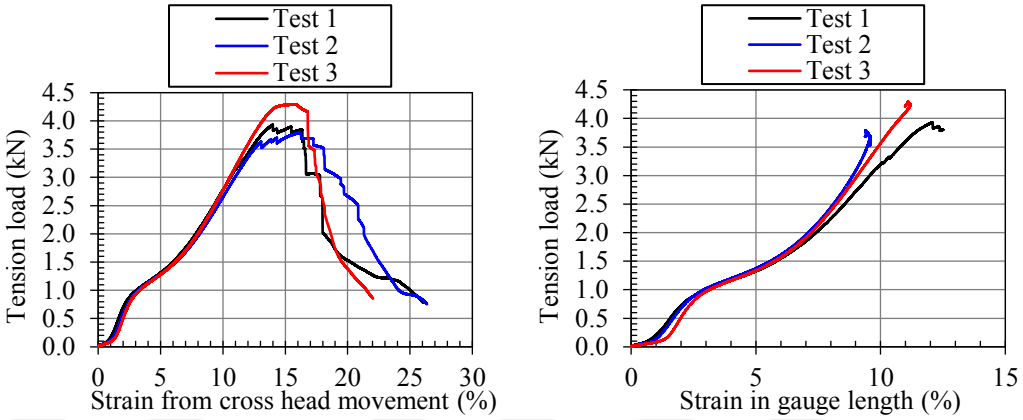


Figure 3.8. Stress-strain curves of geogrid obtained from tensile tests



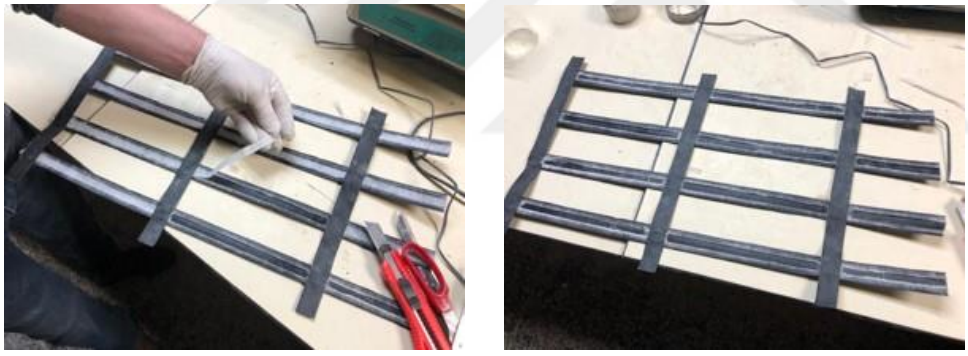
Figure 3.9. The view of the tensile test of the geogrid

Table 3.3. Properties of the geogrid used in tests

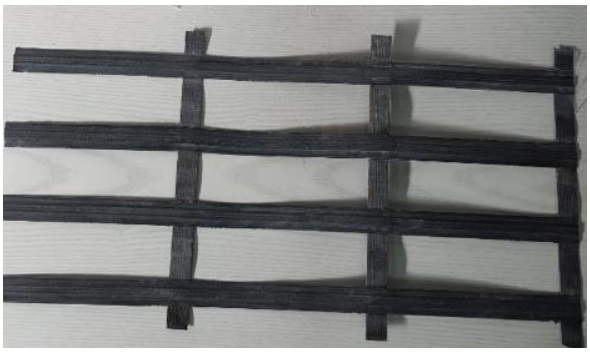
Mechanical properties	Strip tensile longitudinal strength (average value) (kN)		Strip elongation in machine direction at tensile longitudinal strength (average value) (%)		
	4.0		12.8		
Physical properties	*Strip reinforcement polymer	*Strip coating polymer	Thickness (mm)	Strip width (longitudinal) (mm)	Mesh size (mm)
	PET	PE	2.5	24	200x50

*Obtained from the manufacturer

One of the aims of this experimental study was to examine the CFM-geogrid interaction under direct shear failure mode and to determine the expected strength ranges. Another objective is to evaluate the effect of the drainage property of the geogrid (i.e., the geotextile in drainage channels) on the shear strength of the geogrid-CFM interface in this study. For this purpose, one group of experiments was performed by using the geocomposite in Figure 3.7. Another group of experiments was carried out with the same geogrid but without the drainage function. This was provided by removing the geotextile in drainage channels (without damaging the reinforcement strips), as in Figure 3.10a. Geogrid was positioned as shown in Figure 3.10c, allowing its back surface to engage in shear interaction with the soil mixtures. Although the texture of the surface of the longitudinal ribs changed, this ensured that the geogrid, which had exactly the same strength and physical properties, was tested without the drainage feature.



(a) (b)



(c)

Figure 3.10. (a, b) Removal of the geotextile from in-plane drainage channels in geocomposite, (c) geogrid prepared for testing

3.3 Applied Tests

3.3.1 Methylene Blue Spot Test

Methylene blue (MB) dye is used to determine the specific surface area (SSA) of clay minerals. Methylene blue molecule, having the chemical formula of $C_{16}H_{18}N_3SCl$, contains positively charged $C_{16}H_{18}N_3S^+$ and negatively charged Cl^- ions in an aqueous solution. Negatively charged clay mineral surfaces adsorb positively charged $C_{16}H_{18}N_3S^+$ ions. Therefore clay surface area can be determined from the amount of adsorbed MB.

3.3.1.1 Apparatus

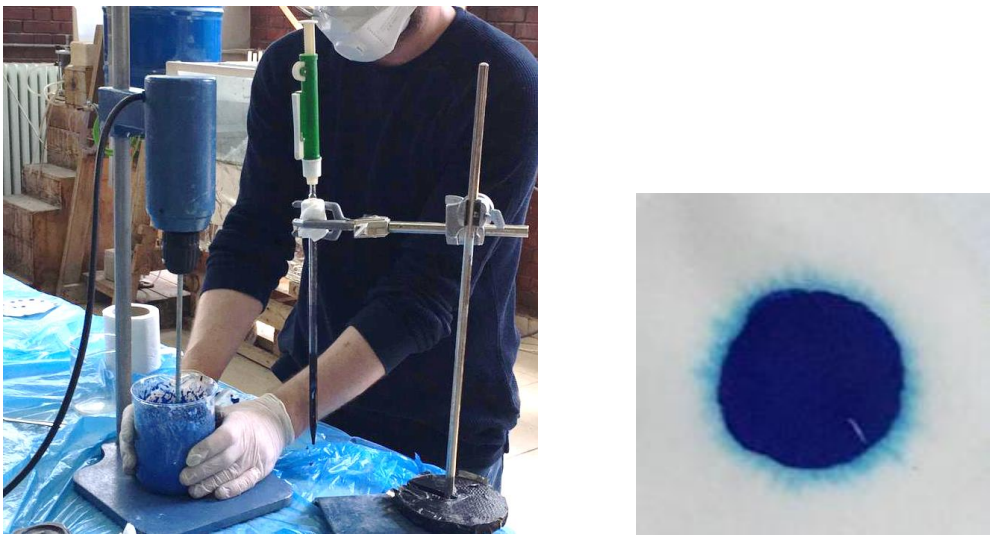
Dry MB powder, distilled water, Fisher P5 filter paper, mixer (400/700 rpm), burette (10 cc with 0.5 cc increments), spoon, beaker, chronometer, and balance were used (Figure 3.11).



Figure 3.11. Methylene blue (MB) spot test apparatus

3.3.1.2 Test Procedure

In this study, the SSA of CFM for soil portions passing through No. 40 and No. 200 sieves was determined by the methylene blue (MB) spot test method. Kandhal and Parker (1998) described a procedure to determine the pavement performance of fine aggregates with plastic fines. This procedure, also used by Santamarina et al. (2002) and Yukselen and Kaya (2008), was followed in this study. According to the procedure, MB solution is prepared by adding 1 g of dry powder to 200 mL of deionized water and mixing. 10 g of soil sample (oven-dried) mixed with 30 mL of deionized water to prepare a soil suspension. The MB solution is added to the prepared soil suspension in 0.5 mL increments. After each addition, the soil suspension is stirred for one minute (Figure 3.12a). Then, a small drop of the mixture is placed on a Fisher P5 filter paper. This process is continued until unadsorbed MB is observed to form a permanent blue halo around the soil suspension spot (Figure 3.12b). Blue halo formation indicates that all active clay surfaces are coated, and MB replaces cations in the double layers. Thus, the test is completed. The amount of adsorbed MB is used to calculate SSA from Equation 3.2.



(a) (b)

Figure 3.12. (a) Mixing of soil suspension after each addition of MB solution, (b) permanent blue halo around the soil suspension spot

$$SSA = \frac{1}{319.87}\frac{1}{200}(0.5\text{N})A_v A_{MB}\frac{1}{10} \quad (3.2)$$

Where N is the number of MB increments, A_v is the Avogadro's number (6.02×10^{23}/mol), and A_{MB} is the area covered by one MB molecule (assumed to be 130 $Å^2$).

3.3.2 Hydraulic Conductivity Tests

Rigid wall hydraulic conductivity tests were applied to SW and SP soil mixtures, which have no particles smaller than 75 μm. Hydraulic conductivities of the remaining eight CFM were measured by flexible wall hydraulic conductivity tests.

3.3.2.1 Rigid Wall Hydraulic Conductivity Tests

3.3.2.1.1 Apparatus

Apparatus used in the test included permeameter cell, constant head filter tank, vacuum pump, manometer tubes, porous metal filter screens, funnel, scoop, tamping rod, and balance. Apparatus, test setup, and the view of the permeameter cell are presented in Figure 3.13.

According to ASTM D2434-19, permeameter cells should have a diameter of at least 8 or 12 times the maximum particle size of the tested soil. Permeameter cell dimensions used in the tests were 80 mm in diameter, and 240 mm in total length. Even though the maximum particle size of SW and SP soil mixtures was 10 mm, more than 95% of their particles were smaller than 9.5 mm (Figure 3.5).



(a)



(b)



(c)

Figure 3.13. (a) Apparatus, (b) test setup, and (c) permeameter cell for constant head hydraulic conductivity test of granular soils

3.3.2.1.2 Test Procedure

In the scope of this study, all CFM specimens to be tested were prepared at 95% of the standard Proctor dry densities. Although standard Proctor testing was not applicable for SW and SP soils, their maximum dry densities were measured as 2.08 g/cm^3 and 1.76 g/cm^3 according to ASTM D4253-16. 95% of the maximum dry densities were used in hydraulic conductivity testing as 1.98 g/cm^3 and 1.67 g/cm^3 for SW and SP soil mixtures. These dry densities correspond to 67% and 63% relative density values for SW and SP, respectively.

Hydraulic conductivities of the SW and SP soil mixtures were measured according to ASTM D2434-19, the permeability of granular soils with the constant head method. The first step was to check for leaks in the valves, pipes, or permeameter by flowing water through the setup without the soil specimen. Then, the dry soil sample was placed as homogenously as possible between metal filter screens in the permeameter cell at the specified densities by compacting the specimen with a tamping rod (having a diameter of 4 mm and smooth side surfaces). After several trials, it was observed that desired dry densities could be achieved by tamping the specimen eight times, applying 20 mm penetration (half of the placed sample thickness) for each 40 mm of soil thickness placed. The locations where the rod tamping was applied were chosen on a circular path 10 mm away from the boundary of the permeameter cell. After the entire specimen was placed and compacted, its upper surface was leveled by placing the metal filter screen, total length of the sample was measured, and the top of the permeameter was hermetically sealed to keep the volume constant during testing. The air in the voids of soil particles was removed using a vacuum pump for at least 15 minutes. Afterwards, the permeameter cell was slowly saturated with de-aired water under the vacuum pressure. Contrary to the recommendation of the relevant standard, water flow in this system was from top to bottom instead of bottom to top (Figure 3.13). After saturation of the permeameter was ensured, the vacuum was disconnected. Valves connected to the manometers were opened and waited until the water levels stabilized. Hydraulic conductivity tests

were repeated two times by preparing different specimens for the same soil mixture. In addition, two tests for the same hydraulic gradient value (i), and at least three different hydraulic gradients (i) varying between 0.1 and 0.8 were used for the same soil specimen.

3.3.2.2 Flexible Wall Hydraulic Conductivity Tests

Saturated hydraulic conductivity tests were carried out according to the ASTM D5084-16 (Method A for constant head test) on all CFM (S12-5, S12-15, S20-5, S20-15, S30-5, S30-15, S40-5, and S40-15) (Figure 3.15). All hydraulic conductivity measurements were repeated at least three times under the same conditions.

3.3.2.2.1 Apparatus

Apparatus used in saturated hydraulic conductivity testing for CFM included triaxial setup with a pressure cell (1700 kPa capacity), vertical displacement gauge (LVDT with a capacity of 50 mm), pressure suppliers (oil/water constant pressure system, 1700 kPa capacity) for cell, inlet, and outlet of the specimens, digital pressure transducers (1700 kPa capacity), volume change transducer, external data acquisition system, filter papers, porous stones, vacuum pump, O-rings, silicon grease, membrane, membrane expander, container, and balance. The view of the apparatus and the test setup with the integrated equipment are presented in Figure 3.14 and Figure 3.15, respectively. Calibrations of all data acquisition instruments were checked prior to testing.



Figure 3.14. Apparatus for flexible wall hydraulic conductivity testing of CFM

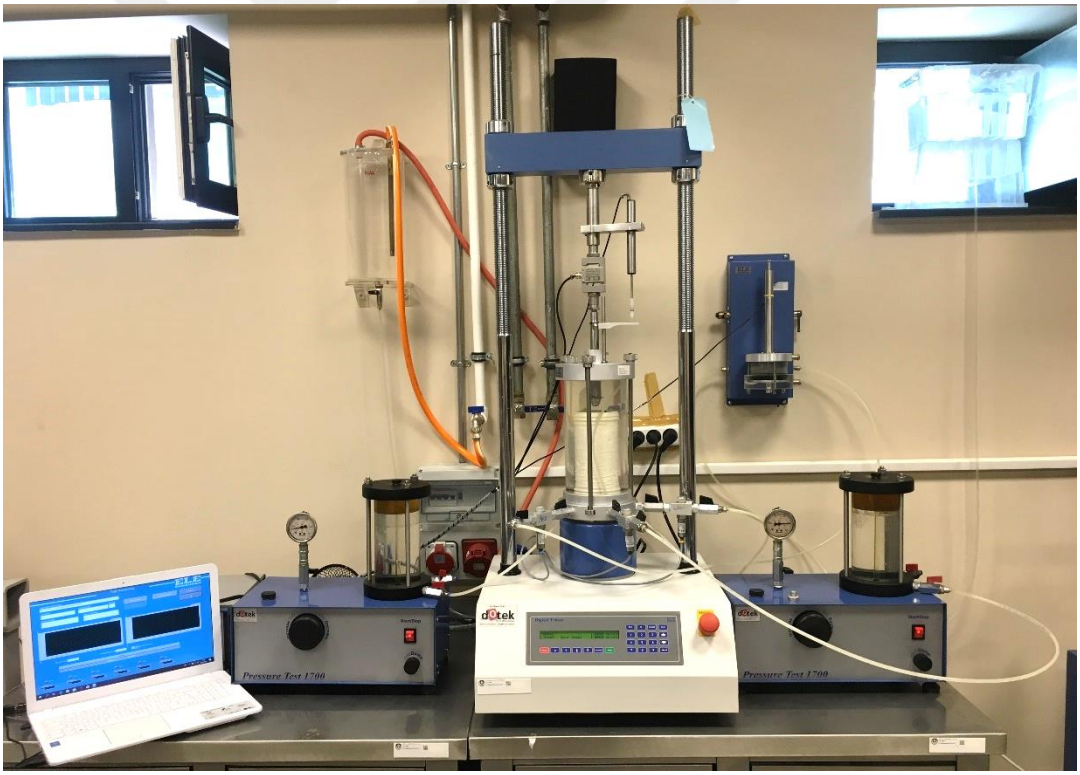


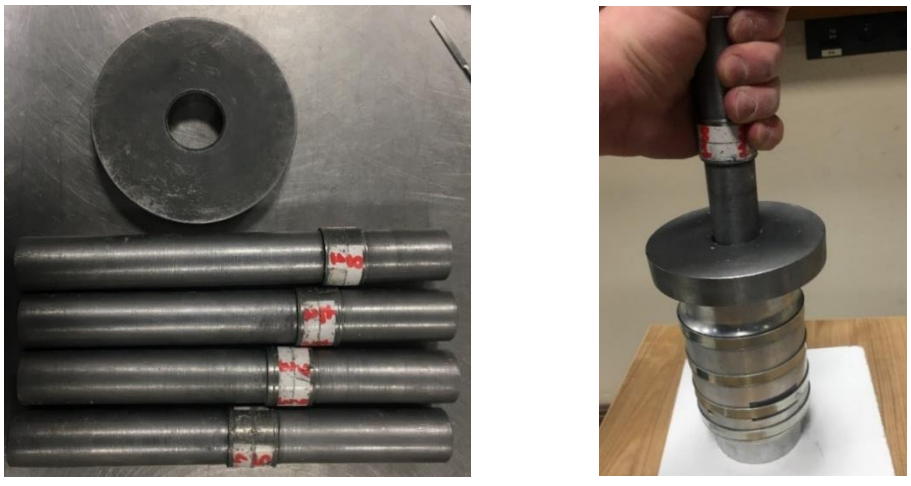
Figure 3.15. Test setup with integrated equipment for flexible wall hydraulic conductivity testing of CFM

3.3.2.2.2 Specimen Preparation

According to ASTM D5084-16, the largest particle size (10 mm for this study, Figure 3.5) should be smaller than one-sixth of the specimen diameter. For this reason, specimens were prepared to have a height of 140 mm and a diameter of 70 mm (L/D=2). The same minimum specimen diameter criteria are specified by the ASTM standards for unconfined compressive and triaxial strength testing. Therefore, the same specimen dimensions and sample preparation procedures were also applied in strength tests.

CFM specimens were not reused in different tests once prepared and tested. Therefore, identical soil mixture and specimen preparation methods were adopted in each test. Index property tests such as sieve analysis and Atterberg limit tests were conducted to ensure that the specimens were prepared in a standardized manner.

Specimens were dynamically compacted in split molds at their optimum moisture contents and 95% of their standard Proctor dry densities. Specimens were compacted at eight different layers according to Ladd (1978)'s undercompaction method. The dynamic compaction apparatus manufactured for the specimen preparation can be seen in Figure 3.16.



(a) (b)

Figure 3.16. Dynamic compaction apparatus: (a) compaction tools (b) split mold

The undercompaction method of Ladd (1978) aims to achieve a uniform density for a specimen by assuming the compaction of the upper layers causes additional compaction for the layers below. The degree of compaction is controlled by adjusting the height of each layer which is calculated from Equations 3.3 and 3.4. Germaine and Germaine (2009) stated that a significant number of variables affect the uniformity of the specimen, including the number of layers, water content, target density, and the amount of undercompaction of the bottom layer. They suggested that 4% undercompaction for the first (bottom) layer (U_{ni}) is a reasonable starting value for most soils. U_{ni} was assumed to be 4% in this study as well.

$$h_n = \frac{h_t}{n_t}\left[(n-1) + \left(1 + \frac{U_n}{100}\right)\right] \tag{3.3}$$

$$U_n = U_{ni} - \left[\frac{U_{ni} - U_{nt}}{n_t - 1} x(n-1)\right] \tag{3.4}$$

where,

n : Number of the layer being considered

h_n : Height of the compacted material at the top of the layer being considered

h_t : Final height of the specimen

n_t : Total number of layers

U_n : Percent undercompaction for layer n

U_{ni} : Percent undercompaction selected for the first layer

U_{nt} : Percent undercompaction selected for the final layer (usually zero)

Calculated layer thicknesses according to the undercompaction method are presented in Figure 3.17.

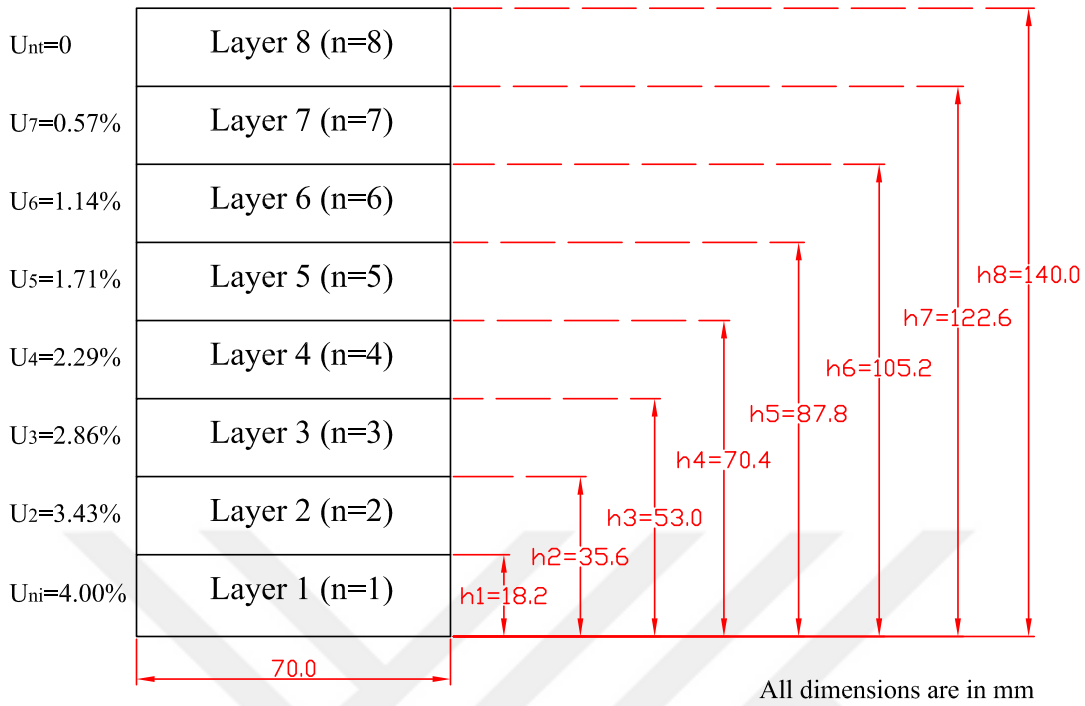


Figure 3.17. Calculated layer thicknesses for cylindrical specimen preparation according to the undercompaction method

CFM masses to provide the desired dry densities were determined as the first stage of the specimen preparation. After each specimen was thoroughly mixed with water until their optimum moisture contents, they were placed in a covered container and allowed to stand one day before compaction. Following the specimen placement and compaction for each layer, surfaces between two adjacent soil layers were slightly loosened to prevent discontinuity. After the compaction of the final layer and splitting the mold, all CFM specimens could stay intact with no significant change in their dimensions (Figure 3.18).



Figure 3.18. CFM specimens prepared in the split mold

3.3.2.2.3 Test Procedure

After the split mold was removed, large gaps caused by coarse particles were coated with a thin layer of moist clay (kaolin) to prevent water flow between the membrane and soil interface (Figure 3.19). This application was beneficial, especially for soils with a lower fines content, such as S12-5 and S12-15 (both with FC=12%).



Figure 3.19. Coating of the large gaps with a thin layer of moistened kaolin clay

The test procedure was applied by following the ASTM D5084-16. Two filter papers and two porous stones, having the same diameter as the specimen, were soaked in de-aired water. After the membrane was placed around the specimen by using a membrane expander, the filter papers were placed on the top and bottom surfaces of the specimen and porous stones on the filter paper surfaces. All pipes, valves, and connections of the apparatus were checked to ensure water-tightness. All pipes were filled with de-aired water so that no visible air bubbles remained in the flowing system. Afterwards, the membrane of the specimen was sealed by placing two O-rings on the top and bottom plates of the apparatus using silicon grease (Figure 3.20).



Figure 3.20. Sealing the specimen between the top and bottom plates with O-rings

The reservoir of the pressure cell was filled with de-aired water, and confining pressure of 25 kPa was applied to the specimen by the cell pressure supplier. A smaller influent and effluent pressures (5 to 10 kPa) were applied to the specimen, and permeant water was flushed through the flow system. After all visible air bubbles were removed from the flow lines, influent and effluent valves were closed. During

the flushing process, the height of the specimens was controlled with the displacement gauge attached to the triaxial apparatus. Afterwards, the specimen was saturated by back pressure. It was intended to measure the hydraulic conductivities in a state closest to the specimens' initially compacted dry densities (95% of the standard Proctor dry density). Therefore, volume changes were kept to a minimum while saturating the specimens. At each pressure increase, back pressures were applied slowly to complete the consolidation stage simultaneously. Thus, no additional consolidation stage was applied at the end. At the last stage of the back pressure saturation, cell pressure of 500 kPa and effective stress of 30 kPa were applied to the specimens. Changes in heights were smaller than 0.5% axial strain (< 0.7 mm), while there was 30 kPa effective stress on specimens at the end of the saturation. Skempton's pore water pressure parameter, B value, was used to confirm the completion of the saturation process. For most of the tests, B values reaching 0.97 or 0.98 could be obtained. However, it was 0.94 in a few tests. Therefore, B value $\geq$ 0.94 criteria were used for those tests to complete the saturation process. Hydraulic conductivity tests were initiated by increasing the influent pressure without decreasing the effluent pressure (flow towards the top). The quantity of the water flow was measured and recorded with time. The height of the specimen was measured in between the hydraulic conductivity test measurements. No significant change in height was detected to affect the hydraulic conductivity calculations. Hydraulic gradient (i) values in between 0.5-2.0 for specimens having hydraulic conductivity between 10^{-3} and 10^{-4} cm/s; 1-5 for 10^{-4} and 10^{-5} cm/s; 2-10 for 10^{-5} and 10^{-7} cm/s were applied according to the maximum hydraulic gradient values recommended in the ASTM 5084-16. Different gradient values were used at the specified ranges for each test. Hydraulic conductivity measurements were considered steady as four or more consecutive measurements fall within ±25% or better of the mean value as stated in the relevant standard.

3.3.3 Unconfined Compressive Strength Tests

3.3.3.1 Apparatus

Unconfined compressive strength (UCS) tests were conducted by using the 5 tons load capacity, displacement-controlled (with a 50 mm bottom platen travel capacity) UCS apparatus. Test setup with the loading frame, S-type load cell (50 kN capacity), and vertical displacement gauge (LVDT with a capacity of 50 mm), which they were connected to the integrated data acquisition system, as well as the other apparatus: caliper, containers, timer, and balance can be seen in Figure 3.21. Calibrations of all data acquisition instruments were checked prior to tests.



(a) (b)

Figure 3.21. (a) Test setup with integrated measuring equipment, and (b) other apparatus for unconfined compressive strength tests

3.3.3.2 Specimen Preparation

The same specimen preparation procedure, described in Section 3.3.2.2.2 for the flexible wall hydraulic conductivity testing, was applied for the UCS testing. Specimens were prepared at their optimum water contents and 95% of their standard Proctor densities and to have a diameter of 70 mm and a height of 140 mm.

3.3.3.3 Test Procedure

UCS tests were performed following the ASTM D2166-16. After checking and recording its initial dimensions, the prepared specimen was placed in the setup, centered between the upper and bottom platens (Figure 3.22). The position of the upper platen was adjusted to make slight contact with the upper surface of the specimen without imposing any compressive load. The displacement gauge and any initially recorded readings were reset from the settings of the device. An axial deformation rate of 1 mm/min, corresponding to an axial strain rate of 0.7%/min, was applied to all CFM specimens in UCS testing. Axial load, deformation, and time were recorded with the initiation of the experiment.



Figure 3.22. Placement of the specimen to the unconfined compressive strength equipment

Axial loading was maintained even after the failure point had been reached to observe the post-peak stress-strain behavior of CFM specimens. Even though specimens were prepared in the laboratory at their optimum moisture contents, obtained by standard Proctor testing, the water content was determined by using the entire specimen after UCS tests. At least three different experiments were conducted to evaluate the repeatability of the results with the same testing parameters and identical CFM specimen preparation.

3.3.4 Isotropically Consolidated Undrained Triaxial Compression Tests

3.3.4.1 Apparatus

Isotropically consolidated undrained (ICU) triaxial compression tests were carried out by using triaxial apparatus (Digital Tritest 50) with a loading frame capacity of 50 kN. The equipment was a displacement-controlled loading device having a bottom platen travel capacity of 100 mm. In addition to the loading frame, the apparatus used in testing included pressure cell (1700 kPa capacity), S-type load cell (10 kN capacity), vertical displacement gauge (LVDT with a capacity of 50 mm), pressure suppliers (oil/water constant pressure system, 1700 kPa capacity) for cell, inlet, and outlet of the specimens, digital pressure transducers (1700 kPa capacity), volume change transducer and an external data acquisition system. Other apparatus used in testing included filter papers, porous stones, vacuum pump, O-rings, silicon grease, membrane, membrane expander, caliper, timer, and balance. The view of the triaxial test setup with the integrated equipment is presented in Figure 3.15. Other apparatus and the view of the compression of the specimen in the loading frame are presented in Figure 3.23 and Figure 3.24, respectively. Calibrations of all data acquisition instruments were checked prior to testing.



Figure 3.23. Apparatus used for triaxial compression tests



Figure 3.24. Loading frame and the cell for triaxial compression tests

3.3.4.2 Specimen Preparation

The same specimen preparation procedure, described in Section 3.3.2.2.2 for the flexible wall hydraulic conductivity testing, was applied for the ICU triaxial compression testing. Specimens were prepared at their optimum water contents and 95% of their standard Proctor densities and to have a diameter of 70 mm and a height of 140 mm.

3.3.4.3 Test Procedure

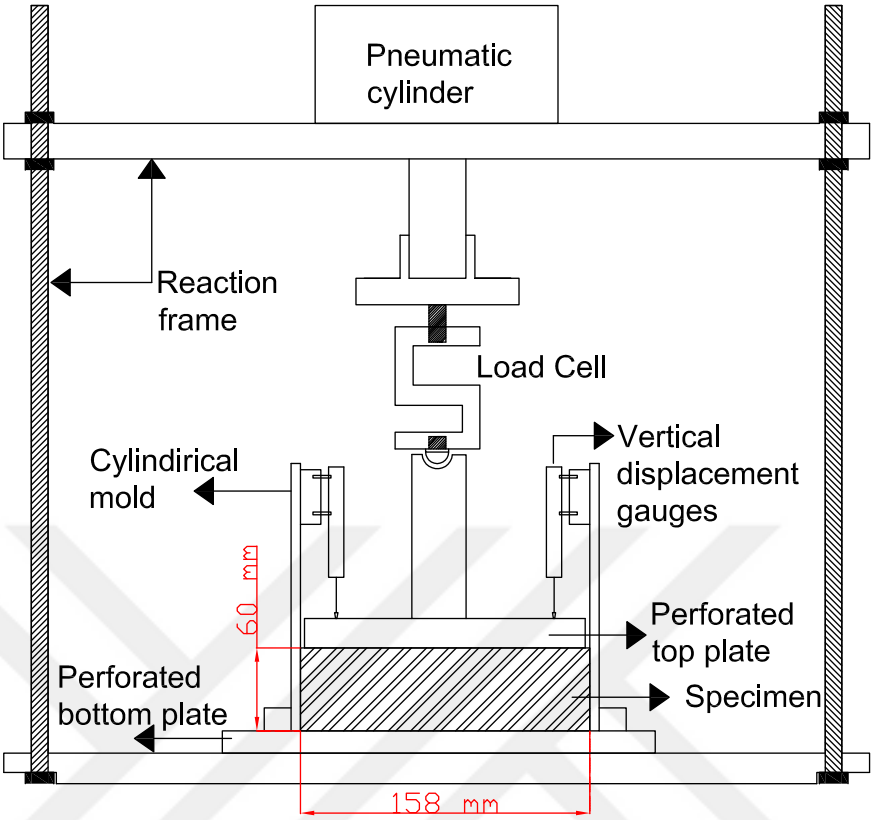
Undrained triaxial compression tests have been conducted after saturation and isotropic consolidation of CFM specimens according to the ASTM D4767–11. Two filter papers and two porous stones (previously boiled in water for saturation and cooled down to room temperature), having the same diameter as the specimen, were soaked in de-aired water. All pipes, valves, and connections of the apparatus were checked to ensure water-tightness. All drainage lines were filled with de-aired water so that no visible air bubbles remained in the flowing system. A rubber membrane was placed around the specimen by using a membrane expander. Filter papers were placed on the upper and bottom surfaces of the specimen and porous disks on the filter paper surfaces. The specimen was mounted inside the triaxial chamber by sealing the top and bottom plates and rubber membrane with two O-rings on each side with the help of silicon grease. Slight contact of the piston and top cap was provided without imposing any load on the specimen, vertical alignment of the loading axis was controlled, and the reading on the displacement gauge was recorded. The pressure chamber was filled with de-aired water without leaving any air space. 25 kPa confining pressure was applied to the specimen by the cell pressure supplier. De-aired water was percolated from the bottom to the top of the specimen under the differential vacuum of 10 kPa. During this process, the height of the specimen was controlled with the displacement gauge attached to the triaxial apparatus. Afterwards, the specimen was saturated by back pressure. Cell pressures

and back pressures were applied slowly in each pressure increment to allow the pore water pressures in the specimen to equalize and to prevent uncontrolled prestressing. 500 kPa back pressure and 30 kPa effective stress were applied to the specimen at the final stage of the back pressure saturation. Changes in the specimen heights (usually smaller than 0.5% axial strain, 0.7 mm, on 30 kPa effective stress) and water volume were measured and recorded. Skempton's pore water pressure parameter, B value, was used to confirm the completion of the saturation process. For most of the tests, B values reaching 0.97 or 0.98 could be obtained. However, it was 0.94 in a few tests. Therefore, B value $\geq$ 0.94 criteria were used for those tests to complete the saturation process. Afterwards, the consolidation stage was initiated. Three sets of tests were conducted for each CFM by consolidating the specimens from both ends under the effective stresses of 40 kPa, 150 kPa, and 300 kPa. Volume change with time was measured and recorded. After completion of the consolidation process, drainage valves were closed. Initial piston friction and upward thrust because of the chamber pressure were recorded to be used in the corrections of the measured axial load. The consolidation time was longer for the CFM specimens having higher fines content and plasticity. According to the observed consolidation data and recommendation of the ASTM D4767–11, an axial deformation rate of 0.05 mm/min (axial strain rate $\approx$ 0.036%/min) was selected for the shearing of all CFM specimens. Stabilized pore water pressure generation was provided under undrained conditions with this axial strain rate even for the CFM having the highest fines content and plasticity. Undrained compression tests were conducted until at least 15% axial strain was reached for each sample. Axial load and deformation, time, and pore water pressures in the specimen were recorded at 0.1% increments until 1% axial strain and thereafter 1% strain increments in accordance with the recommendation of ASTM D4767–11. When the shearing was completed, water content was determined by using the entire specimen. Control tests were conducted to evaluate the repeatability of the test results with the same CFM properties and testing parameters.

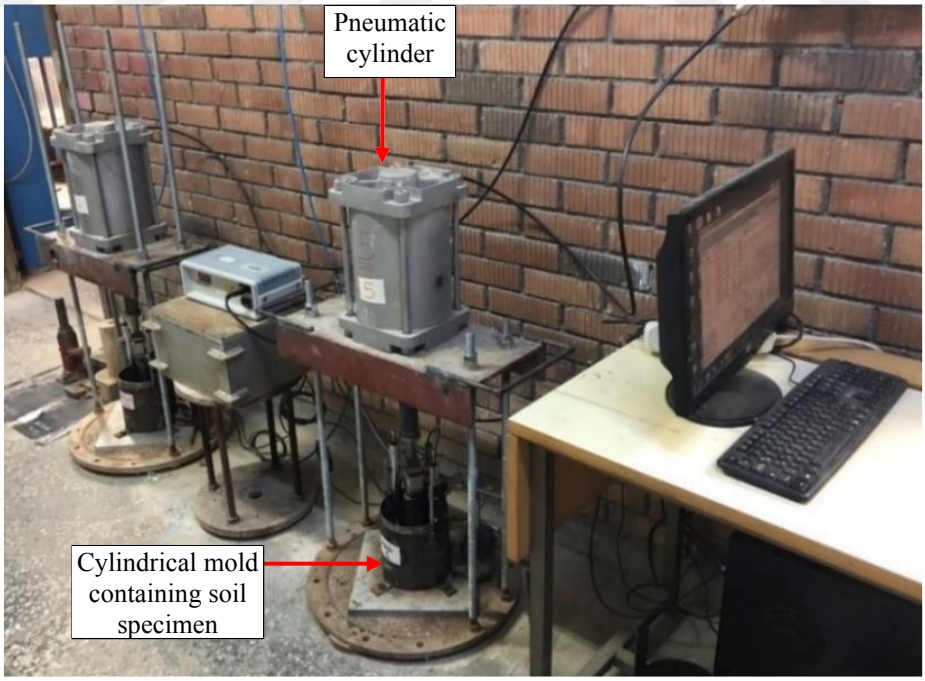
3.3.5 Static Large Compression Tests

3.3.5.1 Apparatus

One-dimensional static compression tests were conducted to be able to determine the compressibility characteristics of CFM having different fines contents and plasticity indices. Schematic representation and general view of the experimental setup are presented in Figure 3.25. The setup was capable of allowing simultaneous testing of two different compression experiments. As seen in Figure 3.25a and Figure 3.26a, instrumentation for one compression test included one S-type load cell (with a capacity of 50 kN), two displacement gauges (potentiometers with a capacity of 100 mm), and a data acquisition system (Appendix B). Steel molds with a diameter of 158 mm and a height of 180 mm were used to prepare and load the specimens with a diameter of 158 mm and a height of 60 mm. The view of the mold, filter papers, loading plate, and the dynamic tamping tool with a 90 mm compaction area are presented in Figure 3.26b.



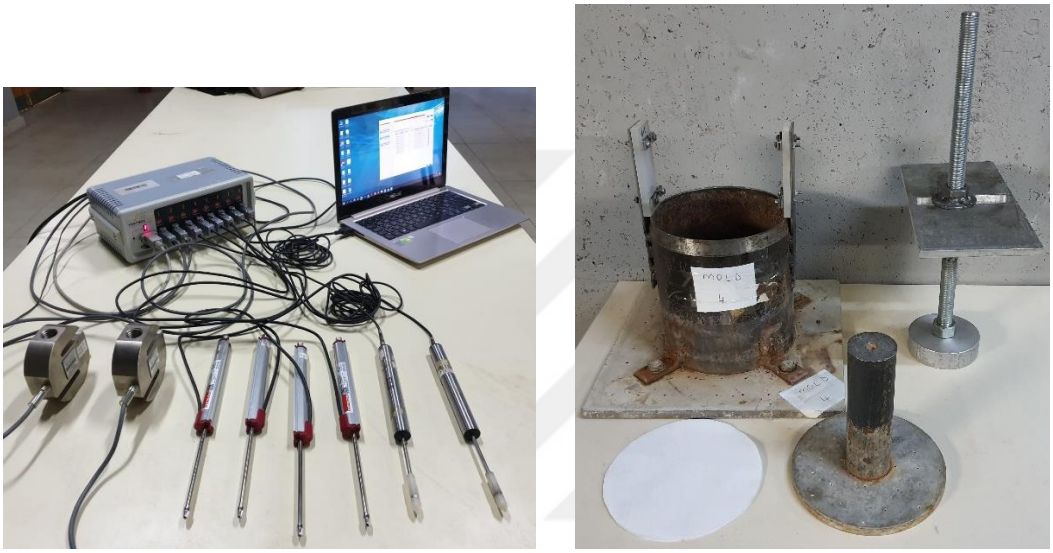
(a)



(b)

Figure 3.25. (a) Schematic, and (b) general view of the setup for compression tests

Specimens were subjected to static compression with the help of a pneumatic cylinder (with a capacity of 10 bar, corresponding to 3.1 tons) and a metal reaction frame. In this setup, the air pressure coming from the compressor was adjusted with a pressure regulator. The air pressure in the pneumatic cylinder was calibrated to provide desired load levels to the specimen. Calibrations of all other data acquisition instruments were checked prior to testing as well.



(a) (b)

Figure 3.26. (a) Equipment for data acquisition, (b) steel mold, filter papers, loading plate, and the compaction apparatus

3.3.5.2 Specimen Preparation

The compression behavior of CFM was aimed to be determined at their optimum moisture contents and 95% of standard Proctor dry densities. Therefore, several trials were performed to prepare the specimens using static compaction with the setup before the compression testing. However, desired densities could not be achieved with this method for the current specimen dimensions and loading capacity of the compression system. Therefore, dynamic compaction of the specimens inside the steel molds was adapted. Specimens were placed in steel molds in three layers. Even

though the undercompaction method proposed by Ladd (1978) requires a minimum of five layers to be applied, layer thicknesses were selected by using the formulas of the method (Equations 3.3 and 3.4) by considering the additional compaction of the lower layers during the compaction of the upper layers. Accordingly, the total specimen thicknesses after each layer is compacted were determined as 20.8 mm after the first layer, 40.4 mm after the second layer, and 60.0 mm after the last layer.

In the first step of the specimen preparation, the CFM masses to provide the desired dry densities were determined. Water was added until the optimum moisture contents of the mixtures were reached. After each specimen was thoroughly mixed, they were placed in a covered container and allowed to stand one day prior to compaction. Filter paper having the same diameter as the steel mold was placed on the perforated bottom plate. Silicon grease was applied to the inner surface of the mold to reduce the friction between the steel mold and the soil specimen. Following the placement and compaction of the material for each layer (Figure 3.27), it was controlled that the compacted layer surfaces were level.



(a) (b)

Figure 3.27. (a) Sample placement, and (b) dynamic tamping with the compaction apparatus

Surfaces between two adjacent soil layers were slightly loosened to prevent discontinuity. Following the compaction of the final layer, total specimen height was controlled, and filter paper and perforated loading plate were placed. Even distribution of the moisture contents and densities were checked by taking three different samples (varying height, center, and near boundary locations) from the two different compacted CFM specimens. Results confirmed that moisture contents varied less than 1.1% and dry densities less than 0.02 g/cm^3.

3.3.5.3 Test Program and Procedure

Two groups of 1-D compression experiments were conducted on all CFM specimens (S12-5, S12-15, S20-5, S20-15, S30-5, S30-15, S40-5, and S40-15). In the first group, compression tests were performed on the specimens prepared as described in Section 3.3.5.2 (dynamically compacted at their optimum moisture contents and 95% of their standard Proctor dry densities).

In the second group, immediately after the specimen preparation as described in Section 3.3.5.2, water was added from the bottom of the specimen for two days, then CFM specimens were submerged in a water bath for one week (Figure 3.28a). A surcharge load of 15 kPa was applied, and vertical displacement from the top of the soil layer was also monitored in this stage to observe if there was any potential swelling or compression behavior. Based on the results, compression behavior was observed during this stage for all CFM ranging from a minimum value of 0.05 mm (an axial strain of 0.08%) to a maximum of 0.35 mm (an axial strain of 0.58%).

In the first group of experiments, compression tests were initiated immediately after the specimen was prepared and in the second group after submerging in the water bath following specimen preparation. Load increment ratio of one was applied in loading, which was obtained by doubling the applied pressure on the specimens. At the end of the test, specimen was unloaded by decreasing the pressure to one-fourth of the preceding pressure level. A total of eight loading stages (six loading and two

unloading stages) were applied as 40, 80, 160, 320, 640, 1280, 320, and 80 kPa. Because of the precision of the loading system with the pneumatic cylinder, pressures could be given at an average of ±5 kPa of the targeted pressures. Based on the measurements of vertical displacement versus time, under each given loading, a maximum displacement rate of 0.006 mm/hr (strain rate of 0.01%/hr) was judged to be acceptable to define that almost all of the vertical compression ceased under the given loading, i.e., this displacement rate is used as a criterion for a loading stage to be finalized and the subsequent stage to be initiated, although rates lower than this value were mostly obtained.



(a) (b)

Figure 3.28. (a) Submersion in a water bath, and (b) submerged compression tests for coarse-fine mixtures

3.3.6 Large Direct Shear Tests

3.3.6.1 Apparatus

A large direct shear testing equipment was manufactured in the scope of this study, which is capable of testing soil and soil-geosynthetic interface shear strength. By this

means, the mechanical behavior of CFM and their interaction with geogrid could be evaluated under direct shear failure mode. The general view and the schematic diagrams of the large direct shear testing equipment are presented in Figure 3.29, Figure 3.30, and Figure 3.31. All large direct shear tests were carried out at METU Civil Engineering Department's Soil Mechanics Laboratory.

The equipment consists of lower and upper shear boxes having 160 and 175 mm heights, respectively, with a 300 mm x 300 mm cross-sectional area. A soil specimen with a total height of 300 mm can be placed to test. However, approximately half of this value was used for the height of the tested soils in this study, considering the required minimum height of specimen as compared to the maximum particle size of the soil (ASTM D5321-14). Therefore, a robust metal stand was used to raise the level of soil in the lower box (Figure 3.31).

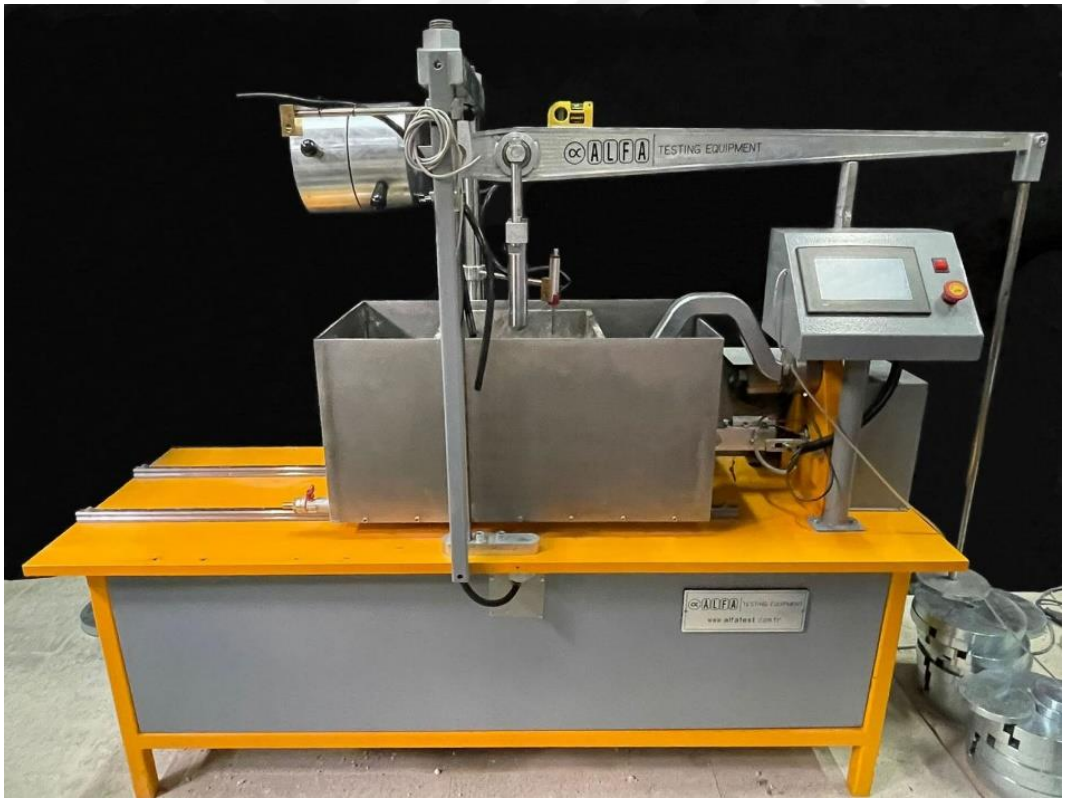


Figure 3.29. General view (side view) of the large direct shear testing equipment at METU Civil Engineering Department

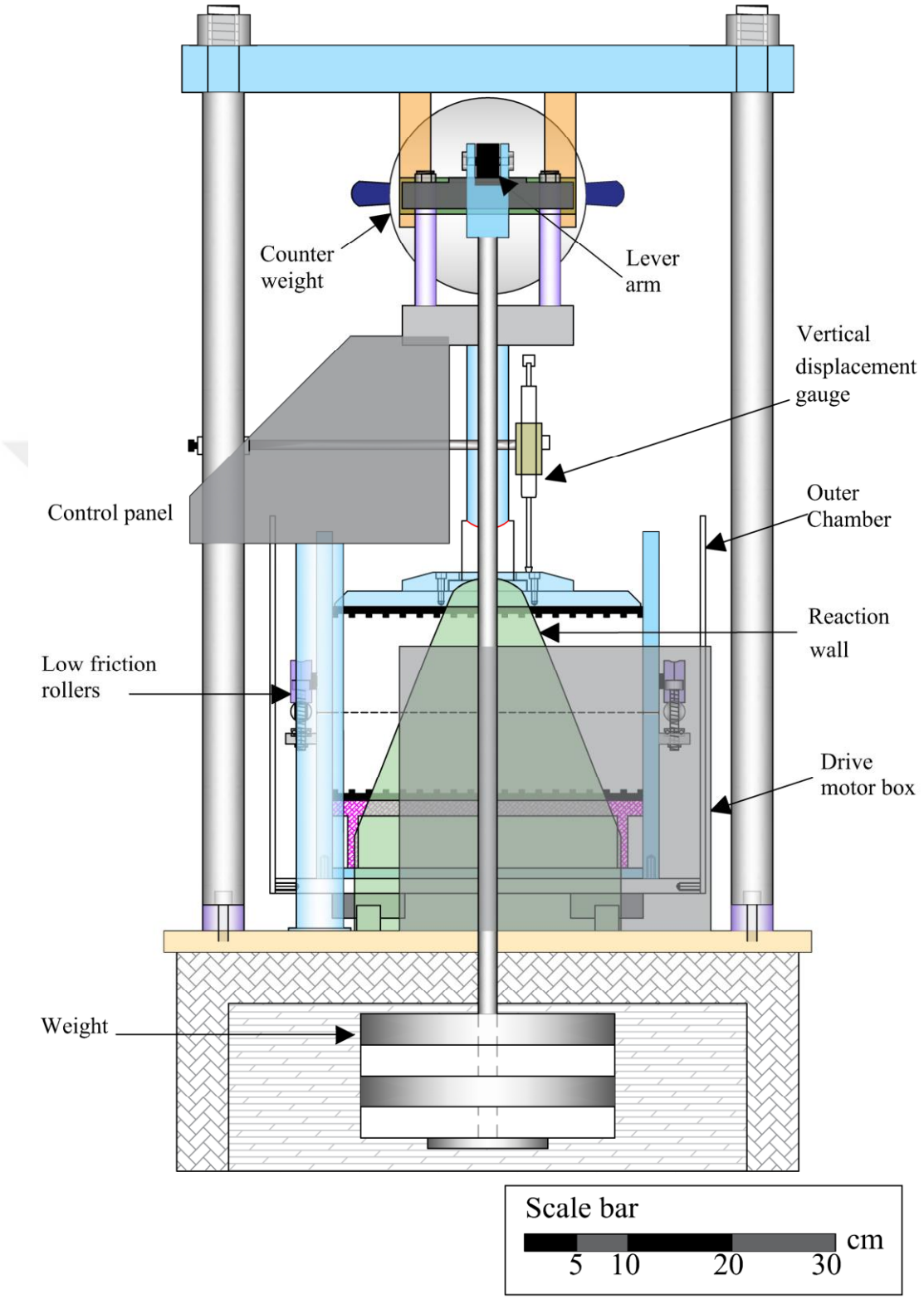


Figure 3.30. Schematic diagram of the front view of the large direct shear testing equipment

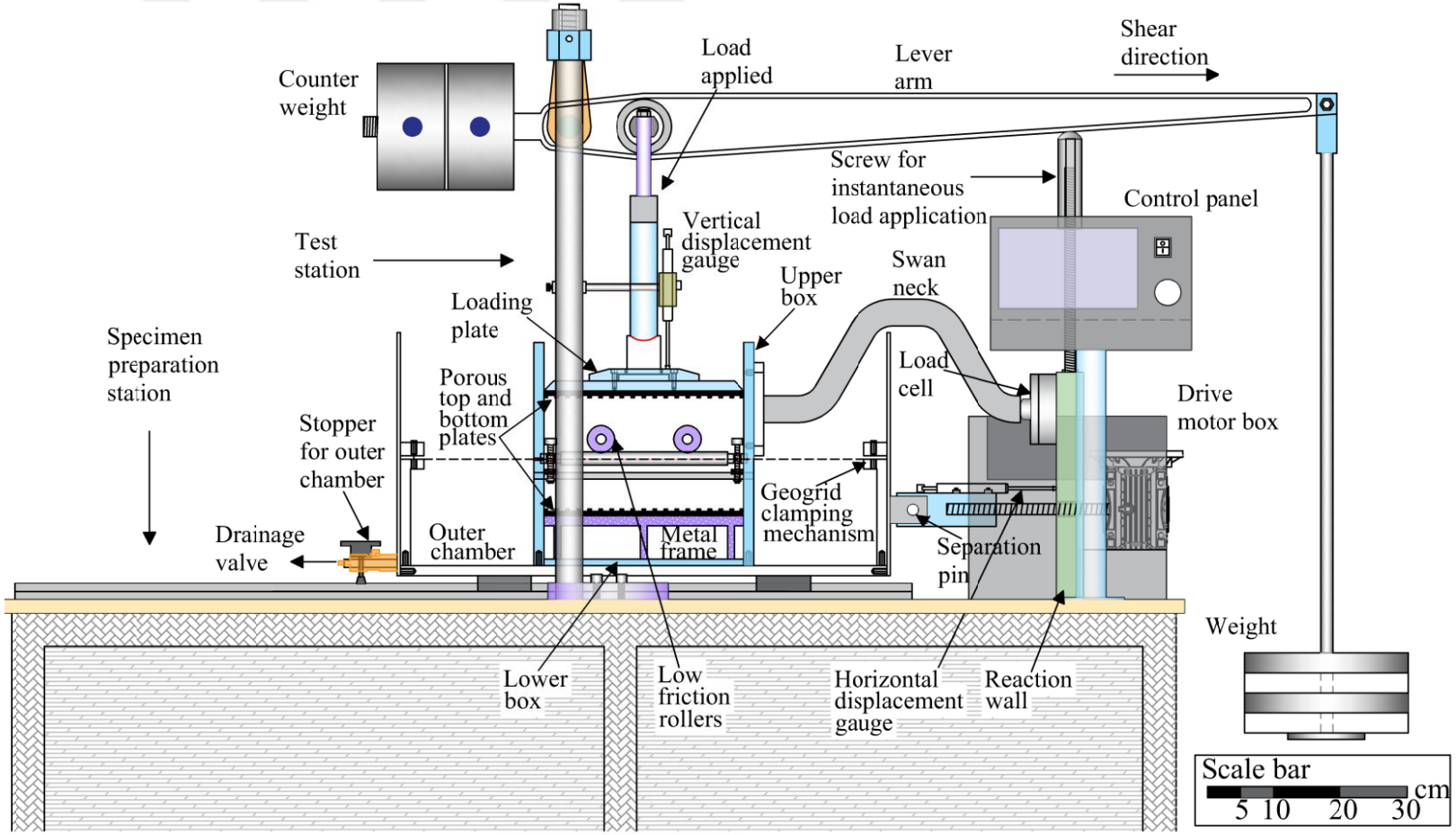


Figure 3.31. Schematic diagram of the side view of the large direct shear testing equipment

The equipment has a displacement-controlled electric drive motor. The displacement induced by the engine is transmitted to the outer chamber through a threaded screw. The outer chamber is the metal container where the lower box is fixed, and it can serve as a water bath to enable water-submerged/saturated testing. During the shear test, the lower box moves together with the outer chamber in the direction of the motor and control panel. On the other hand, the upper box is connected to a stable reaction wall through a rigid steel piece (swan neck), thus ensuring its immobility. The relative movement between the upper and lower boxes generates a shear force in the soil specimen placed into the boxes. The amount of force is measured by a load cell placed between the swan neck and the reaction wall.

The maximum normal and shear loading and testing capacity of the large direct shear apparatus is 2000 kg, which can provide maximum normal stress of 218 kPa on a soil specimen having a 300 mm x 300 mm cross-sectional area. In order to have a safety margin and not cause any damage to the apparatus, the maximum normal stress used in direct shear tests was 155 kPa in this study. The apparatus can provide shearing with a horizontal displacement of up to 50 mm. The normal load is applied to the soil inside the upper box through a loading plate (Figure 3.31), on which the normal force is provided by a dead load and lever arm system having 10:1 leverage ratio. Instantaneous load application is provided by the screw holding the lever arm in the horizontal position. After the desired weight on the hanger is placed, the vertical load is given to the system by rotating the screw and lowering it down.

The large direct shear apparatus consists of testing and specimen preparation stations (Figure 3.31). When a test is completed, and the normal load on the specimen is removed, the outer chamber is disconnected from the drive motor by removing the separation pin and pulled to the sample preparation station. The outer chamber can move in the direction of the shearing axis with the help of the slides underneath. Since there is no reaction frame above the boxes in this station, removal, and placement of the specimen can be done easily. When the apparatus is ready for the next testing, the outer chamber is brought back to the test station, and the separation pin is placed to connect the outer chamber to the drive motor.

Calibrated instruments of the apparatus include one load cell, one horizontal displacement gauge (linear potentiometer with a capacity of 50 mm), and one vertical displacement gauge (linear potentiometer with a capacity of 50 mm) (Appendix B). These are connected to the integrated data acquisition system, which is placed inside the control panel.

The frictional force resulting from the relative movement of the lower and upper boxes may interfere with the shear load measurements of the tested specimen if the flat metal surfaces of the upper and lower boxes touch each other. Therefore, these surfaces should be separated before proceeding to the shearing stage. In this apparatus, low friction steel rollers are mounted on both sides of the upper box, whereas cylindrical bars on which these rollers sit are mounted on both sides of the lower box. Two screws attached to this bar control the vertical movement and position of the bar (Figure 3.32). As this cylindrical bar is lifted up, the upper box moves up on the rollers. Vertical movement and the gap between the upper and lower boxes are controlled by the number of screw turns. When the normal load is applied, and the two boxes are separated, cylindrical bars are lowered down. When there is a soil specimen in the box, the upper box can stand without having contact with any part of the lower box because of the normal load on the soil specimen. Low friction rollers were designed as a precaution to prevent the geogrid from getting stuck between the two boxes in case of a possible tilting of the upper box during shear. After the upper box is raised, the cylindrical bars may be lowered to a position that even if the upper box is tilted during shearing, rollers will touch the bar, and the test will continue with a low frictional effect without geogrid getting squeezed. However, trials indicated that this application was not necessary for tests within the scope of this study. It was seen that shearing could be sustained without supporting the upper box on rollers. In other words, in all tests in this study, rollers were not used to keep the upper and lower boxes separated, and during shearing, the flat metal surfaces of the upper and lower boxes did not touch each other and did not create friction. In addition, it was also observed that there was no significant tilting of the upper box and no geogrid getting squeezed. Therefore, there was no frictional force to be

considered other than the shear force of the soil specimen in the measured load readings.

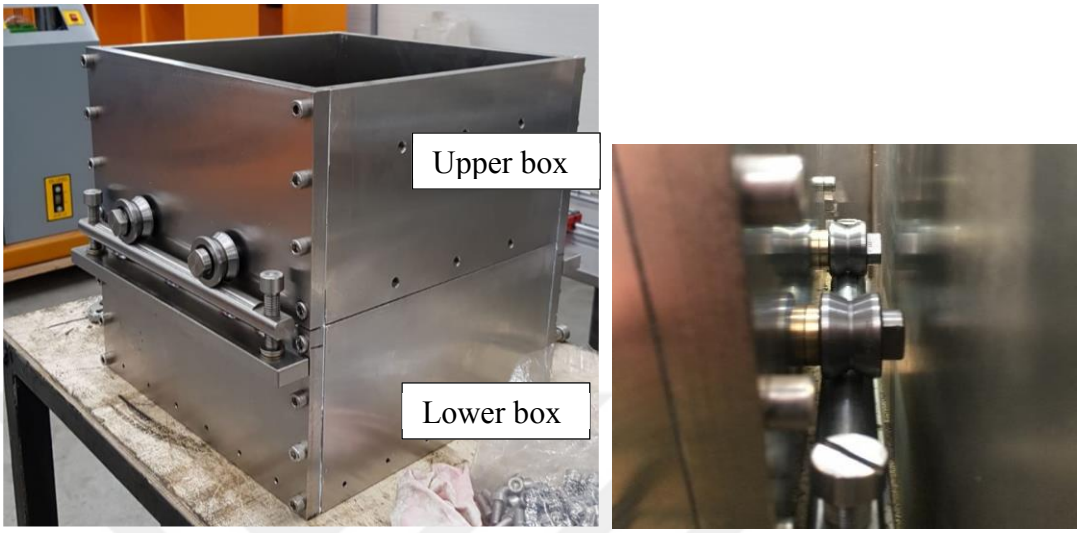


Figure 3.32. The mechanism for the separation of the upper and lower boxes

During shearing, the mass of the upper box is expected to contribute by some amount to normal forces on the failure surface due to drag on the sides of the soil in the upper box; however there is no consensus on the percentage of this contribution. According to ASTM D3080-04, the weight of the upper half of the shear box shall be less than one percent of the applied normal force during shear, so that its contribution can be ignored. If the weight of the box is more than 1% of the applied normal force, either a counterbalance system should be used where the upper box will be kept floating (Germaine and Germaine, 2009), or the weight of the upper box must be accounted in the normal stress calculations. Olson (1989) suggests adding all of the weight of the upper box to the normal force, if a counterbalance system is not used, whereas Germaine and Germaine (2009) and Germaine (2019, personal communication) note that the amount of the contribution to normal force is unknown. Uyeturk (2019) added 50% of the mass of the upper shear box to the normal force on the soil in order to minimize the maximum error in normal stress due to the weight of the upper box. In this study, the weight of the upper shear box is more than 1% of the applied normal

force and all of the weight of the upper box is added to the normal force on the specimen.

The geogrid clamping mechanism, mounted on the outer chamber, is located in the middle of the shear zone between the upper and lower boxes (Figure 3.31). During shear, while the outer chamber, lower box, and the geogrid move together, the shear force is generated between the soil specimen and the upper surface of the geogrid. Geogrid is fixed between two metal plates with three screws along its transverse rib by using the clamping mechanism (Figure 3.33). A mica rubber sheet with the textured surface is placed on both sides along the geogrid's transverse rib so that the geogrid is not slipped during shearing and is not damaged by the compression force of the metal plates.

One of the additional apparatus used for the specimen preparation was dynamic compression tools (Figure 3.34a). 80 mm x 80 mm steel square plate was located at the end of the compaction tools, providing the specimen's compaction into the desired layer thicknesses by dynamic tamping. A separable guiding metal frame was used to compact the loose CFM specimens in the lower box (Figure 3.34b). In addition, the screw slot used to fix the upper and lower boxes during specimen preparation is shown in Figure 3.34b. The top view of the loading plate, serrated porous plates contacting the top and bottom surfaces of the prepared specimen, and other tools used to perform direct shear testing are presented in Figure 3.34c.

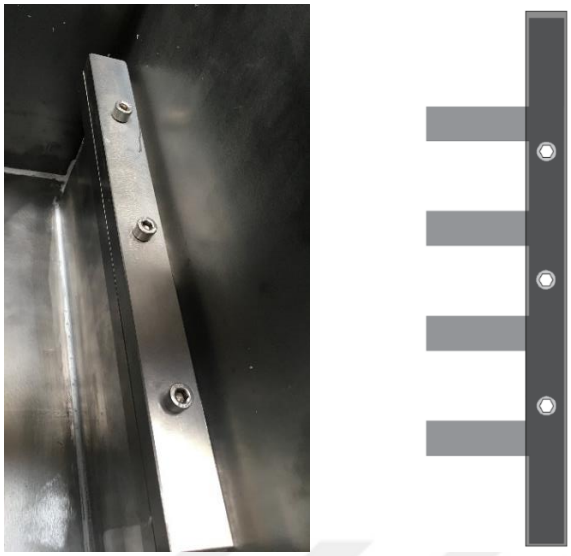
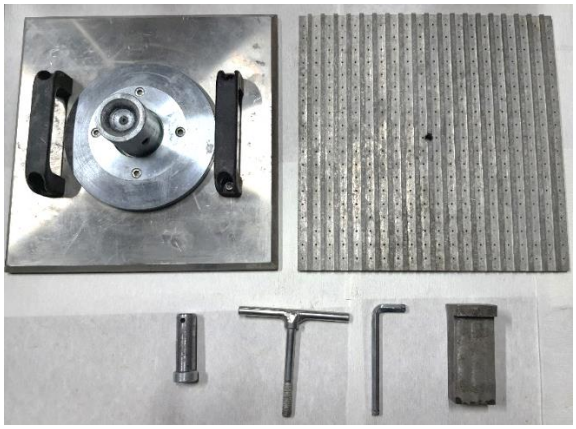


Figure 3.33. The view of the geogrid clamping mechanism



(a) (b)



(c)

Figure 3.34. (a) Dynamic compaction apparatus, (b) guiding frame, (c) porous plates, loading plate, and additional tools

3.3.6.2 Specimen Preparation

Recommendations of the ASTM D5321-14 (Determining the Shear Strength of Soil-Geosynthetic and Geosynthetic-Geosynthetic Interfaces by Direct Shear) were considered for the soil and geogrid specifications and also in the application of the large direct shear tests in the scope of this study. One of the problematic issues emphasized in this standard is testing with fine/compressible soils. Possible settlements during consolidation or shearing may cause the geogrid to move into the soil in the lower box or lose its planar shape and get curved (concave up). Therefore, it is recommended in the standard to place a rigid substrate inside the lower box instead of soil with high compressibility potential. In this method, soil-geogrid interface interaction must be determined analytically from the soil-soil, soil-geogrid, and soil-rigid substrate interactions. Although there are studies using this method in the literature, the mechanical conditions in testing may not simulate the field behavior, as indicated in the relevant standard. In terms of being more suitable for the actual site conditions, experiments in this study were carried out by placing the soil both in the upper and lower boxes by taking precautions. First of all, this was one of the reasons why CFM properties were selected as having relatively low plasticities (5% and 15%) and high in-place dry densities (95% of standard Proctor density, which is the standard application in MSEW projects). In this way, it was aimed to prevent excessive settlements that may cause the abovementioned problems. In addition, prepared CFM were suitable for both practical applications (addressing the restrictions of guidelines or design codes) and had soil properties with transitional behavior that may be used as a backfill in MSEW. Besides, the large static compression tests gave a substantial idea about the ranges of settlements at the applied load levels. As another precaution, the surface on which the geogrid was placed was designed to protrude 2 mm above the lower box level, as can be seen in Figure 3.35. It was observed that geogrids remained in the shear zone and kept their planar shape in the direct shear test trials.



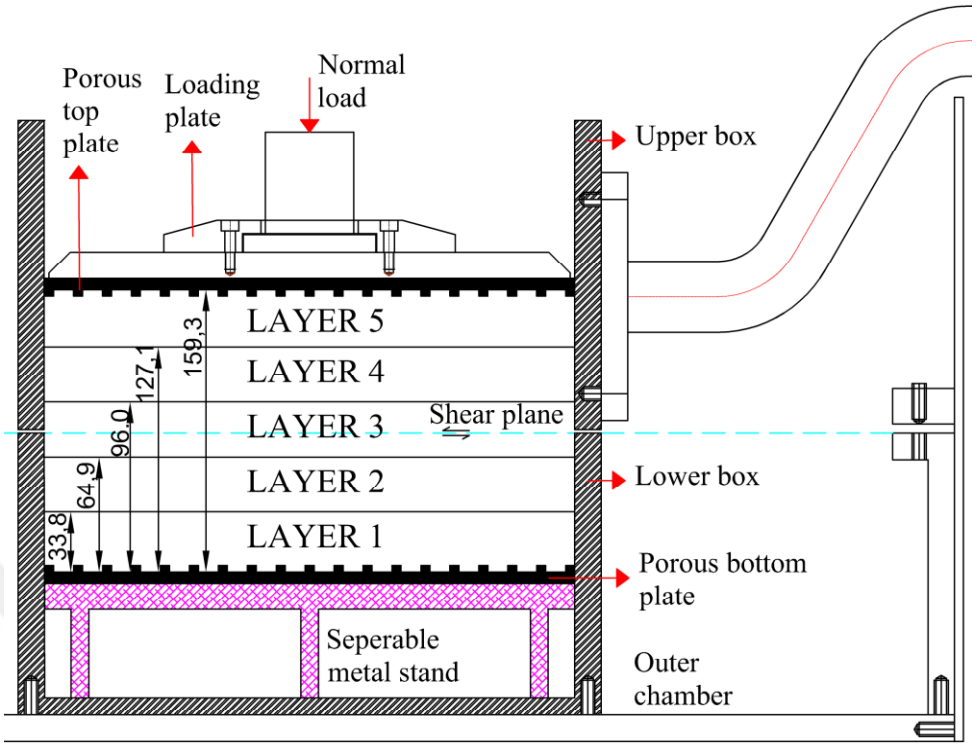
Figure 3.35. Soil surface protruding from the lower box level on which the geogrid will be placed

Sample preparation and testing procedures were developed to perform direct shear tests on a total of ten soil mixtures having an FC of 0%, 12%, 20%, 30%, and 40%, and a PI of 5% and 15%. Test procedures were designed so that each soil sample was prepared and used only once, and a tested specimen was not reused again. Therefore, identical soil mixture and specimen preparation were assured by repeated index tests similar to tests described in Section 3.3.2.2.2.

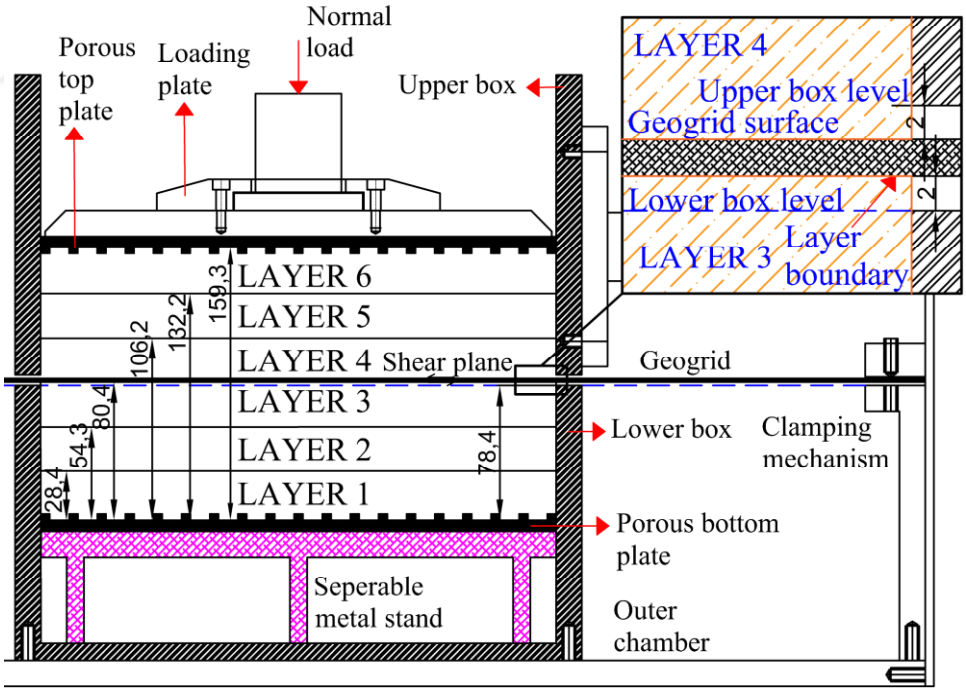
The specimen preparation procedures for SW and SP soil mixtures (dry and having no fines) and eight types of CFM as well as the tests with and without geogrid, showed some variances. The desired dry densities of SW and SP soil mixtures could be achieved by compaction with a tamping rod (having a diameter of 4 mm and smooth side surfaces) after specimen placement. In-place dry densities of SW and SP (95% of their maximum dry densities) were 1.98 g/cm^3 and 1.67 g/cm^3, respectively, as explained in Section 3.3.2.1.2.

It was observed from the 1-D large compression tests (Section 3.3.5) and direct shear test trials that targeted unit weights could not be achieved for CFM (mixtures having fines content and plasticity) without dynamic compaction. For this reason, the specimen preparation of CFM was performed by the undercompaction method proposed by Ladd (1978) (Equations 3.3 and 3.4). The specimen height was divided into five and six layers for tests without and with geogrid, respectively. Layer

thicknesses and the schematic view of the specimens are presented in Figure 3.36. It was aimed that the boundaries between the layers remain outside the shear zone in tests without geogrid so that any layer interfaces do not affect the own shear strengths of CFM. Although, this effect was minimized by slightly loosening the surface of each layer before the next layer was placed and compacted. In tests with geogrid, specimen placement was applied similar to the stages of MSEW construction in practice. The first, second, and third layers were placed and compacted in the lower box so that the upper surface of the third layer protruded 2 mm from the lower box. Afterwards, geogrid was placed and fixed to the outer chamber with the clamping mechanism. After the top box was placed, the fourth, fifth, and sixth layers were compacted, respectively (Figure 3.36b).



(a)



(b)

All dimensions are in mm

Figure 3.36. Schematic view of the specimen preparation with dynamic compaction for (a) CFM without geogrid, (b) CFM with geogrid

The distance from the bottom of the porous plate to the end of the lower box was 78.4 mm (Figure 3.36b). Therefore, as twice this value, the total specimen height was designed to be 156.8 mm. The specimen height of 159.3 mm, which is seen in Figure 3.36, was the equivalent specimen height by considering the volumetric effect of the protrusions of the serrated porous plates.

Initial properties, soil, and water masses of the prepared mixtures for large direct shear tests are presented in Table 3.4. CFM were prepared at their optimum moisture contents and had an in-place dry density equal to 95% of the standard Proctor densities in all the tests.

In most tests (82 tests) in this study, specimens were subjected to shear after the settlements were finalized following the normal stress application. In eight tests, however, specimens were submerged in water for one week during the normal load application stage after they were prepared with the properties in Table 3.4. Specimen preparation procedures for unsaturated and saturated tests were explained in detail in the following subsections.

Table 3.4. Properties, soil, and water masses of the prepared mixtures

Soil code	In-place moisture content, w_{opt} (%)	In-place dry density, ρ_{dry} (g/cm^3)	In-place bulk density, ρ_{bulk} (g/cm^3)	Dry mass of soil mixture, m_{dry} (g)	Water mass in the soil mixture, m_w (g)
SW	-	1.98	-	27977.4	-
SP	-	1.67	-	23597.1	-
S12-5	7.2	2.08	2.23	29426.7	2118.7
S12-15	7.4	2.01	2.15	28332.0	2096.6
S20-5	6.8	2.11	2.25	29830.0	2028.4
S20-15	9.8	1.94	2.13	27367.0	2682.0
S30-5	7.8	2.02	2.18	28605.7	2231.2
S30-15	11.4	1.85	2.06	26142.7	2980.3
S40-5	8.2	1.97	2.13	27784.7	2278.3
S40-15	14.2	1.76	2.01	24903.9	3536.4

3.3.6.2.1 Specimen Preparation Procedure for Unsaturated Tests

The specimen preparation is described below, together with all the procedures for the tests of (i) SW and SP soils without geogrid, (ii) SW and SP soils with geogrid, (iii) CFM without geogrid, and (iv) CFM with geogrid.

- The mixture to be tested was prepared by mixing the dry soil products according to their proportional distributions, as given in Table 3.2. Masses of the prepared mixtures were determined to provide the desired dry densities according to the shear box volume (Table 3.4).
- For the CFM (mixtures having fines content and plasticity), prepared dry masses were thoroughly mixed with water to their optimum moisture contents and allowed to stand for one day prior to specimen preparation (Figure 3.38a).
- The outer chamber was disconnected from the drive motor and brought to the sample preparation station (Figure 3.37a).

If testing of (i) SW and SP soils without geogrid was to be carried out:

- The upper box was fixed by screwing it to the lower box from the outside of the boxes (Figure 3.37b).
- Predetermined mixture mass was placed (Figure 3.37c) inside the boxes by tamping the specimen fifty times with a tamping rod, applying 20 mm penetration (half of the placed sample thickness) for each 40 mm of soil thickness placed.

If testing of (ii) SW and SP soils with geogrid was to be carried out:

- The upper box was removed by unscrewing it from the lower box (Figure 3.37d).
- The mixture mass required for the lower box volume to have desired densities was placed and compacted by tamping the specimen fifty times with a

tamping rod, applying 20 mm penetration (half of the placed sample thickness) for each 40 mm of soil thickness placed.

- Geogrid was fixed to the clamping mechanism and placed on the shear surface, slightly stretched but not overloaded (Figure 3.37e).



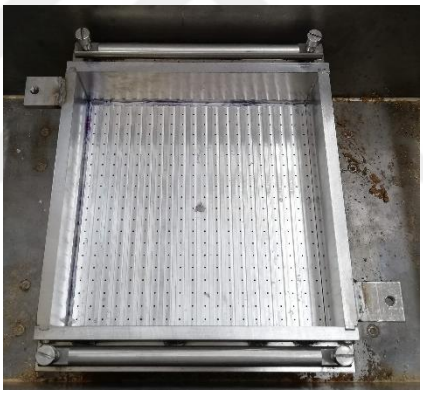
(a) Outer chamber in specimen preparation station



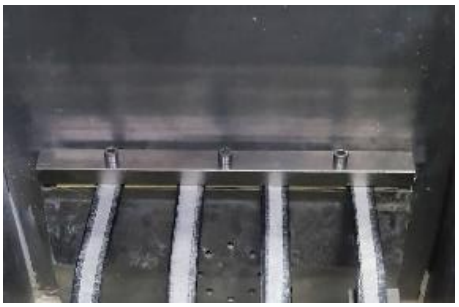
(b) Upper box fixed to the lower box



(c) Specimen placement



(d) Upper box removal



(e) Geogrid fixing to the clamping mechanism



(f) Specimen placement in the upper box

Figure 3.37. Views of specimen preparation stages for the large direct shear test of SW and SP soil mixtures

- The upper box was fixed by screwing it to the lower box from the outside of the boxes.
- The remaining mixture mass was placed and compacted in the upper box as in the lower box (Figure 3.37f).

If testing of (iii) CFM without geogrid was to be carried out:

- The upper box was fixed by screwing it to the lower box from the outside of the boxes (Figure 3.37b).
- CFM mass containing water to the optimum moisture content was placed and compacted in five layers by dynamic tamping (Figure 3.38b).

If testing of (iv) CFM with geogrid was to be carried out:

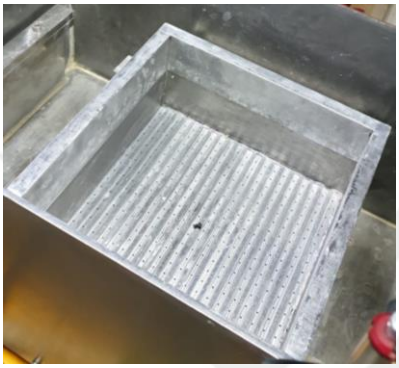
- The upper box was removed, and the guiding frame was placed onto the lower box (Figure 3.38c).
- CFM was laid (Figure 3.38d) and compacted in three layers in the lower box (Figure 3.38e).
- After removing the guiding frame, geogrid was fixed along its transverse rib with the clamping mechanism (Figure 3.38f).
- The geogrid was placed on the surface of the third layer, which was slightly loosened, and protruded 2 mm above the lower box (Figure 3.38g).
- The upper box was carefully put back in place and fixed to the lower box (Figure 3.38h).
- The specimen was placed and compacted with the fourth, fifth, and sixth layers in the upper box.



(a) CFM preparation



(b) CFM compaction in layers



(c) Guiding frame placement



(d) CFM placement in the lower box



(e) CFM compaction in the lower box



(f) Fixing the geogrid



(g) Geogrid placement on the shear surface

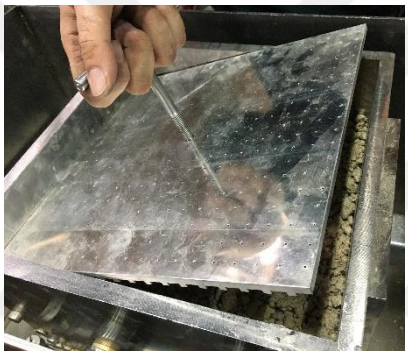


(h) Upper box fixing to the lower box

Figure 3.38. Views of specimen preparation stages for the large direct shear test of CFM

For all tests:

- After checking that the specimen's top surface was at the desired level, the porous top plate (Figure 3.39a) and loading plate (Figure 3.39b) were placed.
- The outer chamber was pulled from the sample preparation station towards the testing station and connected to the drive motor with the help of the separation pin (Figure 3.39c).
- Weights were placed on the hanger to give the desired normal stress by the loading mechanism. However, the loading arm was held by a screw attached to the rigid base, preventing the load transfer to the specimen (Figure 3.39d).



(a) Porous top plate placement



(b) Loading plate placement



(c) Attaching the separation pin



(d) Holding the loaded lever arm

Figure 3.39. Views of specimen preparation stages for the large direct shear test of all mixtures

3.3.6.2.2 Specimen Preparation Procedure for Saturated Tests

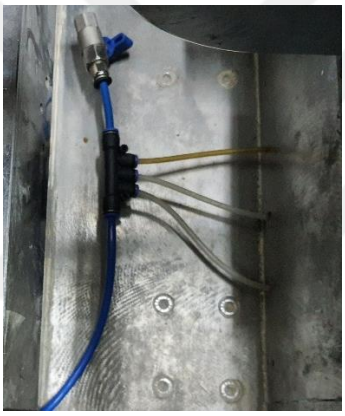
Eight tests were performed by saturating the specimens before direct shear. These include tests of S20-5, S20-15, S40-5, and S40-15 mixtures with geogrids with and without drainage property. Because the tests were for CFM interaction with geogrid, the specimen preparation procedure was the same as described in Section 3.3.6.2.1, (iv) CFM with geogrid. This section explains the additional applications and equipment used in the preparation procedure to saturate the specimen.

Attempts to saturate the specimens by submerging them in a water bath in large compression tests (Section 5.3) indicated that this procedure was not sufficient to provide complete saturation of the specimens in this study. Therefore, a system was designed to supply pressurized water from the bottom and sides of the boxes to the compacted specimen from a water reservoir positioned at 3.6 m above the specimen level (Figure 3.40).

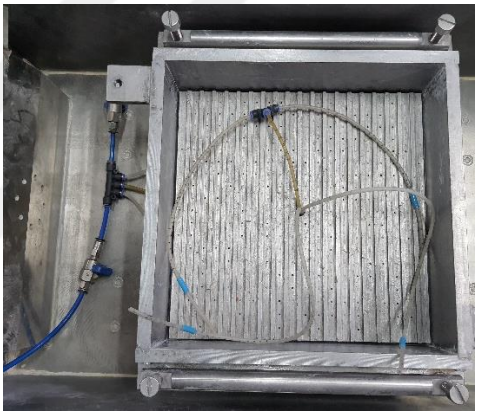


Figure 3.40. Water reservoir placed to supply pressurized water

Pressurized water from the reservoir having an approximately 35 kPa head reached the shear box with plastic pipes (2 mm inner diameter, 4 mm outer diameter) from the side of the lower box (Figure 3.41a) and the bottom of the serrated porous plate (Figure 3.41b). From the point they entered the box from the porous plate, the pipes were perforated with fine holes, and it was aimed for water to leak through the pipe length. Perforated pipes were placed at the bottom of the lower box and then from the corners towards the upper box, as seen in Figure 3.41c,d. The pipes rising from the corners were attached with the help of a separable joint at the shear level where the upper and lower box met. Separation of the pipes in the upper and lower boxes during shear was aimed not to create an additional force on the shear surface.



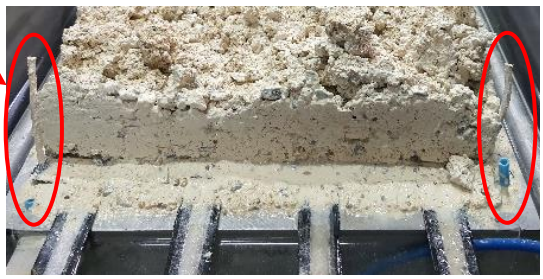
(a) Inflow of pressurized water



(b) Perforated pipes



(c) Positions of the perforated pipes at the bottom of the lower box and sides of the upper box



(d) Position of the perforated pipes at the corners of the upper box at the end of the shear test

Figure 3.41. Pressurized water supply system for the direct shear specimens

After the perforated pipes were placed, the specimen preparation process was started. The specimen was compacted in three levels in the lower box. Then geogrid and the upper box were placed as described in Section 3.3.6.2.1, (iv) CFM with geogrid.

A pressure sensor and two pipes were placed to monitor the water pressure within the compacted specimen 2 cm above the geogrid (4th soil level, Figure 3.36b). Pipes were utilized to monitor the water level inside the specimen, such as a piezometer (Figure 3.42). The water level equilibrium in the outer chamber with the saturated and de-aired piezometer pipes allowed the specimen to be evaluated in terms of its saturation (Figure 3.42). In addition, the water level during shear was also monitored to track the trend of excess pore water pressure within the specimen.

During the specimen placement, pipe ends were wrapped in filter paper and placed above the geogrid strips in one location and between the geogrid strips in the other. The horizontal and vertical positions of the piezometer pipes are shown in Figure 3.43. The pipes were placed along their lengths during the compaction of the specimen, reaching the two corners of the upper box and coming out from the edge of the loading plate.

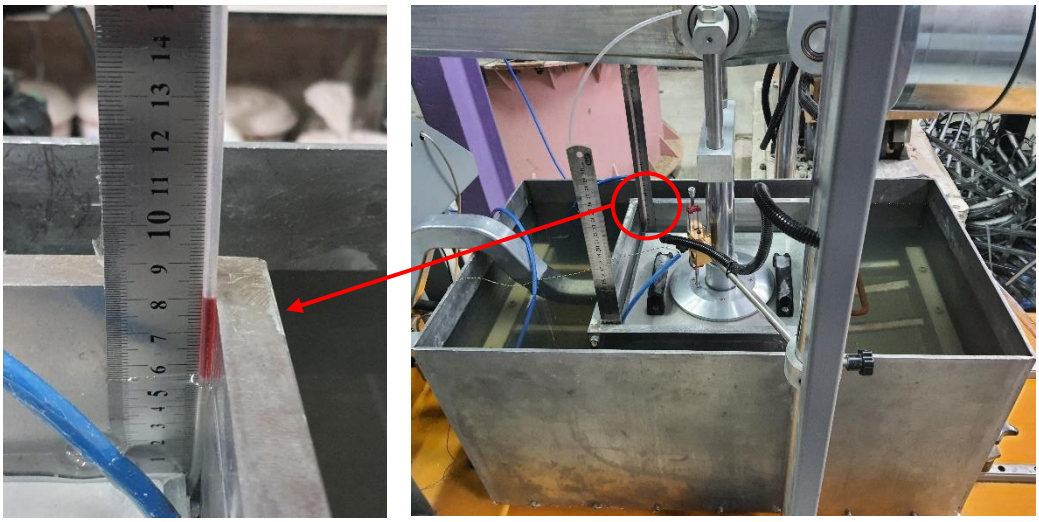


Figure 3.42. Monitoring the water level with piezometer pipes



(a) Horizontal positions of piezometer pipes (b) Vertical position of piezometer pipes

Figure 3.43. Positions of the piezometer pipes within the compacted specimen

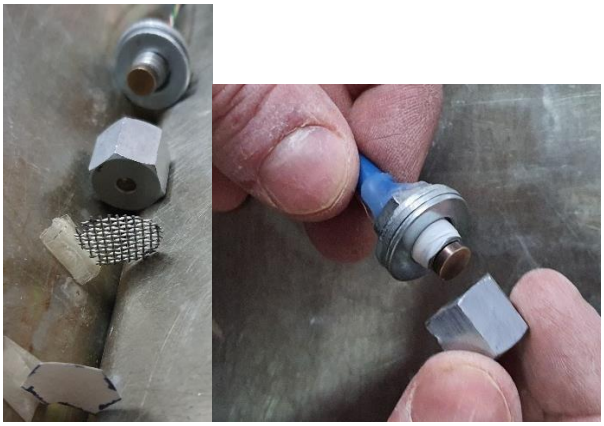
PDB miniature pressure transducer, having 200 kPa capacity, was used to monitor the water pressure within the specimen during settlement/saturation and direct shear stages (Figure 3.44a). The mechanism in Figure 3.44b was designed to cut off the contact of the sensor with the soil where it is placed. The transducer was placed in a casing that does not apply pressure on it. A metal mesh and filter paper were assembled to the casing so that only the pore water contacts the transducer (Figure 3.44b). The part of the transducers' cable to be compacted within the soil was covered with a protective sheath (Figure 3.44c).

The transducer was calibrated after the terminal connections were completed and connected to the data acquisition system. The setup shown in Figure 3.45 was used for this purpose. The transducer was assembled at the bottom of a pressure chamber, where the water pressure is controlled by a pressure supplier (oil/water constant pressure system, 1700 kPa capacity).

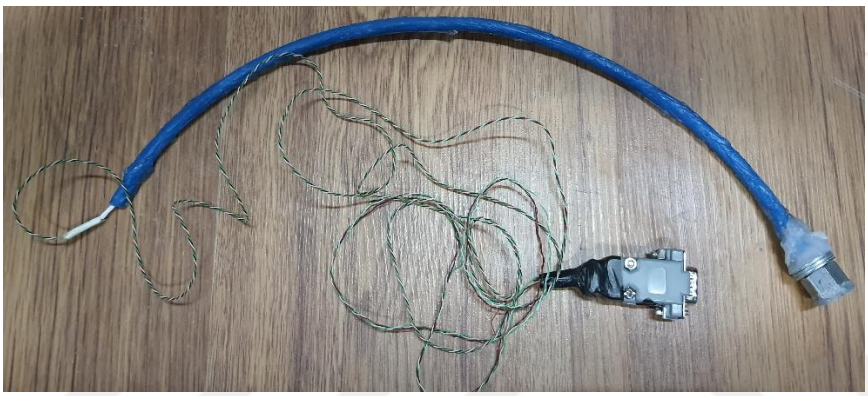
The placement of the transducer and its vertical position in the compacted soil is presented in Figure 3.46.



(a) Pressure transducer



(b) Mechanism transducer is placed



(c) The protective cover for the cable

Figure 3.44. Preparation of the pressure transducer to be placed in the specimen

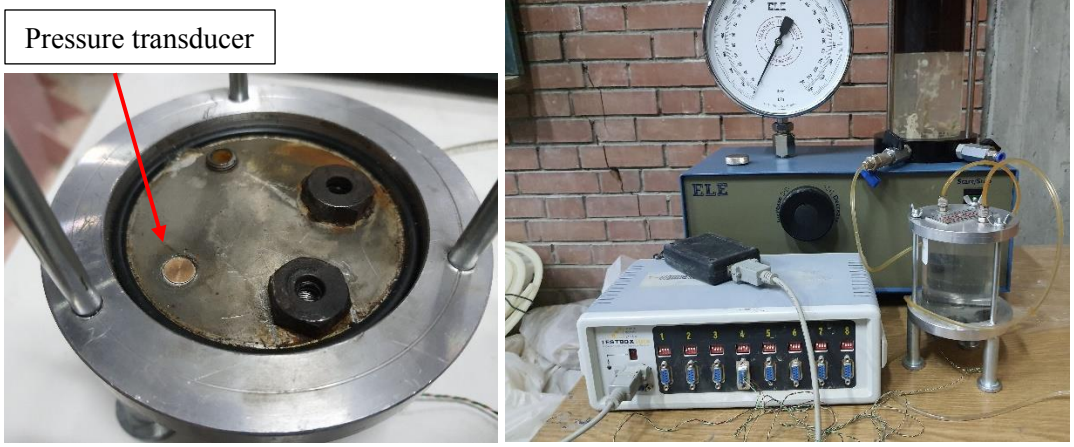


Figure 3.45. Calibration of the pressure transducer



Figure 3.46. (a) Placement, and (b) vertical position of the pressure transducer within the compacted specimen

The transducer was placed at the middle of the box in the compacted soil level just above the geogrid and shear surface. A dummy with the same dimensions as the transducer was used while the specimen was compacted. After the dummy was removed, it created a hole in the compacted specimen, and the sensor's casing was filled with water and placed so that there was no air inside (Figure 3.46a). The cable, covered with a protective sheath, was compacted within the fifth and sixth soil levels, and it came out from the edge of the loading plate, like piezometer pipes (Figure 3.42).

The porous top plate and loading plate were placed as in Figure 3.39, after the compaction of the specimen was completed. Water was given to the specimen from the bottom and sides of the box two minutes after the normal load was applied. Some of the incoming water seeped out from the sides of the shear box and began to fill the outer chamber. Once the outer chamber was filled, water was supplied continuously from the reservoir with the designed system for a couple of days, without allowing the water level to decrease in the outer chamber. Afterwards, the water supply was terminated, and the specimen was allowed to remain submerged in the outer chamber.

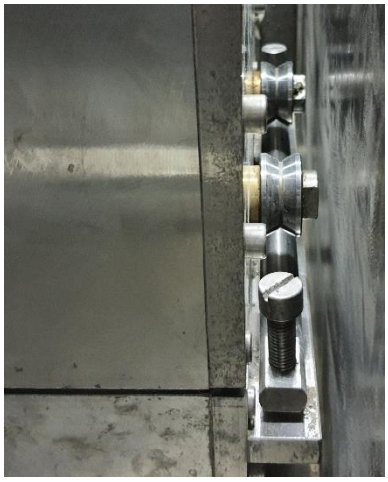
3.3.6.3 Test Procedure

3.3.6.3.1 Settlement Stage

- The vertical displacement gauge was placed on the loading plate. The vertical and horizontal displacement gauge and load cell values were reset from the control panel.
- The software was opened from the computer connected to the control panel. After the normal load information was entered, the communication of the software with the control panel was enabled.
- With the countdown in the software, the normal load was suddenly given to the specimen by lowering the screw holding the lever arm.
- After settlements were stabilized, data acquisition was completed.

3.3.6.3.2 Shearing Stage

- The outer screws connecting the upper and lower boxes were removed.
- Each screw, connected to the cylindrical bars on both sides of the lower box, was turned, and the upper box was lifted on rollers.
- Cylindrical bars were lowered back by unscrewing to avoid friction between the two boxes and geogrid during the test. Thus, the upper box was carried by the soil in it without the help of the rollers (Figure 3.47).



(a)



(b)

Figure 3.47. (a) The position of the rollers, and (b) the gap between the boxes just before the shear test

- Shear rate information was input into the software and the control panel.
- Positions of all measuring devices were checked, and their values were reset.
- The shear was started in synchronization with the computer connected to the control panel.
- The test was finished when the desired horizontal displacement value was reached. The data was recorded, the vertical load was removed, and the outer chamber was brought back to the sample preparation station to remove the tested specimen.

3.3.6.4 Test Program

After the specimen preparation and testing procedures were determined, the repeatability of the direct shear test results was evaluated with trial tests. After the reliability of the test results was verified, experiments were carried out within the scope of the test program, as presented in Table 3.5, Table 3.6, and Table 3.7.

Most direct shear tests in this study were performed with a shear rate of R=0.25 mm/min on specimens having an optimum moisture content and in-place dry

density equal to 95% of the standard Proctor compactness. Variant parameters for these tests included ten different soil mixtures, three different normal stresses (σ_n) as 55, 105, 155 kPa, and tests with and without geogrids, as seen in Table 3.5. Large direct shear tests performed in this group included three parts. In the first part, tests were carried out without geogrid to determine the direct shear resistance and strength parameters of ten soil mixtures. The second part tested the interaction of soils with varying properties and a geogrid having a drainage property (DG). In the third part, twelve tests were carried out using the same geocomposite as the second part tests, but by removing the geotextile in the drainage channels and using the back surface of the geogrid. A specific test in Table 3.5 was defined by the notation: '(Soil code)the magnitude of the initial normal stress-geogrid presence if there is any'. For geogrid presence, 'DG' denotes draining geogrid, and 'G' denotes geogrid. For instance, (S12-15)55-DG refers to the testing of CFM having FC=12% and PI=15%, under 55 kPa of initial normal stress, with the geogrid having a draining feature.

Eight tests were conducted by saturating the specimens before shear as described in Section 3.3.6.2.2. S20-5, S20-15, S40-5, and S40-15 soil mixtures were tested under 105 kPa of initial normal stress with a 0.25 mm/min shear rate, as shown in Table 3.6. A saturated test was defined by the notation: '(Soil code)the magnitude of the initial normal stress-geogrid presence if there is any(saturated specimen)'.

Three tests were performed with R=0.01 mm/min to evaluate the shear rate effect on specimens with a higher fines content and plasticity index (Table 3.7). S20-15, S30-15 and S40-15 soil mixtures were tested after compaction at their optimum moisture content and 95% of the standard Proctor dry densities. A specific test in Table 3.7 was defined by the notation: '(Soil code)the magnitude of the initial normal stress-geogrid presence if there is any(shear rate, R=0.01 mm/min)'.

Table 3.5. Direct shear test program (unsaturated specimens, R=0.25 mm/min)

Test code		'(Soil code)the magnitude of the initial normal stress-geogrid presence if there is any'					
Soil code	Normal stress σ_n, (kPa)	Test code	Geogrid presence	Test code	Geogrid presence	Test code	Geogrid presence
SW	55	(SW)55	Tests without geogrid	(SW)55-DG	Tests with geogrid having drainage property (DG)	-	Tests with geogrid by removing the geotextile in drainage channels (G)
	105	(SW)105		(SW)105-DG			
	155	(SW)155		(SW)155-DG			
SP	55	(SP)55		(SP)55-DG			
	105	(SP)105		(SP)105-DG			
	155	(SP)155		(SP)155-DG			
S12-5	55	(S12-5)55		(S12-5)55-DG			
	105	(S12-5)105		(S12-5)105-DG			
	155	(S12-5)155		(S12-5)155-DG			
S12-15	55	(S12-15)55		(S12-15)55-DG			
	105	(S12-15)105		(S12-15)105-DG			
	155	(S12-15)155		(S12-15)155-DG			
S20-5	55	(S20-5)55		(S20-5)55-DG		(S20-5)55-G	
	105	(S20-5)105		(S20-5)105-DG		(S20-5)105-G	
	155	(S20-5)155		(S20-5)155-DG		(S20-5)155-G	
S20-15	55	(S20-15)55		(S20-15)55-DG		(S20-15)55-G	
	105	(S20-15)105		(S20-15)105-DG		(S20-15)105-G	
	155	(S20-15)155		(S20-15)155-DG		(S20-15)155-G	
S30-5	55	(S30-5)55		(S30-5)55-DG		-	
	105	(S30-5)105		(S30-5)105-DG			
	155	(S30-5)155		(S30-5)155-DG			
S30-15	55	(S30-15)55		(S30-15)55-DG			
	105	(S30-15)105		(S30-15)105-DG			
	155	(S30-15)155		(S30-15)155-DG			
S40-5	55	(S40-5)55		(S40-5)55-DG		(S40-5)55-G	
	105	(S40-5)105		(S40-5)105-DG		(S40-5)105-G	
	155	(S40-5)155		(S40-5)155-DG		(S40-5)155-G	
S40-15	55	(S40-15)55		(S40-15)55-DG		(S40-15)55-G	
	105	(S40-15)105		(S40-15)105-DG		(S40-15)105-G	
	155	(S40-15)155		(S40-15)155-DG		(S40-15)155-G	

Table 3.6. Direct shear test program (saturated specimens, R=0.25 mm/min)

Test code		'(Soil code)the magnitude of the initial normal stress-geogrid presence if there is any(saturated specimen)'			
Soil code	Normal stress σ_n, (kPa)	Test code	Geogrid presence	Test code	Geogrid presence
S20-5	105	(S20-5)105-DG(sat)	Tests with geogrid having drainage property (DG)	(S20-5)105-G(sat)	Tests with geogrid by removing the geotextile in drainage channels (G)
S20-15	105	(S20-15)105-DG(sat)		(S20-15)105-G(sat)	
S40-5	105	(S40-5)105-DG(sat)		(S40-5)105-G(sat)	
S40-15	105	(S40-15)105-DG(sat)		(S40-15)105-G(sat)	

Table 3.7. Direct shear test program (unsaturated specimens, R=0.01 mm/min)

Test code		'(Soil code)the magnitude of the initial normal stress-geogrid presence if there is any(shear rate, R=0.01 mm/min)'	
Soil code	Normal stress σ_n, (kPa)	Test code	Geogrid presence
S20-15	55	(S20-15)55-G(R=0.01)	Tests with geogrid by removing the geotextile in drainage channels (G)
S30-15	155	(S30-15)155-DG(R=0.01)	Tests with geogrid having drainage property (DG)
S40-15	105	(S40-15)105-DG(R=0.01)	

CHAPTER 4

INDEX AND HYDRAULIC CONDUCTIVITY TEST RESULTS

This chapter presents the results of the index, specific surface area, and hydraulic conductivity tests of the soil mixtures prepared in the scope of this study. It also discusses classifying soil mixtures according to widely used classification systems and highlights the shortcomings of these systems for mixed soils. It includes the main findings of the geotechnical properties of the CFM having behavioral transition and the determination of the relationship between the specific surface area, liquid limit, and hydraulic conductivity. In addition, this chapter presents the identification of the threshold fines content that governs the behavioral transitions and compares some measured results with empirical correlations.

4.1 Classification of Soil Mixtures

SW, SP soil mixtures and eight CFM were classified according to Unified Soil Classification System, USCS (ASTM D2487-17), European Soil Classification System, ESCS (EN ISO 14688-2:2018), American Association of State Highway and Transportation Officials, AASHTO M145-91 (2017), and British Standard, BS 1377:1990. Soil descriptions and symbols are presented in Table 4.1.

According to the widely used soil classification systems, sharp material transition boundaries are defined between gravel-sand and sand-fine particle sizes, and the naming is made based on the dominant grain size. Therefore, there are some limitations and drawbacks to the classification of intermediate or transitional soils in terms of representing the contributions of coarse and fine fractions on mechanical, hydraulic, and compressive responses.

Table 4.1. Classification of the prepared soil mixtures

Soil code	USCS (ASTM D2487-17)		ESCS (EN ISO 14688-2:2018)		AASHTO M145-91 (2017)		BS 1377:1990	
	Definition	Symbol	Definition	Symbol	Definition	Symbol	Definition	Symbol
SW	Well-graded SAND with gravel	SW	Sandy well-graded GRAVEL	saGrW	Gravel and sand	A-1-a	Well-graded gravel	GW
SP	Poorly-graded SAND with gravel	SP	Uniformly-graded GRAVEL	GrU	Gravel and sand	A-1-a	Poorly-graded gravel	GP
S12-5	Silty clayey SAND with gravel	SC-SM	Sandy silty clayey GRAVEL	sasiclGr	Gravel and sand	A-1-a	Silty or clayey gravel	G-F
S12-15	Clayey SAND with gravel	SC	Sandy clayey GRAVEL	saclGr	Clayey gravel and sand	A-2-6	Silty or clayey gravel	G-F
S20-5	Silty clayey SAND with gravel	SC-SM	Sandy silty clayey GRAVEL	sasiclGr	Gravel and sand	A-1-b	Very silty or clayey gravel	GF
S20-15	Clayey SAND with gravel	SC	Sandy clayey GRAVEL	saclGr	Clayey gravel and sand	A-2-6	Very silty or clayey gravel	GF
S30-5	Silty clayey SAND with gravel	SC-SM	Gravelly silty clayey SAND	grsiclSa	Silty gravel and sand	A-2-4	Very silty or clayey gravel	GF
S30-15	Clayey SAND with gravel	SC	Gravelly clayey SAND	grclSa	Clayey gravel and sand	A-2-6	Very silty or clayey gravel	GF
S40-5	Silty clayey SAND with gravel	SC-SM	Gravelly silty clayey SAND	grsiclSa	Silty soils	A-4	Gravelly silt or gravelly clay	FG
S40-15	Silty SAND with gravel	SM	Gravelly silty SAND	grsiSa	Clayey soils	A-7-6	Gravelly silt or gravelly clay	FG

SW and SP, two laboratory-prepared soil mixtures, were defined as well-graded and poorly-graded sands with gravel, respectively, according to USCS. ESCS defined the same mixtures as sandy well-graded gravel, and uniformly-graded gravel (saGrW, GrU) due to the differences in the transition between sand and gravel sizes in these two classification systems (Table 4.1). This result was expected as the mixtures' target particle size distributions were determined to be near these transition

zones. Similarly, 'S20-15' soil mixture (FC=20% and PI=15%) was named as 'clayey sand with gravel' according to the USCS; however, ESCS defined the same mixture as 'sandy clayey gravel'.

In addition to the dominant particle size when describing CFM, secondary definitions have been added to the name and symbolization. The insufficiency of the classification systems for identifying dominant characteristics of some prepared soil mixtures can be seen in Table 4.1. For instance, 'S30-5' was defined as 'silty clayey sand with gravel' according to USCS, which gives little information about the dominant characteristics of the soil.

Because in USCS and ESCS, the primary name was defined as whether more than 50% of the soil (by dry weight) consists of fine or coarse particles, dominant properties of all CFM in this study (up to 40% FC) were considered to be governed by coarse particles with these two classification systems. As this boundary is 35% in BS 1377:1990, the classification and the name of S40-5 and S40-15 were primarily governed by fines, whereas the names of all other CFM are governed by coarse particles (Table 4.1).

CFM were also classified according to the Revised Soil Classification System (RSCS) suggested by Park and Santamarina (2017) in Table 4.2. This classification system suggests a gravimetric-volumetric analysis by considering the intermediate zones between the material transitions. Triangular classification charts were prepared for each CFM according to the thirteen classification boundaries, depending on the packing conditions of the mixtures (Figure 4.1 and Figure 4.2).

Table 4.2. Classification of the prepared soil mixtures according to the Revised Soil Classification System (RSCS) suggested by Park and Santamarina (2017)

Soil code	Definition	Symbol	Controlling fraction	
			Mechanical	Fluid
SW	Clean gravel-sand mixture	GS(S)	Gravel & sand	Sand
SP	Clean gravel-sand mixture	GS(S)	Gravel & sand	Sand
S12-5	Transitional mixture	GSF(F)	Gravel-sand-fines	Fines
S12-15	Transitional mixture	GF(F)	Gravel & fines	Fines
S20-5	Transitional mixture	GF(F)	Gravel & fines	Fines
S20-15	Transitional mixture	GF(F)	Gravel & fines	Fines
S30-5	Fine-grained soil	F(F)	Fines	Fines
S30-15	Fine-grained soil	F(F)	Fines	Fines
S40-5	Fine-grained soil	F(F)	Fines	Fines
S40-15	Fine-grained soil	F(F)	Fines	Fines

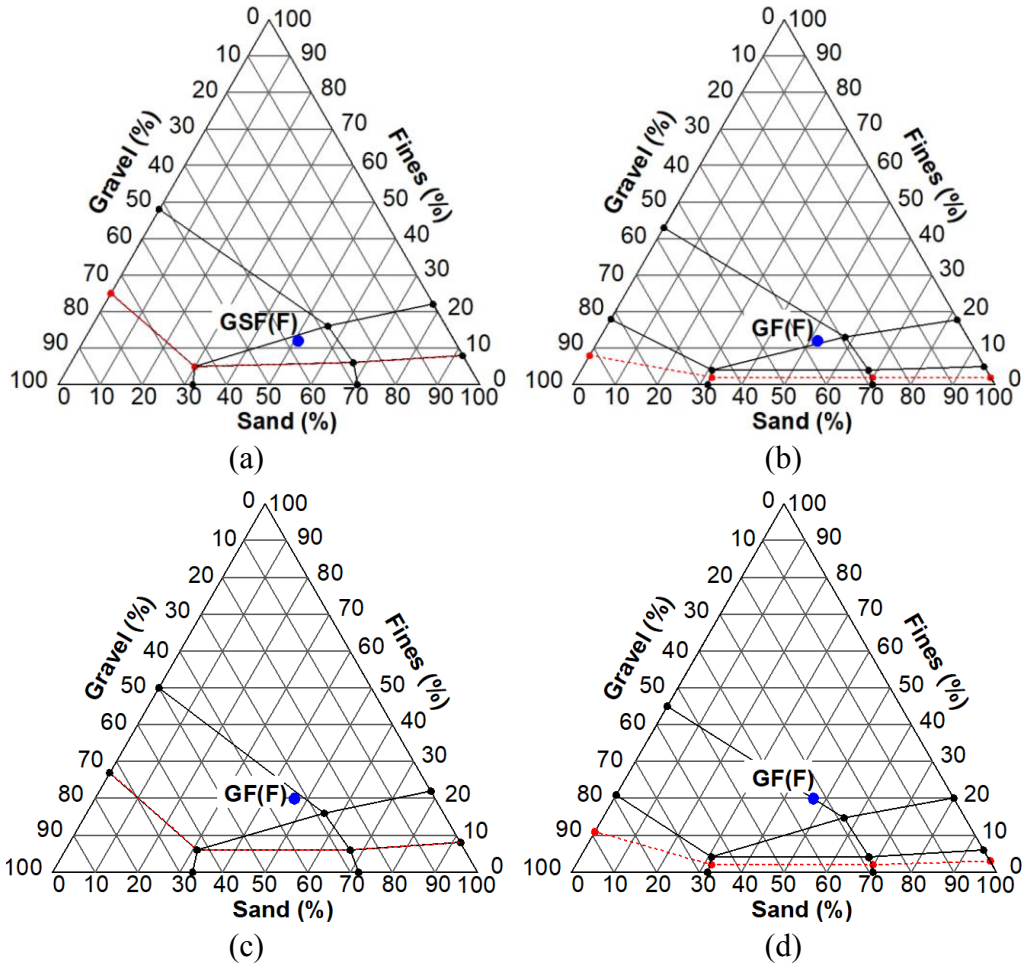


Figure 4.1. Classification charts for (a) S12-5, (b) S12-15, (c) S20-5, (d) S20-15 according to RSCS of Park and Santamarina (2017)

In the RSCS, governing fractions for mechanical and hydraulic behavior are considered separately. For instance, S12-5 (having gravel fraction, F_G=36%; sand fraction, F_S=52% and fine fraction, F_F=12%) was classified as a 'transitional mixture, GSF(F)' where mechanical properties are governed by gravel-sand-fine and hydraulic properties are governed by fines (Figure 4.1a). As the particle packing conditions change, boundaries affecting the mechanical control and flow properties also change, according to the RSCS of Park and Santamarina (2017).

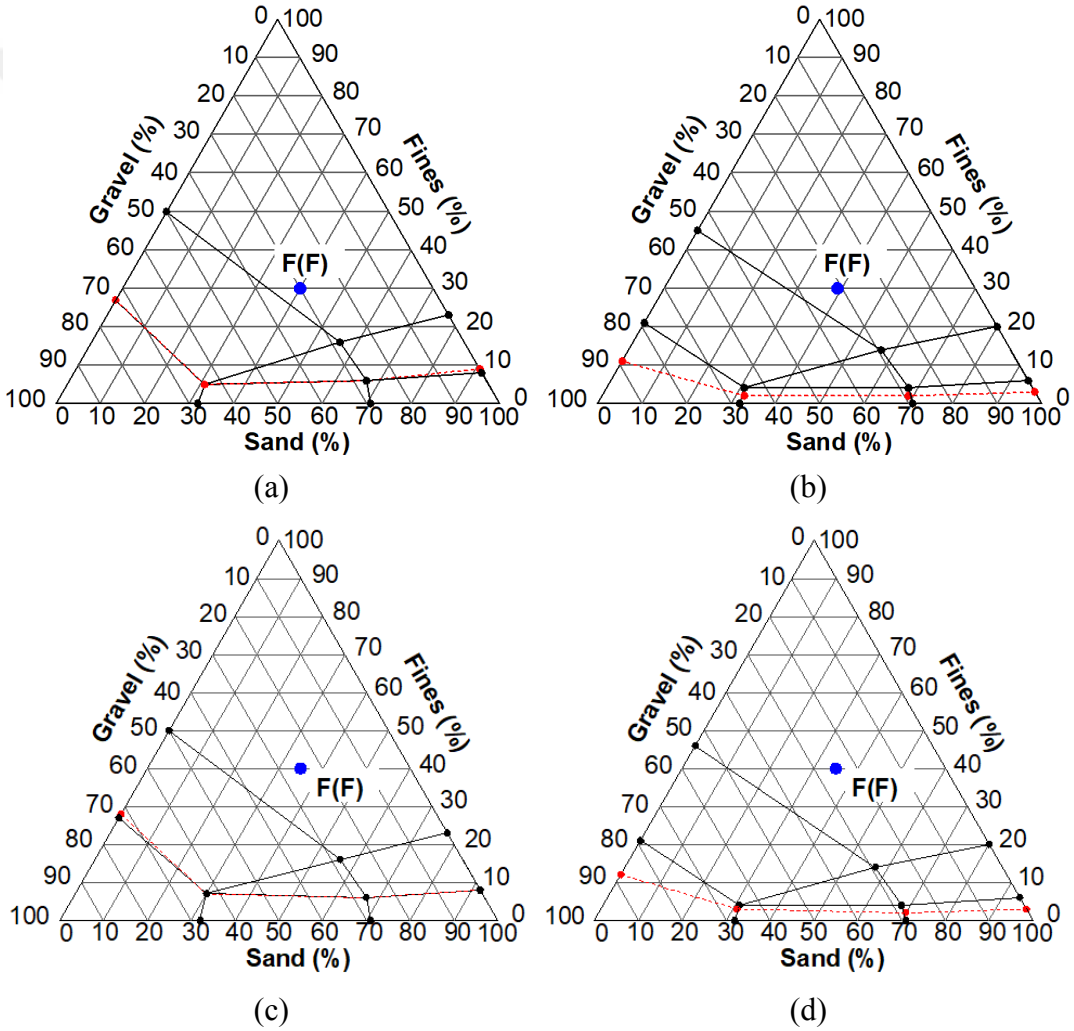


Figure 4.2. Classification charts for (a) S30-5, (b) S30-15, (c) S40-5, (d) S40-15 according to RSCS of Park and Santamarina (2017)

Although the hydraulic behavior of all CFM was classified to be governed by fines (Table 4.2), fines content thresholds that control hydraulic properties could be viewed from the prepared charts (Figure 4.1 and Figure 4.2). Accordingly, CFM having PI=5% had threshold fines content ranging between 5% and 28%, whereas it was between 2% and 12% for CFM having PI=15%. According to the RSCS, an increase in the plasticity index led to a significant reduction in the value of threshold FC, which governs the flow properties. For the mechanical response, behavioral change occurs between 20%-30% fines content according to this classification system. S20-5 and S20-15 are transitional mixtures where mechanical behavior is controlled by gravel and fines. However, S30-5 and S30-15 are mixtures whose mechanical behavior is controlled by fines (Table 4.2). This result appears to be in agreement with previous research findings regarding the compressibility and strength behavior of soil mixtures (Georgiannou et al., 1990; Monkul and Ozden, 2007; Olmez and Ergun, 2008).

4.2 Index Test Results

CFM properties were determined with pre-targeted parameters to represent the behavioral transition between coarse and fine-dominated soils. Atterberg limits for soil samples passing through No. 40 sieve, fine contents, and particle size distributions of the mixtures were essential criteria in this context. Therefore, these have been presented in Section 3.1.3, while describing the methodology of the soil mixture preparation. In addition to the gradation curves of the soil mixtures presented in Figure 3.5, parameters for particle size distribution and average specific gravity results of the total mixtures are presented in Table 4.3.

Minimum and maximum dry density and void ratios of SW and SP soils (according to vibratory table method for granular soils, ASTM D4253-16) and standard Proctor test results for CFM are presented in Table 4.4 and Table 4.5, respectively.

Table 4.3. Specific gravities of CFM and parameters related to the particle size distribution

Soil code	Fines content (%)	*Sand content (%)	*Gravel content (%)	Average specific gravity, G_T	d_{10}, mm	d_{50}, mm	Coefficient of curvature, C_c	Coefficient of uniformity, C_u	*Clay fraction CF (%)	Activity (PI/CF)
SW	0	63.1	36.7	2.67	0.271	3.4	1.9	16	-	-
SP		60.5	39.5	2.67	2.327	4.2	0.9	2	-	-
S12-5	12	51.4	36.5	2.66	0.027	2.9	3.0	154	3.1	1.6
S12-15		51.5	36.2	2.66	0.0065	2.9	12.4	638	5.3	2.8
S20-5	20	47.3	32.5	2.66	0.0125	2.3	2.2	286	3.9	1.3
S20-15		46.6	32.9	2.66	0.0022	2.3	12.4	1626	8.7	1.7
S30-5	30	39.7	30.4	2.66	0.0037	1.1	0.6	811	5.6	0.9
S30-15		38.8	30.8	2.65	0.0018	1.1	1.2	1667	12.0	1.3
S40-5	40	35.2	24.9	2.66	0.0031	0.4	0.1	616	5.9	0.9
S40-15		34.7	24.9	2.64	0.0015	0.4	0.005	1272	16.6	0.9

* According to boundaries defined in USCS

Table 4.4. Maximum and minimum dry densities of SW and SP soil mixtures

Soil code	Min. dry density, ρ_{min} (g/cm^3)	Max. dry density, ρ_{max} (g/cm^3)	Min. void ratio, e_{min}	Max. void ratio, e_{max}
SW	1.78	2.08	0.28	0.50
SP	1.54	1.76	0.52	0.73

Table 4.5. Standard Proctor test results of CFM

Soil code	w_{opt} (%)	Max. dry unit weight, $\gamma_{d,max}$ (kN/m^3)	95% of $\gamma_{d,max}$ (kN/m^3)
S12-5	7.2	21.5	20.4
S12-15	7.4	20.7	19.7
S20-5	6.8	21.8	20.7
S20-15	9.8	20.0	19.0
S30-5	7.8	20.9	19.9
S30-15	11.4	19.1	18.1
S40-5	8.2	20.3	19.3
S40-15	14.2	18.2	17.3

In common geotechnical practice, LL is generally determined on the soil portion passing 0.425 mm (No. 40 sieve). LL of the soil fraction passing 0.075 mm (No. 200 sieve) may not even be available. Stark et al. (2005) proposed Equation 4.1 to predict LL values of ball-milled samples (i.e., passing No. 200 sieve) of heavily overconsolidated clays, claystone, shale, and mudstone, from LL measured from soil portion passing No. 40 sieve in accordance with ASTM D4318-17. In case there is no data, authors used this correlation on samples of heavily overconsolidated clays, claystone, shale, and mudstone to correlate their shear strength equations. By using Equation 4.1, ball-milled LL values were calculated just to evaluate the applicability and the prediction capability of the proposed correlation of Stark et al. (2005) for CFM in case there is no LL data obtained for soil portion passing No. 200 sieve. In further analysis and evaluation in this study, measured results of LL by soil passing No. 40 sieve and No. 200 sieve were used, as the values are presented in Table 4.6.

$$\frac{Ball-milled\ derived\ LL}{ASTM\ derived\ LL} = 0.003(ASTM\ derived\ LL) + 1.23 \quad (4.1)$$

From the soil products used to prepare soil mixtures, non-plastic silt, kaolin, and bentonite included completely fine particles. In other words, all of these soil products passed through both No. 40 and No. 200 sieves. However, fine sand portion of CFM

was obtained by sieving the SW soil through No. 40 sieve. Because SW soil mixture did not include any fines, fine sand portion had particles smaller than 0.425 mm (No. 40 sieve) and larger than 0.075 mm (No. 200 sieve). Therefore, proportional distribution of soil components passing through No. 40 and No. 200 sieves differs. Soil fractions constituting the samples, Atterberg limits, and prediction of Stark et al. (2005) correlation for ball-milled derived liquid limit are presented in Table 4.6.

Table 4.6. Atterberg limits of CFM for portions passing No. 40 and No. 200 sieves

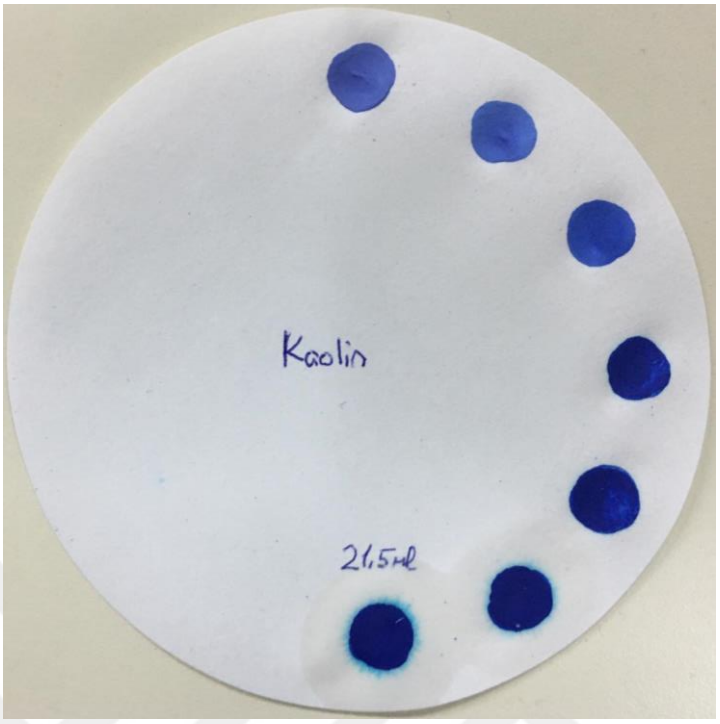
Soil code	Sample finer than	Fractions constituting the testing sample (%)				Atterberg limits (%)			Stark et al. (2005) prediction (%)
		Fine sand	Silt	Kaolin	Bentonite	LL	PL	PI	Ball-milled derived LL
S12-5	No. 40	55.9	16.5	27.6	0.0	19	14	5	24
	No. 200	0.0	37.5	62.5	0.0	34	24	10	
S20-5	No. 40	40.9	37.2	21.9	0.0	19	14	5	24
	No. 200	0.0	63.0	37.0	0.0	28	21	7	
S30-5	No. 40	28.3	45.4	26.3	0.0	22	17	5	29
	No. 200	0.0	63.3	36.7	0.0	27	20	7	
S40-5	No. 40	20.7	57.9	21.4	0.0	22	17	5	29
	No. 200	0.0	73.0	27.0	0.0	25	19	6	
S12-15	No. 40	55.8	0.0	40.6	3.6	31	16	15	41
	No. 200	0.0	0.0	91.8	8.2	69	29	40	
S20-15	No. 40	40.9	0.0	56.0	3.1	34	19	15	45
	No. 200	0.0	0.0	94.7	5.3	54	28	26	
S30-15	No. 40	28.5	0.0	68.6	3.0	40	25	15	54
	No. 200	0.0	0.0	95.8	4.2	52	32	20	
S40-15	No. 40	20.7	0.0	76.6	2.7	42	27	15	57
	No. 200	0.0	0.0	96.6	3.4	50	33	17	
Kaolin	-	0.0	0.0	100.0	0.0	48	34	14	-
Bentonite	-	0.0	0.0	0.0	100.0	499	40	459	-

4.3 Methylene Blue Spot Test Results

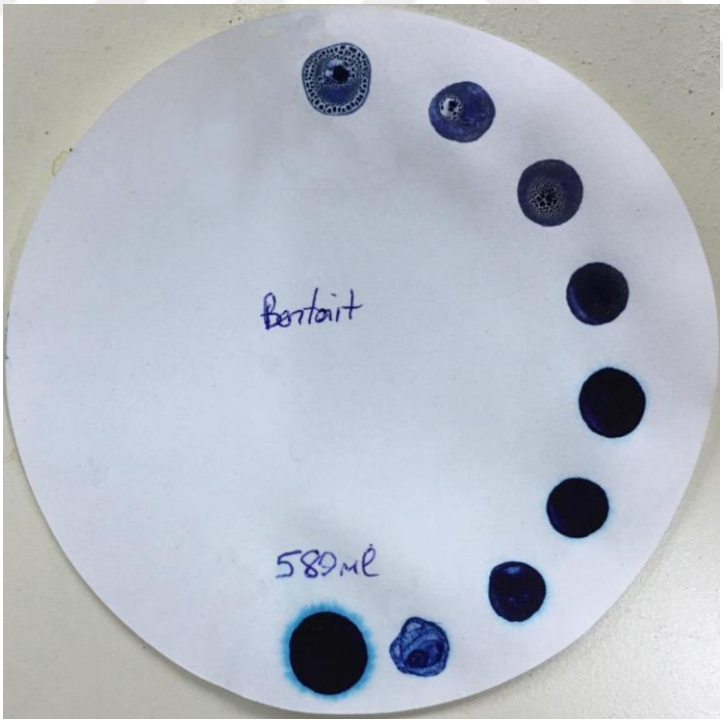
Methylene Blue (MB) spot test results and calculated specific surface area (SSA) values according to Equation 3.2 are presented in Table 4.7. SSA results obtained by samples passing through No. 40 and No. 200 sieves differ depending on the proportional distribution of components because 10 g of dry soil sample was tested in each MB trial and the unit of SSA is m^2/kg. As the amount of cohesive fine particles and associated Atterberg limits of samples changed, measured SSA values also changed. The appearance of the permanent blue halo around the soil suspension spot on filter papers for kaolin, bentonite, S12-5, and S40-15 can be seen in Figure 4.3 and Figure 4.4.

Table 4.7. Methylene Blue spot test results for CFM portions passing No. 40 and No. 200 sieves, kaolin, and bentonite

Soil code	Sample finer than	Atterberg limits (%)			MB spot test results	
		LL	PL	PI	Adsorbed MB (mL)	SSA (m^2/kg)
S12-5	No. 40	19	14	5	7.0	8563
	No. 200	34	24	10	14.0	17126
S20-5	No. 40	19	14	5	5.5	6728
	No. 200	28	21	7	9.0	11010
S30-5	No. 40	22	17	5	7.0	8563
	No. 200	27	20	7	9.0	11010
S40-5	No. 40	22	17	5	5.5	6728
	No. 200	25	19	6	6.5	7952
S12-15	No. 40	31	16	15	30.0	36699
	No. 200	69	29	40	62.0	75845
S20-15	No. 40	34	19	15	29.5	36088
	No. 200	54	28	26	52.0	63612
S30-15	No. 40	40	25	15	33.5	40981
	No. 200	52	32	20	45.0	55049
S40-15	No. 40	42	27	15	31.5	38534
	No. 200	50	33	17	38.0	46486
Kaolin	No. 200	48	34	14	21.5	26301
Bentonite	No. 200	499	40	459	580.0	709519

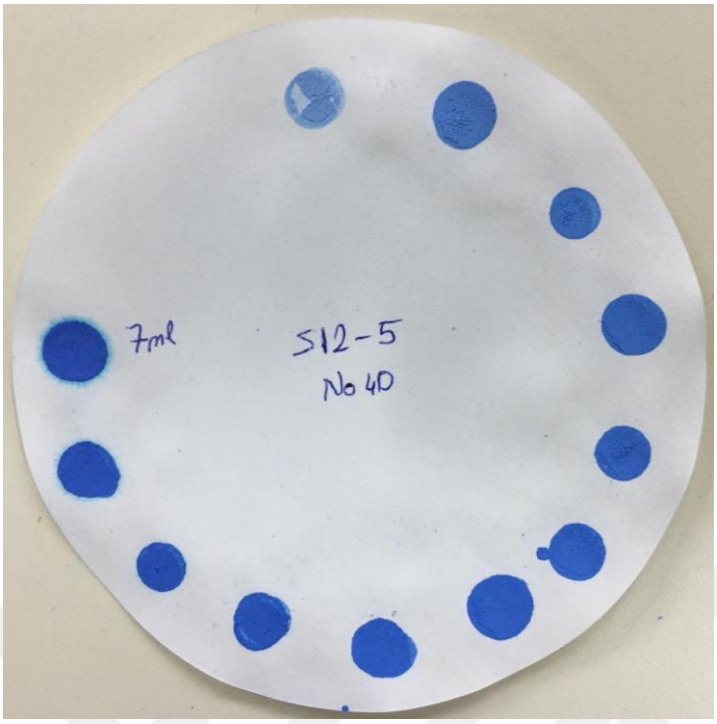


(a)

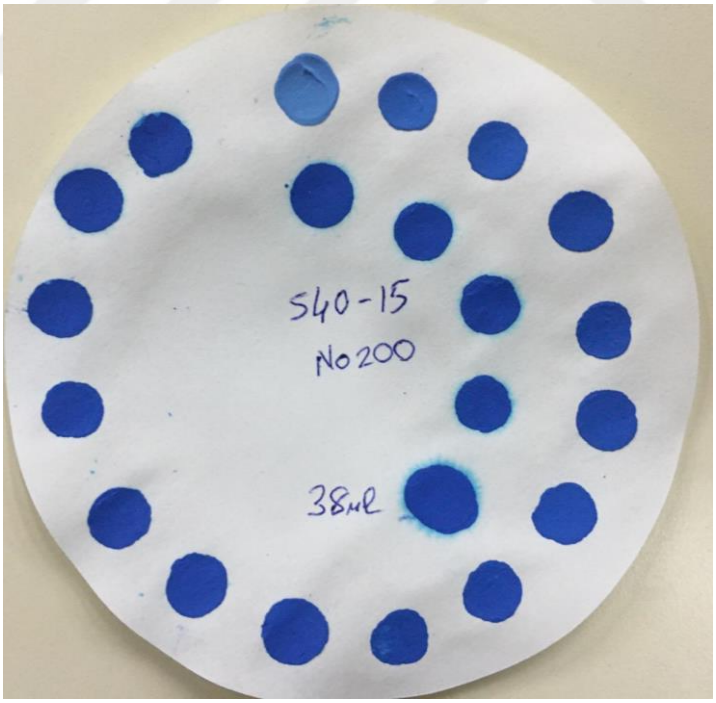


(b)

Figure 4.3. Methylene Blue spot test results for (a) kaolin, (b) bentonite



(a)



(b)

Figure 4.4. Methylene Blue spot test results for (a) S12-5 for sample finer than No. 40 sieve, (b) S40-15 for sample finer than No. 200 sieve

4.4 Saturation of CFM Specimens

Cylindrical CFM specimens (70 mm in diameter and 140 mm in height) were prepared for hydraulic conductivity tests as described in Section 3.3.2.2.2. Although specimen preparation was standardized to obtain CFM with the same physical properties, small variations of the resultant moisture content and dry density values were observed between the different specimens of the same coarse-fine mixture. This affected the void ratio and physical conditions of the specimens, even though to a small extent. Therefore, three specimens for each CFM were used for the calculations of phase parameters. Global void ratio and degree of saturation of soil mixtures' initial states were calculated with the equations of phase relations (Equations 4.2 and 4.3) for each CFM. Results are presented in Table 4.8.

CFM specimens were saturated by back pressure prior to testing by applying B value ≥ 0.94 criteria for the finalization of the saturation. Changes in the height of the specimens and changes in water volume during saturation were monitored and recorded during the process. Equation 4.4 (also presented in ASTM D4767-11) was used for the calculation of saturated void ratios. Interfine and intergranular void ratios, which are presented in Equation 2.1 and Equation 2.2, respectively, were calculated as representative parameters for the fine-grained or coarse-grained dominated behavior. Intergranular and interfine void ratios of the CFM for its state after saturation are presented in Table 4.8.

$$S_r(\%) = \frac{w \,.\, G_T}{e} . 100 \tag{4.2}$$

$$e = \frac{G_T \,.\, \rho_w}{\rho_{dry}} - 1 \tag{4.3}$$

$$\Delta V_{sat} = 3V_0 \frac{\Delta H_s}{H_0} \tag{4.4}$$

where,

S_r : Degree of saturation

w : Moisture content of the specimen

G_T : Average specific gravity of the soil mixture

e : Global void ratio

ρ_w : Density of the water

ρ_{dry} : Dry density of the soil specimen

ΔV_{sat} : Change in volume of the specimen during saturation

V_0 : Initial volume of the specimen

ΔH_s : Change in height of the specimen during saturation

H_0 : Initial height of the specimen

Table 4.8. Void ratios before and after saturation

Soil code	Specimen no	Initial state		State after saturation		
		Global void ratio, e_0	Degree of saturation, $S_{r(in)}$ (%)	Global void ratio, e	Intergranular void ratio, e_s	Interfine void ratio, e_f
S12-5	1	0.279	67.5	0.270	0.448	2.203
	2	0.282	72.6	0.275	0.453	2.237
	3	0.281	73.0	0.270	0.448	2.203
S12-15	1	0.329	65.5	0.317	0.502	2.582
	2	0.329	69.6	0.317	0.502	2.582
	3	0.322	59.9	0.313	0.497	2.551
S20-5	1	0.263	68.5	0.254	0.575	1.239
	2	0.261	68.6	0.250	0.570	1.221
	3	0.265	63.7	0.252	0.573	1.231
S20-15	1	0.373	75.4	0.359	0.707	1.756
	2	0.374	72.4	0.372	0.724	1.819
	3	0.377	76.3	0.360	0.708	1.760
S30-5	1	0.327	79.0	0.320	0.899	1.042
	2	0.331	72.2	0.331	0.914	1.077
	3	0.322	69.5	0.307	0.881	1.001
S30-15	1	0.446	77.7	0.427	1.054	1.396
	2	0.457	79.5	0.445	1.081	1.456
	3	0.429	76.1	0.410	1.031	1.342
S40-5	1	0.373	64.7	0.354	1.276	0.864
	2	0.361	60.4	0.345	1.262	0.843
	3	0.363	62.3	0.343	1.258	0.837
S40-15	1	0.525	73.8	0.508	1.541	1.251
	2	0.505	72.9	0.485	1.502	1.195
	3	0.502	75.9	0.479	1.493	1.180

4.5 Hydraulic Conductivity Test Results

4.5.1 Rigid Wall Hydraulic Conductivity Test Results

Tests for SW and SP soil mixtures were performed with a constant head permeameter system, and saturated hydraulic conductivities were calculated by using Darcy's Law under the form presented in Equation 4.5. Hydraulic conductivity test results, including average values and coefficient of variations (COV% = standard deviation/mean) for each soil mixture, are presented in Table 4.9.

Table 4.9. Hydraulic conductivity test results of SW and SP soil mixtures

Soil code	In-placed dry density (g/cm^3)	Test no	Hydraulic conductivity, k_{sat}		
			Test results (cm/s)	Average (cm/s)	COV. (%)
SW	1.98	1	6.07×10^{-2}	8.36×10^{-2}	50.9
		2	6.09×10^{-2}		
		3	6.14×10^{-2}		
		4	5.23×10^{-2}		
		5	5.23×10^{-2}		
		6	5.18×10^{-2}		
		7	6.81×10^{-2}		
		8	6.10×10^{-2}		
		9	6.97×10^{-2}		
		10	1.55×10^{-1}		
		11	1.77×10^{-1}		
		12	1.33×10^{-1}		
SP	1.67	1	7.22×10^{-1}	2.23	43.3
		2	7.20×10^{-1}		
		3	7.23×10^{-1}		
		4	2.67×10^{0}		
		5	2.66×10^{0}		
		6	2.68×10^{0}		
		7	2.68×10^{0}		
		8	2.17×10^{0}		
		9	3.04×10^{0}		
		10	1.86×10^{0}		
		11	3.34×10^{0}		
		12	3.48×10^{0}		

$$k = \frac{\Delta Q . L}{A . \Delta h . \Delta t} \quad (4.5)$$

where,

k : Hydraulic conductivity

ΔQ : Quantity of flow for a given time interval

L : Length of the specimen

A : Cross-sectional area of the specimen

Δh : Average head loss across the specimen

Δt : Time interval

4.5.2 Flexible Wall Hydraulic Conductivity Test Results

Hydraulic conductivity tests were performed as described in Section 3.3.2.2.3 after the saturation of CFM specimens. Because Method A (Constant Head) of ASTM D5084-16 was applied in testing, Equation 4.5 was used to calculate the saturated hydraulic conductivities of CFM.

Hydraulic conductivity test results, including the average values and coefficient of variations (COV% = standard deviation/mean) for each CFM, are presented in Table 4.10.

Table 4.10. Hydraulic conductivity test results of CFM

Fines content (%)	PI (%)	*w (%)	*Dry unit weight (kN/m^3)	Hydraulic conductivity, k_{sat}		
				Test results (cm/s)	Average (cm/s)	COV. (%)
12	5	7.2	20.4	5.58×10^{-4} 7.60×10^{-4} 7.91×10^{-4} 1.03×10^{-3} 1.19×10^{-3} 1.41×10^{-3} 1.62×10^{-3}	1.05×10^{-3}	33.5
	15	7.4	19.7	2.04×10^{-5} 2.57×10^{-5} 3.51×10^{-5} 3.66×10^{-5} 4.28×10^{-5} 4.76×10^{-5} 5.43×10^{-5}	3.75×10^{-5}	29.3
20	5	6.8	20.7	2.76×10^{-6} 3.20×10^{-6} 3.30×10^{-6} 1.27×10^{-5} 8.71×10^{-5} 2.67×10^{-4}	6.28×10^{-5}	153.5
	15	9.8	19.0	4.28×10^{-6} 4.34×10^{-6} 1.09×10^{-5} 1.16×10^{-5} 1.18×10^{-5} 2.91×10^{-5}	1.20×10^{-5}	69.0
30	5	7.8	19.9	3.16×10^{-5} 4.53×10^{-5} 4.63×10^{-5} 6.03×10^{-5} 7.57×10^{-5}	5.19×10^{-5}	28.9
	15	11.4	18.1	1.26×10^{-6} 1.73×10^{-6} 4.28×10^{-6} 4.40×10^{-6}	2.91×10^{-6}	49.1
40	5	8.2	19.3	1.96×10^{-5} 2.22×10^{-5} 3.11×10^{-5}	2.43×10^{-5}	20.3
	15	14.2	17.3	8.72×10^{-8} 1.07×10^{-7} 1.81×10^{-7}	1.25×10^{-7}	32.4

* Targeted specimen preparation (initial) values

4.6 Discussion of Results

4.6.1 Index Properties

Standard Proctor test results for CFM in this study are presented in Figure 4.5 and Figure 4.6. The decrease in fines content (FC) and plasticity index (PI) resulted in a decrease in optimum moisture content and an increase in maximum dry unit weight (Figure 4.5). S20-5 soil mixture, being the only exception, gave a slightly higher maximum dry unit weight and smaller optimum moisture content compared to S12-5 mixture.

Approximately a linear relationship was observed between the peak points of the compaction curves for CFM having the same PI (Figure 4.6a). The PI increase resulted in a decrease in the slope of the lines defining maximum dry unit weights and optimum moisture contents. Variation of maximum dry unit weight with fines content (FC) is shown in Figure 4.6b. An approximately linear relationship was observed between the soil mixtures having the same PI, with S20-5 still being the only outlier.

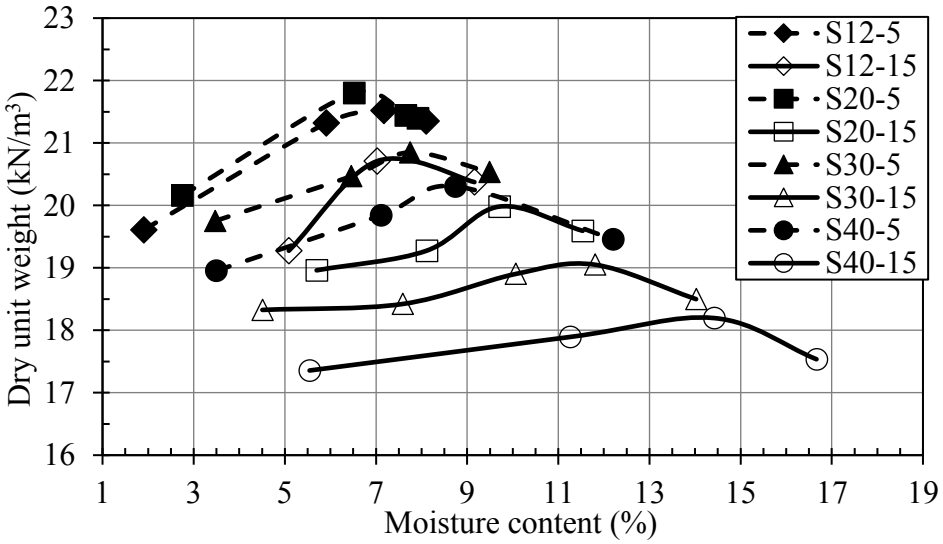


Figure 4.5. Standard Proctor compaction curves for CFM

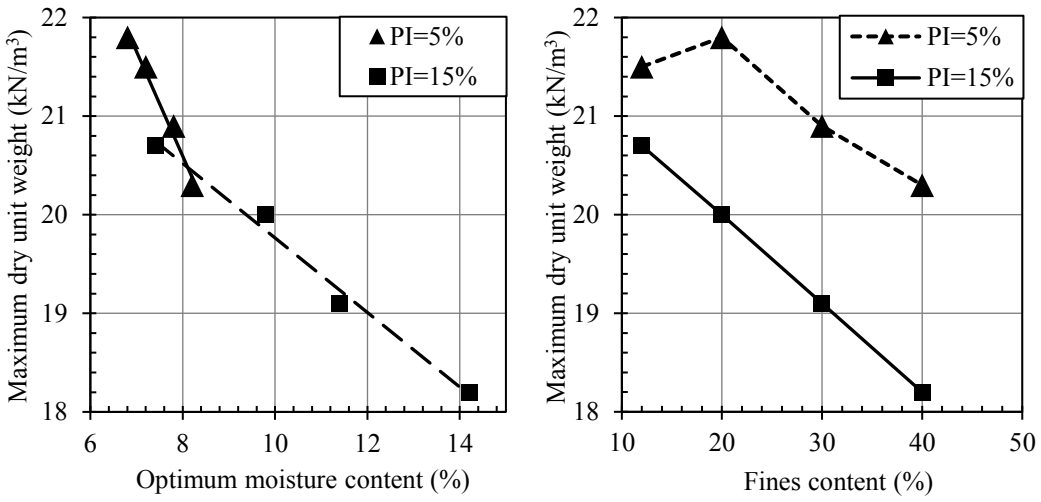


Figure 4.6. Maximum dry unit weight with (a) optimum moisture contents, (b) fines contents

An increase in the liquid limits (LL) for soil samples passing through No. 40 sieve was observed with the increase in fines (Table 4.6). However, Atterberg limits of the CFM for the soil portion passing through No. 200 sieve were observed to decrease, although fines content and percent of the plastic components increased (Table 4.6 and Figure 4.7). The former can be explained by the effect of fine sand fraction, having particles between 0.425 mm and 0.075 mm. As shown in Figure 4.7c, as the fines content increased (FC=12% to FC=40%), percent fraction of the cohesionless fine sands constituting the sample decreased. This decrease in fine sand caused the LL values of the samples passing through No. 40 sieve to increase almost linearly, even for the same or a lesser amount of plastic fines (Figure 4.7c and Table 4.6). It should be kept in mind that CFM were prepared to have PI=5% and PI=15% for the portions passing through No. 40 sieve. Based on the results, it can be concluded that the cohesionless soils having different particle sizes significantly affect the Atterberg limits and make the evaluation difficult. Therefore, evaluating the Atterberg limits of CFM for the soil fraction passing through the No. 200 sieve is recommended to better represent the effect of Atterberg limits on CFM, especially if the mixture contains a significant amount of fine sand and silt.

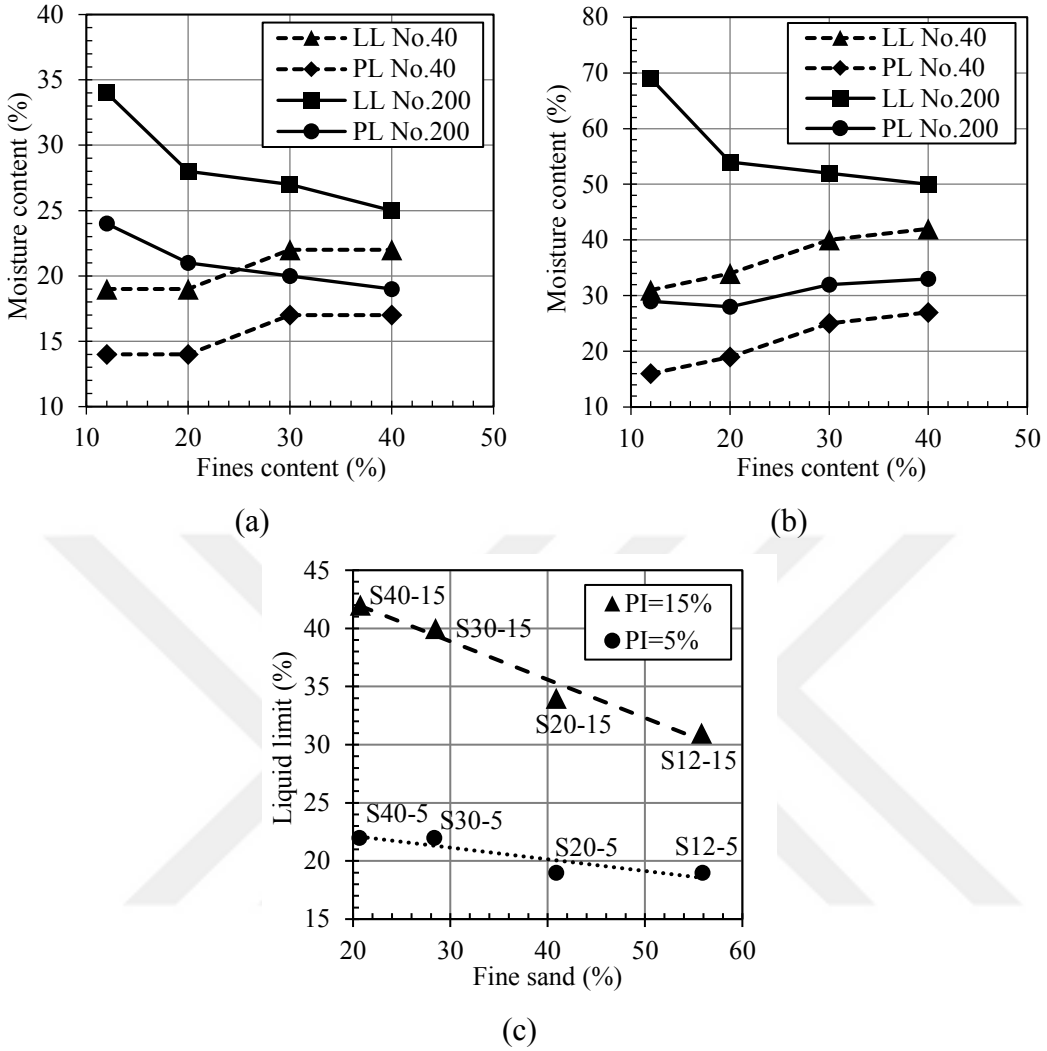


Figure 4.7. (a) LL and PL for PI=5% CFM (S12-5, S20-5, S30-5, S40-5), (b) LL and PL for PI=15% CFM (S12-15, S20-15, S30-15, S40-15), and (c) change in LL with fine sand for CFM samples passing No. 40 sieve

4.6.2 Specific Surface Area

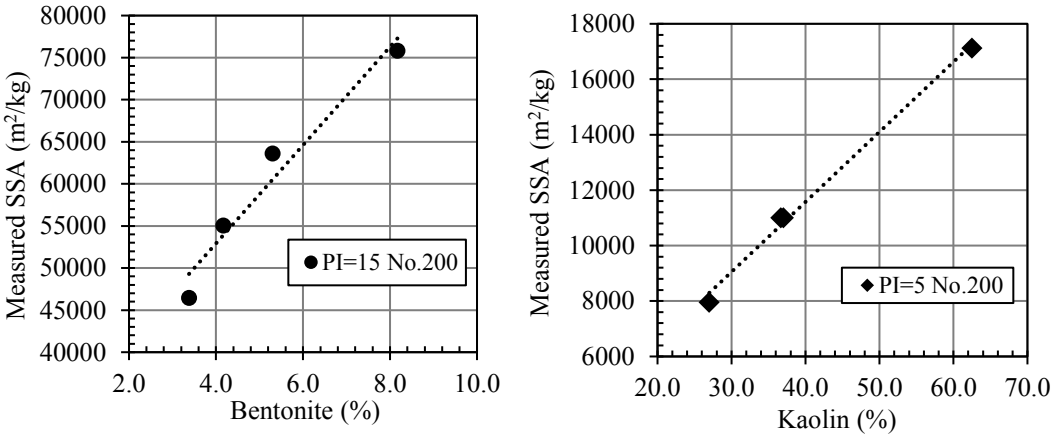
Specific surface areas (SSA) determined by the MB spot test method for the plastic portions of the CFM are presented in Table 4.7. Measured SSA values are compared with the estimations of empirical correlations, presented in Table 2.4, and the results are summarized in Table 4.11.

Table 4.11. Results of specific surface area (SSA) and comparison with empirical predictions

Soil	Sample finer than	MB spot test measurement results		Prediction by weighted averages of plastic fine fractions' SSA values (m^2/kg)	SSA Prediction of Sanzeni et al. (2013) (m^2/kg)	Empirical predictions for cohesive soil (m^2/kg)		Empirical predictions for coarse soil (m^2/kg)		Total SSA (m^2/kg)
		Adsorbed MB (mL)	SSA (m^2/kg)			Farrar and Coleman (1967)	Chapuis and Aubertin (2003)	Santamarina et al. (2002)	Chapuis and Légaré (1992)	
S12-5	No. 40	7.0	8563	7249	2899	200	16072	-	-	2059
	No. 200	14.0	17126	16438	6575	27920	32914	-	-	
S20-5	No. 40	5.5	6728	5752	2301	200	16072	-	-	2205
	No. 200	9.0	11010	9731	3893	15500	24852	-	-	
S30-5	No. 40	7.0	8563	6912	2765	5600	19039	-	-	3306
	No. 200	9.0	11010	9645	3858	14600	24302	-	-	
S40-5	No. 40	5.5	6728	5636	2255	5600	19039	-	-	3183
	No. 200	6.5	7952	7101	2841	10280	21725	-	-	
S12-15	No. 40	30.0	36699	36287	27065	21800	28826	-	-	9105
	No. 200	62.0	75845	82120	61252	89480	92608	-	-	
S20-15	No. 40	29.5	36088	36931	25654	27200	32421	-	-	12726
	No. 200	52.0	63612	62512	43431	62660	61486	-	-	
S30-15	No. 40	33.5	40981	39173	26030	38000	40189	-	-	16518
	No. 200	45.0	55049	54791	36414	58880	57844	-	-	
S40-15	No. 40	31.5	38534	39086	24917	41600	42967	-	-	18597
	No. 200	38.0	46486	49397	31510	56000	55169	-	-	
Kaolin CF=40%	-	21.5	26301	-	-	52400	51942	-	-	-
Bentonite CF=89%	-	580.0	709519	-	-	864200	-	-	-	-
Silt	-	-	-	-	-	-	-	184	257	-
Fine sand	-	-	-	-	-	-	-	9	10	-
SW	-	-	-	-	-	-	-	2	4	-

Measured SSA of the plastic portions of CFM was compared with the correlations of Farrar and Coleman (1967) and Chapuis and Aubertin (2003). Even though these correlations were developed solely for clayey soils, they predicted SSA values which were between 35-168% of the measured values for samples passing No. 40 and No. 200 sieves (Table 4.11). Farrar and Coleman (1967) suggested their correlation for soils with liquid limits (LL) varying between 40% and 80%. Therefore, poor estimations were obtained for CFM in this study which had low liquid limits. Better predictions were observed for CFM having PI=15% (S12-15, S20-15, S30-15, and S40-15), with both empirical correlations due to the higher liquid limits. SSA of the coarse fraction was estimated by using the correlations of Santamarina et al. (2002) and Chapuis and Légaré (1992) (Table 2.4). Results indicated that both correlations gave similar predictions to each other.

Linear correlations were observed between measured SSA and percent fraction of kaolin (for CFM with PI=5%) and bentonite (for CFM with PI=15%) for samples passing No. 200 sieves (Figure 4.8). Arab et al. (2015) also reported linear correlations between the percentages of kaolin/bentonite and adsorbed MB values.



(a) (b)

Figure 4.8. (a) SSA change with bentonite content for CFM with PI=15% and passing through No. 200 sieve, (b) SSA change with kaolin content for CFM with PI=5% and passing through No. 200 sieve

SSA of the cohesive soils can be predicted by the weighted average of individual SSA of the plastic fine fractions constituting the sample, as inferred from Figure 4.8. For instance, the portion of S20-15 soil mixture passing through No. 200 sieve had 94.7% and 5.3% kaolin and bentonite fractions, respectively (Table 4.6). Kaolin and bentonite had 26301 m^2/kg and 709519 m^2/kg measured SSA values (Table 4.11). SSA measurement of S20-15 specimen (for portion passing No. 200 sieve) was 63612 m^2/kg. SSA value of 62512 m^2/kg (0.947x26301+0.053x709519) was predicted if the percent weight of the plastic fine fractions constituting the sample was considered. This approach predicted SSA values within 90%-120% of the measured SSA results, as seen in Table 4.11. In addition, this approach gave better SSA predictions rather than considering only the clay fractions (particles smaller than 0.002 mm), as proposed by Sanzeni et al. (2013), which underestimated the SSA by 2 to 3 times. This may be attributed to the effect of fine particles between 0.075 mm and 0.002 mm. In the correlation of Sanzeni et al. (2013), only clay fraction (particles smaller than 0.002 mm) is assumed to be related with the plastic nature of the soils (Table 2.4). This effect was more significant, especially for low plastic clays. Stark and Hussain (2013) suggested that as the amount of clay minerals (clay fraction, CF) in the sample increases, clay fractions that can be measured from the soil passing through No. 40 and No. 200 sieves ($CF_{No.40}$ and $CF_{No.200}$) become more coherent with each other. Stark et al. (2005) also attributed this to the fact that the dispersing agent, sodium hexametaphosphate is more effective in high plasticity soils than in low plasticity soils, or passing the material through No. 40 sieve is sufficient to disaggregate the material when CF is high.

Representative SSA of a coarse-fine mixture will be in between the SSA of coarse and fine fractions. The total SSA of soils was calculated as in the proposed equation below (Equation 4.6) according to the weighted average of the SSA's of the relevant fractions composing CFM.

$$SSA_{TOTAL} = FC \cdot SSA_F + (1 - FC) \cdot SSA_C \quad (4.6)$$

Where FC is the fines content (particles smaller than No. 200 sieve, and written as a decimal in Equation 4.6), SSA_F and SSA_C are the specific surface area of the fines content and coarse-grained content of the soil (based on No. 200 sieve), respectively.

4.6.3 Volume Change During Saturation

The initial void ratios (at 95% Proctor compaction dry density) and void ratios after saturation of the CFM specimens prepared for the flexible wall hydraulic conductivity testing are presented in Table 4.8. The plot of initial values of the void ratio with the void ratio after saturation can be seen in Figure 4.9. The initial void ratios of all CFM tested in this study were in the range of 0.26 to 0.53. Void ratios decreased during saturation in all CFM by amounts ranging between 0.2% and 5.7% of their initial void ratios.

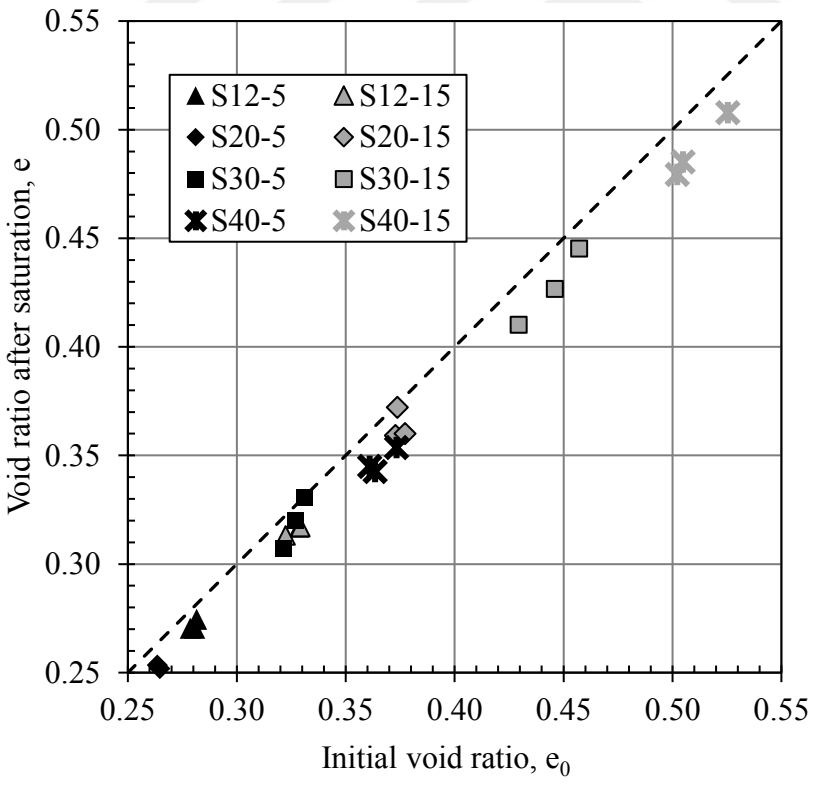


Figure 4.9. Relationship between initial void ratio (e_0) at the 95% Proctor compaction and the void ratio after saturation (e)

4.6.4 Threshold Fines Content Based on Particle Packing

Calculated values of global, intergranular, and interfine void ratios of CFM in the saturated state (Table 4.8) were plotted together with fines content in Figure 4.10.

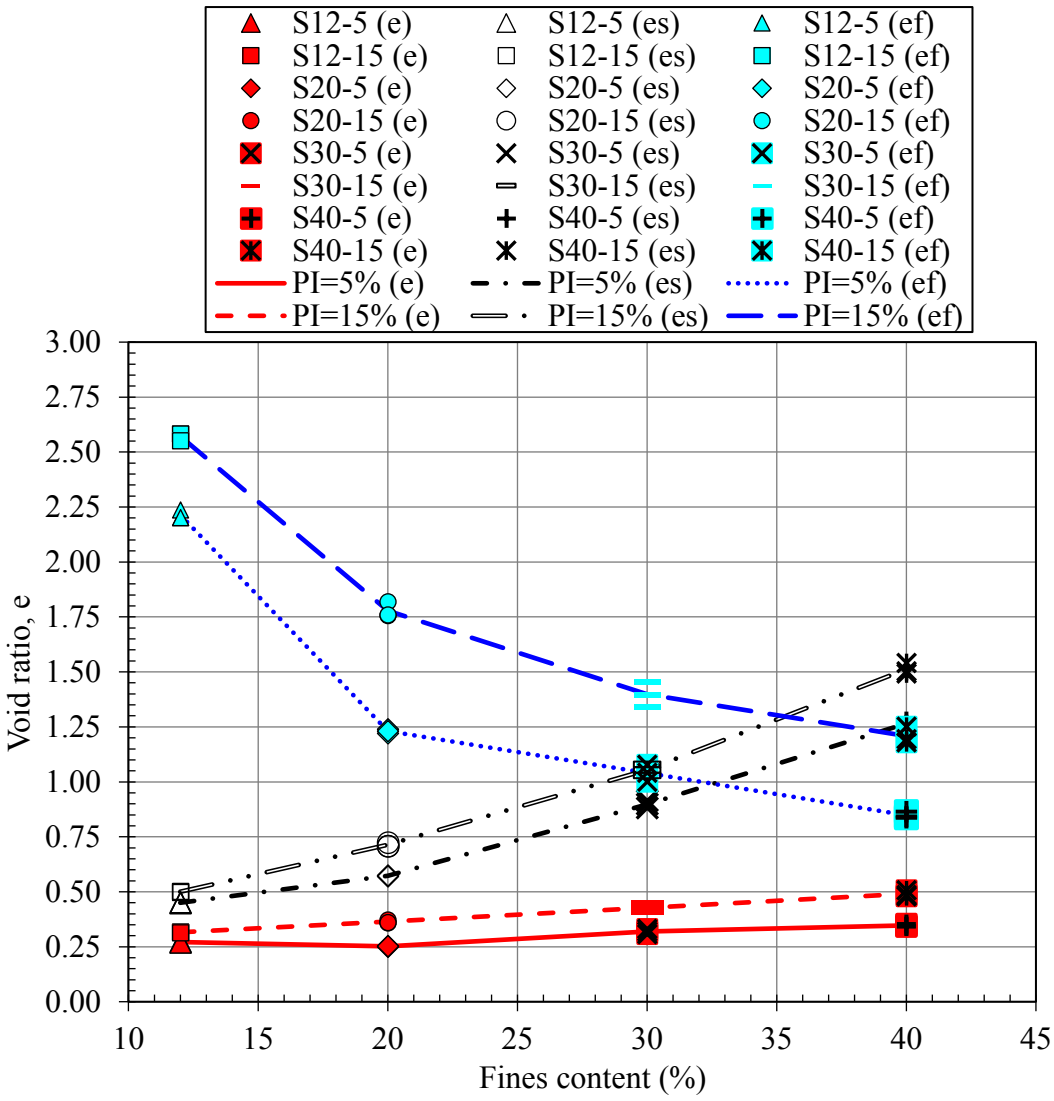


Figure 4.10. Relationship between FC with global void ratio after saturation (e), intergranular void ratio (e_s), and interfine void ratio (e_f)

Intergranular and interfine void ratios showed more apparent change with fines content as compared to the global void ratio. The maximum void ratio (e_{max}) of SW

soil mixture, which constituted the coarse fraction of all CFM, was 0.50 (Table 4.4). As described by Monkul and Ozden (2005), if the intergranular void ratio (e_s) of the mixture is higher than the maximum void ratio of the coarse fraction, it indicates fines occupying the voids between the coarse particles and coarse particles not in contact with each other in the soil matrix; therefore, soil behavior is dominated by fines. Intergranular void ratio (e_s) exceeded 0.50 for FC higher than 15% for CFM having a PI=5%. This boundary FC was 12% for CFM having a PI=15% (Figure 4.10). Therefore, 15% and 12% FC can be considered as the threshold FC between the fine and coarse fraction-dominated soils in terms of particle packing for PI=5% and PI=15%, respectively. A slight decrease in threshold FC with the increase in PI was observed where the other affecting parameters were the same.

Results obtained with "the intergranular void ratio" concept, in terms of the dominance of coarse and fine grains in particle packing, were observed similarly with "the clay-phase domination" concept (Equation 2.8) proposed by Mitchell and Soga (2005).

When the intergranular void ratio (e_s) is lower than 0.50, and coarse particles dominate the overall behavior, intergranular relative density (Equation 2.7) can be used to quantify the compaction degree of coarse particles in the soil matrix. Average intergranular relative densities were calculated as 23% and 0% for saturated S12-5 and S12-15 specimens, respectively. In calculations, the maximum and minimum void ratios of the host granular soil, SW, were 0.50 and 0.28, respectively (Table 4.4). Lower intergranular void ratios indicate denser packing of coarse particles and result in higher intergranular relative density. As the intergranular void ratio approaches the maximum void ratio of the host granular soil, intergranular relative density decreases. The transition between fine and coarse fraction-dominated soils can also be identified with the intergranular relative density being zero. The similar conclusion drawn from Figure 4.10 can also be seen in Figure 4.11. Intergranular relative density approached zero for the threshold fines content of 15% for CFM with PI=5% and 12% for CFM with PI=15%.

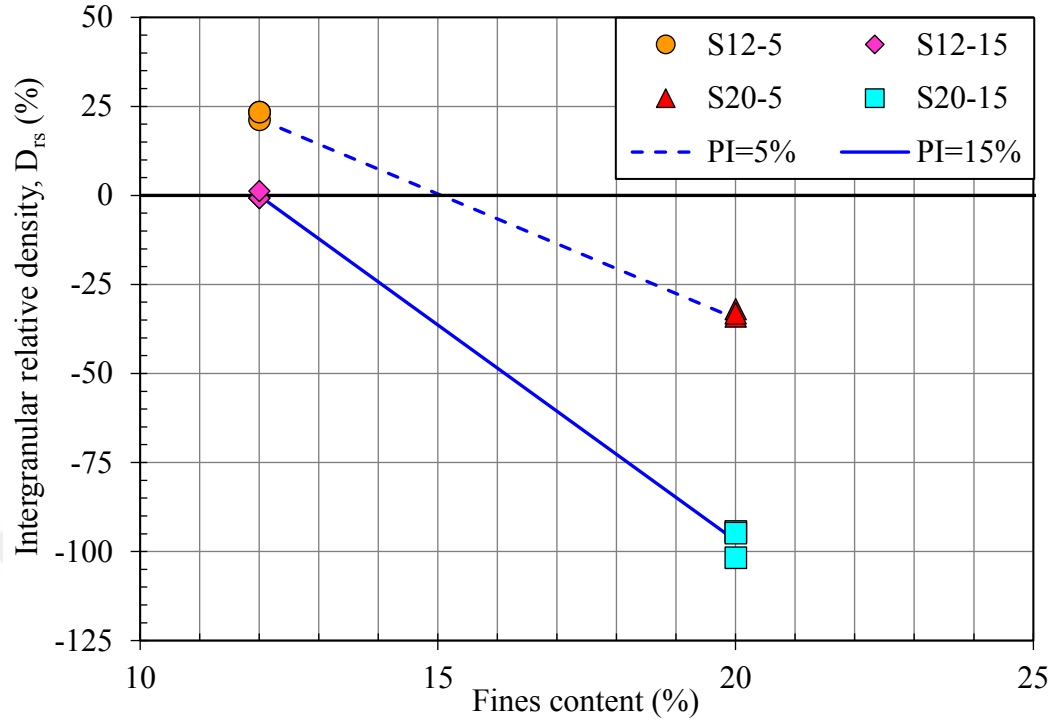


Figure 4.11. Relationship between intergranular relative density and fines content of CFM

4.6.5 Hydraulic Conductivity

The plot of hydraulic conductivity test results against fines content for all CFM, SW, and SP soil mixtures is presented in Figure 4.12. The ranges of variation of all test results were indicated, along with the average values for each CFM.

The average results for the rigid wall hydraulic conductivity tests of SW and SP soil mixtures were 8.36×10^{-2} cm/s and 2.23 cm/s, respectively (Figure 4.12). According to the boundaries defined by Casagrande and Fadum (1940), SW soil mixture was in the range of sandy soils (i.e., clean sand and gravel mixtures). 63.1% of the soil constituting the SW mixture passed through the No. 4 sieve (4.75 mm) (Table 4.3). Therefore, SW was classified as predominantly sandy soil containing gravel according to the USCS, as also consistent with the Casagrande and Fadum (1940) boundaries. On the other hand, SP soil mixture is near the boundary of clean

gravel and sandy soils with respect to the classification of soils according to their hydraulic conductivity by Casagrande and Fadum (1940). It consisted of coarse-graded sand and gravel only. According to USCS, SP soil mixture was classified as poorly-graded sand with gravel (60.5% of its particles passed through 4.75 mm), and according to BS 1377:1990, poorly-graded gravel (3.1% passed through 2.0 mm) (Table 4.3 and Figure 3.5). Measured hydraulic conductivity results and the definitions of SP according to different classification systems confirmed that SP soil mixture was behaviorally on the gravel-sand transition boundary.

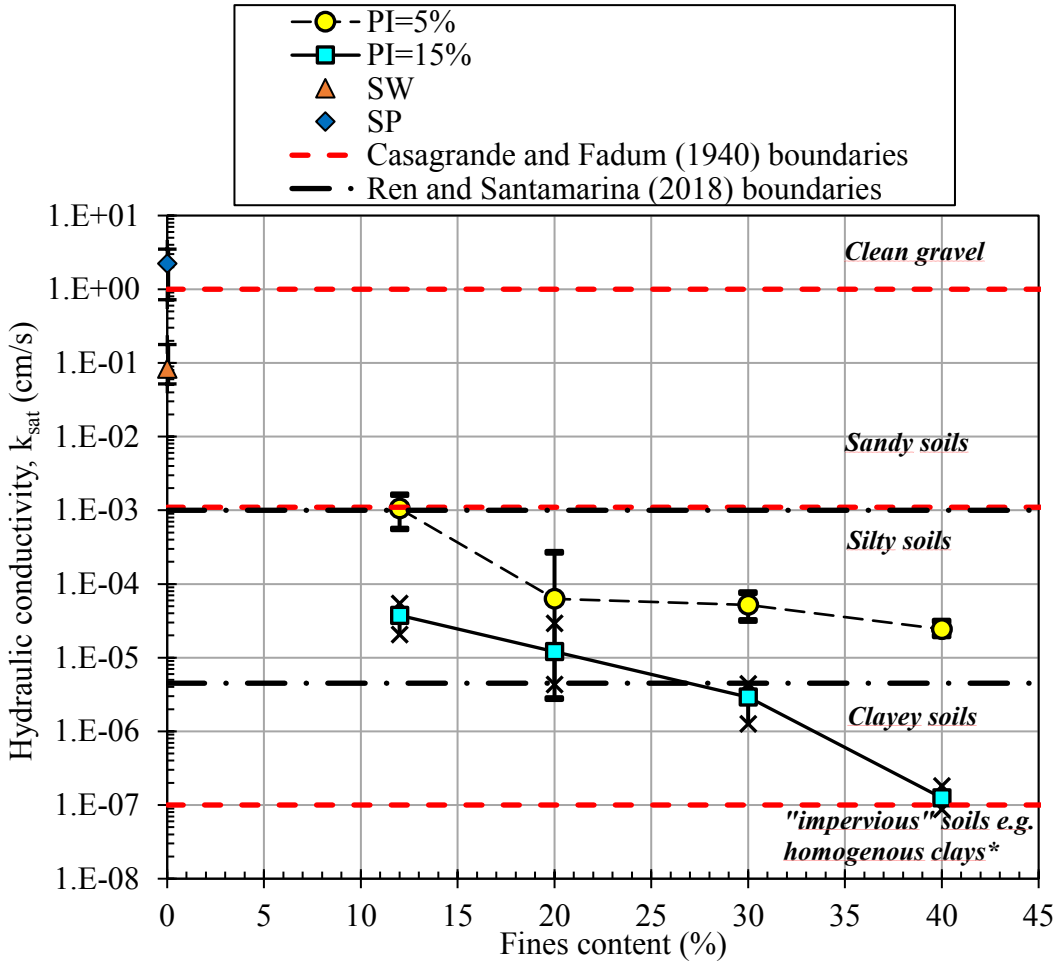
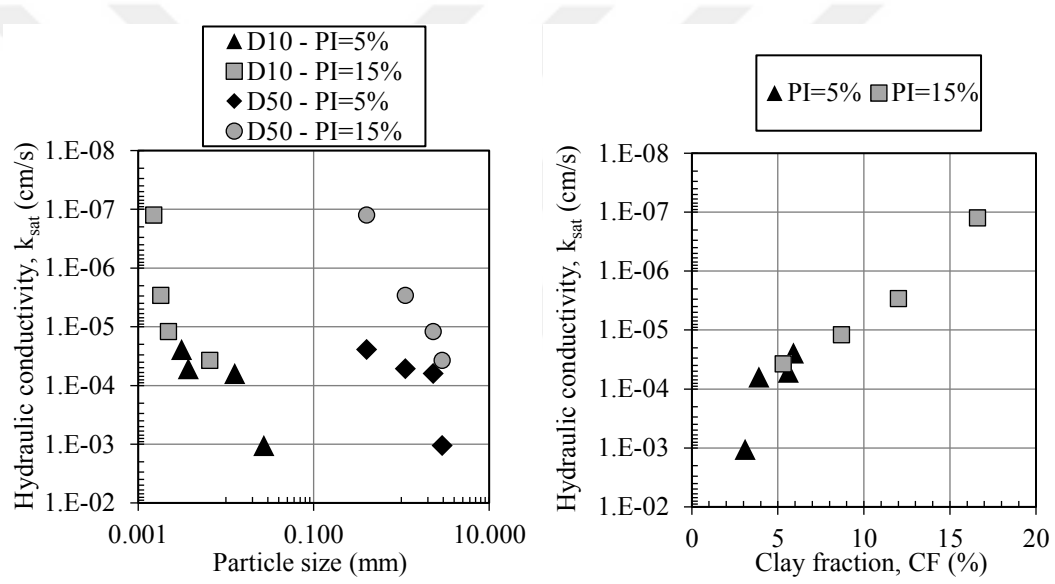


Figure 4.12. Hydraulic conductivity with fines content and plasticity index for saturated soil mixtures (*according to Casagrande and Fadum, 1940)

Hydraulic conductivity values tended to decrease with the increase of FC and PI for the eight CFM. The amount of decrease in hydraulic conductivity was lower in mixtures having PI=5% (Figure 4.12). Lower hydraulic conductivity was observed for higher PI for the CFM having the same FC. Different than other tests, variances in test results are higher for S20-5 and S20-15, although six different experiments were executed in both CFM, and a standard specimen preparation methodology was applied in each test. Hydraulic conductivity values increased as D_{10} increased (Figure 4.13a). They decreased with an increase in clay fraction, and approximately a linear correlation was observed for CFM with PI=15% (Figure 4.13b).



(a) (b)

Figure 4.13. Changes in hydraulic conductivity (a) with d_{10}, d_{50} values of CFM, (b) with clay fractions of CFM

Evaluation of hydraulic conductivity values with global and intergranular void ratio, particle size distribution, and clay fraction of CFM indicated that, as the fines content and plasticity increase, fine particles dominate the behavior in terms of fluid flow characteristics. Hydraulic conductivities significantly changed between fines content of 12% and 20% for PI=5%, whereas it was around 30% for PI=15% (Figure 4.12, Figure 4.13, and Figure 4.14).

Global void ratio, intergranular, and interfine void ratios were plotted with hydraulic conductivity values in Figure 4.14. Although hydraulic conductivity changed dramatically for the CFM having the same PI value, global void ratios of the mixtures changed in a narrow range. In addition, hydraulic conductivities decreased as the global void ratio slightly increased (Figure 4.14). This result indicates that the global void ratio is not an indicative parameter for hydraulic conductivity of transitional soils as much as the intergranular and interfine void ratio.

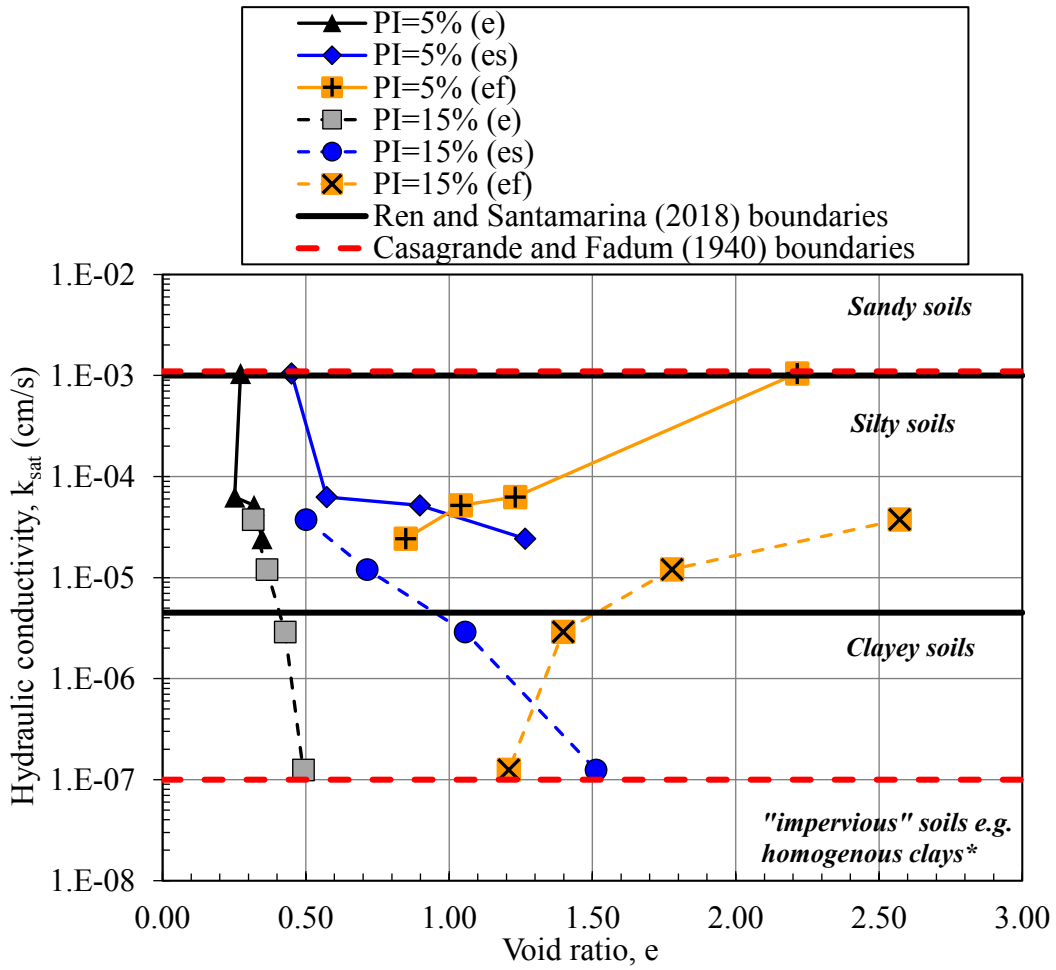


Figure 4.14. Hydraulic conductivity versus global void ratio (e), intergranular void ratio (e_s), and interfine void ratio (e_f) (*according to Casagrande and Fadum, 1940) for CFM specimens

According to the classification of soils regarding their hydraulic conductivities by Ren and Santamarina (2018) and Casagrande and Fadum (1940), S12-5 was on the sandy soil – silty soil boundary. All CFM having PI=5%, S12-15, and S20-15 was in the range of silty soils, whereas S30-15 and S40-15 were in the range of clayey soils, according to Ren and Santamarina (2018) (Figure 4.12 and Figure 4.14).

4.6.5.1 Comparison of Measured Hydraulic Conductivities with Empirical Predictions in Literature

Several empirical correlations were developed in the literature, as summarized in Section 2.3.2, for the prediction of the hydraulic conductivity of soils. The Kozeny (1927) – Carman (1956) equation, widely known as the KC equation, is one of the most widely used empirical correlations for sandy soils. It relates hydraulic conductivity with void ratio and specific surface area (SSA) of soils (Equation 2.11). However, accurate estimation of the effective porosity and SSA data associated with hydraulic flow is one of the main difficulties in using KC or other related equations, as also stated by Hong et al. (2020). It should also be added that the estimation of these variables is more problematic for CFM than for pure cohesionless or plastic materials. Variations in the calculated values of SSA cause significant differences because the square of SSA is inversely proportional to the hydraulic conductivity (Equation 2.11).

KC and related equations underpredicted the hydraulic conductivities of CFM in this study by one to four orders of magnitude according to the calculated SSA values from MB spot tests and empirical methods (Table 4.11). A similar conclusion was reported by Dewhurst et al. (1999) that the KC equation underpredicted their measured data. However, it should be noted that the coarse particle angularity of CFM in this study may create a significant problem in using the predictive equations. Chapuis (2004) reported poor estimations by using Equation 2.13 for crushed materials. The angularity of particles increases tortuosity and internal resistance, which results in a change in pore void geometry different than natural soils. Carrier

(2003) suggested more advanced formulas to be used for coarser soils because of the internal friction.

The hydraulic conductivity predictions of Equation 2.10 and Equation 2.13, which are the empirical correlations of Hazen (1892, 1911) and Chapuis (2004), respectively, were compared with the measured hydraulic conductivities of CFM in Figure 4.15.

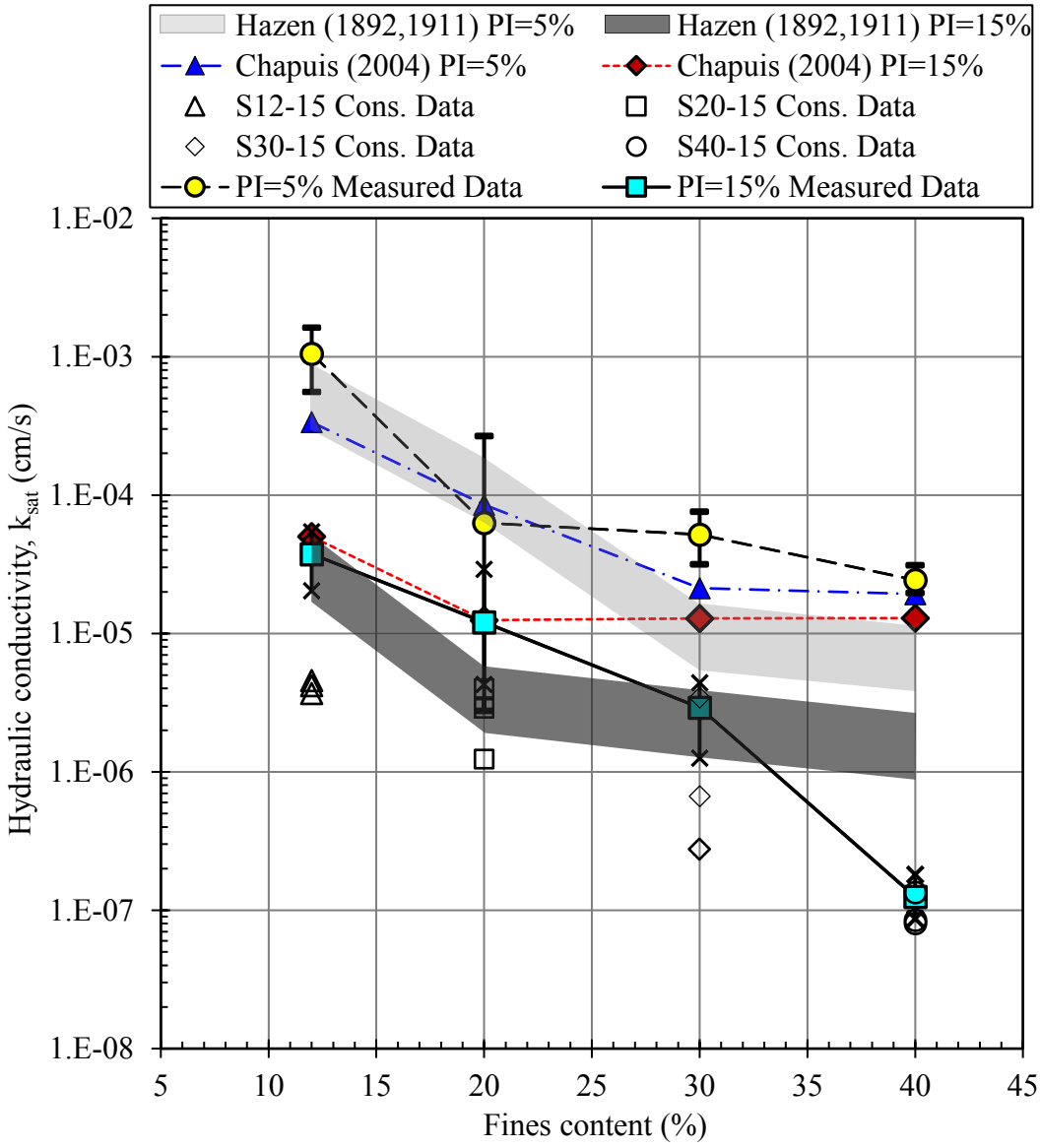


Figure 4.15. Comparison of hydraulic conductivity results with the empirical predictions

The simple form of the Hazen (1892, 1911) formulation (Equation 2.10) is generally valid for sands having an effective diameter, d_{10} values, between 0.01-0.30 cm, and coefficient of uniformity (C_u) less than 5. Nevertheless, predictions of the formulation were plotted in Figure 4.15 by assuming Hazen's coefficient C_H to be between 40 to 120, according to the suggestion of Holtz and Kovacs (1981). The predictive equation of Chapuis (2004), consisting of the $e^3/(e+1)$ term from the KC equation and d_{10}^2 from Hazen's formulation (Equation 2.13), was stated to be valid for any non-plastic material, and poor estimations can be obtained with crushed materials. Nevertheless, Toumpanou et al. (2021) reported a reliable correlation between the compound parameter of $[(d_{10})^2e^3/(1 + e)]$ and the hydraulic conductivity of sand-sized crushed limestone in their study. Correlations of Hazen (1892, 1911) and Chapuis (2004) (Equation 2.10 and Equation 2.13, respectively) could predict the measured hydraulic conductivity of CFM within an order of magnitude except S40-15 in this study. Equations overpredicted the hydraulic conductivity of S40-15 which had the highest FC and PI values (Figure 4.15).

In the scope of Isotropically Consolidated Undrained (ICU) triaxial strength tests (performed according to ASTM D4767-11), three different experiments have been conducted for each CFM by consolidating the specimens under effective stresses of 40 kPa, 150 kPa, and 300 kPa prior to shearing. Consolidation parameters (coefficient of consolidation, c_v, and coefficient of volume compressibility, m_v) were calculated from the volume change properties with time and the height of the specimen (described in Section 5.4.3.1). Consolidation data of CFM was also used to predict the hydraulic conductivity indirectly, based on the equations of consolidation theory (Equations 2.20, 2.21, and 2.22). Although predictions underestimated the hydraulic conductivities, they could predict the measured data within an order of magnitude (Figure 4.15). Time-dependent drainage and consolidation did not seem to occur for CFM having a PI=5%. Dafalla et al. (2015) pointed out that data obtained from oedometer underpredicted their hydraulic conductivity measurements. However, they stated that the underprediction was in the range of two to three orders of magnitude.

CHAPTER 5

UNCONFINED COMPRESSION, TRIAXIAL COMPRESSION AND COMPRESSIBILITY TEST RESULTS

This chapter presents the compressive strength determination via the unconfined compression tests, shear strength, and stiffness via the consolidated undrained triaxial compression tests, and compressibility properties based on consolidation data of saturated CFM specimens and one-dimensional static large compression tests. Variation of strength and compression response of the CFM with fines content, plasticity index, normal stress, and consolidation pressure is evaluated to identify the behavioral transitions and possible use of these materials as backfill soil in the design of the MSEW.

5.1 Unconfined Compressive Strength Test Results

For each CFM, three unconfined compressive strength (UCS) tests were performed with the same testing parameters for checking the repeatability. Unconfined compressive strengths were calculated by correcting the cross-sectional area of the specimen according to the axial strain level. Equations 5.1, 5.2, and 5.3 were used to calculate the axial strains and compressive stresses, as given in ASTM D2166-16.

Test results are presented in Table 5.1. The coefficient of variation (COV) of the unconfined compressive strength and strain at failure of the three tests were between 2.2%-9.4% and 3.2%-22.4%, respectively. Based on these results, it can be stated that the specimen preparation procedure of CFM and heterogeneity – the position and amount of the coarse and fine particles in failure surfaces – do not significantly affect the measurements of the unconfined compressive strength. Instead of evaluating the mean values of three UCS tests, a representative test was selected for

each CFM to be compared with other results in Section 5.4.1 in the discussion part. Selected representative tests were indicated by the symbol (*) in Table 5.1.

$$\varepsilon_1 = \frac{\Delta L}{L_0} \text{x} 100 \tag{5.1}$$

$$A_{cor.} = \frac{\mathrm{A}_0}{\left(1 - \frac{\varepsilon_1}{100}\right)} \tag{5.2}$$

$$\sigma_{UCS} = \frac{P}{A_{cor.}} \tag{5.3}$$

where,

ΔL : Length change of specimen as read from the vertical displacement indicator

L_0 : Initial length of the specimen

ε_1 : Axial strain (expressed as a percentage)

$A_{cor.}$: Corrected average cross-sectional area of the specimen

A_0 : Initial cross-sectional area of the specimen

σ_{UCS} : Unconfined compressive stress

P : Axial load

Failure criterion of the UCS test in ASTM D2166-16 is indicated as the observation of load reduction with increasing strain or loading the specimen until 15% axial strain is reached. However, tests were continued after the failure point had been reached to observe the post-peak stress-strain behavior. Evaluations regarding compressive stress with axial strain, the values of strain at failure, and behavior after failure are discussed in Section 5.4.1.

Table 5.1. Unconfined compressive strength test results

Soil code	Test No	Unconfined compressive strength, q_u (kPa)	Mean unconfined compressive strength (kPa)	COV for unconfined compressive strength (%)	Axial strain at failure, ε_f (%)	COV for axial strain at failure (%)
S12-5	1	22	23	9.4	1.07	17.2
	2*	21			0.83	
	3	26			0.71	
S12-15	1*	90	91	3.6	1.40	3.2
	2	87			1.51	
	3	95			1.48	
S20-5	1	82	79	2.6	1.94	22.4
	2	77			1.14	
	3*	79			1.39	
S20-15	1*	93	95	7.0	2.83	14.1
	2	104			2.36	
	3	88			3.34	
S30-5	1	95	102	7.0	1.86	15.4
	2	112			1.68	
	3*	100			1.27	
S30-15	1*	160	161	2.6	1.97	9.1
	2	166			1.96	
	3	156			1.61	
S40-5	1*	133	134	2.2	1.48	9.5
	2	138			1.63	
	3	131			1.29	
S40-15	1	165	161	2.3	2.36	18.3
	2*	161			1.99	
	3	156			3.08	

*Representative test

Failure surfaces of the repeated tests for each CFM were similar. Views after failure for the representative test results, indicated in Table 5.1, are presented in Figure 5.1. According to the results, more apparent failure surfaces were observed with an increase in fines content and plasticity index. Observed failure surfaces with increasing fines content were more pronounced in CFM with PI=15% than PI=5%. More apparent bulging was detected in the middle of the specimens for CFM having fines content less than 20% for both PI=5% and PI=15% (Figure 5.1).



(a) S12-5



(b) S12-15



(c) S20-5



(d) S20-15



(e) S30-5



(f) S30-15



(g) S40-5



(h) S40-15

Figure 5.1. Failure surfaces after unconfined compressive strength tests of CFM

5.2 Triaxial Compression Test Results

5.2.1 Consolidation of Saturated Specimens

Coarse-fine mixtures were subjected to isotropic consolidation under effective stresses of 40, 150, and 300 kPa after saturation of the specimens. Discharged volume during consolidation was monitored with time while the final height was measured at the end of the consolidation. Equations 4.4, 5.4, and 5.5, as given in ASTM D4767-11, were used to calculate the height and cross-sectional area of the specimens after consolidation.

$$\Delta V_{sat} = 3V_0 \frac{\Delta H_s}{H_0} \tag{4.4}$$

$$H_c = H_0 - \Delta H_0 \tag{5.4}$$

$$A_c = (V_0 - \Delta V_{sat} - \Delta V_c)/(H_c) \tag{5.5}$$

where,

ΔV_{sat} : Change in volume of the specimen during saturation

V_0 : Initial volume of the specimen

ΔH_s : Change in height of the specimen during saturation

H_0 : Initial height of the specimen

H_c : Height of the specimen after consolidation

ΔH_0 : Change in height of the specimen at the end of consolidation

A_c : Cross-sectional area of the specimen after consolidation

ΔV_c : Change in volume of the specimen during consolidation

In this section, the percent change in volume during consolidation is referred to as "volumetric strain", although it is not shear-induced volumetric strain. Volumetric strain, which is the ratio of the discharged volume during consolidation to the saturated volume of the specimen, $(\Delta V_c/V_{sat})$x100, were plotted against time for PI=5% and PI=15% in Figure 5.2 and Figure 5.3, respectively.

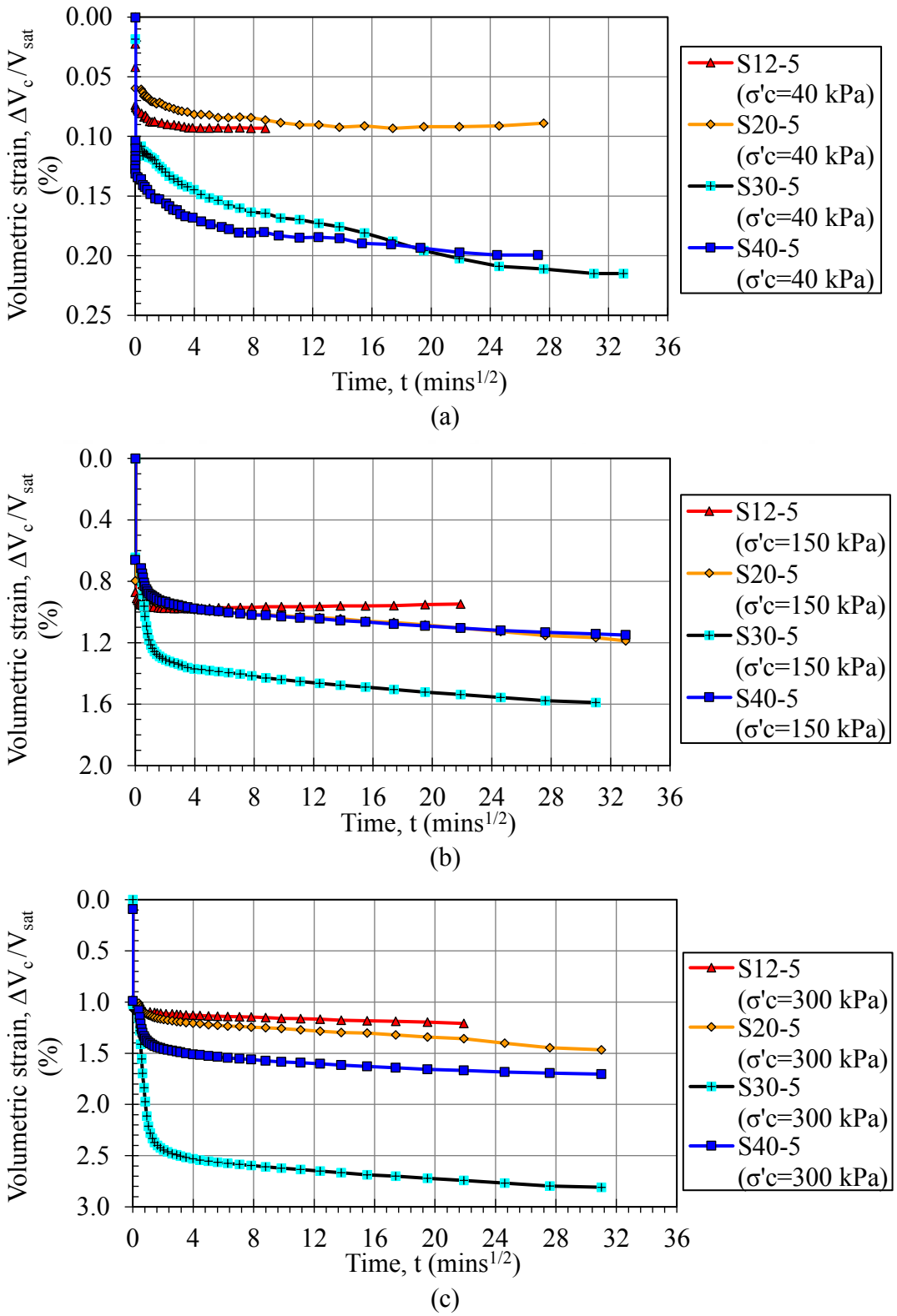


Figure 5.2. Percent volumetric strain with time for CFM having PI=5% under consolidation pressures of (a) σ'_c=40 kPa, (b) σ'_c=150 kPa, and (c) σ'_c=300 kPa

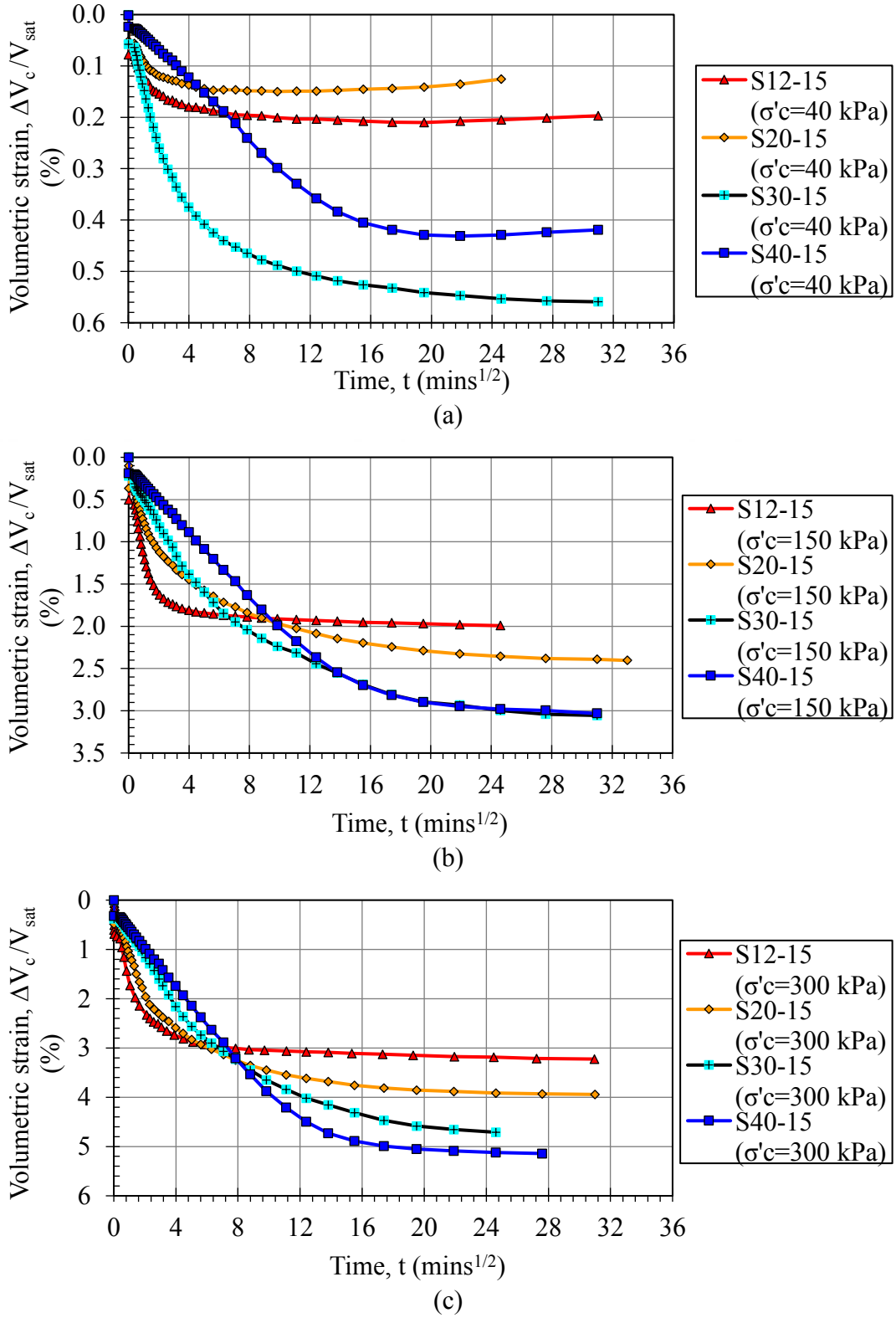


Figure 5.3. Percent volumetric strain with time for CFM having PI=15% under consolidation pressures of (a) σ'_c=40 kPa, (b) σ'_c=150 kPa, and (c) σ'_c=300 kPa

An increase in percent volumetric strain (or percent volume change during consolidation) with an increase in FC was observed as a general trend for all CFM. While time-dependent drainage was observed in CFM with PI=15%, a significant part of the volumetric discharge occurred immediately after applying consolidation pressures in CFM with PI=5% (Figure 5.2). Therefore, the finalization of consolidation and stabilization of the specimen volumes were faster for PI=5%. For the same FC, specimens with PI=15% showed more volumetric strain than PI=5% in all consolidation pressures.

5.2.2 Triaxial Compression Tests

Undrained triaxial compression tests were performed on coarse-fine mixtures (CFM) with an axial deformation rate of 0.05 mm/min after isotropically consolidating the saturated specimens. Pore water pressures generated with axial strain were measured separately from the top and bottom outlets of the specimen. Pore water pressures, axial load, axial deformation, and time were recorded. Pore water pressure readings at the top and bottom outlets were generally the same during shear, indicating that the deformation rate given above was sufficient to provide a stabilized level of pore water pressure generation throughout the specimen height. Therefore, reported pore water pressures are the average values measured from the top and bottom readings.

Corrections were applied to calculate the corrected deviatoric stress during axial compression. Firstly, the forces generated from uplift pressure due to cell pressure and the piston friction were measured and subtracted from axial load readings. Axial stress induced by the rubber membrane was calculated using Equations 5.7 and 5.8 as given in ASTM D4767-11 and subtracted from the deviatoric stress for each axial strain.

The cross-sectional area of the specimen was corrected for each axial strain level by using Equations 5.6 and 5.9, and the deviatoric stresses were calculated by using Equation 5.10, as indicated in ASTM D4767-11.

$$\varepsilon_1 = \frac{\Delta H}{H_c} \tag{5.6}$$

$$\Delta(\sigma_1 - \sigma_3)_m = \frac{4E_m t_m \varepsilon_1}{D_c} \tag{5.7}$$

$$D_c = \sqrt{\frac{4A_c}{\pi}} \tag{5.8}$$

$$A_{cor.} = \frac{\mathrm{A}_c}{(1 - \varepsilon_1)} \tag{5.9}$$

$$(\sigma_1 - \sigma_3) = \frac{P}{A_{cor.}} \tag{5.10}$$

where,

ε_1 : Axial strain for the given axial load (as decimal form)

ΔH : Change in height of the specimen as determined from vertical deformation indicator

H_c : Height of the specimen after consolidation

$\Delta(\sigma_1 - \sigma_3)_m$: Membrane correction to be subtracted from the measured principal stress difference

E_m : Young's modulus for the membrane material

t_m : Thickness of the membrane

D_c : Diameter of the specimen after consolidation

A_c : Cross-sectional area of the specimen after consolidation

$A_{cor.}$: Corrected average cross-sectional area of the specimen

$\sigma_1 - \sigma_3$: Measured principal stress difference (deviatoric stress)

P : Given applied axial load (corrected for uplift and piston friction)

Specimen views after the triaxial compression test are presented in Figure 5.4. The initial height of the prepared specimens was 140 mm.

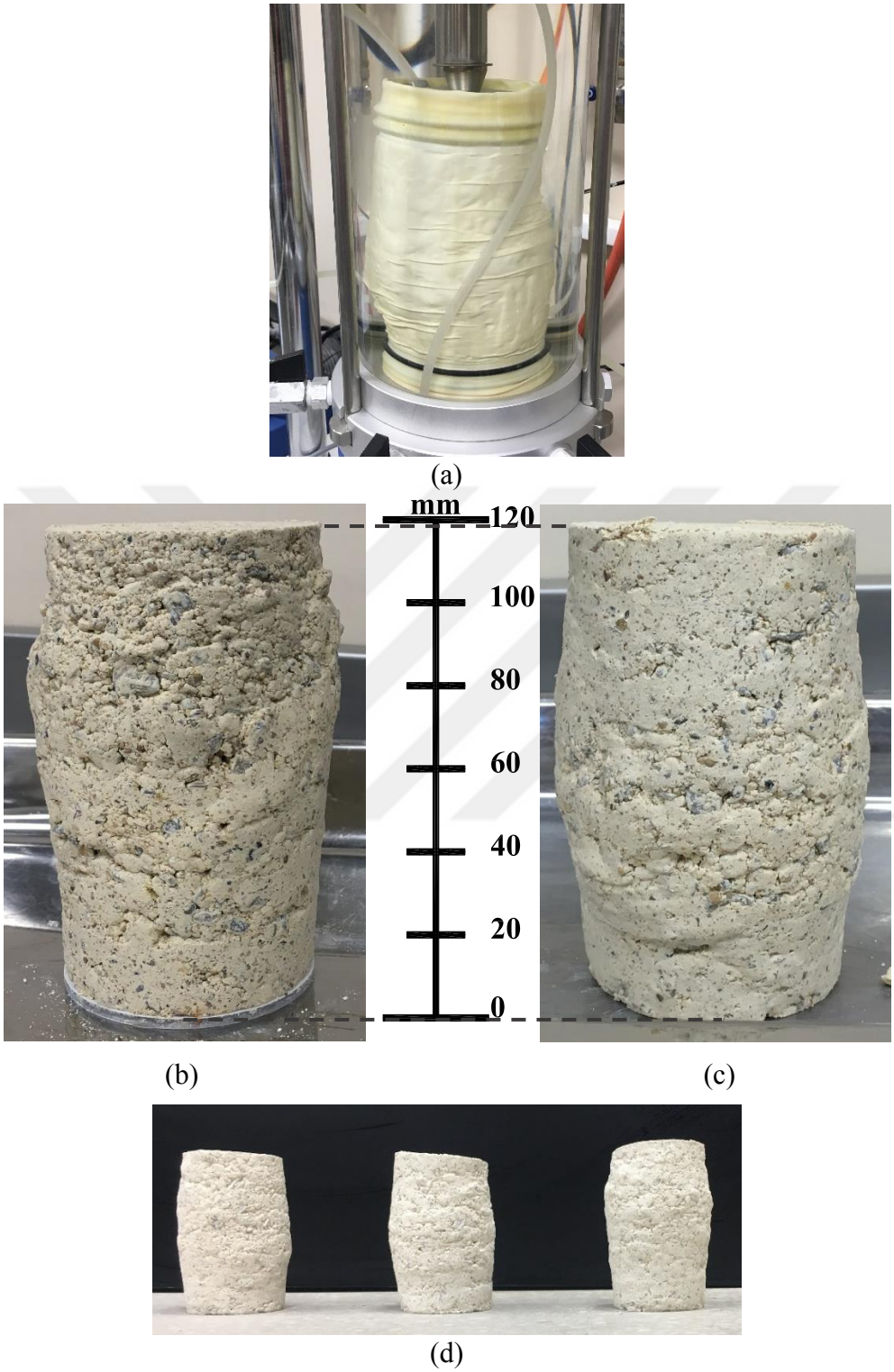


Figure 5.4. (a) View of the specimen in the triaxial cell after a completed test, failure shapes of the specimens for (b) S20-15, (c) S30-15, and (d) failure shapes of the S40-5 (after oven-drying) for tests having different consolidation pressures

Repeatability of the undrained triaxial compression test results was evaluated on three CFM specimens, S12-15, S30-5, and S40-5. Plots of the corrected deviatoric stress and average pore water pressures with axial strain are presented in Figure 5.5. Behavioral tendencies of stress and pore water pressure in repeated tests were observed to be the same. Tests for S30-5 and S40-5 showed strain-softening after a peak deviatoric stress had been reached, while deviatoric stress of S12-15 increased with axial strain until the end of the test. Peak deviatoric and ultimate (residual) stresses, as well as generated pore water pressures of repeated tests, are presented and compared in Table 5.2.

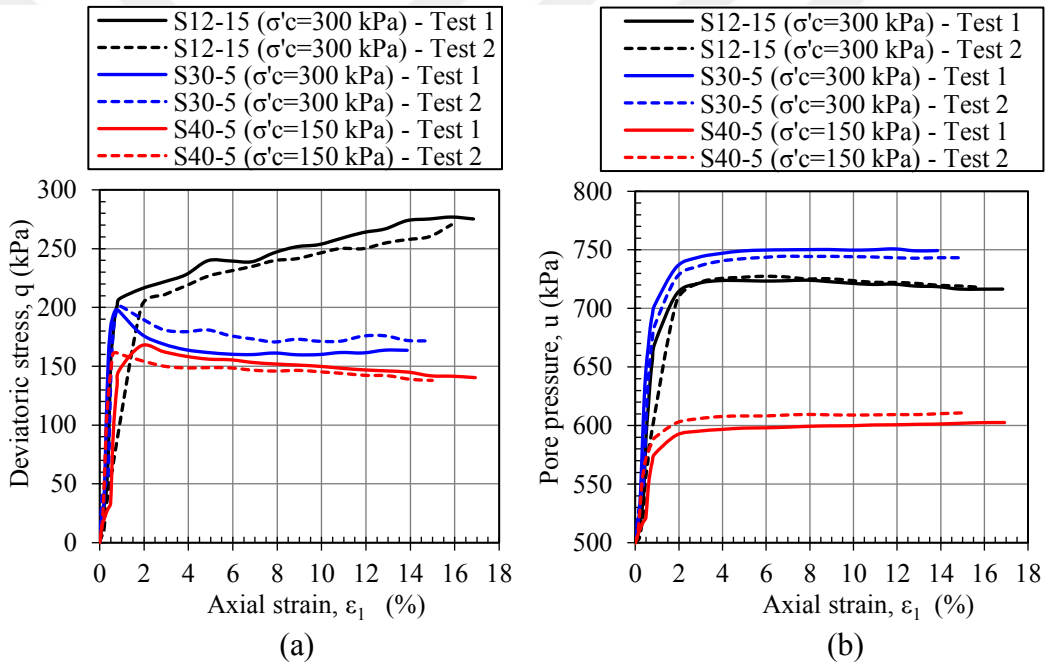


Figure 5.5. Repeated triaxial test results (a) deviatoric stress with axial strain, (b) pore pressure with axial strain

Table 5.2. Repeated triaxial test results

Soil code	Peak deviatoric stress (kPa)	Residual deviatoric stress (kPa)	Total pore water pressure at peak deviatoric stress (kPa)
S12-15 Test 1	275.2	-	724.0
S12-15 Test 2	270.3	-	727.5
S30-5 Test 1	198.1	161.0	750.3
S30-5 Test 2	201.5	171.2	744.6
S40-5 Test 1	167.6	141.5	602.6
S40-5 Test 2	161.1	138.9	610.8

The percent variance of the resultant deviatoric stresses for the repeated tests ranged between 1.7% and 6.3%, whereas the percent variance ranged between 0.5% and 1.4% for the peak pore water pressures (Table 5.2).

Corrected deviatoric stress and pore pressure with axial strain results for the triaxial compression tests under consolidation pressures (σ'_c) of 40, 150, and 300 kPa are presented in Figure 5.6.

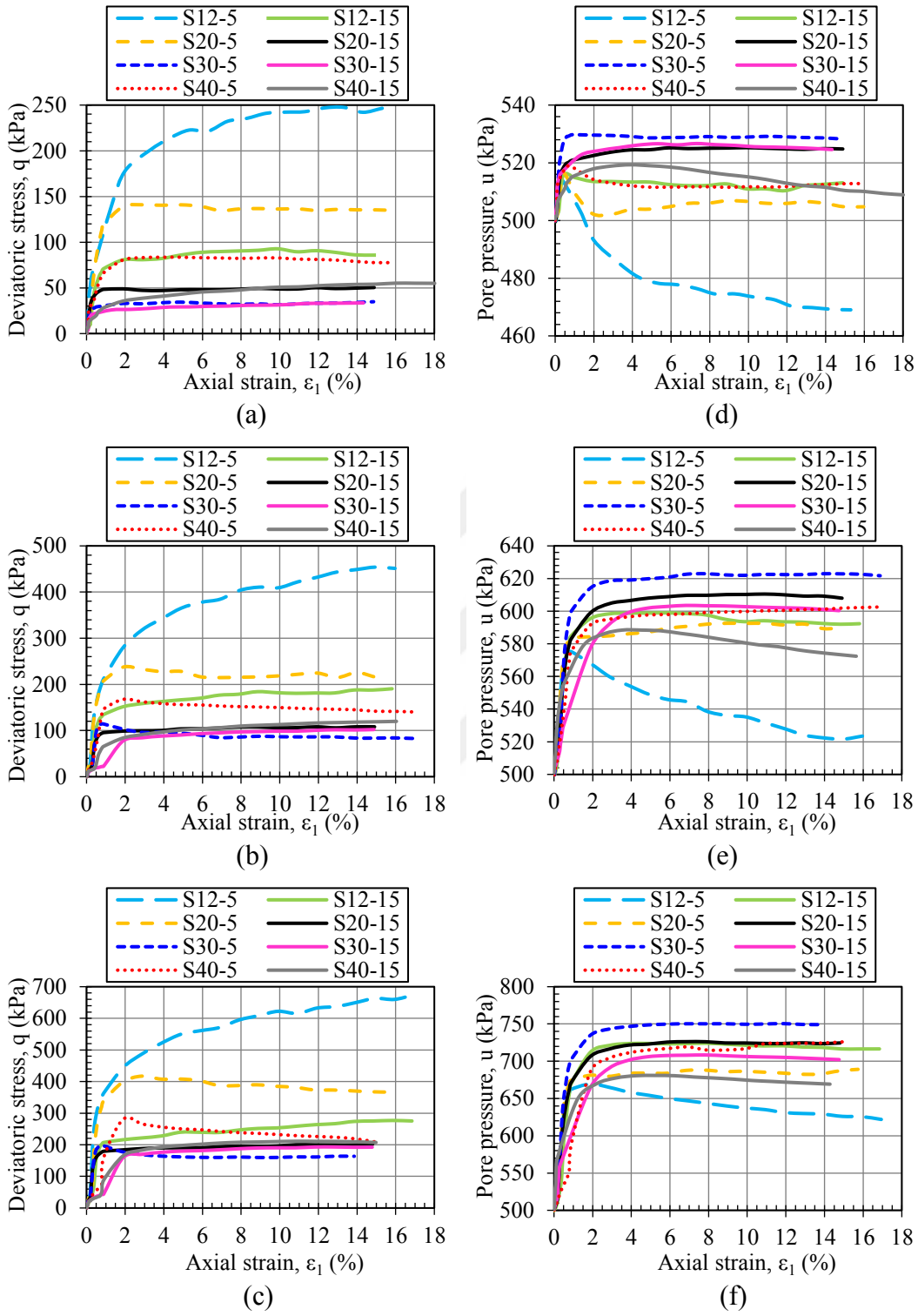


Figure 5.6. Deviatoric stress with axial strain for (a) σ'_c=40 kPa, (b) σ'_c=150 kPa, and (c) σ'_c=300 kPa; pore pressure with axial strain for (d) σ'_c=40 kPa, (e) σ'_c=150 kPa, and (f) σ'_c=300 kPa

5.3 Static Large Compression Tests

Unsubmerged and submerged compression tests were conducted on all CFM. Specimen preparation methodology, which is dynamically compacting the specimens at optimum water content, w_{opt} and to 95% of their standard Proctor dry densities with an initial height of 60 mm, was the same for both groups as described in Section 3.3.5.2. Unsubmerged tests were performed by applying loading stages directly after specimen preparation. The degree of saturation and initial void ratio of specimens were calculated by Equations 4.2 and 4.3 and presented in Table 5.3. The initial degrees of saturation after specimen preparation ranged between 58% and 78%. In submerged tests, on the other hand, specimens were submerged in water within their molds for a week, and compression tests were initiated while the specimen was immersed in water. Trial tests of bulk density and final moisture content on several CFM have shown that this process did not provide complete saturation of the specimens. Additionally, degrees of saturation at the end of the compression tests were calculated using the specimen's final water content and void ratio after compression (Table 5.3). Submerging the specimens in water increased the degrees of saturation from 57%-78% to 79%-93% at the end of the test. It can be inferred that degrees of saturation of the specimens after submersion and just before the start of the compression test should be lower than the reported degrees of saturation at the end of the test.

$$S_r(\%) = \frac{w \,.\, G_T}{e} . 100 \tag{4.2}$$

$$e = \frac{G_T \,.\, \rho_w}{\rho_{dry}} - 1 \tag{4.3}$$

where,

S_r : Degree of saturation

w : Moisture content of the specimen

G_T : Average specific gravity of the soil mixture

e : Global void ratio

ρ_w : Density of the water

ρ_{dry} : Dry density of the soil specimen

Table 5.3. Phase parameters of the specimens in compression tests

Soil code	Unsubmerged tests		Submerged tests	
	Global void ratio just before compression test, e_0	Initial degree of saturation, $S_{r(in)}$ (%)	Initial degree of saturation before submersion, $S_{r(in)}$ (%)	Degree of saturation at the end of the test, $S_{r(final)}$ (%)
S12-5	0.277	71	70	79
S12-15	0.333	58	57	80
S20-5	0.263	70	69	82
S20-15	0.370	70	74	90
S30-5	0.318	66	72	81
S30-15	0.435	70	74	88
S40-5	0.357	62	61	87
S40-15	0.498	78	78	93

Axial strains during the loading and unloading stages of the compression test were calculated as given in Equation 5.11.

$$\varepsilon_a = \frac{\Delta H_c}{H_0} \tag{5.11}$$

where,

ΔH_c : Change in height of the specimen during compression test

H_0 : Initial height of the specimen

Tests on two CFM, unsubmerged S40-5, and submerged S20-15 specimens, were performed twice to evaluate the repeatability of the compression results. Axial strain and displacement with time plots of the repeated tests for 40, 80, 160, 320, 640, 1280, 320, and 80 kPa loading stages are presented in Figure 5.7.

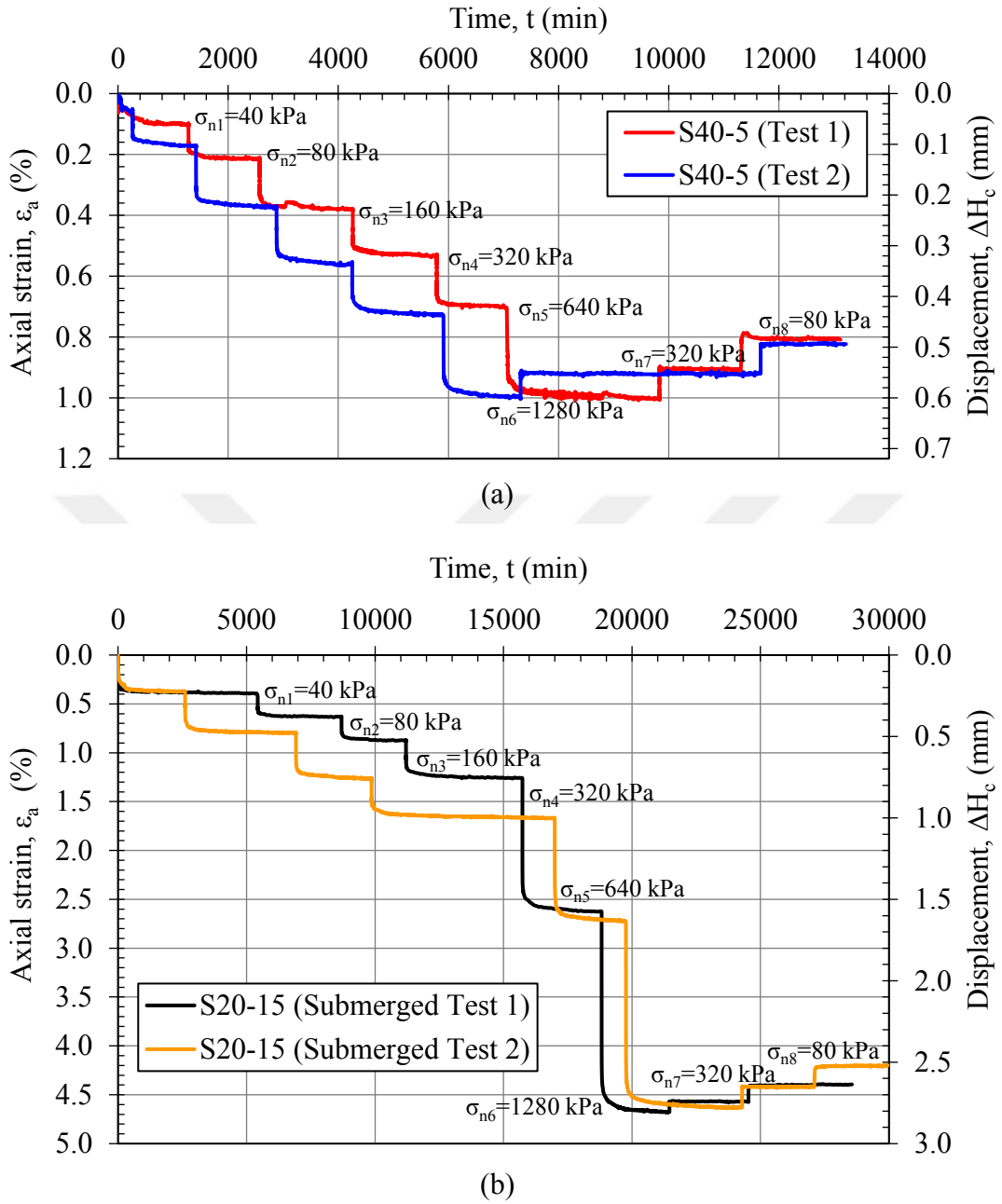


Figure 5.7. Axial strain with time plots of the repeated compression tests on CFM for (a) unsubmerged tests of S40-5, (b) submerged tests of S20-15

As can be seen from Figure 5.7, the vertical displacements of the repeated tests for the same loading stages varied between 0.01-0.07 mm for unsubmerged tests of S40-5 and 0.01-0.23 mm for submerged tests of S20-15. Therefore, the tests were considered repeatable, and one test was conducted for each CFM.

The view of the specimen in the mold and outside of the mold after compression tests are presented in Figure 5.8.



(a) (b)

Figure 5.8. (a) View of the specimen in the mold, (b) after the compression tests

Axial strain and displacement with time plots of all CFM for both unsubmerged and submerged tests are presented in Figure 5.9.

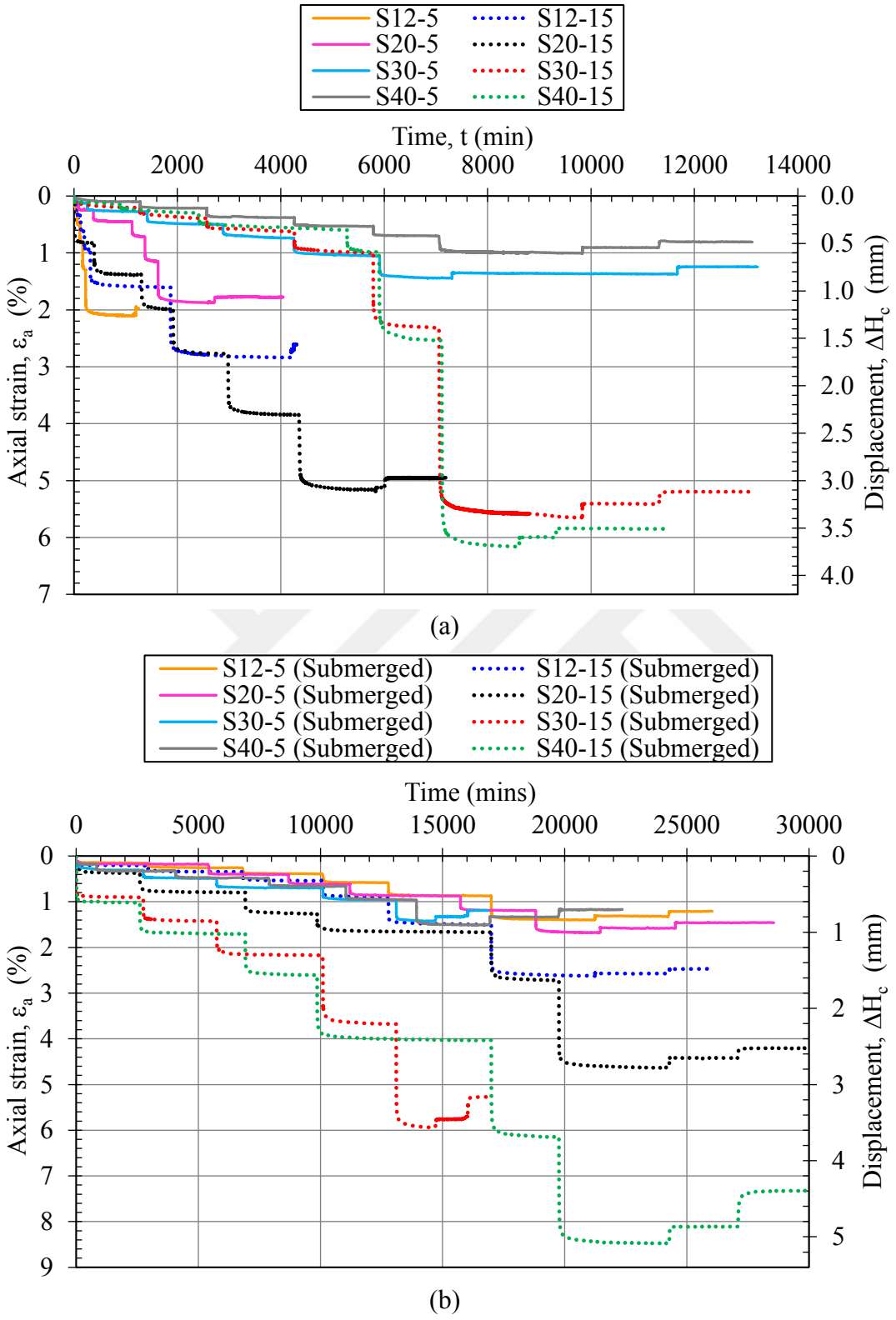


Figure 5.9. Compression test results for (a) unsubmerged tests, (b) submerged tests

5.4 Discussion of Results

5.4.1 Discussion of Unconfined Compression Test Results

Representative test results, indicated in Table 5.1, were used to evaluate the relationship between unconfined compressive strength (UCS), axial strain at failure, fines content, and plasticity indices of CFM. Compressive stress with axial strain plots of soil mixtures showed that an increase in fines content and plasticity increased the UCS of soil mixtures (Figure 5.10).

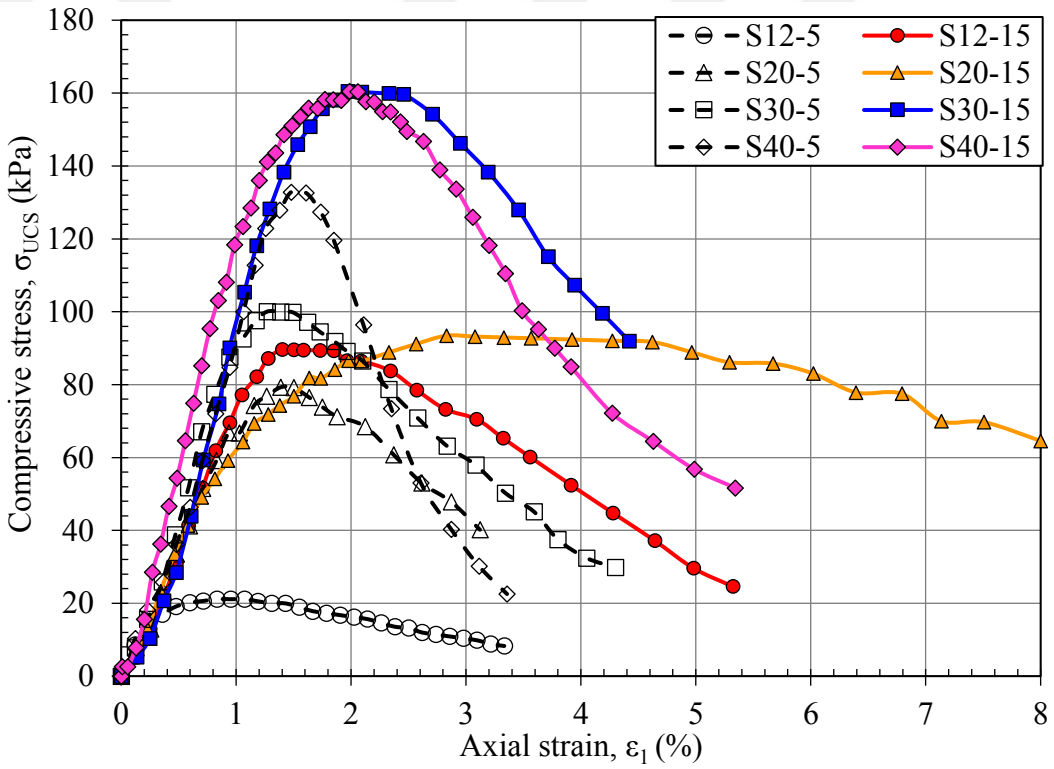


Figure 5.10. Compressive stress with axial strain plots of representative unconfined compression tests

Plots of UCS and axial strain at failure with fines content (FC) of representative tests are presented in Figure 5.11. There was an increasing compressive strength with fines content for all CFM, and the mechanical response was changed significantly

between fines content of 20% and 30% for CFM with PI=15% (Figure 5.11a). Post-peak behavior in compressive stress with axial strain (Figure 5.10) and axial strain at failure with fines content (Figure 5.11b) allowed observing the ductile/brittle response of the CFM with respect to each other. Higher PI for the same FC values increased axial strain at failure on all CFM. In general, an increase in FC for the same PI also increased the strain values at failure and more ductile response was observed. However, a higher strain at failure compared to other data was observed in S20-15 (FC=20%, PI=15%) (Figure 5.11b) as an apparent outlier. This outlier behavior in FC=20% specimens was also observed in other repeated tests. Besides, the rate of decrease in compressive stress after peak value was seen as the lowest in S20-15, which showed the most ductile behavior. Similarly, as described in Section 4.6.5, hydraulic conductivity test results of the S20-5 and S20-15 showed distinctly different behavior from other CFM specimens despite several repeated tests conducted and the same specimen preparation methodology being applied.

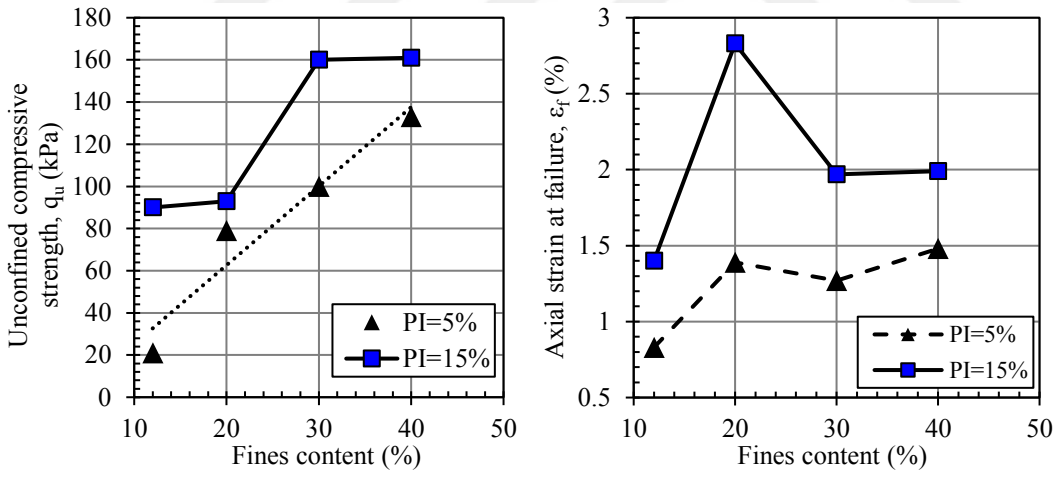


Figure 5.11. Representative test results for (a) unconfined compressive strength with fines content, (b) axial strain at failure with fines content

Unconfined compressive strength test is one of the quickest and commonly used laboratory tests in geotechnical practice. However, the suitability of this test for the evaluation of undrained shear strength for intermediate soils is still a debate.

Terzaghi et al. (1996) and Tanaka et al. (2001) stated that factors contributing to over and underestimation of the actual strength values such as sample disturbance, mode of shear, shear rate effect, anisotropy in strength balance each other to give a reasonably accurate estimation of the mobilized undrained shear strength for cohesive soils by using UCS test. However, Tanaka et al. (2001) added that this does not hold true for intermediate soils, and tests result in underestimating the actual values because the residual effective strength loss is too high to be compensated by other parameters.

Correlations have been proposed for Japanese intermediate soils by considering cohesionless particle content, plasticity index, or sample disturbance. Nakase et al. (1972) proposed a method for modifying the UCS test results of intermediate soils according to sand particle size and plasticity index. Tsuchida et al. (2020) described a "combined method" in which the design strength of intermediate soil is selected by comparing UCS and CU triaxial test results. Consolidation pressure in CU tests is selected depending on the in-situ vertical effective overburden stress. Soils are divided into clusters according to sampling quality. Design strength is determined using CU triaxial strength results reduced by coefficients or UCS values based on these clusters.

Whether the CFM will behave in a drained, partially-drained or undrained way in a MSEW is expected to be related to FC and PI values, as well as drainage, loading rate and conditions in the field. Therefore, UCS test results are not reported as undrained shear strength values for CFM in this study.

5.4.2 Discussion of Triaxial Compression Test Results

Triaxial compression test results and calculated parameters are summarized in Table 5.4. Modified Mohr-Coulomb failure envelopes of all CFM are presented in Figure 5.12. Failure envelopes were determined according to the peak deviatoric stresses in tests.

Table 5.4. Summary of the triaxial compression test results

Soil code	Consolidation pressure, σ'_c (kPa)	Peak deviator stress, q_{peak} (kPa)	Axial strain at failure, ε_f (%)	Excess pore water pressure at failure, u_{excess} (kPa)	Pore pressure parameter at failure, A_f	Void ratio		Secant deformation modulus at 50% of the peak strength, E_{50} (MPa)
						After saturation e	After consolidation e_c	
S12-5	40	247.6	13.3	-30.2	-0.12	0.277	0.275	11.8
	150	454.1	15.0	21.6	0.05	0.279	0.267	20.6
	300	674.1	16.9	121.9	0.18	0.277	0.262	48.8
S12-15	40	92.8	9.9	11.0	0.12	0.320	0.317	11.6
	150	190.6	15.8	92.3	0.48	0.317	0.291	22.7
	300	275.2	14.9	216.5	0.79	0.321	0.278	28.1
S20-5	40	140.9	2.9	2.1	0.02	0.252	0.251	17.6
	150	237.4	1.9	84.3	0.36	0.251	0.236	33.9
	300	417.1	2.9	179.7	0.43	0.252	0.233	50.9
S20-15	40	49.4	8.9	25.1	0.51	0.373	0.371	16.5
	150	107.6	8.9	110.2	1.02	0.369	0.336	14.5
	300	200.2	10.8	223.9	1.12	0.367	0.313	40.0
S30-5	40	34.4	4.9	28.6	0.83	0.315	0.312	14.3
	150	114.3	0.8	95.1	0.83	0.310	0.289	15.9
	300	198.1	0.8	194.7	0.98	0.314	0.277	36.7
S30-15	40	33.5	14.3	24.6	0.73	0.420	0.412	11.0
	150	102.1	14.9	100.3	0.98	0.417	0.374	4.3
	300	193.0	12.8	204.4	1.06	0.422	0.355	7.4
S40-5	40	83.6	4.9	11.6	0.14	0.346	0.343	9.3
	150	167.6	1.9	91.6	0.55	0.347	0.332	15.2
	300	280.7	1.9	186.6	0.67	0.345	0.322	17.5
S40-15	40	55.2	16.0	10.1	0.18	0.488	0.482	3.3
	150	119.9	16.0	72.4	0.60	0.490	0.444	7.5
	300	211.2	11.0	174.1	0.82	0.491	0.414	9.6

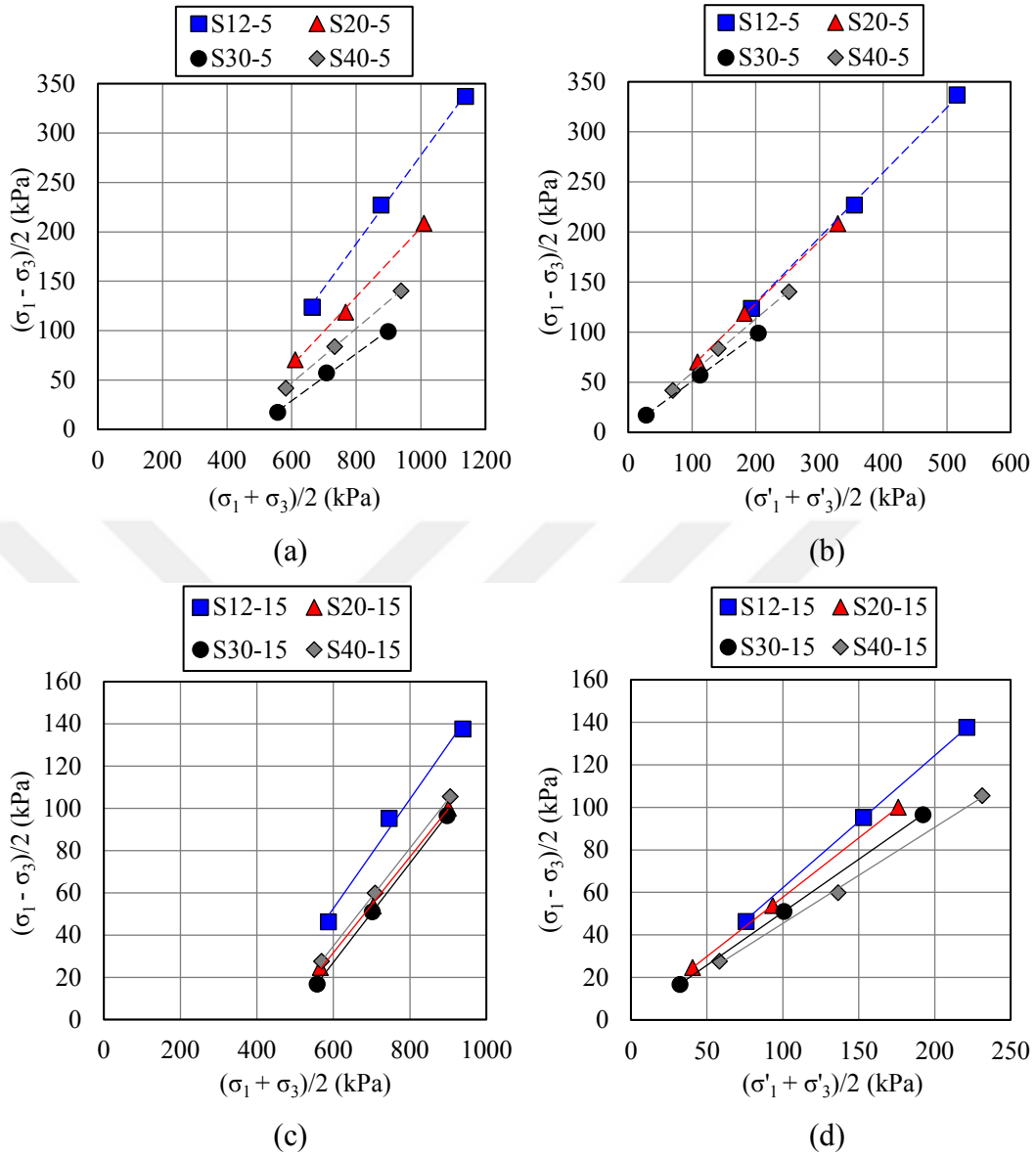


Figure 5.12. Modified Mohr-Coulomb failure envelopes for total stress (a), (c), and effective stress (b), (d)

Effective principal stresses were calculated by subtracting measured average pore water pressures from total pressures when the peak (maximum) deviatoric stress is obtained, i.e., at failure. Modified total stress and effective stress envelopes of all CFM showed a linear correlation with consolidation pressure. The square of the correlation coefficient, R^2 value, was between 0.99 and 1 for all envelopes (Figure 5.12).

Total and effective shear strength parameters for CU triaxial tests were calculated from modified failure envelopes using Equations 5.12 and 5.13, and the results are presented in Table 5.5.

$$\phi = \sin^{-1}(\tan \alpha) \tag{5.12}$$

$$c' = \frac{\text{a}}{\cos \phi'} \tag{5.13}$$

where,

ϕ : Angle of internal friction

α : Slope of the modified Mohr-Coulomb envelope

c' : Effective cohesion

a : Intercept of the modified Mohr-Coulomb envelope with the y-axis

ϕ' : Effective angle of internal friction

Table 5.5. Shear strength parameters of coarse-fine mixtures from consolidated undrained triaxial compression tests

Soil code	Angle of internal friction, ϕ_{CU} (°)	Effective angle of internal friction, ϕ' (°)	Effective cohesion, c' (kPa)
S12-5	26.6	40.4	0
S12-15	15.0	38.4	0
S20-5	20.4	38.7	4.5
S20-15	13.1	33.9	2.3
S30-5	13.8	27.7	5.0
S30-15	13.6	29.9	0.9
S40-5	16.0	32.6	6.7
S40-15	13.4	26.9	0

As seen in Table 5.5, the angle of internal friction as a result of consolidated undrained tests varied between 13.4° and 26.6°, whereas the effective angle of internal friction varied between 26.9° and 40.4° for all CFM tested. As a general trend, increasing FC for the same PI, as well as increasing PI for the same FC, resulted in a decrease in both undrained and effective angle of friction values (Figure 5.13). For a given FC, PI=15% soils had a slightly less effective friction

angle (range between 2° to 6°) than PI=5% soils, except for S30-5. In CFM having PI=5%, a decrease in friction angle (both undrained and drained) was observed until FC=30%, afterwards an increase again in FC=40% (Figure 5.13).

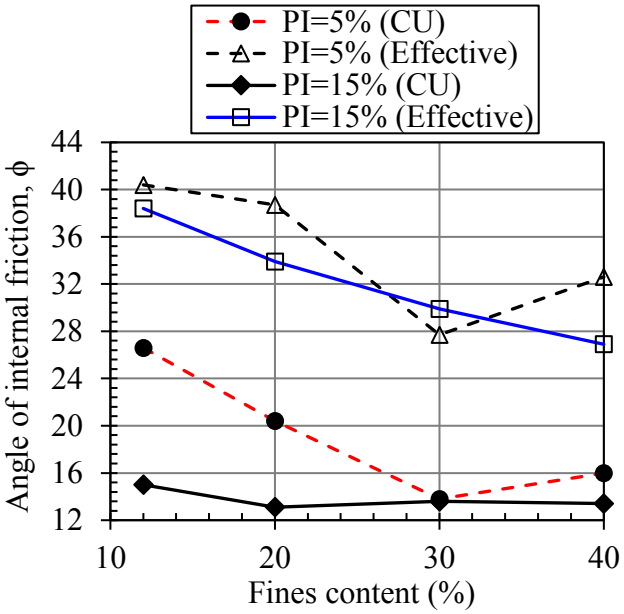
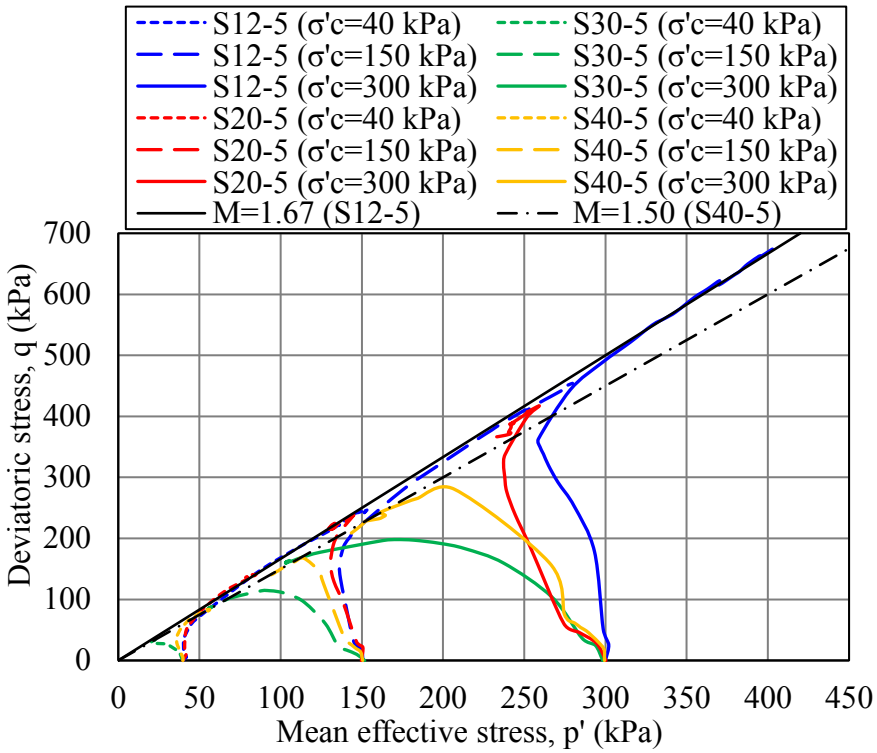


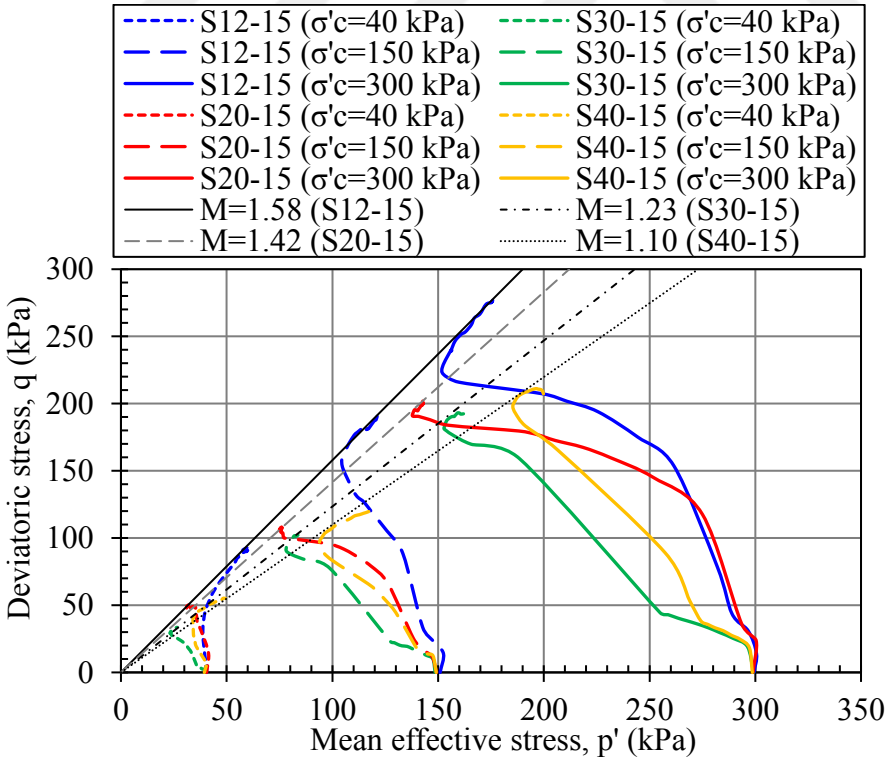
Figure 5.13. Variation of consolidated undrained and effective angle of internal friction with fines content

The effect of FC on the undrained friction angle was quite small for PI=15% compared to PI=5%. A significant variation in undrained friction angle can be seen between the CFM with PI=5% and PI=15% up to FC=20%, while the effect of PI decreased for higher FC than 30% (Figure 5.13). In addition, it was observed in Table 5.5 that cohesion intercept values of CFM with PI=5% were slightly more than PI=15%.

Stress paths of CFM are plotted in Figure 5.14, while the change in mean effective stress during the undrained triaxial tests is presented in Figure 5.15.

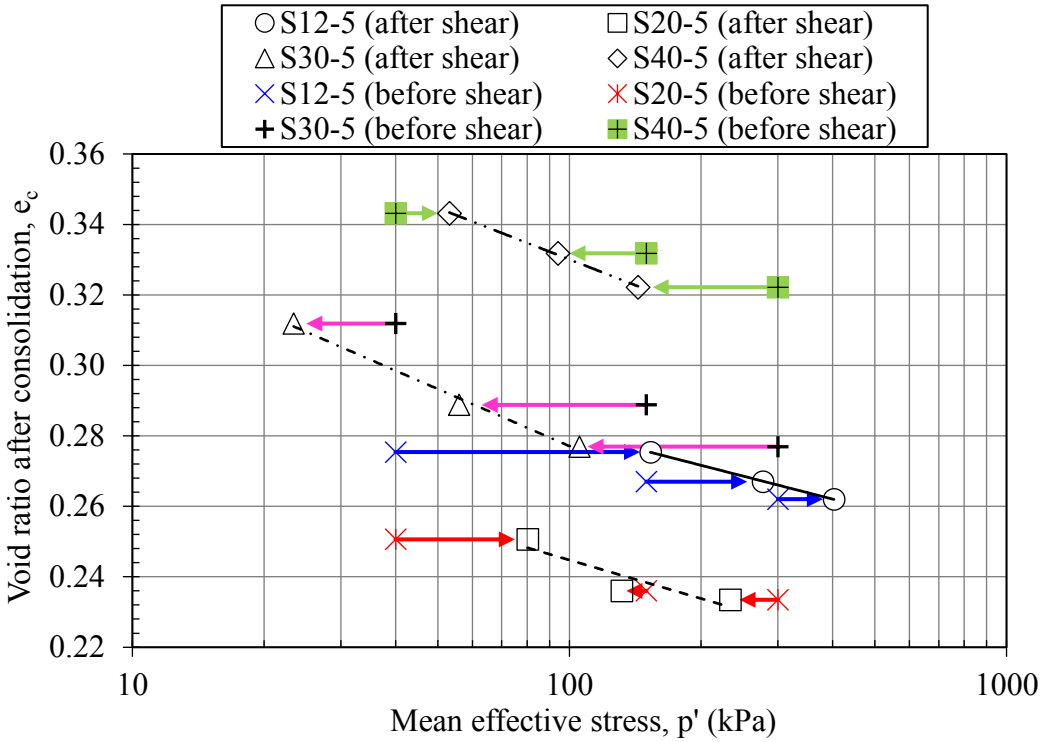


(a)

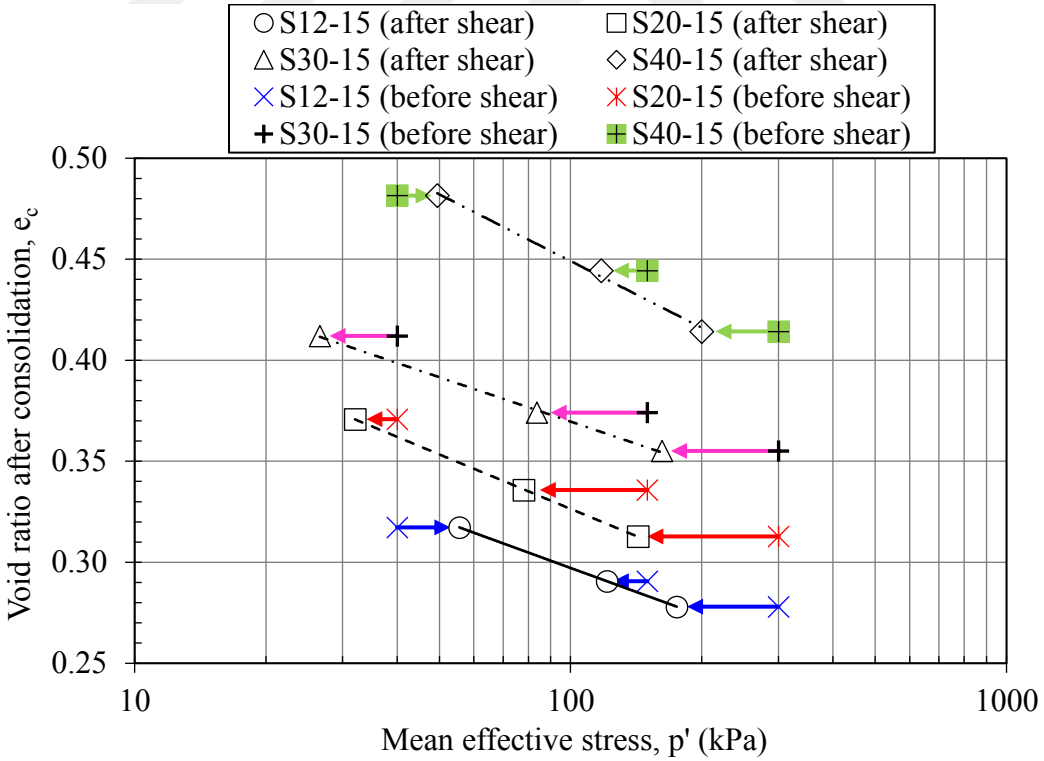


(b)

Figure 5.14. Stress paths during undrained triaxial tests for (a) PI=5%, (b) PI=15%



(a)



(b)

Figure 5.15. Mean effective stress change in e-p' space for (a) PI=5%, (b) PI=15%

Stress ratios at critical state, M (q/p') were drawn on p'-q space in Figure 5.14. M values are also presented in Table 5.6 and Figure 5.16 to evaluate the variation with fines content and plasticity index.

Table 5.6. Critical state parameters of coarse-fine mixtures from triaxial tests

Soil code	p'-q space	ν-p' space	
	Stress ratio at critical state, M	Intercept, Γ	Gradient, λ
S12-5	1.67	1.345	0.014
S12-15	1.58	1.455	0.034
S20-5	1.64	1.317	0.016
S20-15	1.42	1.506	0.039
S30-5	1.56	1.385	0.023
S30-15	1.23	1.516	0.032
S40-5	1.50	1.427	0.021
S40-15	1.10	1.668	0.048

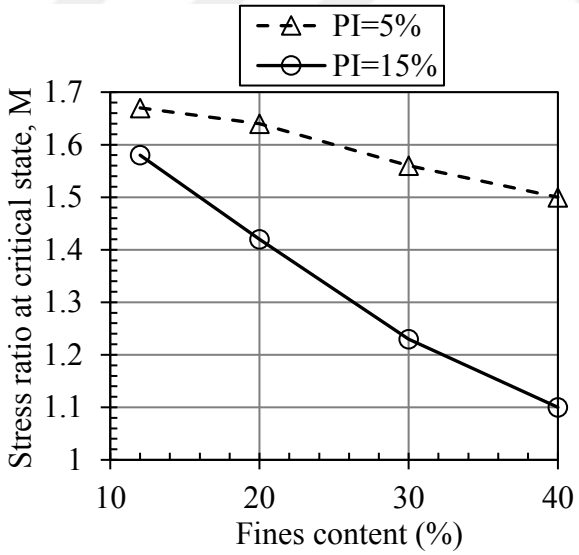


Figure 5.16. Variation of stress ratio at critical state with fines content and plasticity index

Stress ratios at critical state (M) were in a relatively narrow range for lower plasticity indices (between 1.50 and 1.67 for PI=5%, 1.10 and 1.58 for PI=15%). M values were directly proportional both with fines content and plasticity index (Figure 5.16). The change of M with FC for the same PI value was approximately linear. The rate of decrease of M with FC was sharper for higher PI values. The effect of PI on the variance of M values for the same FC increased with fines content. Therefore, undrained triaxial tests in this study show that PI is a more influential parameter for higher FC values in respect of shear strength response.

Mean effective stresses (p') at critical state and void ratio of the same CFM for different consolidation pressures showed an approximate linear correlation as seen in Figure 5.15. The square of the correlation coefficient, R^2 value, was 0.82 only for S20-5; it was between 0.99 and 1 for all other CFM. As a general trend, the gradient (λ) of the critical state line for a given PI slightly increased as FC increased (Figure 5.15 and Table 5.6). The gradient (λ) of the CFM with PI=15% was observed to be almost twice the gradient values of PI=5% for the same FC. In addition, the intercept of the critical state lines (Γ) also increased with FC and PI.

Undrained triaxial test results of CFM were classified into three groups according to the contractive-dilative tendencies of the specimens during shear in Figure 5.17, Figure 5.18, and Figure 5.19. These three groups were (i) specimens having low initial contraction followed by dilation, (ii) specimens having high initial contraction followed by dilation, and (iii) specimens having contraction. It should be noted that all CFM specimens were initially compacted at their 95% of standard Proctor dry densities.

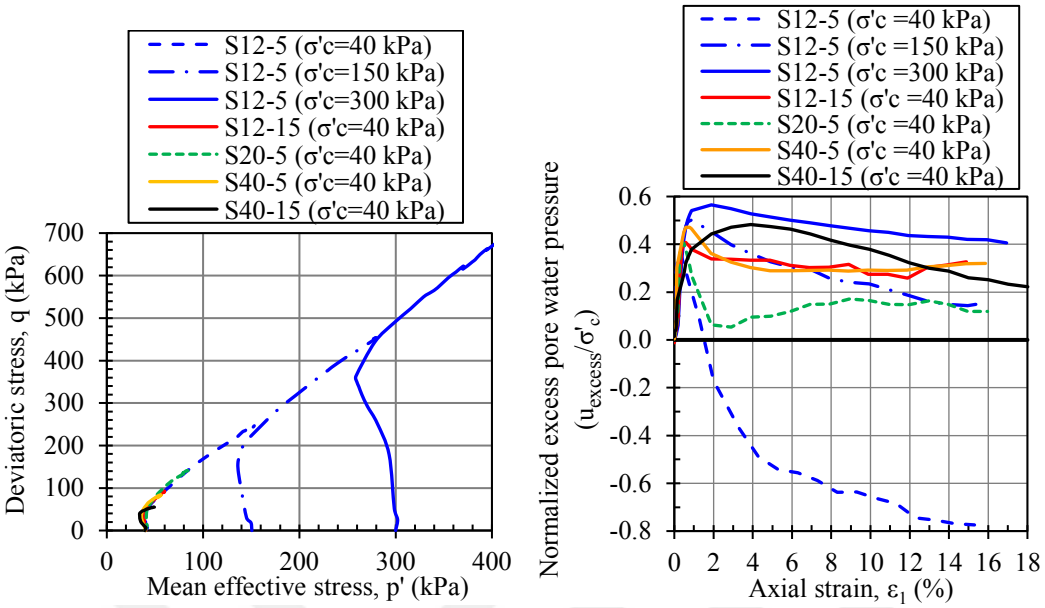


Figure 5.17. Specimens having low initial contraction followed by dilation in undrained triaxial tests

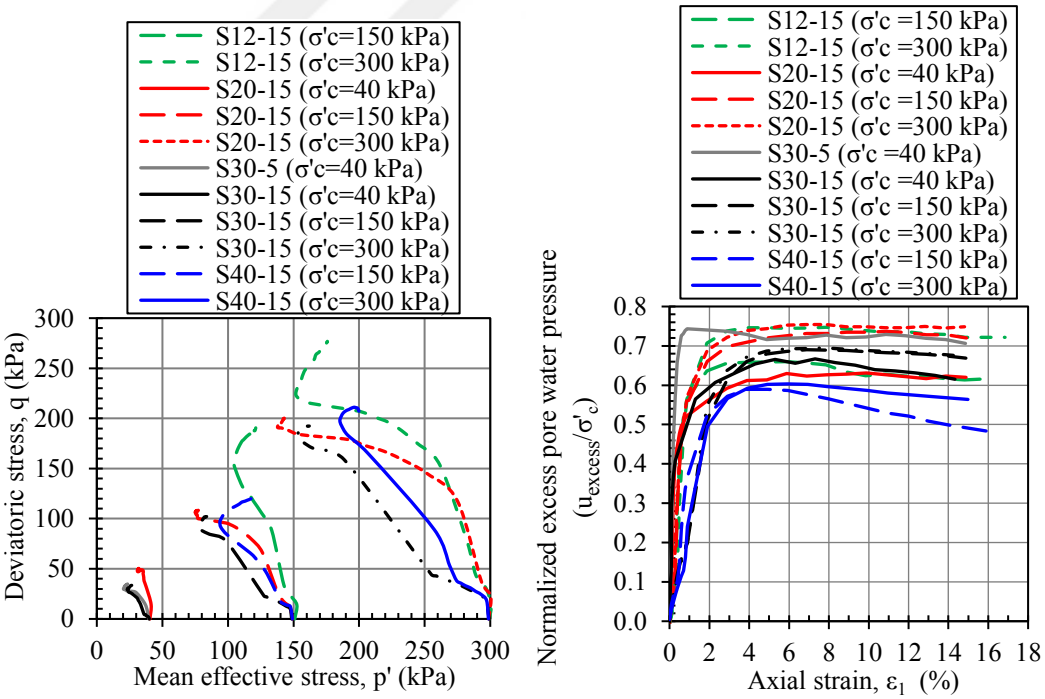


Figure 5.18. Specimens having high initial contraction followed by dilation in undrained triaxial tests

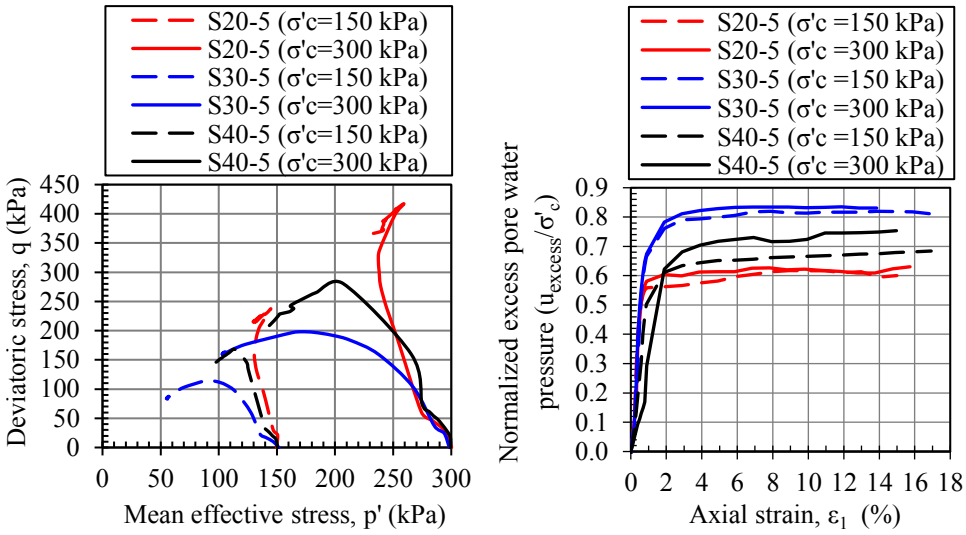


Figure 5.19. Specimens having contraction in undrained triaxial tests

Stress paths in p'-q space and pore water pressure variation were used to determine the volumetric tendencies of the CFM. Generated excess pore water pressure during undrained loading was normalized with the consolidation pressure. Thus, CFM specimens consolidated under different effective stresses could be compared.

Most of the tested CFM tended to contract first, followed by the dilative response, as shown in Figure 5.17 and Figure 5.18. CFM in this study were divided into three groups according to the similarity of their volumetric tendencies during undrained loading.

In Figure 5.17, specimens having relatively low initial contraction followed by dilation were grouped. Mean effective stresses decreased until a phase-transformation point (the boundary between contractive and dilative responses) and increased after that. Excess pore water pressures increased with initial contraction up to 37%-56% of initial consolidation pressures. Afterwards, excess pore water pressure decrease was observed to 12%-40% of initial consolidation pressures (Figure 5.17). As the only exception, S12-5 consolidated under 40 kPa effective stress showed negative excess pore water pressure during undrained loading. In addition to S12-5 at all consolidation pressures, specimens S12-15, S20-5, S40-5, and S40-15 consolidated under 40 kPa effective stresses had similar behavior.

Specimens having relatively high initial contraction followed by dilation, i.e., the group that especially included most of the CFM with PI=15% can be seen in Figure 5.18. Shapes of the stress paths resemble stress paths observed in Figure 5.17; however, a higher amount of mean effective stress decrease was observed in this group. In addition, excess pore water pressures increased with initial contraction up to 59%-75% of initial consolidation pressures. Afterwards, as an indicator of the following dilative response, excess pore water pressure decreased to ranges between 48% and 74% of initial consolidation pressures (Figure 5.18). A relatively smaller amount of excess pore water pressure decrease after the initial contraction was observed in this group compared to the specimens in Figure 5.17.

While S12-5 showed high dilation at all consolidation pressures, it was observed that tendencies of the volumetric response shifted towards contraction for PI=5% as FC increased. Specimens of S30-5 and S40-5 consolidated under 150, and 300 kPa effective stresses showed contractive response accompanied by strain-softening (Figure 5.6b,c), as seen in Figure 5.19. Stress paths of S20-5 for 150 and 300 kPa consolidation pressures differed slightly from S30-5 and S40-5, although S20-5 also showed a contractive response in its ultimate (residual) state. This can be interpreted as 20% fines content being the threshold where the volumetric tendency of the CFM with PI=5% switched from dilation-dominated response to contraction-dominated response with the accompanied FC increase. In terms of excess pore water pressure, a higher amount of increase was observed up to 2% axial strain, and pore water pressure continued to increase slightly thereafter. The increase in measured excess pore water pressure ranged between 62% and 83% of the specimens' consolidation pressures (Figure 5.19).

According to their initial contraction response, specimens in Figure 5.17 and Figure 5.18 were categorized as relatively low and high, respectively. Two normalized, unitless parameters were used to quantify the degree of initial contraction tendency, as in Figure 5.20.

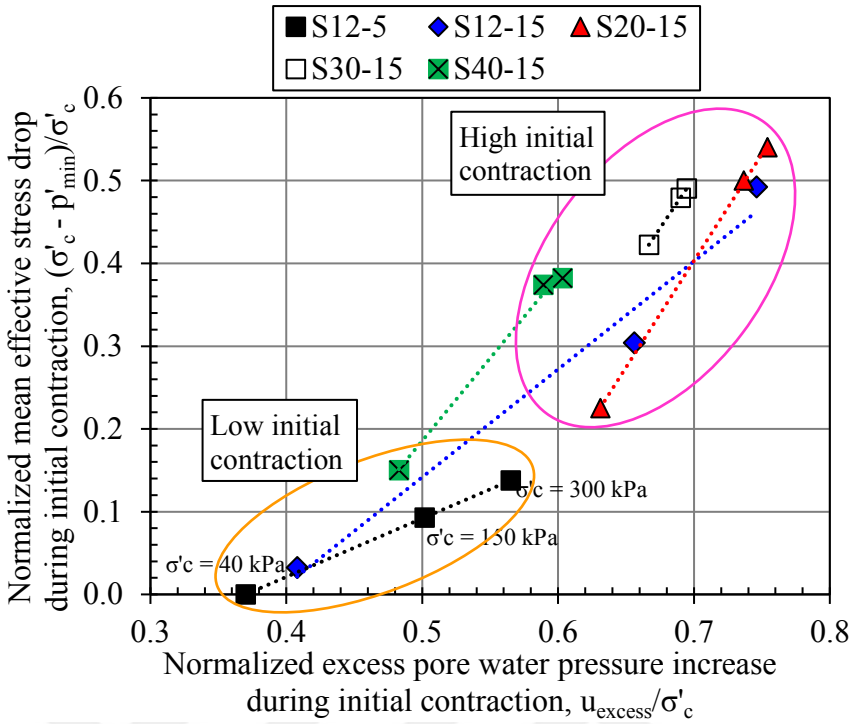


Figure 5.20. Quantification of initial contraction tendencies in undrained loading

In Figure 5.20, u_{excess}/σ'_c indicates excess pore water pressure increase, whereas $(\sigma'_c-p'_{min})/\sigma'_c$ expresses the amount of mean effective stress reduction during the initial contraction. In other words, these two parameters can be evaluated as a means of quantifying the increase of u_{excess} and decrease of p' relative to the consolidation pressure.

It was observed that the amount of initial contraction tendencies increased proportionally with the consolidation pressure for all CFM showing contraction (Figure 5.17, Figure 5.18, and Figure 5.20). Besides, both of the normalized parameters showed an approximately linear increase depending on the consolidation pressure, as seen in Figure 5.20. Accordingly, this study confirms that initial contractions up to the phase transformation point could be reasonably quantified by both the amount of increase in excess pore water pressure and decrease in mean effective stress.

In this study, initial contractions of CFM were classified as "relatively low" when u_{excess}/σ'_c was less than 0.56 and $(\sigma'_c-p'_{min})/\sigma'_c$ was less than 0.15 (Figure 5.20). When the normalized parameters were higher, a "relatively high" initial contraction of the CFM can be defined. After classifying the volumetric behavior of the tested CFM according to the criteria described above, the results are summarized in Table 5.7.

Table 5.7. Classification of coarse-fine mixtures according to contractive-dilative tendencies during undrained triaxial strength tests

Soil code	Consolidation pressure, σ'_c (kPa)	Low initial contraction followed by dilation	High initial contraction followed by dilation	Contraction
S12-5	40	✓		
	150	✓		
	300	✓		
S12-15	40	✓		
	150		✓	
	300		✓	
S20-5	40	✓		
	150			✓
	300			✓
S20-15	40		✓	
	150		✓	
	300		✓	
S30-5	40		✓	
	150			✓
	300			✓
S30-15	40		✓	
	150		✓	
	300		✓	
S40-5	40	✓		
	150			✓
	300			✓
S40-15	40	✓		
	150		✓	
	300		✓	

CFM with PI=15% showed high initial contraction followed by dilation independent of FC increase as a general trend. However, volumetric tendencies significantly varied with fines content for mixtures having a lower plasticity index (PI=5%) (Table 5.7). This conclusion suggests that FC and PI should not be evaluated as two independent parameters in terms of volumetric and related mechanical response.

Variation of axial strain at failure (ε_f) with fines content and plasticity index is presented in Figure 5.21. Peak strengths were reached at higher axial strain values in CFM with PI=15% compared to PI=5% independent from consolidation pressures. ε_f was higher than 9% for all CFM with PI=15%. For S12-5 (PI=5% and FC=12%), higher ε_f values were measured since strain-hardening behavior was observed at all consolidation pressures. Axial strains at failure (ε_f) were lower than 5% for CFM with PI=5% and higher FC than 12%. These mixtures showed strain-softening behavior towards an ultimate (residual) value after reaching a peak strength. The amount of strain-softening in S20-5, S30-5, and S40-5 was calculated with Brittleness Index (I_B) proposed by Bishop (1967) in Equation 2.37, and the results are presented in Figure 5.22. I_B = 1 would indicate significant brittleness, i.e., very small ultimate (residual, or critical state) shear strength and highly contractive response, whereas I_B = 0 indicates no brittleness, a dilative response, and no strain softening.

$$I_B = \frac{\tau_p - \tau_r}{\tau_P} \tag{2.37}$$

where,

τ_p : Peak (yield) shear strength

τ_r : Ultimate (residual or critical state) shear strength

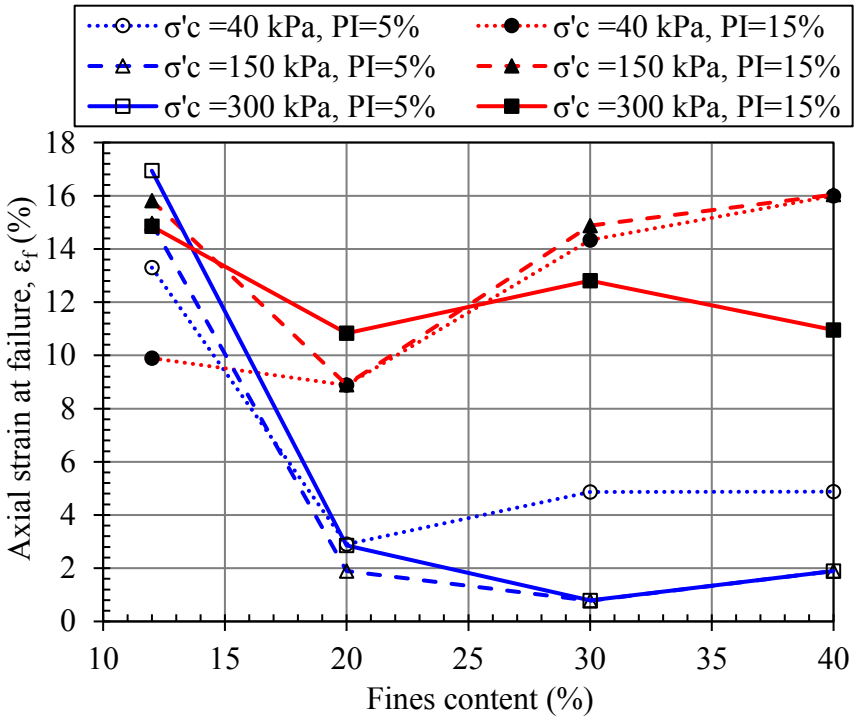


Figure 5.21. Variation of axial strain at failure with fines content and plasticity index in undrained triaxial tests

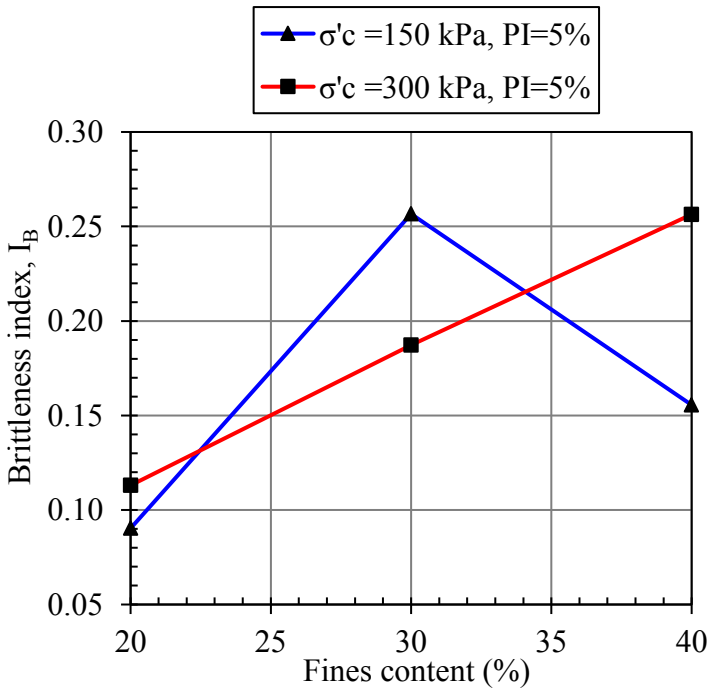


Figure 5.22. Brittleness indices of CFM with PI=5%

Brittleness indices ranged between 0.09 and 0.26 for S20-5, S30-5 and S40-5 consolidated under effective stresses of 150 and 300 kPa. There was a general trend of a slight increase in brittleness index with an increase in fines content.

Variation of pore pressure parameter at failure (A_f) with fines content and plasticity index is presented in Figure 5.23. The pore pressure parameter for saturated CFM was calculated by using Equation 5.14, as described by Skempton (1954).

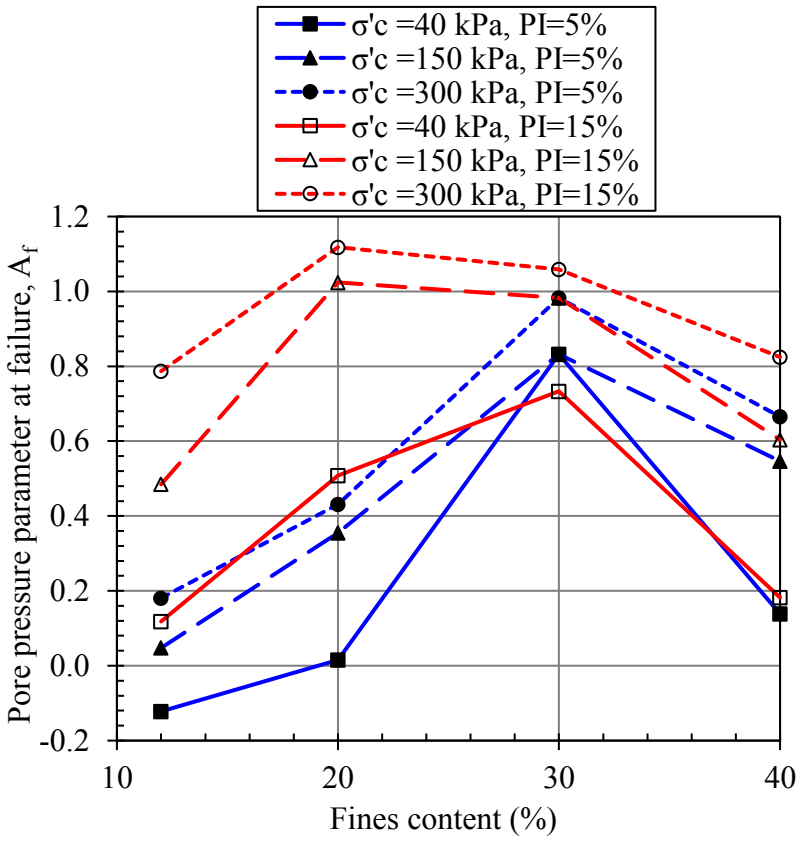


Figure 5.23. Pore pressure parameter at failure (A_f) with fines content

$$\Delta u = \Delta\sigma_3 + A(\Delta\sigma_1 - \Delta\sigma_3) \quad (5.14)$$

where,

Δu : Change in pore water pressure

A : Skempton's pore pressure parameter

$\Delta\sigma_3$: Change in minor principle stress

$\Delta\sigma_1$-$\Delta\sigma_3$: Change in deviatoric stress

As a general trend, CFM with a higher plasticity index (PI=15%) for the same FC had relatively larger A_f values than CFM having lower plasticity index (PI=5%). As the fines content increased from 30% to 40%, pore pressure change decreased, and the deviatoric stress at failure increased at all consolidation pressures for both PI=5% and PI=15%. Therefore, A_f increased up to FC=30% and decreased thereafter at FC=40%. Among all CFM tested, S12-5 consolidated under 40 kPa effective stress showed a negative A_f value (-0.12). As seen in Figure 5.23, all other CFM generally had A_f values positive and less than about 1.

Skempton (1954) classified soils having A_f in between 0 and 0.5 as lightly overconsolidated clays; 0.25 and 0.75 as compacted sandy clays, whereas 0.5 and 1 as normally consolidated clays. Bishop and Henkel (1962) reported that A_f values of 0 and 0.5 corresponded to loose sand and alluvial sandy clays, respectively. According to their experimentation on Weald and London clays, they also stated that A_f values between 0.5 and 1 corresponded to clays having OCR between 1 and 2. Terzaghi et al. (1996) reported that for contractive soils and rocks, values of A_f from slightly above zero to higher than 2 have been measured in the laboratory. A clay soil with an OCR of 6 to 8 may develop A_f values near zero. Highly overconsolidated dense soils and rocks, especially when they are under low effective confining stresses, can develop high negative shear-induced pore water pressures and can have A_f values of, typically, up to about -0.3 (Terzaghi et al., 1996). As a general trend in this study, CFM with PI=5%, having 12% to 20% fines, had A_f between 0 and 0.5, whereas fines content of 30% and 40% generally corresponded to 0.5 and 1. It was also seen from Figure 5.23 that the effect of PI on A_f was more dramatic at low FC values as 12% and 20%. In addition, it can be inferred that A_f, the relationship between the pore pressure generation associated with the deviatoric stress increase at failure, is co-dependent on parameters of FC and PI.

Lambe and Whitman (1969) stated that the secant deformation modulus is usually evaluated from zero to 0.5 or 0.33 of the peak deviatoric stress when referring to Young's modulus. This corresponds to the elastic range of the soil and common working stresses encountered in most geotechnical problems. One-half of the peak deviatoric stresses were reached at axial strain up to a maximum of 1.3% in this study.

Variation of the secant deformation modulus at 50% of the peak strength (E_{50}) and its normalized value according to consolidation pressure (E_{50}/σ'_c) were plotted with fines content and plasticity index in Figure 5.24 and Figure 5.25.

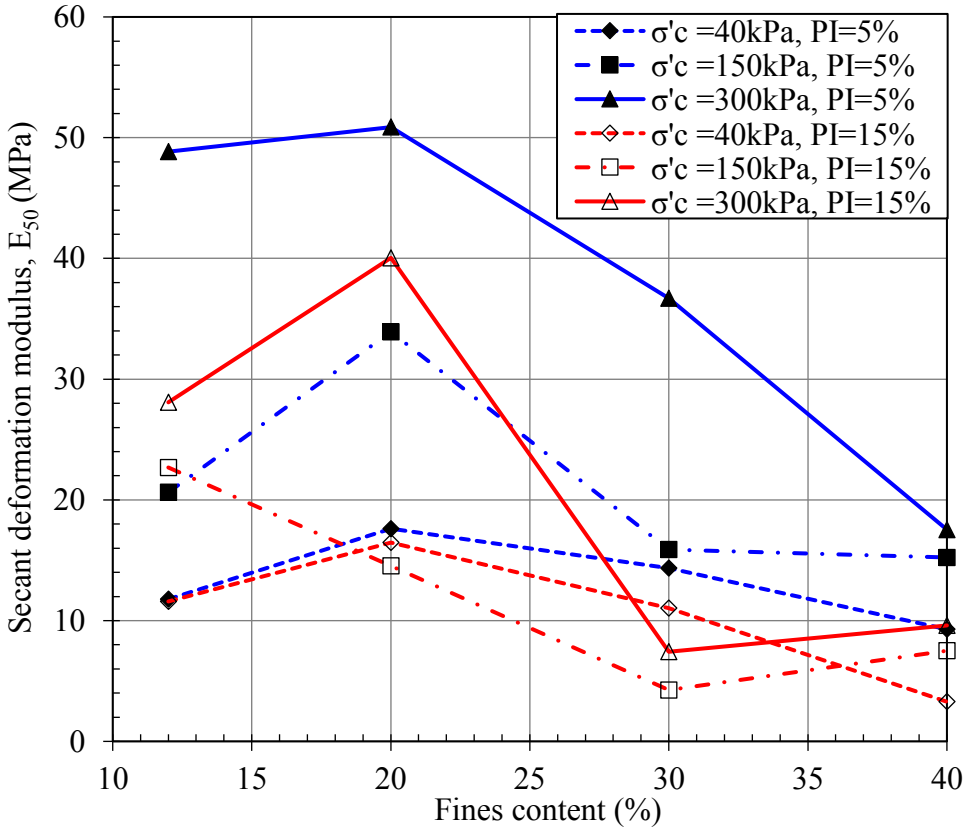


Figure 5.24. Secant deformation modulus at 50% of the peak strength with fines content and plasticity index

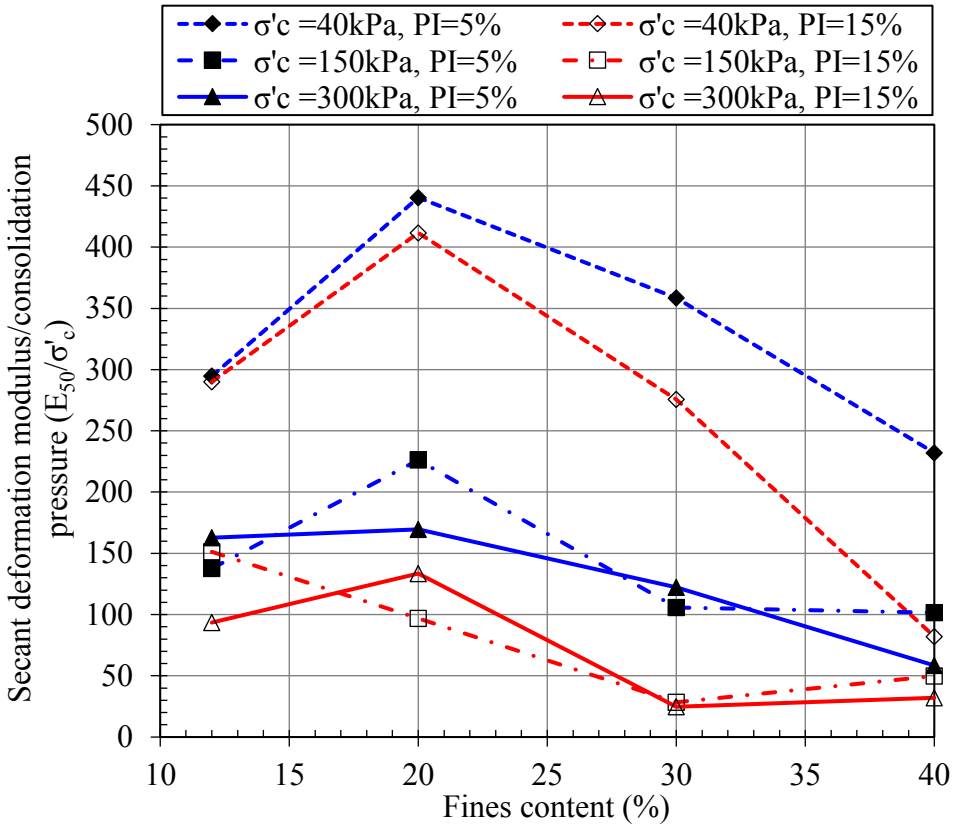


Figure 5.25. Normalized secant deformation modulus at 50% of the peak strength with fines content and plasticity index

Bowles (1988) presented the elastic modulus range of clayey soils based on their consistencies by pointing out that the intervals depend on factors such as confinement pressure and the method of testing (undrained, drained, unconfined, confined). According to Bowles (1988), the elastic deformation modulus of the soft, medium, and sandy clay range between 5-25 MPa, 15-50 MPa, and 25-250 MPa. E_{50} values for the tested CFM ranged between 4 MPa to 51 MPa in this study (Figure 5.24).

Values of the secant deformation modulus (E_s) at the axial strain values of 0.5%, 1%, 5%, 10%, and 15% for the tested CFM are presented in Figure 5.26, Figure 5.27, and Figure 5.28, depending on the fines content, plasticity index and, consolidation pressure.

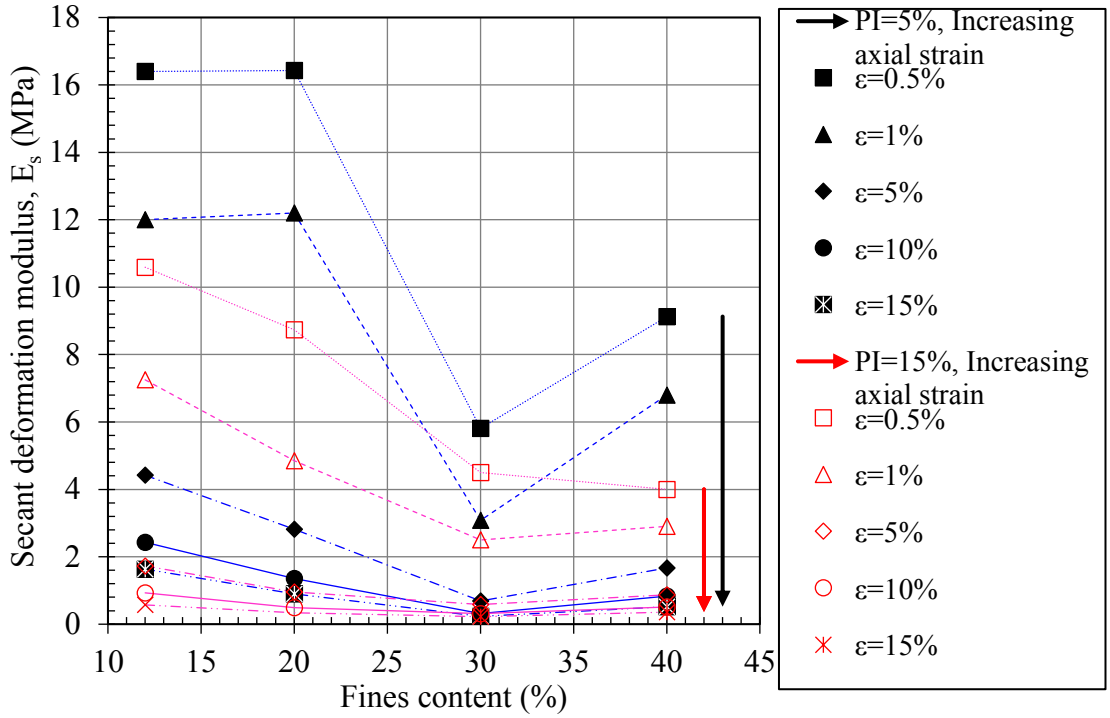


Figure 5.26. Secant deformation modulus with fines content for σ'_c=40 kPa

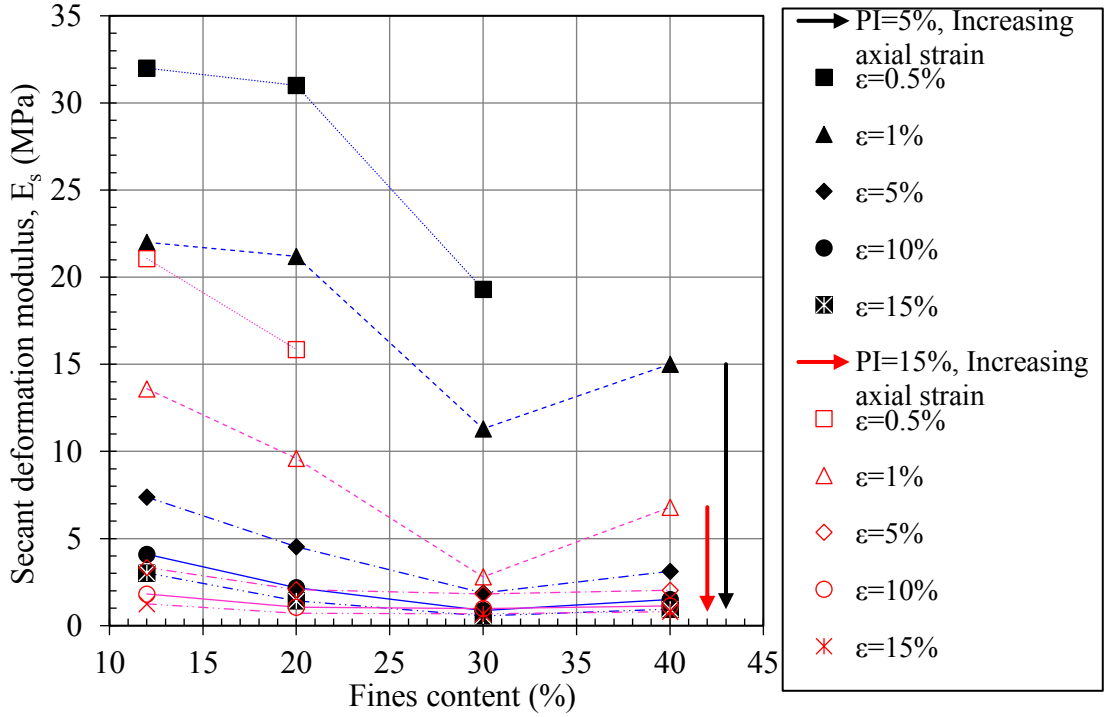


Figure 5.27. Secant deformation modulus with fines content for σ'_c=150 kPa

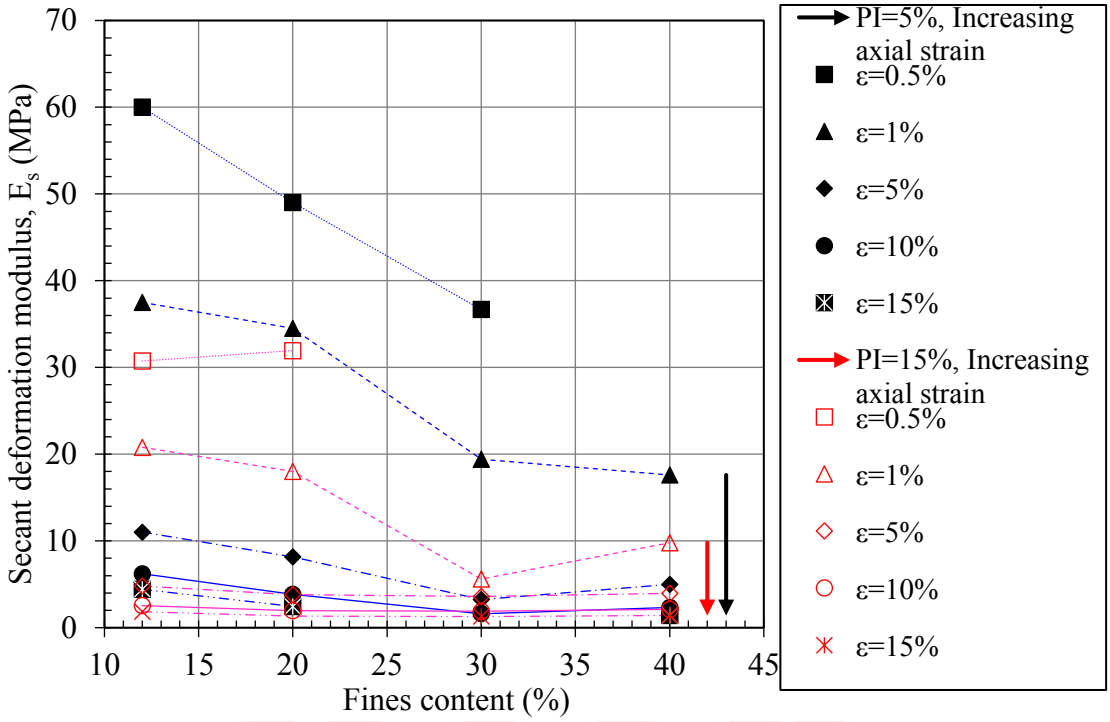


Figure 5.28. Secant deformation modulus with fines content for σ'_c=300 kPa

When PI=5% and PI=15% were compared for all consolidation pressures, CFM with a lower PI had a higher secant deformation modulus for all fines contents as expected. Decrease in the modulus with increasing axial strain for the same FC was larger for CFM with lower PI.

Secant deformation modulus observed at 0.5% axial strain was plotted against consolidation pressure in Figure 5.29. Deformation modulus ranged between 4 and 16.4 MPa for consolidation pressure (σ'_c) of 40 kPa; 15.8 and 32 MPa for σ'_c=150 kPa, and 30.7 and 60 MPa for σ'_c=300 kPa. It should be noted that the deformation modulus (at ε_1=0.5%) of S40-5, S30-15, and S40-15 for σ'_c=150 kPa and σ'_c=300 kPa were not included in Figure 5.27 and Figure 5.28. Because artifacts in tests at small strain values caused unrealistic deformation modulus, as shown in deviatoric stress and axial strain plots (Figure 5.30).

A general trend of decreasing secant deformation modulus was observed up to 30% fines content, then increased at 40% FC. According to the undrained triaxial test

results in this study, stiffness and peak strength were seen to be slightly larger at FC=40% as compared to FC=30%. This result was observed for both plasticities and all consolidation pressures for CFM specimens which were initially compacted to 95% of their standard Proctor dry densities at optimum moisture contents.

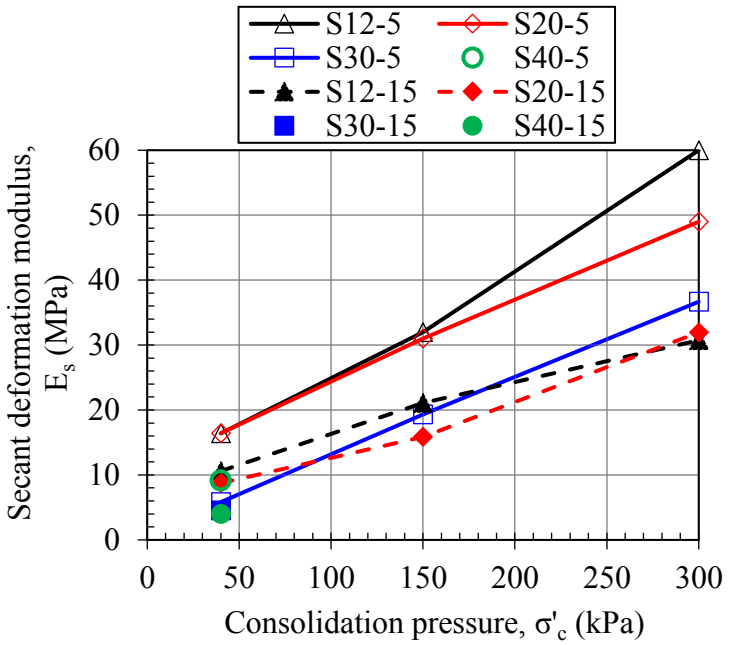


Figure 5.29. Secant deformation modulus at 0.5% axial strain with consolidation pressure

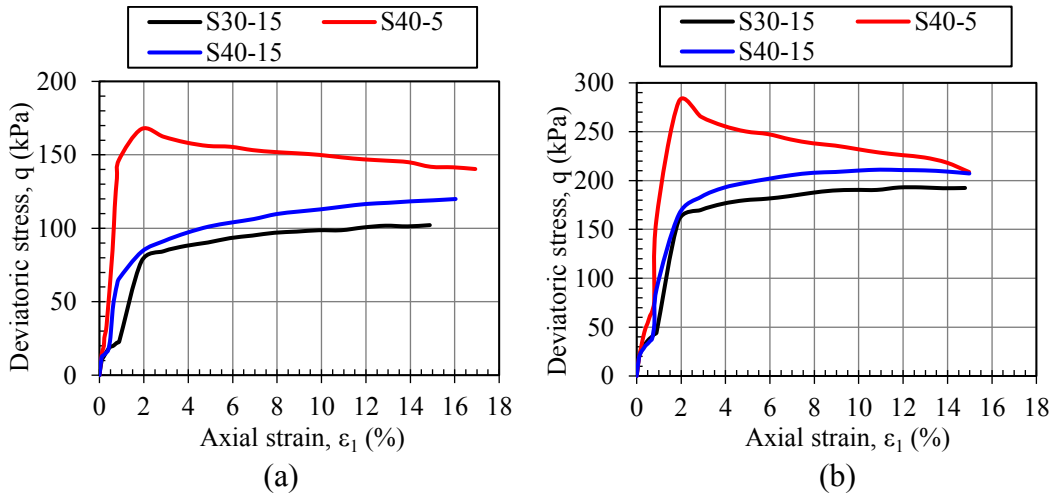


Figure 5.30. Deviatoric stress measurements in small strains for S40-5, S30-15, and S40-15 (a) σ'c=150 kPa, (b) σ'c=300 kPa

5.4.3 Discussion on Compressibility

5.4.3.1 Discussion of Consolidation of Saturated Specimens in Triaxial Test

Consolidation parameters and indirect estimation of hydraulic conductivities for CFM with PI=15% were calculated using Equations 2.20, 2.21, and 2.22, and the results are presented in Table 5.8. Sudden volumetric decreases were observed immediately after applying consolidation pressures in CFM with PI=5% (Figure 5.2). In addition, a significant part of the consolidation-related water discharge occurred quite rapidly. Therefore, derivation of the consolidation parameters for CFM with PI=5% was not considered appropriate.

30 kPa effective stress was applied on CFM specimens at the final stage of the saturation process as described in Section 3.3.4.3. Effective stress increases during consolidation under 40, 150, and 300 kPa were calculated accordingly.

$$k_{sat} = c_v . m_v . \gamma_w \tag{2.20}$$

$$m_v = \left(\frac{\Delta e}{1 + e_0}\right) \frac{1}{\Delta \sigma'} \tag{2.21}$$

$$c_v = \left(\frac{0.848 d^2}{t_{90}}\right) \tag{2.22}$$

where,

k_{sat} : Saturated hydraulic conductivity

c_v : Coefficient of consolidation

m_v : Coefficient of volume compressibility

γ_w : Unit weight of water

Δe : Void ratio change during consolidation

$\Delta \sigma'$: Effective stress increase during consolidation

d : Drainage distance

t_{90} : Time corresponding to 90% of the primary consolidation is completed

The results for the estimation of saturated hydraulic conductivity by using the formulations of consolidation were compared with the measured saturated hydraulic conductivity of the CFM in Section 4.6.5.1 (Figure 4.15).

Table 5.8. Consolidation parameters of saturated CFM specimens with PI=15%

Soil code	Consolidation pressure, σ'_c (kPa)	Void ratio after saturation, e	Void ratio after consolidation, e_c	Coefficient of volume compressibility, m_v (1/kPa)	Coefficient of consolidation, c_v (cm^2/s)	Hydraulic conductivity, k_{sat} (cm/s)
S12-15	40	0.320	0.317	2.0×10^{-4}	1.9×10^{-1}	3.69×10^{-6}
	150	0.317	0.291	1.7×10^{-4}	2.6×10^{-1}	4.19×10^{-6}
	300	0.321	0.278	1.2×10^{-4}	3.9×10^{-1}	4.58×10^{-6}
S20-15	40	0.373	0.371	1.3×10^{-4}	2.3×10^{-1}	2.88×10^{-6}
	150	0.369	0.336	2.0×10^{-4}	2.0×10^{-1}	4.02×10^{-6}
	300	0.367	0.313	1.5×10^{-4}	8.6×10^{-2}	1.24×10^{-6}
S30-15	40	0.420	0.412	5.6×10^{-4}	6.3×10^{-2}	3.44×10^{-6}
	150	0.417	0.374	2.6×10^{-4}	2.7×10^{-2}	6.67×10^{-7}
	300	0.422	0.355	1.8×10^{-4}	1.6×10^{-2}	2.76×10^{-7}
S40-15	40	0.488	0.482	4.2×10^{-4}	3.3×10^{-3}	1.35×10^{-7}
	150	0.490	0.444	2.5×10^{-4}	3.4×10^{-3}	8.49×10^{-8}
	300	0.491	0.414	1.9×10^{-4}	4.3×10^{-3}	8.07×10^{-8}

The coefficients of consolidation (c_v) for the CFM presented in Table 5.8 were below the c_v ranges given for the clays in the literature except S40-15. NAVFAC DM 7.1 (2022) states c_v intervals for disturbed and undisturbed clay samples according to their liquid limit. According to NAVFAC DM 7.1 (2022) for LL=42% (LL of S40-15, Table 4.6), c_v values correspond to 8 m^2/year (2.5×10^{-3} cm^2/s) and 44 m^2/year (1.4×10^{-2} cm^2/s) for virgin compression and recompression lower bound for undisturbed samples, respectively. As seen in Table 5.8, calculated c_v values for S40-15 were closer to the values reported for the virgin compression range of undisturbed samples. Calculated c_v values for S30-15 (LL=40%), on the other hand, were slightly above the recompression lower bound for undisturbed samples according to the NAVFAC DM 7.1 (2022). In terms of coarse-fine mixtures' c_v values in this study, fines content of 30% to 40% at PI=15% can be considered as the threshold at which normally-consolidated clay-like behavior begins to be observed.

The final volumetric strains of the CFM observed at the end of the consolidation are presented with fines content and plasticity index in Figure 5.31. Volumetric strains were calculated according to the amount of the measured discharged volumes in consolidation, as explained in Section 5.2.1.

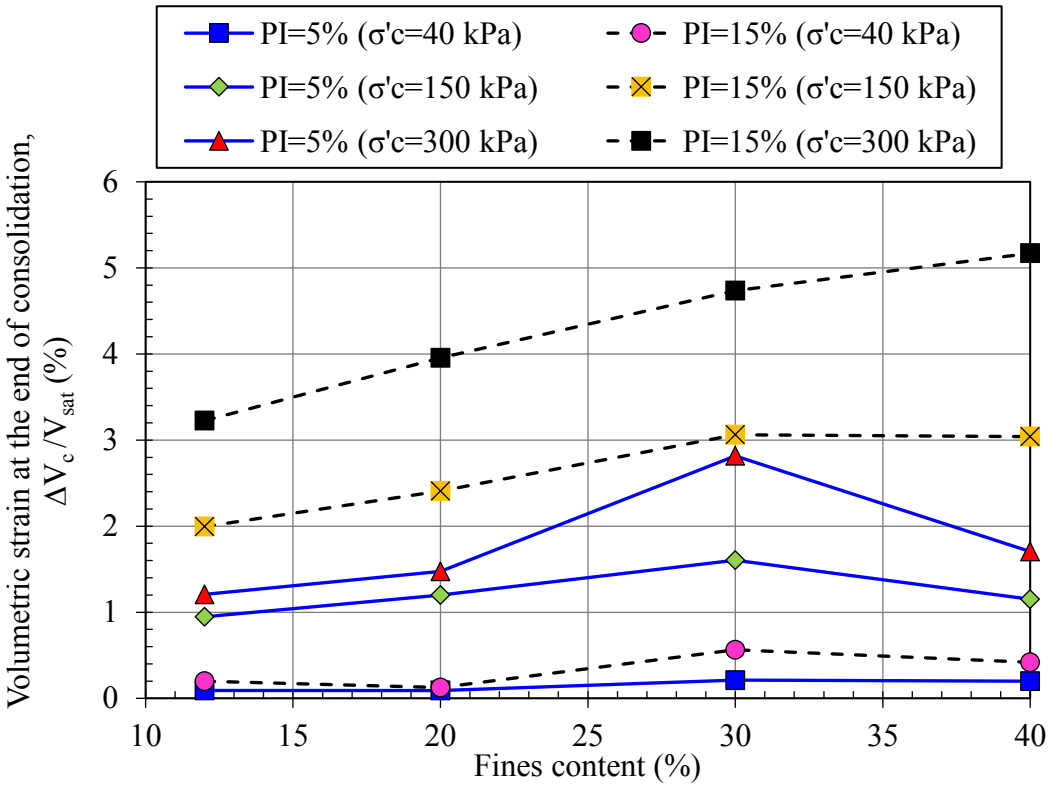


Figure 5.31. The final volumetric strain of all CFM at the end of the consolidation

As a general trend, an increase in the volumetric strain was observed with consolidation pressure, fines content, and plasticity index, as expected. The effect of consolidation pressure on volumetric strain increase seemed to be more significant for more plastic soils (Figure 5.31). The volumetric strain difference between PI=15% and PI=5% increased slowly with FC, and it was finally found to be three times at FC=40% and σ'_c=300 kPa. Consolidation under effective stresses of 40, 150, and 300 kPa caused a decrease in saturated volumes of specimens ranging between 0.09% to 2.8% for PI=5%; 0.1% to 5.2% for PI=15%. An increase in percent

volumetric strain up to FC=30% and a slight decrease thereafter to FC=40% was observed, more prominently in CFM with PI=5% (Figure 5.31).

Changes in the values of intergranular relative density with respect to fines content and plasticity index under different consolidation pressure are presented in Figure 5.32.

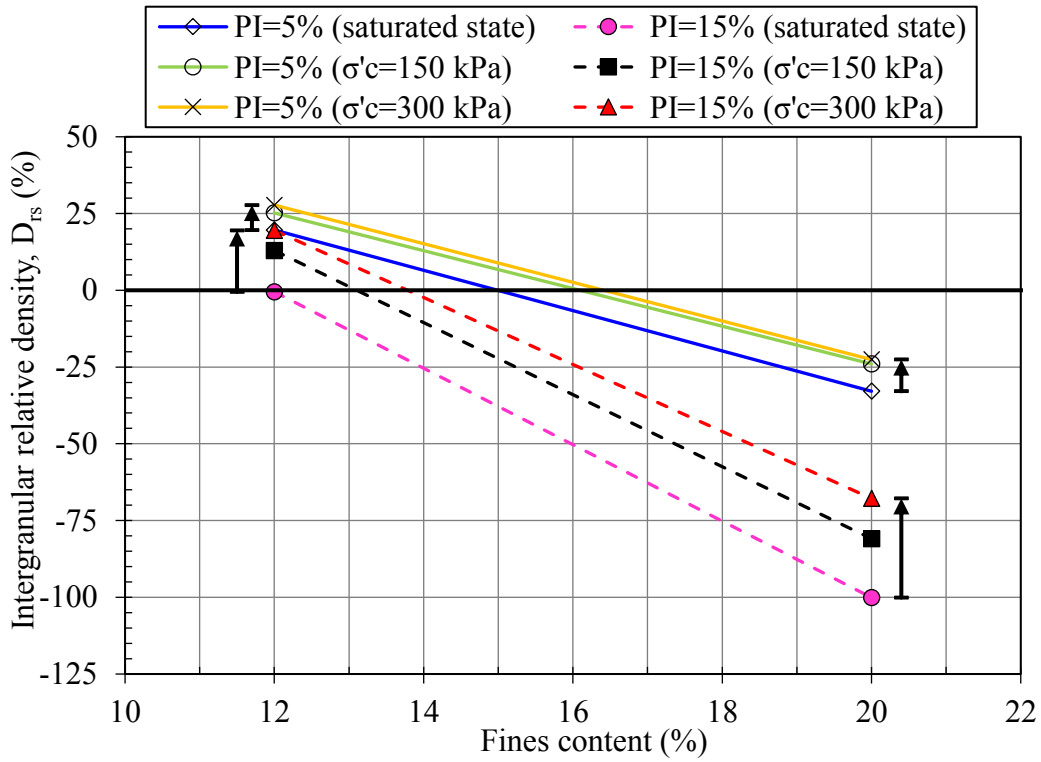


Figure 5.32. Change in intergranular relative density with fines content for different consolidation pressures

Intergranular relative density is the modified relative density which is a measure of the compactness degree of the coarse fraction in a soil mixture relative to the minimum and maximum densities of the coarse fraction (Equation 2.7). When the intergranular void ratio reaches the maximum void ratio of the coarse fraction, coarse particles start to be apart from each other. This transition from coarse-grained to fine-grained domination in terms of particle packing can be distinguished with intergranular relative density being zero.

Intergranular relative density values at 12% and 20% fines content were connected by a straight line to visualize the approximate threshold fines content in the transition zone, although there was no other data between 12% and 20% fines content, and that the relation in Figure 5.32 may not be linear. Fines content at transition increased with the increasing consolidation pressure, as seen in Figure 5.32. Corresponding to the intergranular relative density value of zero, threshold FC was determined as 15% for PI=5% and 12% for PI=15% at the saturated state, indicating that compacted saturated CFM having larger FC values may, most likely, have a more clay-like consolidation behavior. It was observed that it increased to 16.5% for PI=5% and approximately 14% for PI=15% under 300 kPa consolidation pressure. Because the CFM in this study was initially prepared by compacting the specimens up to 95% of their standard Proctor densities, void ratio change under increasing effective stress was relatively smaller. Therefore, changes in intergranular void ratio, intergranular relative density, and consequently variation of the threshold FC were smaller. In terms of particle packing, threshold FC variation associated with the effective stress increase can be expected to be more significant in soils with higher void ratios.

An increase in effective confining pressure resulted in higher intergranular relative density (D_{rs}) for the same specimen (Figure 5.32). In other words, coarse skeleton inside the soil mixture gets closer to each other and become more effective in force transfer at higher stress states while other variables are constant. Intergranular relative density could be evaluated to quantify the increasing effect of coarse particles in the force transfer mechanism. For S12-5, D_{rs} increased from 19.5% to 27.8% for saturated state and σ'_c=300 kPa, respectively, while it increased from 0% to 19.5% for S12-15 (Figure 5.32).

The change in intergranular relative density for CFM with PI=15% was in a higher range than CFM with PI=5%, as seen in Figure 5.32. In addition, intergranular relative density values for the same mixture became closer to each other for PI=5% compared to PI=15% with the increase of the consolidation pressure (Figure 5.32). This can be explained by the saturated void ratios and void ratio variation being greater at PI=15% than at PI=5%.

5.4.3.2 Discussion of Static Large Compression Tests

Displacement and axial strain with time plots for unsubmerged and submerged tests of CFM are presented in Figure 5.9. Cumulative percent axial strain observed at the end of each loading stage for CFM with PI=5% and 15% were tabulated in Table 5.9 and Table 5.10, respectively.

Table 5.9. Cumulative percent axial strain observed at the end of each loading stage for CFM with PI=5%

Soil code	Axial strain, ε_a (%)							
	S12-5		S20-5		S30-5		S40-5	
	*UT	**ST	*UT	**ST	*UT	**ST	*UT	**ST
Stage 1 Loading (σ_{n1}=40 kPa)	0.17	0.15	0.11	0.18	0.13	-	0.10	0.18
Stage 2 Loading (σ_{n2}=80 kPa)	0.30	0.26	0.25	0.40	0.28	0.31	0.22	0.33
Stage 3 Loading (σ_{n3}=160 kPa)	0.51	0.39	0.45	0.62	0.50	0.49	0.38	0.48
Stage 4 Loading (σ_{n4}=320 kPa)	0.83	0.59	0.72	0.88	0.74	0.70	0.53	0.66
Stage 5 Loading (σ_{n5}=640 kPa)	1.30	0.87	1.15	1.19	1.05	0.96	0.71	0.96
Stage 6 Loading (σ_{n6}=1280 kPa)	2.10	1.40	1.88	1.67	1.44	1.43	1.00	1.49
Stage 7 Unloading (σ_{n7}=320 kPa)	2.08	1.33	1.87	1.58	1.37	1.33	0.91	1.33
Stage 8 Unloading (σ_{n8}=80 kPa)	1.97	1.21	1.78	1.46	1.25	1.19	0.81	1.17

*UT: Unsubmerged tests
**ST: Submerged tests

Table 5.10. Cumulative percent axial strain observed at the end of each loading stage for CFM with PI=15%

Soil code	Axial strain, ε_a (%)							
	S12-15		S20-15		S30-15		S40-15	
	*UT	**ST	*UT	**ST	*UT	**ST	*UT	**ST
Stage 1 Loading (σ_{n1}=40 kPa)	0.15	0.21	0.83	0.37	0.21	-	0.15	1.02
Stage 2 Loading (σ_{n2}=80 kPa)	0.35	0.35	1.38	0.79	0.40	0.91	0.30	1.70
Stage 3 Loading (σ_{n3}=160 kPa)	0.62	0.54	1.99	1.27	0.62	1.42	0.60	2.60
Stage 4 Loading (σ_{n4}=320 kPa)	0.95	0.89	2.77	1.66	1.00	2.17	0.99	4.03
Stage 5 Loading (σ_{n5}=640 kPa)	1.61	1.51	3.85	2.72	2.31	3.68	2.54	6.15
Stage 6 Loading (σ_{n6}=1280 kPa)	2.84	2.62	5.16	4.63	5.65	5.93	6.17	8.47
Stage 7 Unloading (σ_{n7}=320 kPa)	2.73	2.57	5.12	4.42	5.41	5.76	6.00	8.11
Stage 8 Unloading (σ_{n8}=80 kPa)	2.61	2.47	4.95	4.20	5.20	5.27	5.85	7.32

*UT: Unsubmerged tests
**ST: Submerged tests

Normal stresses in loading stages were applied between 40 to 1280 kPa, and it was 1280 to 80 kPa in unloading. Cumulative axial strains for the maximum stress applied (stage 6 - σ_{n6}=1280 kPa) for the CFM with PI=5% were in the range of 1.00%-2.10% and 1.40%-1.67% for unsubmerged and submerged tests, respectively. No significant difference in axial strain values was observed for CFM having PI=5% despite the fines content increase and submersion of the specimens.

For the CFM with PI=15%, on the other hand, axial strains observed under the maximum vertical stress were in the range of 2.84%-6.17% and 2.62%-8.47% for unsubmerged and submerged tests, respectively (Table 5.10). A considerable

increase in axial strain was observed with fines content at the loading stage in which the maximum stress was applied. The increase in axial strain from FC=12% to FC=20% was more drastic than other fines contents. In addition, submersion of S30-15 and S40-15 (CFM with higher fines content) increased the axial strains under the maximum stress by 0.3% and 2.3%, respectively.

Plots of void ratio and normal stress for unsubmerged and submerged compression tests are presented in Figure 5.33 and Figure 5.34. Axial displacements at the end of each loading stage were considered for the void ratio calculations using Equation 4.3.

$$e = \frac{G_T \cdot \rho_w}{\rho_{dry}} - 1 \tag{4.3}$$

where,

e : Global void ratio

G_T : Average specific gravity of the soil mixture

ρ_w : Density of the water

ρ_{dry} : Dry density of the soil specimen

As a general trend, unsubmerged and submerged e-logσ_n plots of CFM with PI=5% were observed to be similar for the same fines content (Figure 5.33a and Figure 5.34). The void ratio of specimens with PI=5% varied in a narrow range compared to PI=15%, as no significant settlement increase was observed with the increase of FC.

While the void ratio variation with normal stress for unsubmerged and submerged tests of S12-15 and S20-15 was observed to be similar to each other, differences were seen for S30-15 and S40-15. An increase in the degree of saturation increased the amount of total displacements for both S30-15 and S40-15. However, the slope of the compression line for submerged tests was observed to be smaller. This can be explained by the fact that higher displacements were observed in submerged tests at all loading stages compared to unsubmerged tests. Settlements of unsubmerged tests

for S30-15 and S40-15 increased after 320 kPa of normal stress (Figure 5.33b).

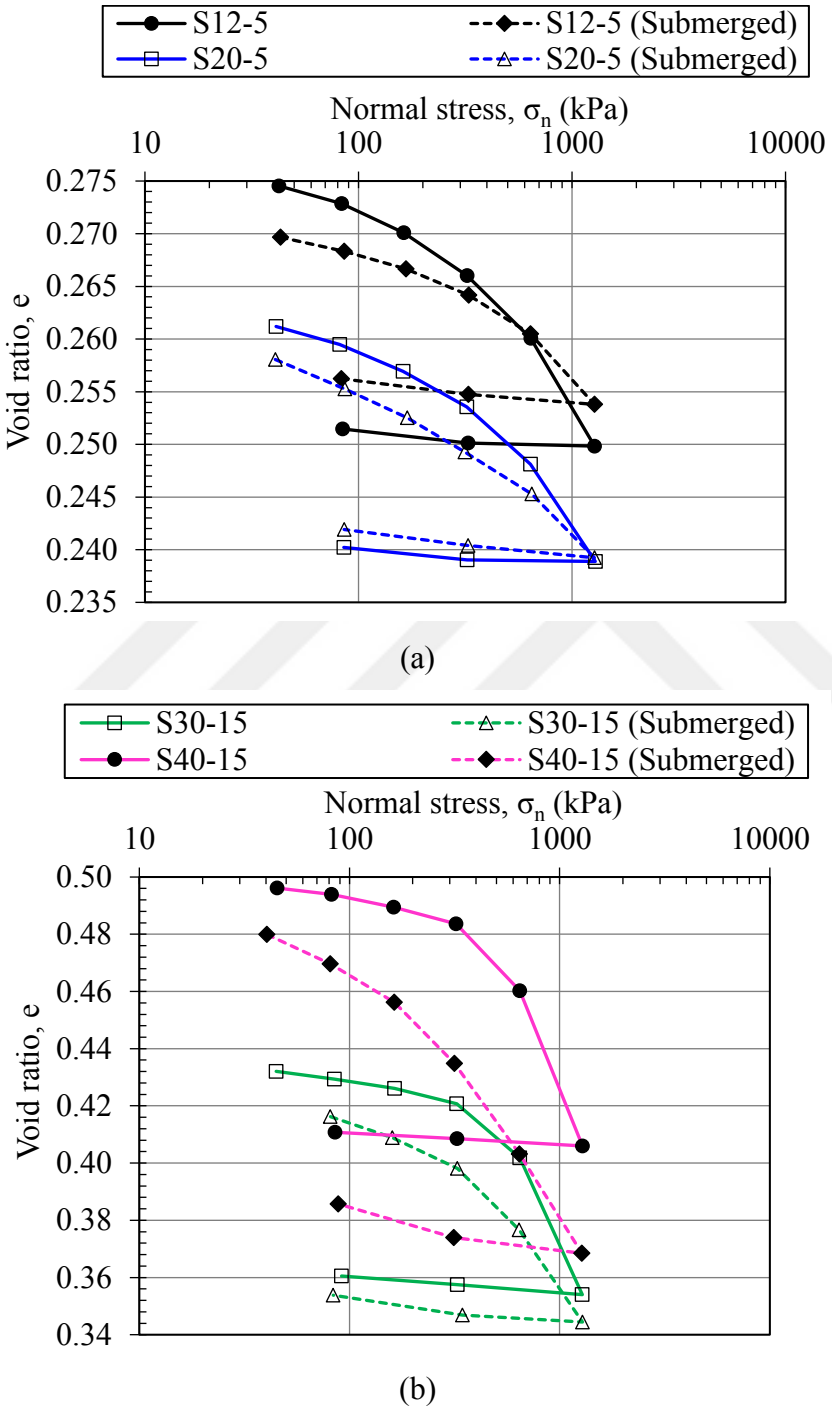


Figure 5.33. Void ratio change with normal stress for unsubmerged and submerged compression tests of (a) S12-5 and S20-5, (b) S30-15 and S40-15

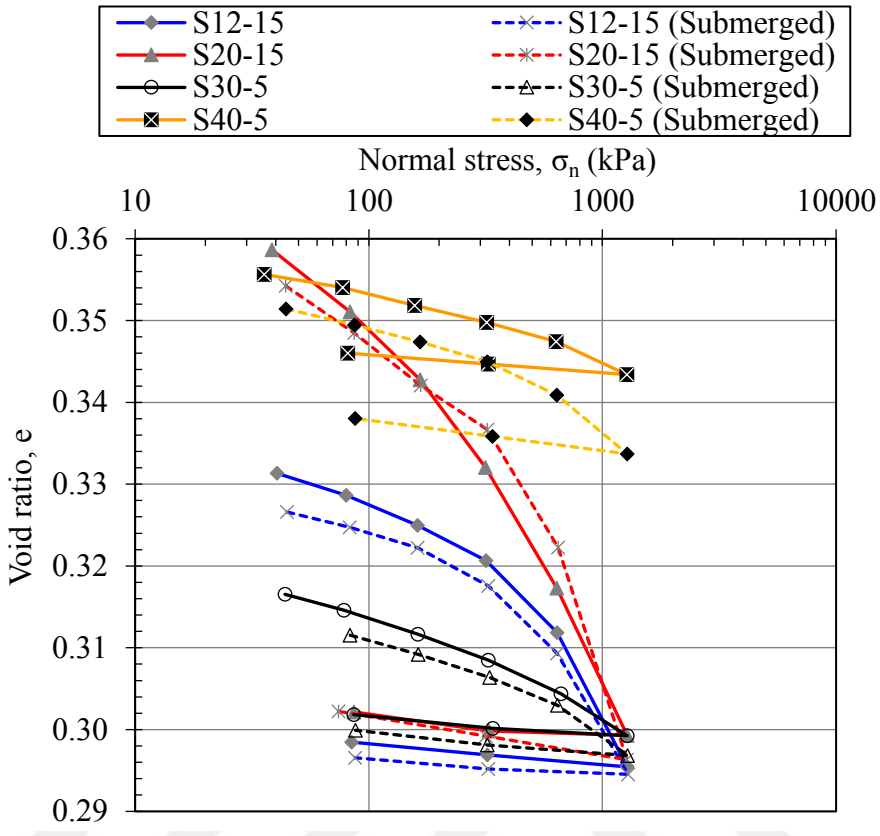


Figure 5.34. Void ratio change with normal stress for unsubmerged and submerged compression tests of S12-15, S20-15, S30-5 and S40-5

Compression index (C_C) and rebound index (C_s) were calculated from the e-logσ_n plots. Their variations are presented with fines content and plasticity index in Figure 5.35 and Figure 5.36. Compression indices (C_C) were determined according to the slope of the compression line between 640 kPa and 1280 kPa, whereas rebound indices (C_s) were determined between 1280 kPa and 80 kPa. Compression indices of CFM with PI=5% changed in a relatively smaller range. C_C varied between 0.013 and 0.034 for unsubmerged tests, whereas 0.021 and 0.024 for submerged tests (Figure 5.35). Mesri and Vardhanabhuti (2009) studied the compression characteristics of granular materials on different sand mineralogies and particle shapes. Ranges of C_C for PI=5% and the normal stress intervals in this study correspond to compression indices reported by Mesri and Vardhanabhuti (2009) for quartz sand.

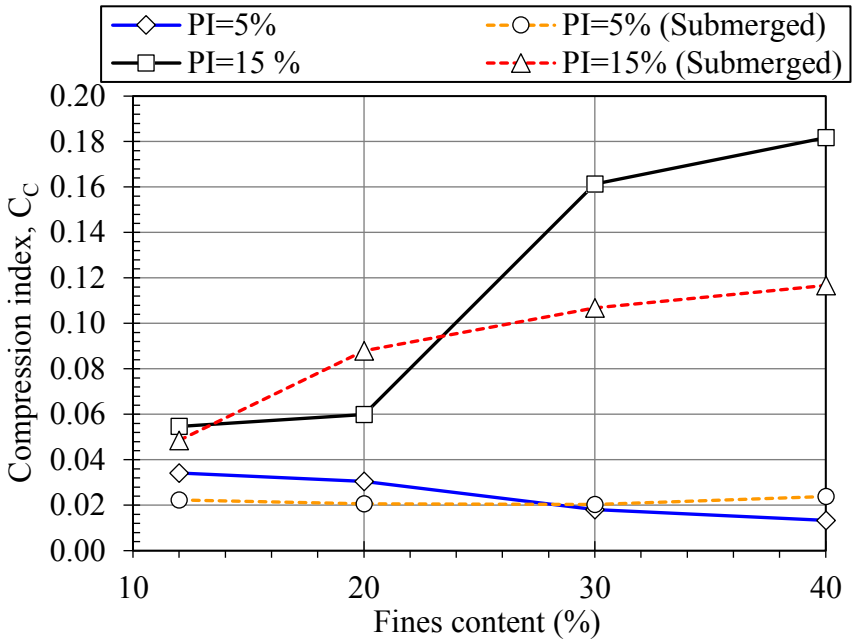


Figure 5.35. Compression index variation with fines content and plasticity index for unsubmerged and submerged tests

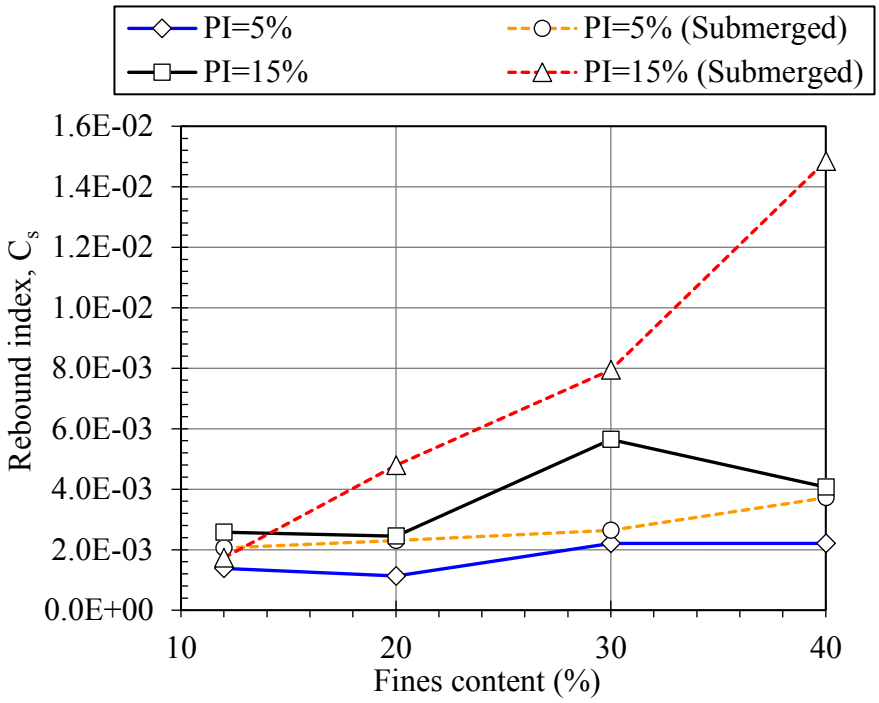


Figure 5.36. Rebound index variation with fines content and plasticity index for unsubmerged and submerged tests

Higher PI values resulted in larger compression indices and axial strain under one-dimensional compression. The effect of higher PI on C_C increased for larger FC values (Figure 5.35). In other words, an apparent increase in compression indices (C_C) was observed with increasing fines content for both unsubmerged and submerged tests of CFM with PI=15%. C_C varied between 0.055 and 0.182 for unsubmerged tests, whereas 0.049 and 0.117 for submerged tests.

As a general trend, the rebound index (C_s) increased with FC and PI, while the most significant increase with FC was observed in PI=15% for submerged tests. C_s ranged between 1.1 x 10^{-3} and 3.7 x 10^{-3} for PI=5%, whereas 1.7 x 10^{-3} and 1.5 x 10^{-2} for PI=15% (Figure 5.36).

Changes in intergranular relative density (D_{rs}) under different normal stresses during compression tests are presented in Figure 5.37.

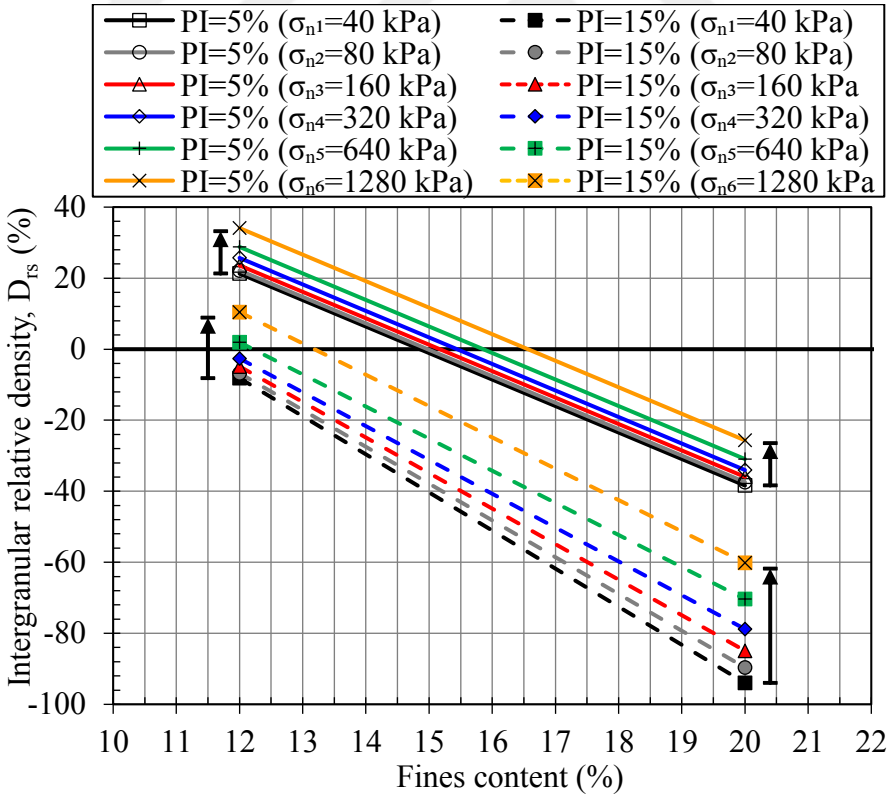


Figure 5.37. Change in intergranular relative density with fines content for unsubmerged CFM in compression tests

The outcomes observed in Figure 5.37 are almost identical to the results obtained in Figure 5.32 (intergranular relative density variation of saturated specimens due to isotropic consolidation under different effective stresses in triaxial tests). Intergranular relative densities calculated for 12% and 20% fines were linearly connected as there was no other data in between. Threshold FC increased with the normal stress from approximately 15% to 16.5% for PI=5%, whereas from 12% to 13% for PI=15%.

Secant constrained modulus (M_s), defined as the ratio of axial stress change to axial strain change, describes the elastic modulus of materials when there is no strain in lateral directions (Equation 5.15).

$$M_s = \frac{\Delta\sigma_n}{\Delta\varepsilon_a} \tag{5.15}$$

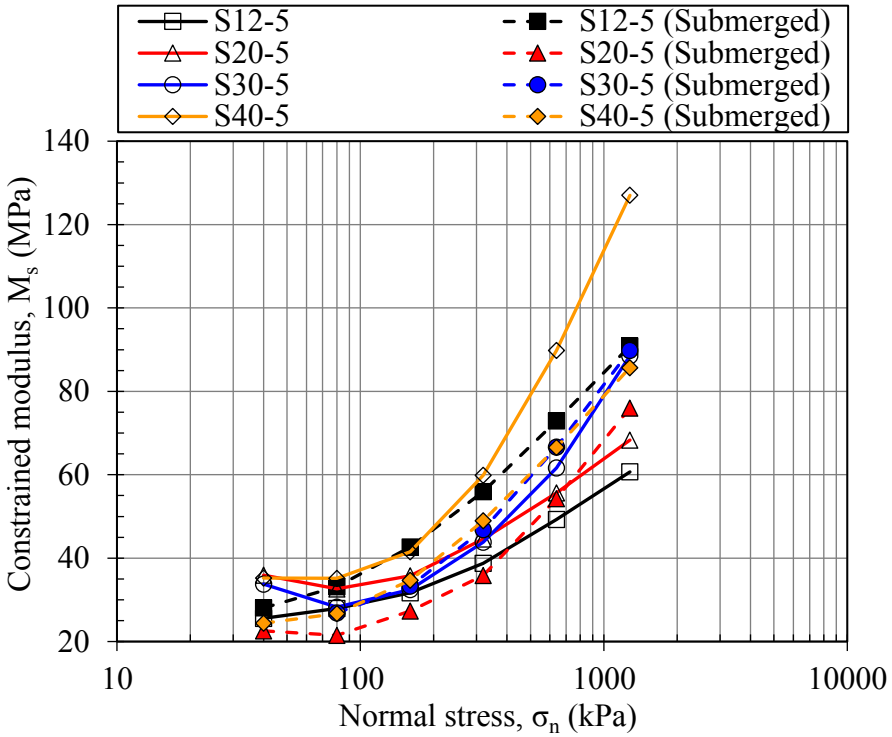
where,

$\Delta\sigma_n$: Change of axial stress in laterally constrained state

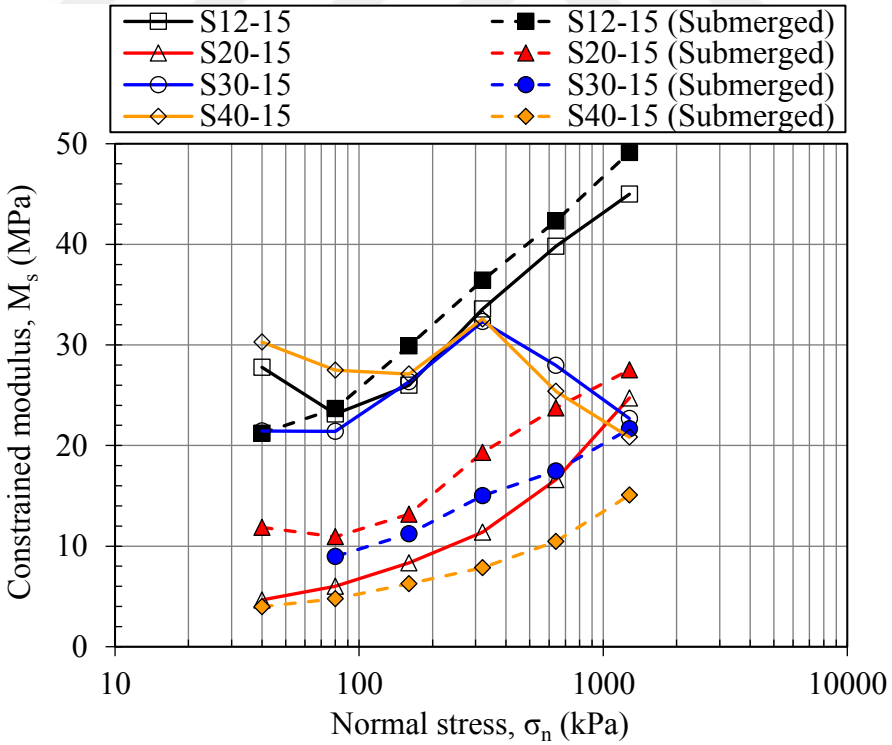
$\Delta\varepsilon_a$: Change of axial strain in laterally constrained state

Variations of the secant constrained modulus (M_s) of CFM with PI=5% and PI=15% are presented in Figure 5.38. M_s was calculated from zero to normal stress applied at a loading stage by using Equation 5.15. As seen in Figure 5.38a, higher M_s values were observed with the normal stress increase in all CFM for PI=5%. M_s values ranged between 22 and 127 MPa.

M_s values of CFM with PI=15% were significantly less than that of CFM with PI=5%. Secant constrained moduli (M_s) were in between 4 and 49 MPa for CFM with PI=15%, as seen in Figure 5.38b. Although there was a general trend of increasing M_s with normal stress, modulus for unsubmerged tests of S30-15 and S40-15 varied according to the normal stress applied.



(a)



(b)

Figure 5.38. Secant constrained modulus as a function of normal stress for CFM with (a) PI=5%, and (b) PI=15%

In terms of the use of coarse-fine mixtures in MSEW, static vertical stresses in the field are expected to be around 40-200 kPa for an average wall height of 2-10 m (possible additional external loading on a 10-m-high MSEW is not considered). Compression of CFM in this study (PI=5% and PI=15%, FC up to 40%; initially prepared at 95% of standard Proctor density and w_{opt}) was evaluated according to the large compression test results under laterally constrained compression conditions. Since confined compression values at exactly 200 kPa vertical stress are not available in the current study, axial strain values at vertical stress of 320 kPa will be mentioned as a conservative value of expected axial strain under 200 kPa vertical stress (320 kPa may correspond to the vertical stresses in a 16-m-high MSEW). Accordingly, axial strains in the loading stage corresponding to 320 kPa were in the range of 0.5%-0.9% for PI=5% and 0.9%-4.0% for PI=15%, even though specimens were submerged in water (Table 5.9 and Table 5.10). These vertical strain values may or may not be acceptable for the end-of-construction vertical deformations for an MSEW.

CHAPTER 6

LARGE DIRECT SHEAR TEST RESULTS

This chapter presents the results of large direct shear tests conducted on the laboratory-prepared well-graded, and poorly-graded sand mixtures without fines (SW and SP) and eight coarse-fine mixtures (CFM) in this study. Mixtures' own shear strength properties and their interaction with geogrids in direct shear failure mode were investigated. Two geogrids were used, one of which had in-plane drainage property, and the other was the same geogrid but without the drainage function as the geotextile in its channels was removed without damaging the reinforcement strips. Specimens having an optimum moisture content and in-place dry density equal to 95% of the standard Proctor compactness level were tested under three normal stresses (σ_n) as 55, 105, and 155 kPa. Besides the 0.25 mm/min displacement rate applied in this study, the effect of the shear rate on strength response was evaluated in three tests with a shear rate of 0.01 mm/min. In addition, eight tests were performed after saturating the specimens during 105 kPa of normal load application. CFM with 20% and 40% of fines and 5% and 15% of PI were used for saturated tests.

Shear strengths of mixtures under different normal stresses and soil-geogrid interface shear resistances were determined. Peak and ultimate (residual) strength relations, variation of interface bond strength with FC and PI, as well as dilative/contractive response of CFM were discussed within the scope of this chapter.

6.1 Test Results

Soil mixtures were prepared at their optimum moisture contents and allowed to stand for one day prior to compaction, as specimen preparation and its procedure are

detailed in Section 3.3.6.2. Moisture content measurements for samples taken just before compaction and after the direct shear tests indicated that moisture contents of the CFM during the test varied between 0.1% and 1.4%.

In this study, recommendations of the ASTM D5321-14 for soil and geogrid specifications were considered. Formulations, given in Equations 6.1, 6.2, 6.3, and 6.4, were used to calculate normal and shear stresses on specimens. As the dimensions of the upper and lower boxes in the large direct shear apparatus were the same in this study, corrections for the specimen contact area according to the amount of shear displacement were made for both normal and shear stress calculations, as suggested by the relevant standard.

$$A_C = A_0 - L.\Delta d \tag{6.1}$$

$$\tau = \frac{F_S}{A_C} \tag{6.2}$$

$$\sigma_n = \frac{F_N}{A_C} \tag{6.3}$$

$$\tau = c_a + \sigma_n.\tan\delta \tag{6.4}$$

where,

A_C : Corrected area in large direct shear tests

A_0 : Initial cross-sectional area of the specimen

Δd : Horizontal (shear) displacement

L : Length of the shear box

τ : Corrected shear stress

F_S : Shear force

σ_n : Corrected normal stress

F_N : Normal load

c_a : Adhesion intercept

δ : Angle of friction of the soil-geogrid interface

6.1.1 Settlement Stage

Before the direct shear, the settlement stage of the compacted specimens was initiated under the desired normal stresses. The dead load of the weights suspended on the lever arm, which has a 10:1 mechanical advantage (Figure 6.1), was adjusted to provide 50, 100, and 150 kPa. Besides, the weight of the upper box, porous, and loading plates, which were carried by the compacted soil specimen (approximately 5 kPa of additional normal stress), were also considered in stress calculations to give a total of 55, 105, and 155 kPa normal stresses.



Figure 6.1. Settlement stage of large direct shear tests

Precautions were considered to prevent geogrid from being out of the shear zone and losing its planar shape, as indicated in Section 3.3.6.2, by considering the remarks of ASTM D5321-14 to test fine, compressible soils with geosynthetics. For this reason, the soil level where the geogrid is placed protruded 2 mm above the lower box to tolerate the compression of the specimen. In this study, since the soil mixture with the highest settlement potential was S40-15 (FC=40%, PI=15%), the evaluation within this scope was made by considering S40-15. SW and SP were tested in dry conditions, whereas tests with CFM were performed on specimens compacted at

95% of the standard Proctor dry density and optimum moisture content. However, eight specimens of CFM were also tested after the compacted specimens were saturated during the settlement stage, as described in Section 3.3.6.2.2.

The settlement plots of the specimens with time are shown in Figure 6.2. Axial strains were calculated for the total specimen height placed in lower and upper boxes (Section 3.3.6.2). In the figure, the test properties were represented by the notation: '(Soil code)the magnitude of the initial normal stress-geogrid presence if there is any(saturated specimen)' as described in Section 3.3.6.4.

Tests of the SW (dry) and S40-15 (at optimum moisture content) soil mixtures under the highest normal stress (σ_n=155 kPa) indicated the settlement range of the soils with the lowest and highest compression potential in this study. Settlements of the total specimen height were in the range of 1-3 mm (Figure 6.2). The settlement stage of the dry/coarse soil mixtures (SW, SP) was completed in a couple of minutes, whereas it took approximately one to four hours for S40-15 and other CFM.

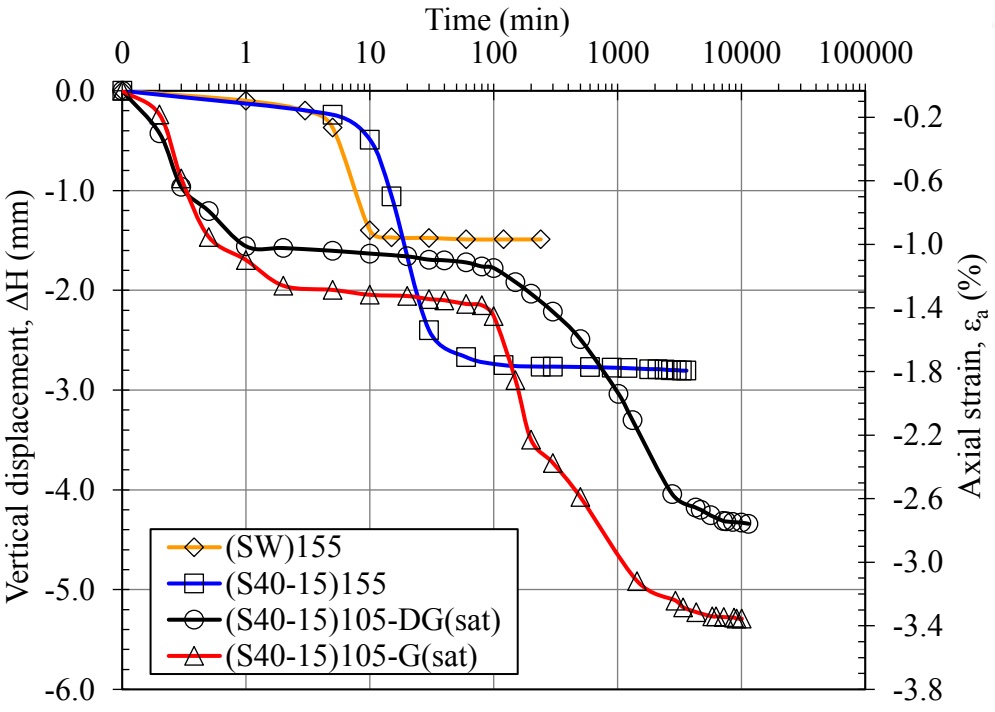
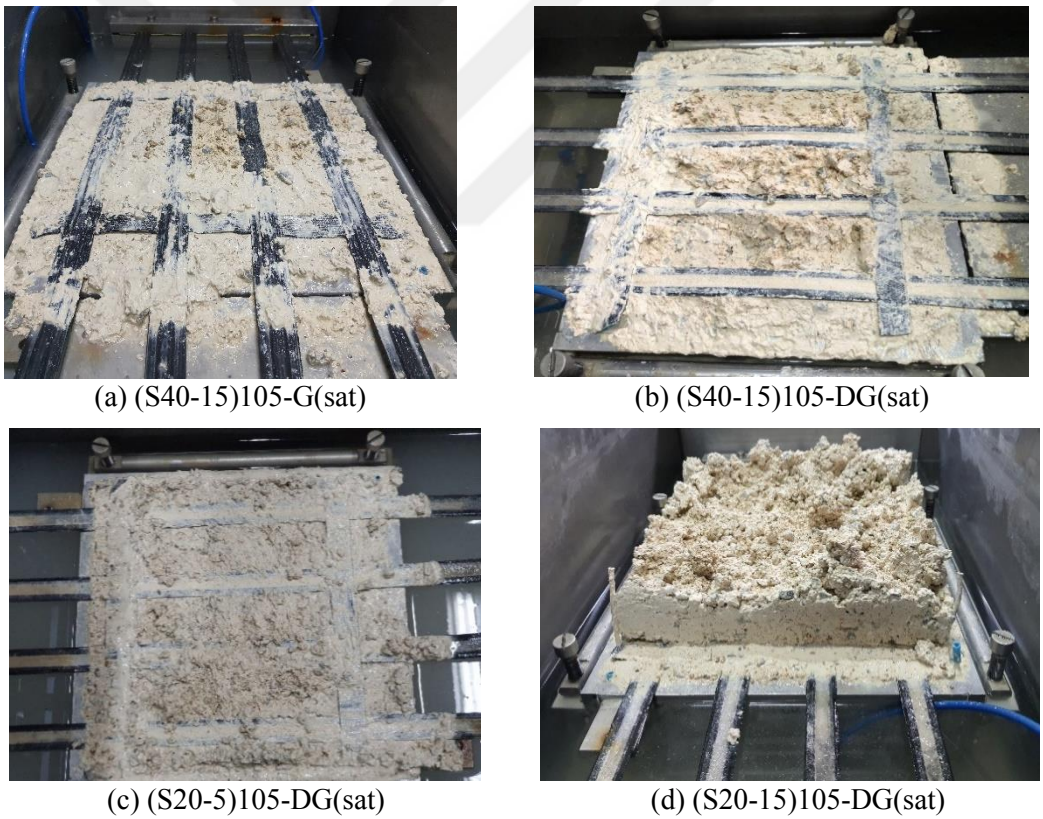


Figure 6.2. Vertical displacement plots of specimens in the settlement stage

In the saturated direct shear tests, S40-15 showed 4.3 mm and 5.3 mm vertical displacement, corresponding to 2.7% and 3.3% axial strains during the settlement stage. Although this stage lasted for one week, it was observed that most of the settlements took place within the first day.

The position of the geogrids and failure surface views of the saturated tests after direct shear are presented in Figure 6.3, whereas views of the tests for specimens at optimum moisture content for different soil mixtures, geogrid surfaces, and normal stress alternatives are presented in Figure 6.4. The view of the failure surfaces at the upper face of the lower box and the positions of the geogrids after direct shear indicated that geogrids remained within the direct shear zone on a planar surface for each specimen tested in this study.



(a) (S40-15)105-G(sat) (b) (S40-15)105-DG(sat)

(c) (S20-5)105-DG(sat) (d) (S20-15)105-DG(sat)

Figure 6.3. The position of the geogrids and the views of the failure surfaces after direct shear tests for saturated specimens



(a) (S12-5)155-DG



(b) (S20-15)55-DG



(c) (S30-5)105-DG



(d) (S20-5)55-G



(e) (S30-15)155-DG

Figure 6.4. The position of the geogrids and the views of the failure surfaces after direct shear tests for specimens compacted at optimum moisture content

6.1.2 Shearing Stage

At the beginning of the experimentation program, trial tests were performed on the SW and SP soil mixtures with the same testing parameters, and the sensitivity and

repeatability of the test results were evaluated. Plots of the corrected shear stress with horizontal displacement are presented in Figure 6.5. Behavioral tendencies of the repeated tests were observed to be the same for all tests and normal stress alternatives. For SW and SP soil mixtures, a reduction in stress was observed up to a residual value after a peak shear strength was observed. Peak shear strengths were observed between 5 mm and 10 mm of shear displacements, corresponding to 1.7% and 3.3% relative horizontal displacements (Δd/L, Length of the shear box, L=300 mm). The percent variance of the peak shear strengths for the repeated tests ranged between 4.3% and 6.5%, whereas the percent variance ranged between 1.2% and 2.5% for the ultimate (residual) shear strengths (Figure 6.5).

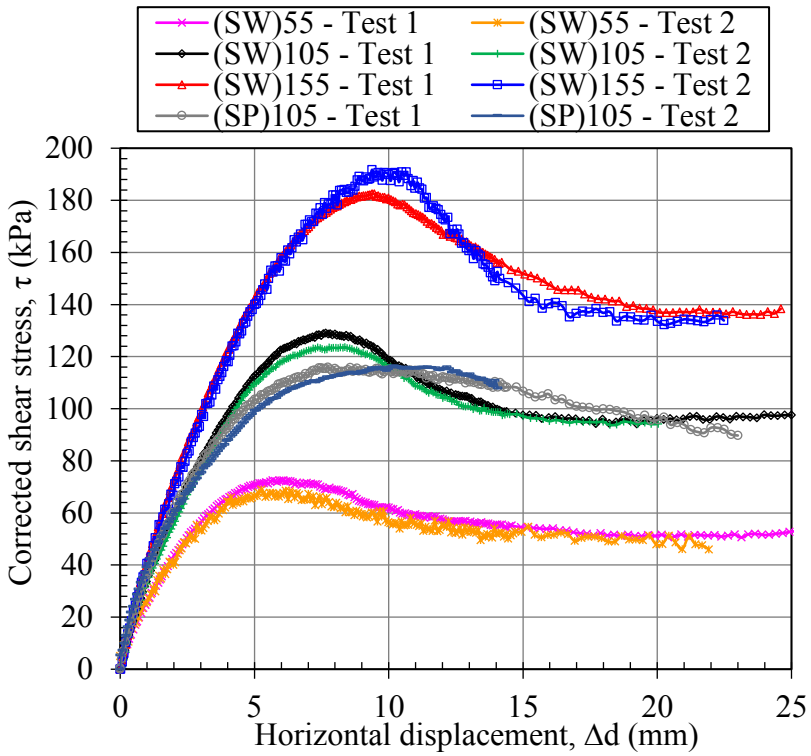


Figure 6.5. Corrected shear stress with horizontal displacement plots of the repeated direct shear tests

All direct shear test results in the scope of the experimentation program in this study, including the corrected shear stress with horizontal displacement and vertical displacement with horizontal displacement plots, are presented in Appendix A.

6.2 Discussion of Results

6.2.1 Discussion of Shear Strength of Soil Mixtures

Shear strength properties of soil mixtures without geogrid in direct shear failure mode are presented in this section. The shape of the observed failure surfaces for the mixtures having the highest and lowest fines content and plasticity index (S12-5, S12-15, S40-5, and S40-15) under different normal stresses are presented in Figure 6.6. Soil specimens were dispersed while removing the upper box after the test only in the S12-5 soil mixture. Therefore, soils in the upper box and part of the failure surface are shown in Figure 6.6d. Failure surfaces of mixtures having a high fines content and especially more plasticity index were observed to be more explicit. In Figure 6.6a, the traces formed due to the movement of coarse particles in the clay matrix during shear can be seen on the failure surface of the S40-15 soil mixture. More uneven failure surfaces were detected for mixtures having PI=5% and lower fines contents.

The shear strength properties of each soil mixture in direct shear failure mode were investigated, and test results are presented in Figure A.1 to Figure A.5 in Appendix A. Corrected peak shear strengths of SW, SP (dry) soil mixtures, and eight CFM ranged between 56.8-72.4 kPa for σ_n=55 kPa; 102.0-129.0 kPa for σ_n=105 kPa and 141.6-182.5 kPa for σ_n=155 kPa (Table 6.1).

It was observed that the behavior of SW and SP soil mixtures (well-graded and poorly-graded sands with gravel) resemble a typical shear strength response of medium-dense/dense sand. A peak shear strength was observed at first 5-12 mm of shear displacement and reduced to a residual value after that. A small initial contraction (0.01-0.25 mm, accompanied by strength increase up to the peak value); thereafter, volumetric expansion was monitored as seen in the vertical displacement plots (Figure A.1). The amount of initial contraction increased with the normal stress.



(a) (S40-15)55



(b) (S12-15)105



(c) (S40-5)105 (d) (S12-5)155

Figure 6.6. The shape of the failure surfaces after direct shear tests of CFM

Failure envelopes of SW and SP soil mixtures are presented in Figure 6.7. Because mixtures were completely dry and had no fines (no particles smaller than 0.075 mm), envelopes were passed through the zero point that there would be no cohesion. The square of the correlation coefficients for the envelopes was around 0.99.

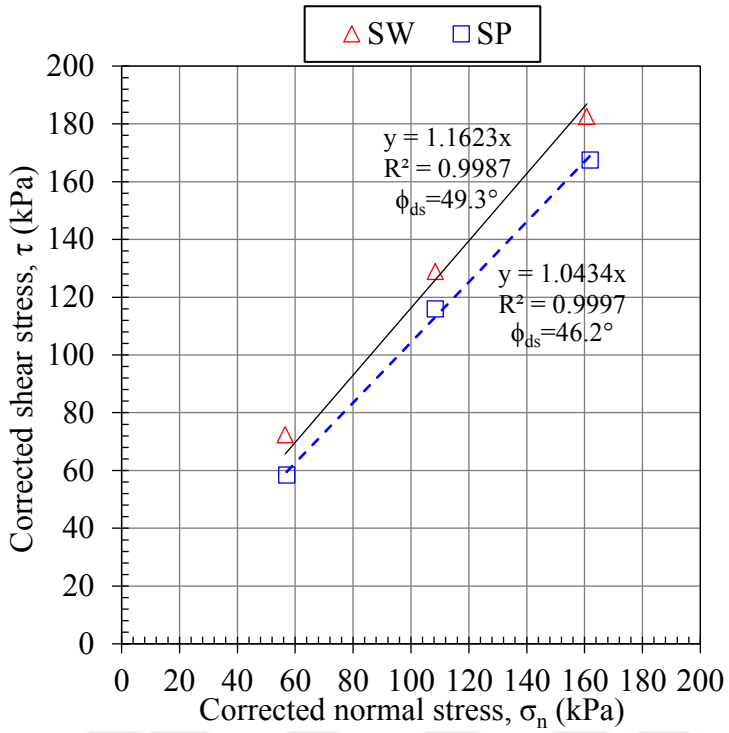
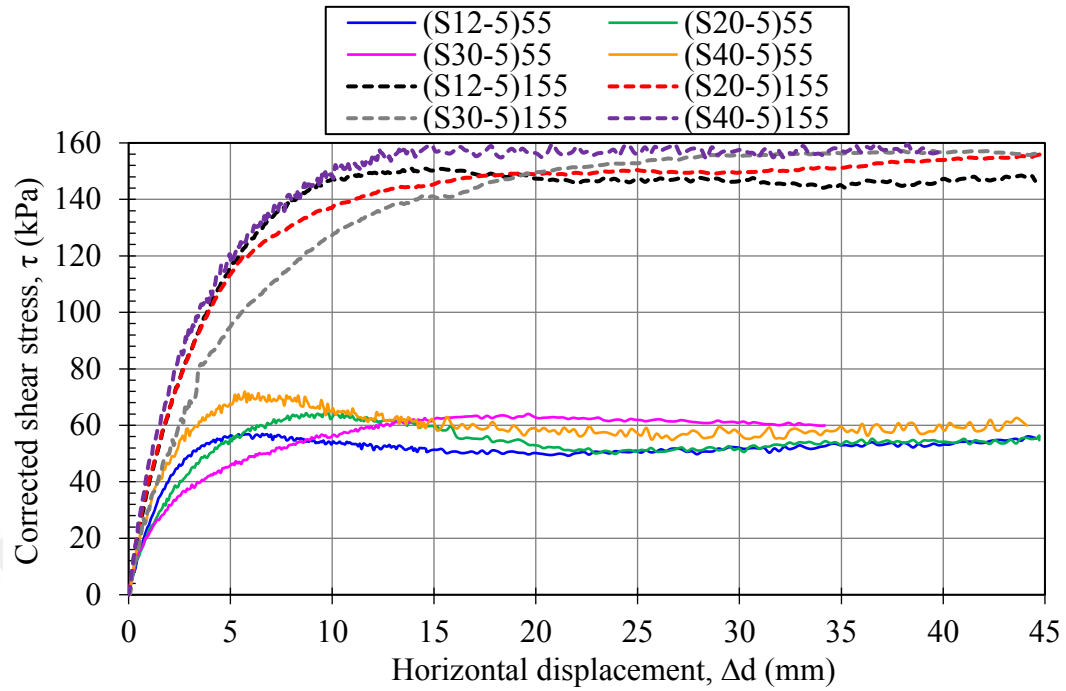
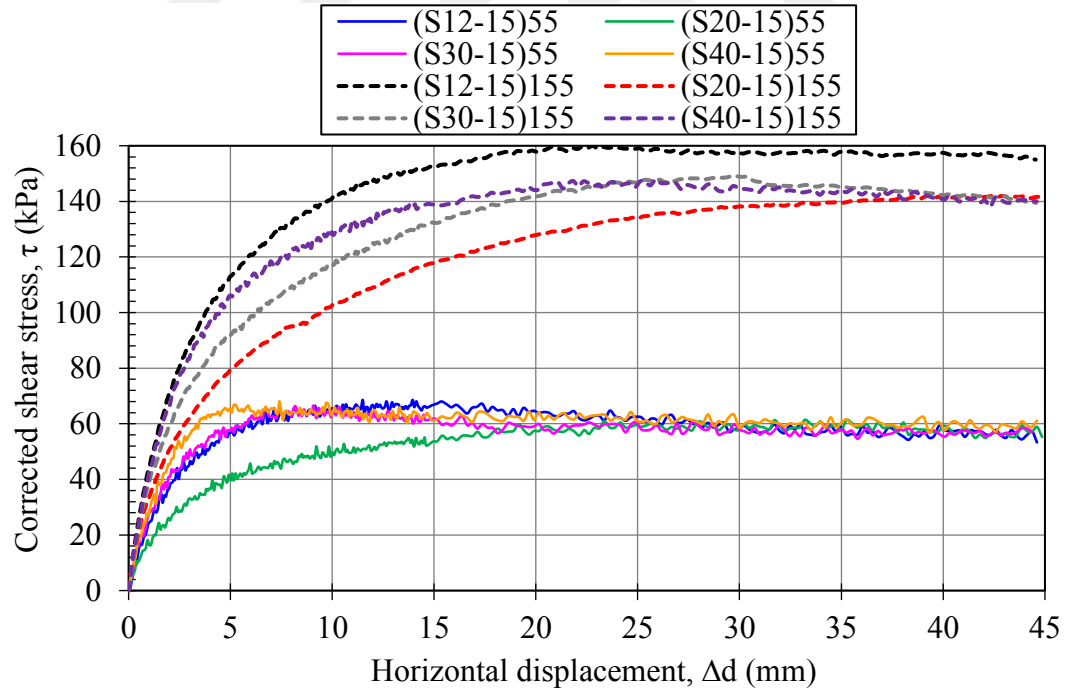


Figure 6.7. Failure envelopes of SW and SP soil mixtures

Corrected shear stress with horizontal displacement plots of CFM under 55 and 155 kPa normal stresses are presented in Figure 6.8. For σ_n=55 kPa, CFM with both PI=5% and PI=15% generally tended to reach peak strength and show strength reduction thereafter to an ultimate (residual) value. However, as normal stress increased up to 155 kPa, the amount of strength reduction after the peak strength significantly reduced or became zero (Figure 6.8a). Although the shear stress-horizontal deformation plots showed similar trends under σ_n=155 kPa for both PI=5% and PI=15%, peak strengths were generally reached at smaller displacements in CFM with PI=5% compared to CFM with PI=15% for the same FC.



(a)



(b)

Figure 6.8. Corrected shear stress with horizontal displacement plots of CFM having (a) PI=5%, and (b) PI=15%

All CFM in this study showed a small initial contraction followed by an expansive volumetric response (similar to SW and SP soil mixtures) under normal stress of 55 kPa (Figure A.2 to Figure A.5). Contractive/dilative behavior of CFM during shear for σ_n=105 kPa and σ_n=155 kPa are presented in Figure 6.9. Higher normal stresses increased the amount of initial contraction and decreased the following dilation for all specimens. Although all CFM with PI=5% showed dilation by different amounts following the initial contraction under all normal stresses, the amount of initial contraction significantly increased with normal stress for FC higher than 12%. However, S12-5 showed a dominant dilative response with low initial contraction during shear under all normal stresses. This outcome is in agreement with the results obtained in the triaxial testing of CFM with PI=5% (Table 5.7).

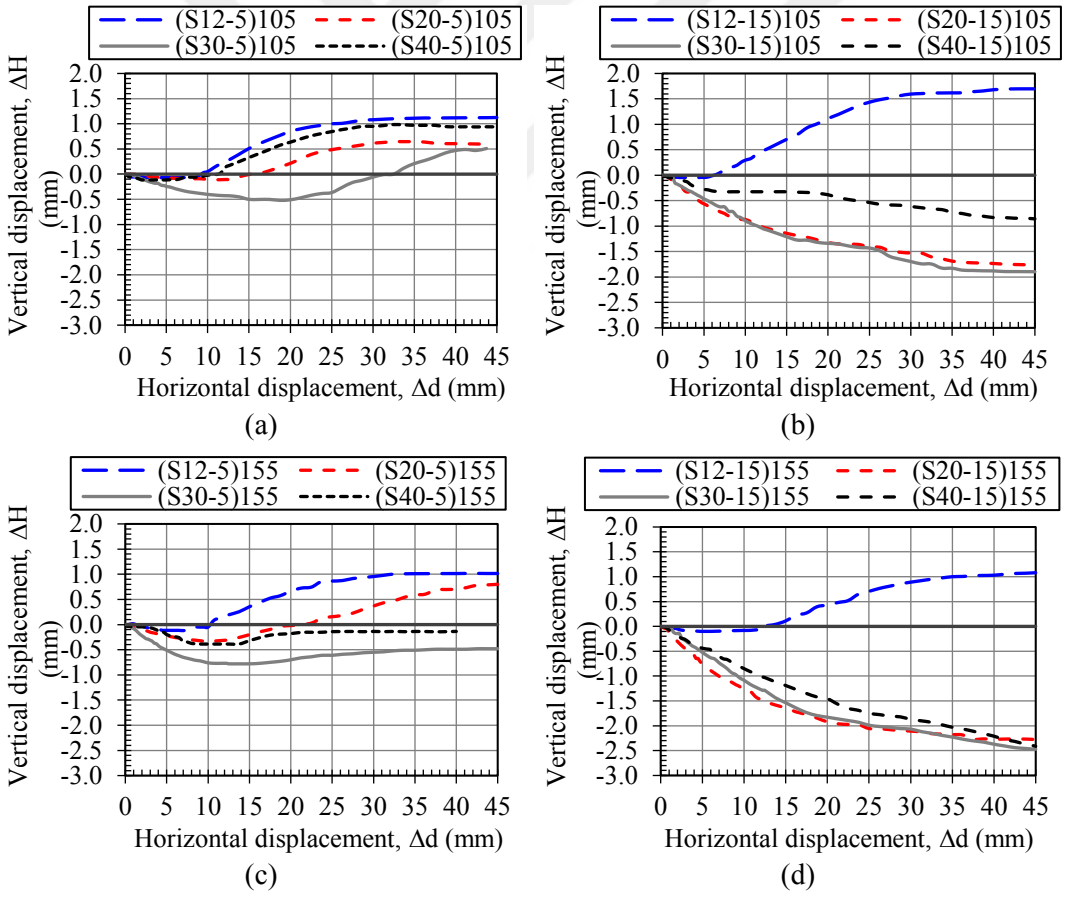


Figure 6.9. Vertical displacement with horizontal displacement plots of CFM for (a) PI=5% and σ_n=105 kPa, (b) PI=15% and σ_n=105 kPa, (c) PI=5% and σ_n=155 kPa, and (d) PI=15% and σ_n=155 kPa

Similarly, the specimen with FC=12% and PI=15% (S12-15) showed a dominant dilatant response after a small initial contraction. However, contraction was observed for specimens with FC higher than 12% under normal stresses of 105 kPa or higher (Figure 6.9).

Table 6.1. Shear strength properties of soil mixtures in direct shear tests

Soil code	Test code	For peak strength					For ultimate (residual) strength	
		Corrected normal stress, σ_n (kPa)	Corrected shear strength, τ_p (kPa)	Relative horizontal displacement at peak, $\Delta d/L$ (%)	Cohesion intercept, c (kPa)	Angle of internal friction, ϕ_{ds}	Corrected normal stress, σ_n (kPa)	Corrected shear strength, τ_r (kPa)
SW	(SW)55	56.5	72.4	1.9	0	49.3	58.9	51.3
	(SW)105	108.4	129.0	2.5			111.4	96.2
	(SW)155	160.8	182.5	3.1			166.9	136.9
SP	(SP)55	57.0	58.4	2.7	0	46.2	59.4	49.4
	(SP)105	108.4	115.9	2.6			-	-
	(SP)155	161.9	167.5	3.8			-	-
S12-5	(S12-5)55	56.5	56.8	1.8	7.0	41.3	58.7	50.1
	(S12-5)105	109.8	102.8	3.8			115.9	99.7
	(S12-5)155	163.7	150.9	4.9			167.2	146.7
S12-15	(S12-15)55	58.2	66.5	4.7	16.9	40.3	61.5	57.1
	(S12-15)105	112.5	112.1	6.2			112.5	112.1
	(S12-15)155	168.6	160.0	7.6			173.0	157.8
S20-5	(S20-5)55	57.3	64.1	3.1	18.2	38.0	59.7	51.3
	(S20-5)105	110.1	102.0	4.1			113.3	97.5
	(S20-5)155	166.0	149.1	6.2			166.0	149.1
S20-15	(S20-15)55	62.0	61.3	10.6	19.1	34.5	62.0	61.3
	(S20-15)105	119.5	102.2	11.6			119.5	102.2
	(S20-15)155	178.8	141.6	12.9			178.8	141.6
S30-5	(S30-5)55	58.8	63.3	5.7	17.6	38.4	-	-
	(S30-5)105	116.9	112.3	9.6			119.6	109.9
	(S30-5)155	176.2	156.5	11.6			176.2	156.5
S30-15	(S30-15)55	57.0	66.3	2.7	26.1	35.3	59.0	56.6
	(S30-15)105	114.1	107.4	7.5			114.1	107.4
	(S30-15)155	173.3	148.8	10.1			-	-
S40-5	(S40-5)55	56.8	70.7	2.3	28.9	38.8	59.1	58.4
	(S40-5)105	110.4	125.3	4.3			121.6	114.0
	(S40-5)155	164.0	157.0	5.0			164.0	157.0
S40-15	(S40-15)55	56.5	66.9	1.8	30.7	34.9	61.7	60.0
	(S40-15)105	110.3	113.7	4.3			113.9	109.1
	(S40-15)155	167.7	144.6	7.1			179.8	140.5

Area corrected peak shear and normal stresses, relative horizontal displacement at peak strength, resultant cohesion intercept, and angle of internal friction obtained from failure envelopes (having R^2 between 0.98 and 1), as well as ultimate (residual) strength values are summarized in Table 6.1. Variations of the cohesion intercept and angle of internal friction with fines content and plasticity index are presented in Figure 6.10.

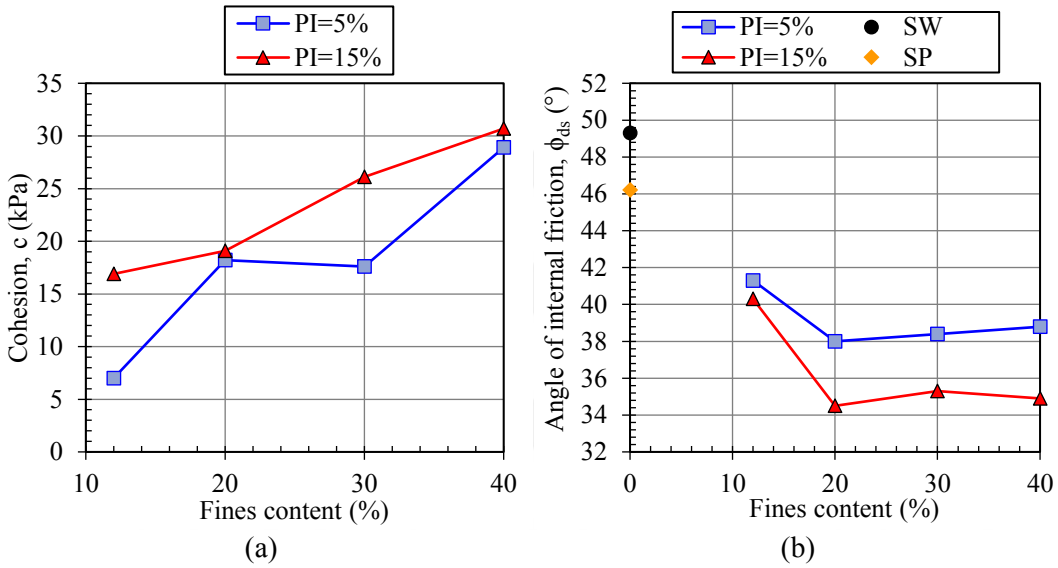


Figure 6.10. Cohesion intercept and angle of internal friction variation with fines content and plasticity index

Cohesion intercept tended to increase with fines content and plasticity index. S12-5 (FC=20%, PI=5%; having a cohesion value of 7 kPa) was the lowest among all CFM. Cohesion intercept of other mixtures ranged between 16.9 and 30.7 kPa.

Angles of internal friction for SW (D_r=67%) and SP (D_r=63%) soil mixtures (dry and including no fines) were the highest among all mixtures tested (Figure 6.10b). For CFM that have the same coarse skeleton with SW soil mixture as the granular portion, friction values were around 40°- 41° for FC=12%. For other CFM having higher fines content, friction values reduced around to 38° for PI=5% and 35° for PI=15%.

CFM with PI=5% had slightly higher friction values (1° to 4°) compared to PI=15% for the same FC. The difference between friction values with plasticity index was the highest at FC=40%.

FHWA (2009) states that a reinforced wall backfill material shall exhibit an effective (drained) angle of internal friction of not less than 34 degrees. In this study, coarse-fine mixtures (CFM, at optimum moisture content, $S_r \approx$ 60-80%) compacted to 95% of the standard Proctor maximum dry densities were tested with a shear rate of 0.25 mm/min. It was observed that the S20-15 and S40-15 soil mixtures, which had the lowest internal friction angles, were higher than 34°, and all CFM satisfied the minimum friction angle requirement of FHWA (2009).

Variation of the relative horizontal displacement ($\Delta d/L$) at peak strength with fines content, plasticity index, and normal stress is presented in Figure 6.11. SW and SP soil mixtures showed peak strength earlier compared to CFM. Normal stress increased the horizontal displacement (Δd) at peak strength in all mixtures tested. $\Delta d/L$ values ranged between 1.8% (shear displacement of Δd=5.4 mm) and 12.9% (shear displacement of Δd=38.7 mm) for all tested specimens. As a general trend, up to FC=20%, CFM with PI=5% tended to reach peak strength earlier than CFM with PI=15%, which reversed after FC=20%. In addition, FC=30% for PI=5% and FC=20% for PI=15% showed higher relative horizontal displacements at peak as an outlier trend under all normal stresses.

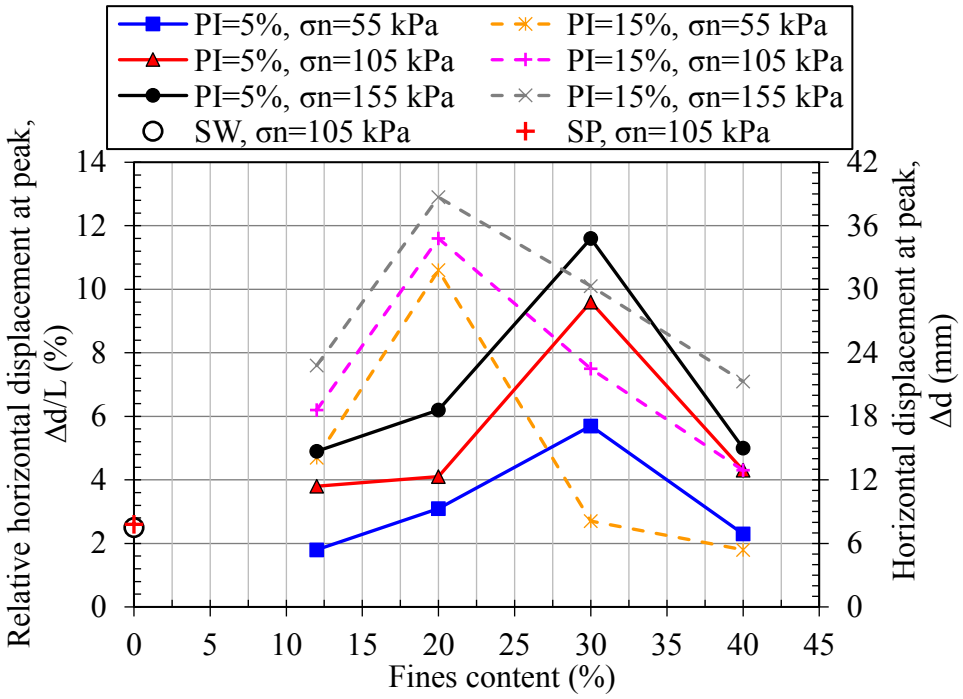


Figure 6.11. Relative horizontal displacement variation with fines content, plasticity index, and normal stress

6.2.2 Discussion of Shear Strength of Soil Mixture-Geogrid Interface

Shear strength responses of the soil mixture-geogrid interface in direct shear failure mode are presented in this section. The views of the observed failure surfaces at the end of the tests under different normal stresses are presented in Figure 6.12. While the after-test view of the dry SW soil mixture with the geogrid is presented in Figure 6.12a, other views belong to coarse-fine mixtures (CFM). Figure 6.12b is the view of the failure surface seen on the surface of the lower box, whereas Figure 6.12c,d is the view of the bottom surface of the upper box. The bond of the soil in between the grid apertures and the traces of the soil that slide from the surface of the geogrids' strips can be clearly distinguished (Figure 6.12).

Deformation of the geogrids' transverse ribs observed in some tests can be seen in Figure 6.13. Although this was not evident on every failure surface, transverse ribs

of geogrids may contribute to the direct shear resistance by providing passive strength and causing soil deposition in front of the ribs for some CFM in this study.

Direct shear test results of soil mixtures with geogrids (corrected shear strength with horizontal displacement and vertical displacement with horizontal displacement plots) are presented in Figure A.6 to Figure A.12 in Appendix A.

The shear strength properties of each test (peak and ultimate/residual shear strength with corresponding normal stresses and relative horizontal displacement, $\Delta d/L$, values) are summarized in Table 6.2. Corrected peak shear strengths of soil mixture and geogrid interface ranged between 47.4-59.7 kPa for σ_n=55 kPa; 82.9-104.2 kPa for σ_n=105 kPa and 108.9-158.0 kPa for σ_n=155 kPa (Table 6.2).

While all the other parameters were the same, geogrid existence caused both an increase and decrease in the horizontal displacement values in which the peak and ultimate (residual) strengths were reached (or relative horizontal displacement at peak, $\Delta d/L$), as seen from Table 6.1 and Table 6.2.



(a) (SW)105-DG



(b) (S20-15)155-G



(c) (S40-5)55-DG (d) (S40-15)155-DG

Figure 6.12. Failure surface views of soil mixture-geogrid interface in direct shear tests



(a) (S30-15)155-DG



(b) (S20-5)105-DG



(c) (S40-5)55-G

Figure 6.13. Deformation of the transverse ribs in direct shear tests

Table 6.2. Shear strength properties of soil mixture-geogrid interface

Soil code	Test code	For peak strength of the interface					For ultimate (residual) strength of the interface	
		Corrected normal stress, σ_n (kPa)	Corrected shear strength, τ_p (kPa)	Relative horizontal displacement at peak, $\Delta d/L$ (%)	Cohesion intercept, c_a (kPa)	Angle of friction, δ	Corrected normal stress, σ_n (kPa)	Corrected shear strength, τ_r (kPa)
SW	(SW)55-DG	56.6	47.4	2.0	0	42.2	59.7	38.6
	(SW)105-DG	108.2	101.2	2.4			111.4	89.3
	(SW)155-DG	160.2	144.4	2.8			162.2	133.7
SP	(SP)55-DG	56.7	48.0	2.1	0	43.1	58.5	41.3
	(SP)105-DG	109.7	95.5	3.8			120.0	75.1
	(SP)155-DG	161.8	158.0	3.7			170.7	129.8
S12-5	(S12-5)55-DG	57.4	51.1	3.4	4.9	39.1	57.4	51.1
	(S12-5)105-DG	120.9	104.2	12.7			120.9	104.2
	(S12-5)155-DG	176.2	147.6	11.6			176.2	147.6
S12-15	(S12-15)55-DG	57.6	54.0	3.7	6.7	39.8	60.2	51.8
	(S12-15)105-DG	110.7	100.2	4.6			113.3	98.2
	(S12-15)155-DG	181.6*	157.5*	14.2*			-	-
S20-5	(S20-5)55-DG	57.0	52.3	2.7	5.8	41.0	60.2	46.0
	(S20-5)55-DG (repeat)	56.9	57.9	2.6			59.7	54.1
	(S20-5)105-DG	109.6	102.0	3.7			111.8	100.6
	(S20-5)155-DG	166.9	150.5	6.7			166.9	150.5
S20-15	(S20-15)55-DG	61.6	47.5	10.0	7.7*	34.6*	61.6	47.5
	(S20-15)105-DG	121.5*	97.1*	13.1*			-	-
	(S20-15)155-DG	181.5*	130.2*	14.2*			-	-
S30-5	(S30-5)55-DG	56.7	54.1	2.2	10.4	38.3	58.7	48.5
	(S30-5)105-DG	112.5	101.6	6.1			112.5	101.6
	(S30-5)155-DG	181.5*	152.9*	14.2*			-	-
S30-15	(S30-15)55-DG	56.4	49.1	1.7	10.1*	35.5*	58.9	44.4
	(S30-15)105-DG	122.5*	100.0*	13.8*			-	-
	(S30-15)155-DG	181.7*	138.2*	14.3*			-	-
S40-5	(S40-5)55-DG	56.6	54.7	2.0	1.6	41.8	59.8	51.2
	(S40-5)55-DG (repeat)	56.3	53.6	1.4			57.0	51.3
	(S40-5)105-DG	117.1	97.7	9.8			117.1	97.7
	(S40-5)105-DG (repeat)	111.6	100.1	5.4			111.6	100.1
	(S40-5)155-DG	166.1	155.1	6.2			170.0	151.8
S40-15	(S40-15)55-DG	56.2	51.5	1.3	16.0	32.2	59.5	43.0
	(S40-15)105-DG	109.1	84.4	3.2			109.1	84.4
	(S40-15)155-DG	161.0	117.4	3.3			166.3	114.3

*Tests that did not reach an ultimate (residual) shear strength by the end of the test

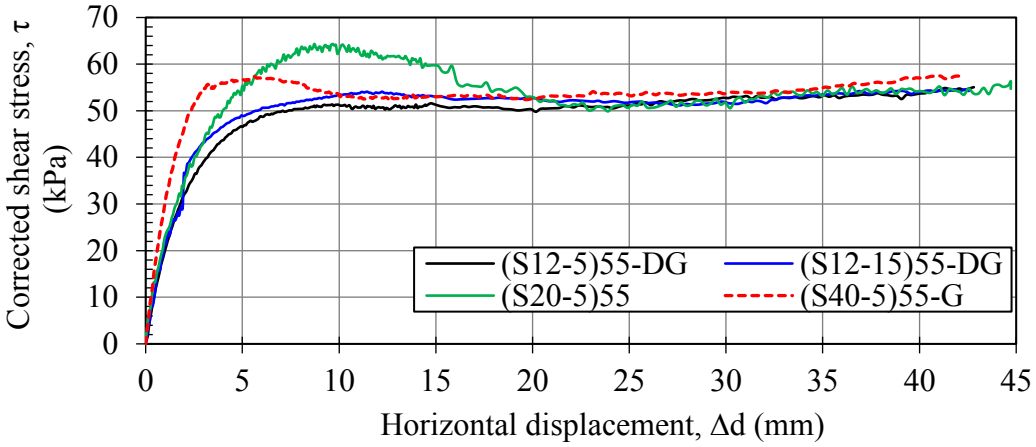
Table 6.2 (Continued).

Soil code	Test code	For peak strength of the interface					For ultimate (residual) strength of the interface	
		Corrected normal stress, σ_n (kPa)	Corrected shear strength, τ_p (kPa)	Relative horizontal displacement at peak, $\Delta d/L$ (%)	Cohesion intercept, c_a (kPa)	Angle of friction, δ	Corrected normal stress, σ_n (kPa)	Corrected shear strength, τ_r (kPa)
S20-5	(S20-5)55-G	56.6	59.7	2.0	10.3	38.5	60.1	53.1
	(S20-5)105-G	114.2	92.0	7.5			114.2	92.0
	(S20-5)155-G	165.3	146.8	5.8			165.3	146.8
S20-15	(S20-15)55-G	64.4*	54.7*	13.9*	8.8*	34.2*	-	-
	(S20-15)105-G	123.0*	88.5*	14.2*			-	-
	(S20-15)155-G	179.8*	133.2*	13.4*			-	-
S40-5	(S40-5)55-G	56.5	57.3	1.8	20.2	35.5	57.5	53.0
	(S40-5)105-G	109.2	103.6	3.3			112.2	100.1
	(S40-5)155-G	181.7*	147.5*	14.3*			-	-
S40-15	(S40-15)55-G	56.3	51.7	1.4	22.6	28.1	58.0	46.0
	(S40-15)105-G	109.3	82.9	3.4			109.3	82.9
	(S40-15)155-G	163.1	108.9	4.5			169.0	103.8

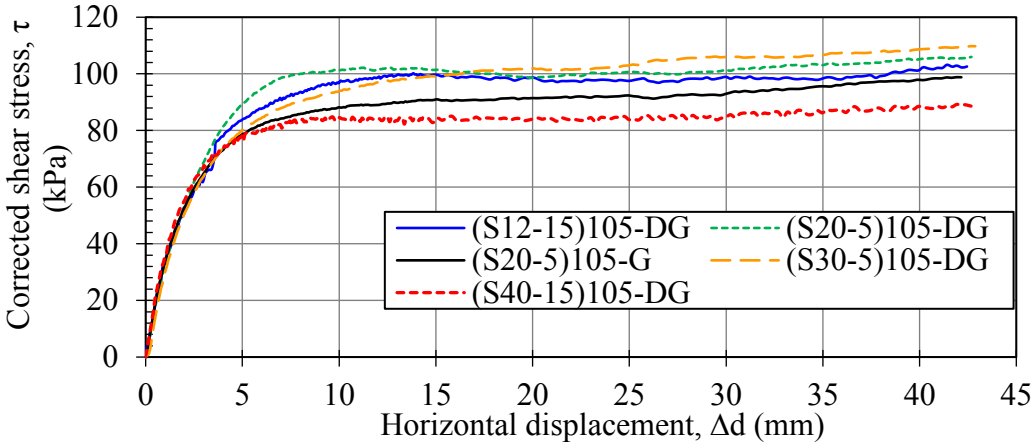
*Tests that did not reach an ultimate (residual) shear strength by the end of the test

A slight increase in shear stress was observed after the ultimate (residual) strength was reached in some tests, as given in Figure 6.14. This generally occurred after ranges of 25-30 mm horizontal displacement. Increases in stress values after an ultimate (residual) value have been reached were not taken into account to determine the peak and residual strength values.

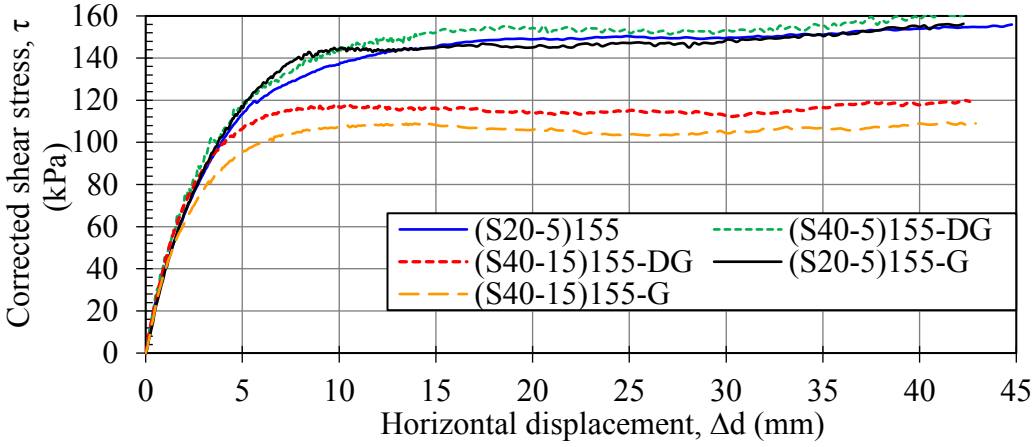
In some tests, where the interface strength of the geogrid and the soil mixture was evaluated, it was observed that the shear strength did not reach an ultimate (residual) stress value and continued to increase until the end of the test. These tests are indicated by the symbol (*) in Table 6.2, and the corrected shear stress-horizontal displacement plots are presented in Figure 6.15. Peak shear strengths for these specimens were determined as the stress observed at the end of the test, which corresponded to approximately 14-15% of the box length (relative horizontal displacement, $\Delta d/L$). Tests were finalized near this relative horizontal displacement value because the equipment has a maximum horizontal displacement capacity of 50 mm.



(a)



(b)



(c)

Figure 6.14. Corrected shear stress with horizontal displacement plots of CFM having a slight stress increase after ultimate (residual) strength was reached for (a) σ_n=55 kPa, (b) σ_n=105 kPa, and (c) σ_n=155 kPa

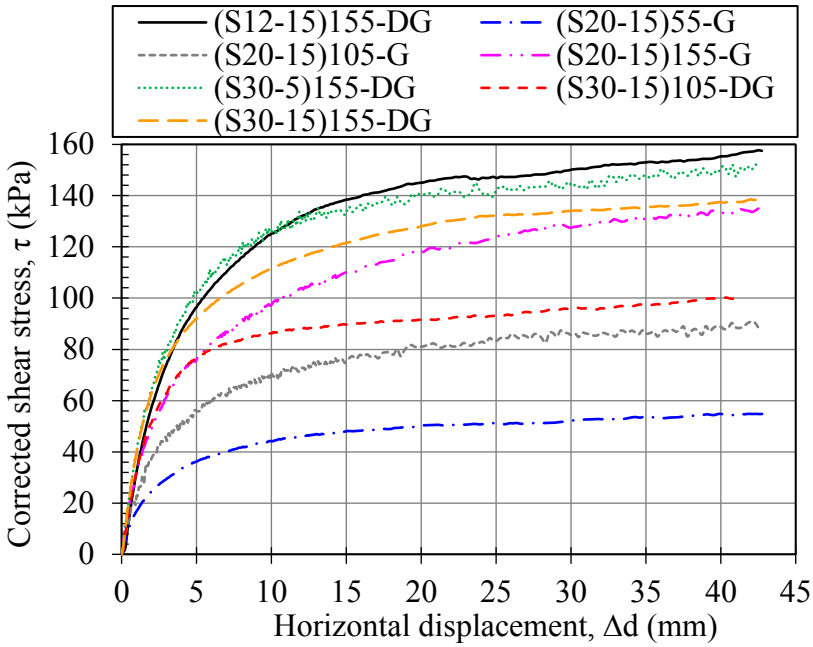


Figure 6.15. Corrected shear stress with horizontal displacement plots of tests not reaching an ultimate (residual) strength

Failure envelopes of SW and SP soil mixtures and coarse-fine mixtures (CFM) for tests with and without geogrid are presented in Figure 6.16 and Figure 6.17. The squares of the correlation coefficients for the envelopes were mainly higher than 0.997.

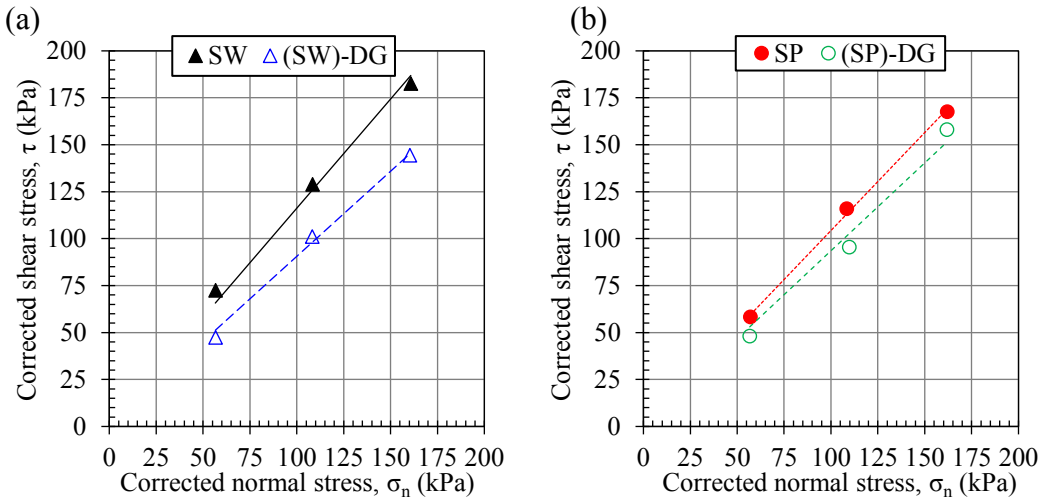


Figure 6.16. Failure envelopes for (a) SW and (b) SP soil mixtures for tests with and without geogrid

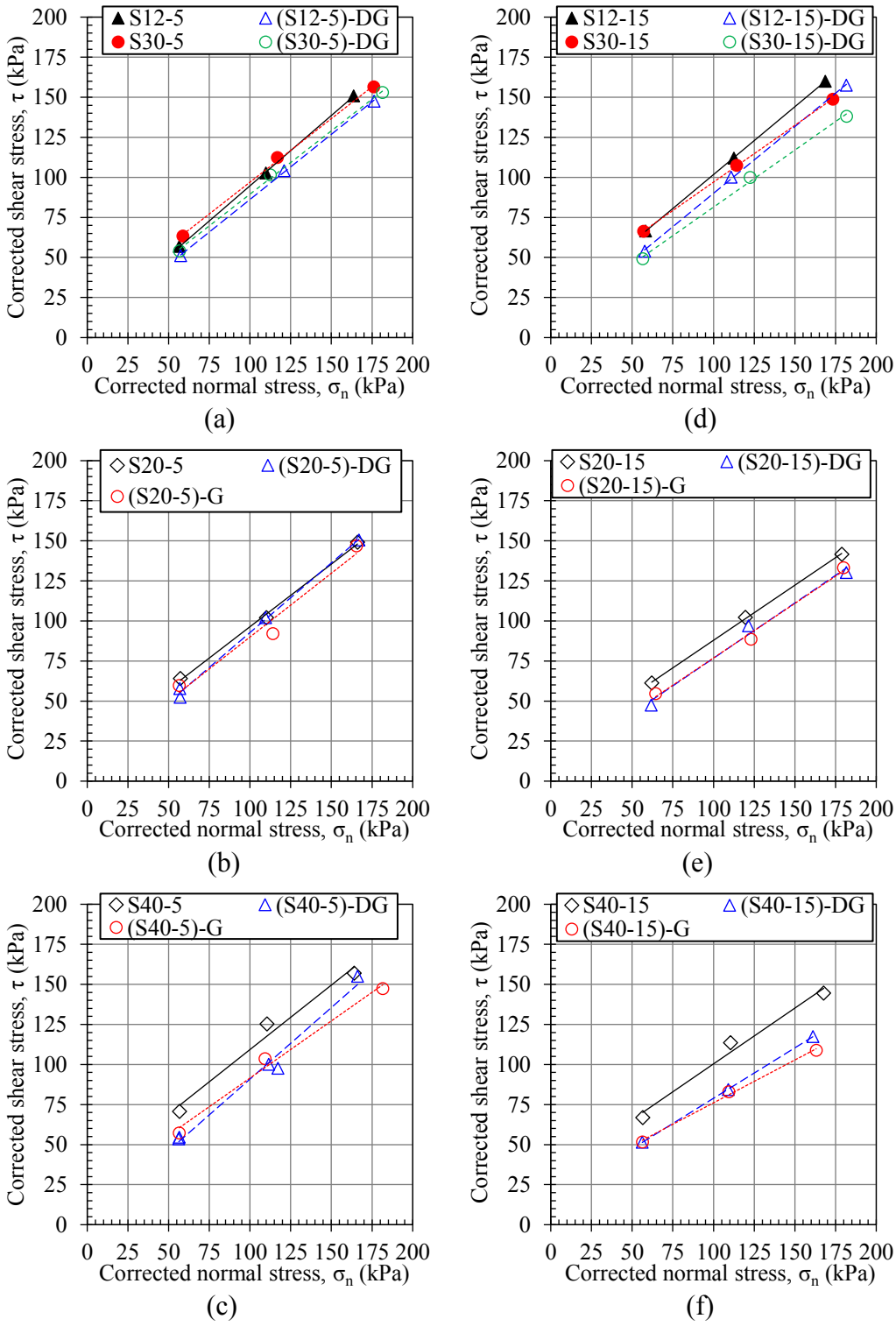


Figure 6.17. Failure envelopes for CFM having PI=5% (a, b, and c); and CFM having PI=15% (d, e, and f) for tests with and without geogrid

Cohesion intercept (c_a) and angle of friction (δ), observed in direct shear tests of soil mixtures and geogrid interfaces, were obtained from Figure 6.16 and Figure 6.17, and their values are presented in Table 6.2. Comparisons of the shear strength parameters for tests with and without geogrids are presented in Table 6.3.

Three tests [(S20-5)55-DG, (S40-5)55-DG, (S40-5)105-DG] were repeated twice for the testing of S20-5 and S40-5 soil mixtures with geogrid having a draining property (DG) by considering the obtained interface strength parameters to be outliers. However, as shown in Table 6.2 and Figure 6.17b,c, repeated tests did not significantly vary, and they did not considerably change the observed cohesion intercept (c_a) and angle of friction (δ) of the interface.

Table 6.3. Comparison of the shear strength parameters of soil mixtures with and without geogrid from direct shear tests

Soil code	Tests without geogrid		Tests with geogrid having draining property (DG)		Tests with geogrid without draining property (G)	
	Cohesion intercept,c (kPa)	Angle of internal friction, ϕ_{ds}	Cohesion intercept,c_a (kPa)	Angle of friction, δ	Cohesion intercept,c_a (kPa)	Angle of friction, δ
SW	0.0	49.3	0.0	42.2		
SP	0.0	46.2	0.0	43.1		
S12-5	7.0	41.3	4.9	39.1		
S12-15	16.9	40.3	6.7	39.8		
S20-5	18.2	38.0	5.8	41.0	10.3	38.5
S20-15	19.1	34.5	7.7*	34.6*	8.8*	34.2*
S30-5	17.6	38.4	10.4	38.3		
S30-15	26.1	35.3	10.1*	35.5*		
S40-5	28.9	38.8	1.6	41.8	20.2	35.5
S40-15	30.7	34.9	16.0	32.2	22.6	28.1

*Tests that did not reach an ultimate (residual) shear strength by the end of the test

Interaction of CFM with geogrid was investigated to evaluate the expected field performance of these materials in direct shear failure mode by preparing them at 95% of the standard Proctor dry density and optimum moisture content. Because these are the restrictions in many design manuals together with the FC and PI criteria in which the backfill soils are recommended to be placed, these specifications govern the field performance. Therefore, cohesion intercept and angle of friction, obtained for the

normal stress range of 55-155 kPa, were determined (Table 6.3) for the soil mixtures in this study.

Cohesion intercept (c_a) significantly decreased when soil mixtures interacted with geogrids for each specimen tested (Table 6.3). In other words, failure envelopes shifted downwards for the tests with geogrid of the same mixture (Figure 6.17). The variation of the friction angle of the interface (δ), on the other hand, differed with fines content and plasticity index. An apparent reduction in the values of δ was observed for SW and SP soil mixtures when they were tested with geogrids. The friction angle of the CFM-geogrid interface was observed to be slightly higher in some tests and lower in others compared to tests without geogrid.

Koerner (2005) suggested parameters to calculate the efficiency of the geogrid-soil interface on cohesion and angle of friction as in Equation 6.5 and Equation 6.6. Variation of the efficiencies with fines content for the soil mixtures in this study is presented in Figure 6.18.

$$E_c = (c_a/c).100 \quad (6.5)$$

$$E_\phi = (\tan\delta/\tan\phi).100 \quad (6.6)$$

where,

E_c : Efficiency on cohesion

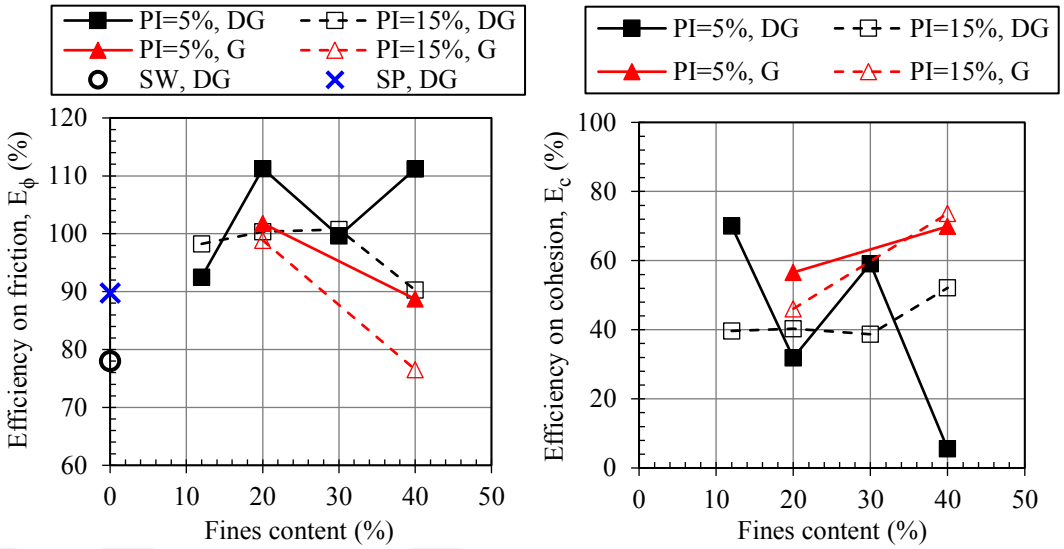
E_ϕ : Efficiency on friction

c_a : Adhesion of soil to geogrid

c : Cohesion of soil to soil

δ : Friction angle of soil to geogrid

ϕ : Friction angle of soil to soil



(a) (b)

Figure 6.18. Variation of (a) efficiency on friction, and (b) efficiency on cohesion with fines content

Efficiency on friction (E_ϕ) ranged between 76.5% and 111.3%, whereas efficiency on cohesion (E_c) ranged between 5.5% and 73.6% for the soil mixtures in this study (Figure 6.18). Koerner (2005) reported E_ϕ values between 72% and 107% for bidirectional and unidirectional geogrids tested with dry, well-graded angular sand prepared with 90% relative density. Although the E_ϕ values stated in this study and for granular materials in Koerner (2005) are close, it should be noted that contrary to this study, in Koerner (2005), the geogrid-soil interface was tested by attaching the geogrids to a rigid wooden block instead of an upper box filled with soil.

Almohd et al. (2005) reported efficiency values for the interaction of four different geogrids and low plastic clay (PI=15%, LL=42%) during pullout tests. Accordingly, E_c values were between 17.5% and 65.8%, whereas E_ϕ ranged between 45.5% and 161.5%. The ranges of E_c and E_ϕ observed for cohesive materials in Almohd et al. (2005) also agree with the values in this study.

Interface shear strength coefficients (α, $\tau_{interface}/\tau_{soil\ to\ soil}$) calculated for the peak and ultimate (residual) strength of soil mixtures in this study are presented in Table 6.4.

Table 6.4. Peak and ultimate (residual) interface shear strength coefficients of soil mixtures

Soil code	Initial normal stress, σ_n (kPa)	Tests with geogrid having draining property (DG)		Tests with geogrid without draining property (G)	
		α_{peak}	α_{res}	α_{peak}	α_{res}
SW	55	0.65	0.75		
	105	0.78	0.93		
	155	0.79	0.98		
SP	55	0.82	0.84		
	105	0.82	-		
	155	0.94	-		
S12-5	55	0.90	1.02		
	105	1.01	1.05		
	155	0.98	1.01		
S12-15	55	0.81	0.91		
	105	0.89	0.88		
	155	0.98*	-		
S20-5	55	0.82	0.90	0.93	1.04
	105	1.00	1.03	0.90	0.94
	155	1.01	1.01	0.98	0.98
S20-15	55	0.77	0.77	0.89*	-
	105	0.95*	-	0.87*	-
	155	0.92*	-	0.94*	-
S30-5	55	0.85	-		
	105	0.90	0.92		
	155	0.98*	-		
S30-15	55	0.74	0.78		
	105	0.93*	-		
	155	0.93*	-		
S40-5	55	0.77	0.88	0.81	0.91
	105	0.78	0.86	0.83	0.88
	155	0.99	0.97	0.94*	-
S40-15	55	0.77	0.72	0.77	0.77
	105	0.74	0.77	0.73	0.76
	155	0.81	0.81	0.75	0.74

- No residual value observed

*Tests that did not reach an ultimate (residual) shear strength by the end of the test

For tests with draining geogrid, variation of the peak interface shear strength coefficient with fines content, plasticity index, and normal stress is presented in Figure 6.19. α_{peak} values calculated for SW, SP soil mixtures, and CFM in this study varied between 0.65 and 1.01 (Table 6.4). As a general trend, it was observed that CFM with PI=5% results in higher bond efficiencies (higher α_{peak}) when interacting with geogrid than CFM with PI=15% under the same normal stress. α_{peak} values

decreased in the range of 0-0.19 from PI=5% to PI=15%, while all other variables were the same. Although there were fluctuations regarding the variation of α_{peak} with FC, the highest and the lowest values were observed at FC=12% and FC=40%, respectively. Except for the S40-5 tested under σ_n=155 kPa, all other α_{peak} values were between 0.73 and 0.83 for FC=40% (Table 6.4). While all other variables were the same, it was observed that normal stress significantly increased the interface coefficient as a general trend (Table 6.4 and Figure 6.19). α_{peak} increased between 0.04 and 0.22 (approximately similar increase for PI=5% and PI=15%) with the increase of normal stress from 55 kPa to 155 kPa.

Peak and ultimate (residual) interface shear strength coefficients were plotted together in Figure 6.20 for soil mixtures in this study. Accordingly, α_{res} ranged between 0.72 and 1.05. In the majority of the experiments, α_{res} were observed to be higher than the α_{peak}, and both values were less than 1. In other words, although the interaction of CFM with geogrid caused shear strength reduction in most cases, it had a more active role in the peak strength decrease.

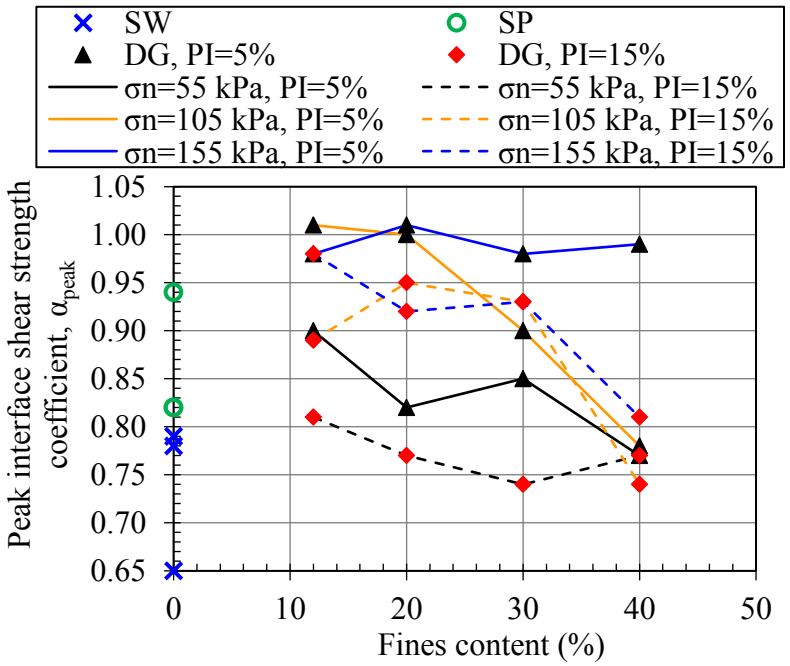


Figure 6.19. Variation of the peak interface shear strength coefficient with fines content for tests with draining geogrid

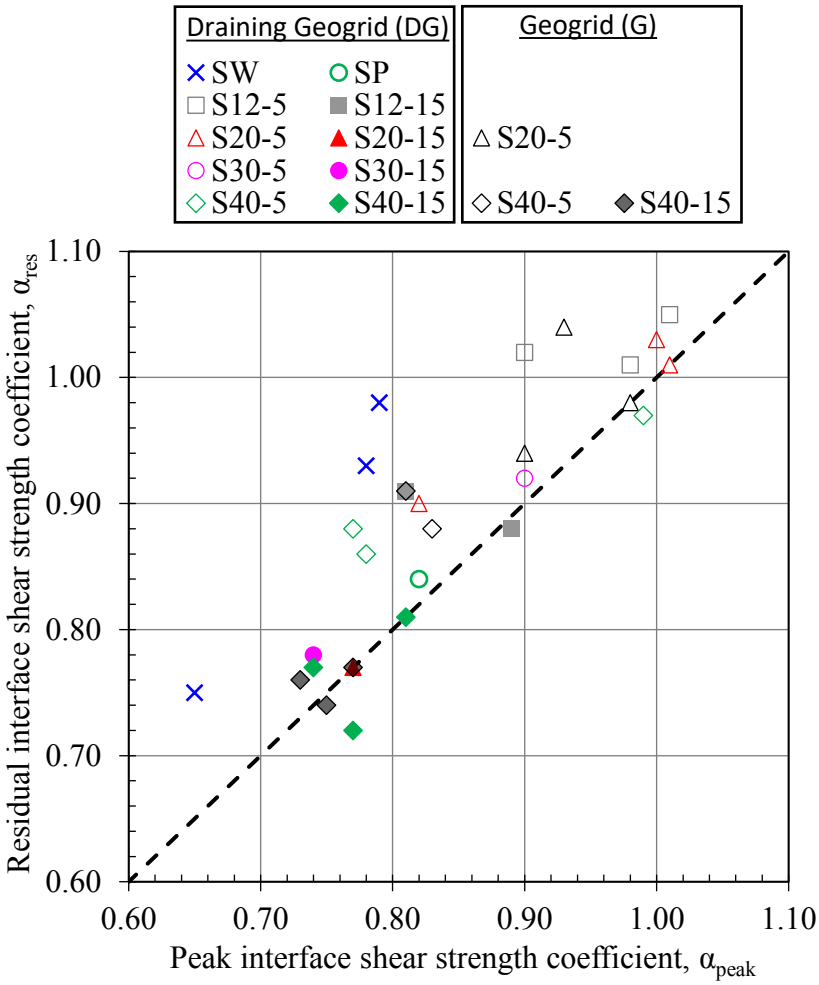


Figure 6.20. Comparison of the peak and ultimate (residual) interface shear strength coefficients of soil mixtures

It is noteworthy that the tests exhibiting the highest bond interaction occurred at S12-5 and S20-5 (containing FC and PI=5%) rather than SW or SP soil mixtures (having no fines). α_{peak} was observed to be higher than α_{res} only in tests with soil mixtures having FC=40% (Figure 6.20).

Vertical displacement with horizontal displacement plots during shear are presented in Figure 6.21 by comparing tests with and without geogrid for CFM having 12% and 30% fines and three different initial normal stresses. It was observed that the geogrid presence affected the volumetric behavior in both directions. In other words, it can have an increasing or decreasing effect on dilation and contraction.

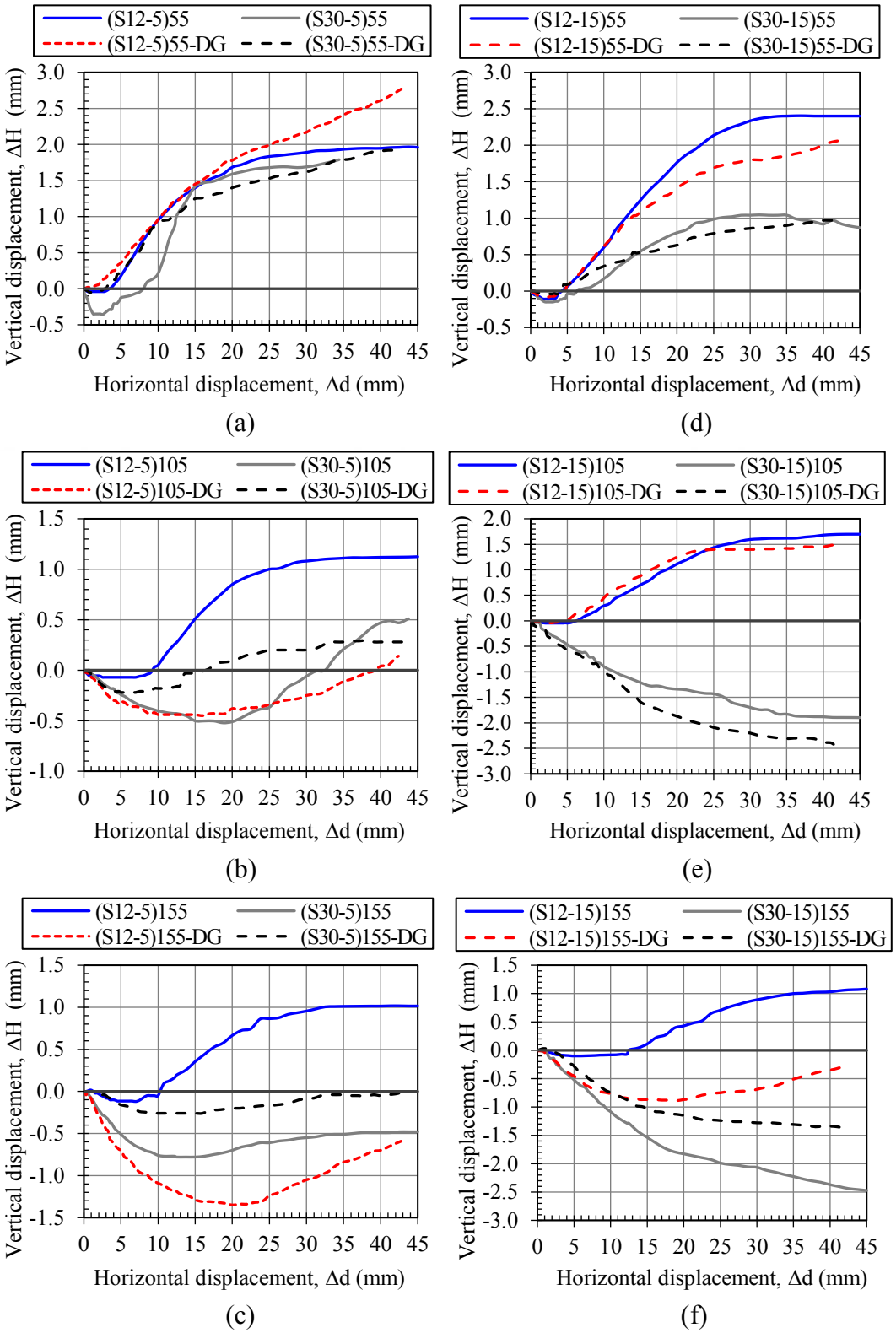


Figure 6.21. Vertical displacement with horizontal displacement plots of CFM with and without geogrid for PI=5% (a, b, c), and for PI=15% (d, e, f)

6.2.2.1 Discussion of Direct Shear Tests on Saturated Specimens

Specimens' degrees of saturation before and after water supply (application described in Section 3.3.6.2.2) were calculated using phase relations (Equations 4.2 and 4.3), and the results are presented in Table 6.5. After specimen preparation, initial degrees of saturation ($S_{r(in)}$), calculated according to the measured initial moisture content of the specimens, ranged between 63% and 76%. Final degrees of saturation ($S_{r(final)}$), on the other hand, were calculated using the specimen's final water contents and void ratio after settlement/saturation and shear stages. Final water contents were determined by the average of samples taken from four different parts of the specimen after test. Because final water content could be determined after the shear test was completed, volumetric changes in specimens due to the settlements after normal load application and shear were also considered in the corresponding final void ratio. $S_{r(final)}$ values ranged between 91% and 98% except tests for S20-15. For this mixture, final saturation degrees of 87% and 89% were calculated (Table 6.5). $S_{r(final)}$ values were used just to evaluate whether the designed water supply system could saturate the specimens. Because compression was generally observed in tests, it can be expected that the degrees of saturation prior to the shear tests may be lower than the reported degrees of saturation at the end. However, compared to $S_{r(final)}$ values in water submerged specimens in large compression tests (Table 5.3), it was observed that the designed water supply system was efficient in increasing the saturation degrees of the direct shear specimens.

Another evaluation was made by considering the water levels in piezometer pipes. Before the shear test started, in all tests, the water level in the outer chamber reached equilibrium with the saturated and de-aired piezometer pipes that remained in the specimen. Besides, the water level change was observed in the piezometer pipes (both rise and fall) during shear in accordance with the volumetric behavior and measured excess pore water pressure. This confirmed that the water could move freely and generate excess pore water pressure within the specimen in saturated direct shear tests.

Table 6.5. Phase parameters of the saturated specimens in direct shear tests

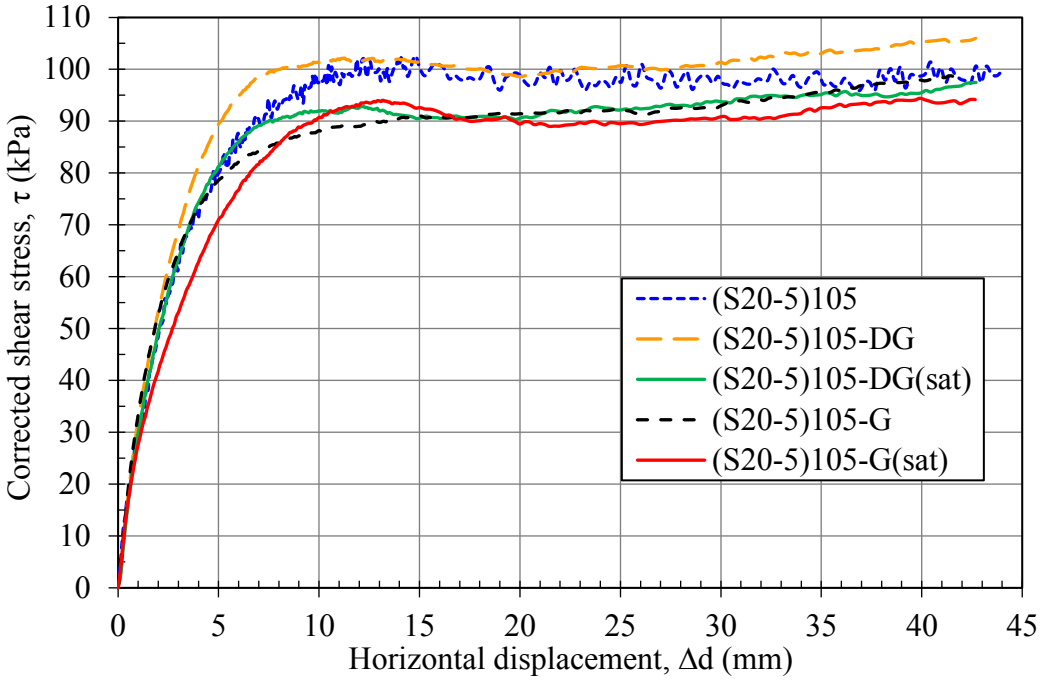
Soil code	Test code	Target moisture content (%)	After specimen preparation		After saturation/settlement stage and shear test	
			Measured initial moisture content (%)	Initial degree of saturation, $S_{r(in)}$ (%)	Final measured moisture content (%)	Final degree of saturation, $S_{r(final)}$ (%)
S20-5	(S20-5)105-DG(sat)	6.8	7.2	73	9.5	96
	(S20-5)105-G(sat)		7.0	71	9.3	91
S20-15	(S20-15)105-DG(sat)	9.8	10.6	74	11.3	87
	(S20-15)105-G(sat)		10.4	72	11.4	89
S40-5	(S40-5)105-DG(sat)	8.2	8.3	63	11.8	92
	(S40-5)105-G(sat)		9.0	66	11.8	94
S40-15	(S40-15)105-DG(sat)	14.2	14.4	76	16.3	97
	(S40-15)105-G(sat)		14.5	76	16.3	98

Corrected shear stress plots of saturated S20-5, S20-15, S40-5, and S40-15 specimens under 105 kPa initial normal stress are presented in Figure 6.22 and Figure 6.23. Measured results were compared with tests of unsaturated (at optimum moisture content) specimens with and without geogrid, while other variables were the same (see Section 3.3.6.4 for notations describing test codes). Peak and ultimate (residual) strength values for saturated tests are also summarized in Table 6.6. Stress increases after an ultimate (residual) value was reached were not considered in determining peak and residual strength values, as explained in Section 6.2.2.

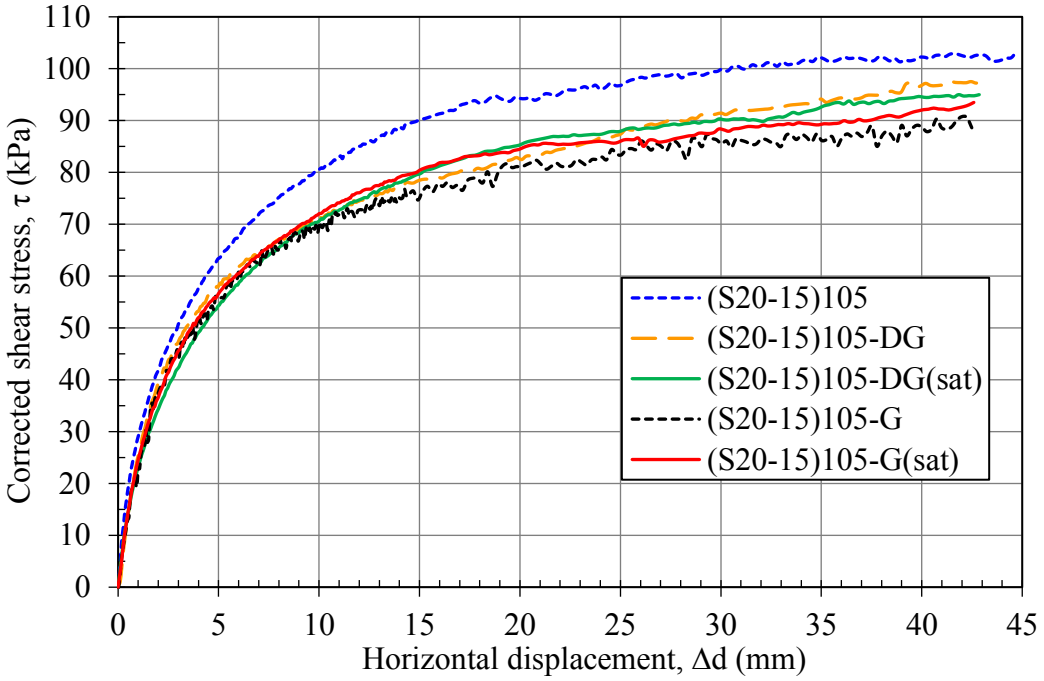
Table 6.6. Shear strength properties of saturated tests

Soil code	Test code	For peak strength of the interface			For ultimate (residual) strength of the interface	
		Corrected normal stress, σ_n (kPa)	Corrected shear strength, τ_p (kPa)	Relative horizontal displacement at peak, $\Delta d/L$ (%)	Corrected normal stress, σ_n (kPa)	Corrected shear strength, τ_r (kPa)
S20-5	(S20-5)105-DG(sat)	110.0	92.8	4.0	110.9	91.0
	(S20-5)105-G(sat)	110.3	94.0	4.3	112.1	90.2
S20-15	(S20-15)105-DG(sat)	123.2	95.0	14.3	*	*
	(S20-15)105-G(sat)	123.1	93.5	14.2	*	*
S40-5	(S40-5)105-DG(sat)	120.7	99.6	12.5	120.7	99.6
	(S40-5)105-G(sat)	120.9	95.7	12.6	120.9	95.7
S40-15	(S40-15)105-DG(sat)	114.5	69.1	7.8	114.5	69.1
	(S40-15)105-G(sat)	118.4	58.9	10.8	118.4	58.9

*Tests that did not reach an ultimate (residual) shear strength by the end of the test

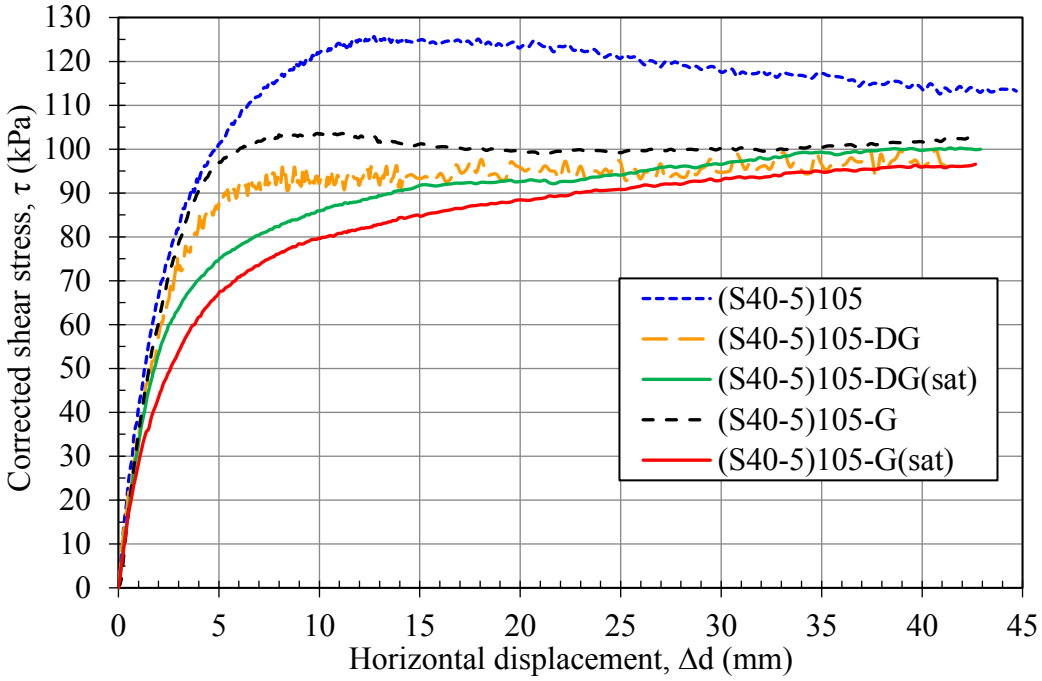


(a)

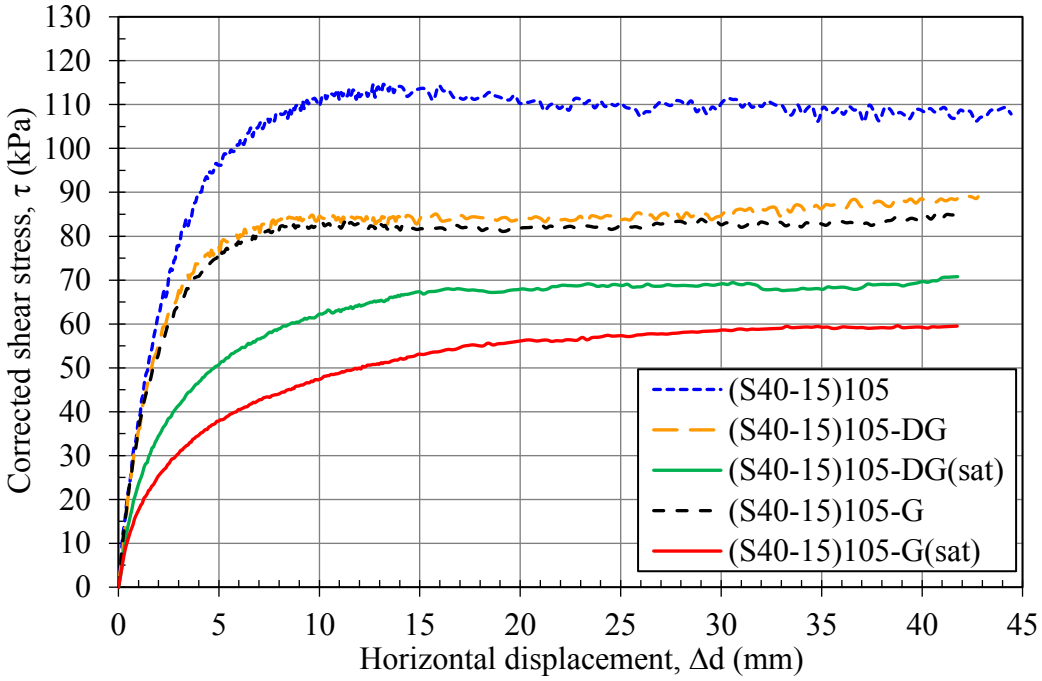


(b)

Figure 6.22. Comparison of the saturated tests' corrected shear stress with horizontal displacement plots for (a) S20-5, and (b) S20-15



(a)



(b)

Figure 6.23. Comparison of the saturated tests' corrected shear stress with horizontal displacement plots for (a) S40-5, and (b) S40-15

Although saturating the S20-5 (FC=20%, PI=5%) resulted in an approximately 9% decrease in strength compared to unsaturated condition (at optimum moisture content) for the tests with draining geogrid, there was no significant variation in the strength behavior for the tests with draining geogrid and geogrid without drainage when the specimens were saturated (Figure 6.22). Besides, saturating the specimens, and tests performed with draining geogrid and geogrid without drainage did not cause a significant difference in strength values for S20-15 (FC=20%, PI=15%). It should also be noted that relatively lower saturation degrees (87% and 89%) of the S20-15 measured at the end of the test might have an effect on this result. It was also observed that the increase of the stress with horizontal displacement showed similar trends for the tests with the same plasticity index. Although the peak strength values determined for PI=5% and PI=15% were close, in S20-15 specimens, it was reached in higher shear displacements compared to S20-5. In fact, peak strengths were determined according to the stress values at the end of the test in S20-15 because ultimate (residual) values were not reached within the applied shear displacement of the equipment.

For unsaturated specimens of S40-5 (FC=40%, PI=5%), tests performed with geogrids had approximately 20% lower peak shear strength value than the specimen's own strength (test without geogrid) (Figure 6.23a). In the tests performed with the geogrid without drainage property (geotextiles removed), the saturated test showed an approximately 8% lower peak strength compared to the unsaturated case, while there was no such difference between the saturated and unsaturated cases of tests with draining geogrid (Figure 6.23a). Saturating the specimens increased the shear displacements where the peak strengths were reached both for tests having geogrids with and without drainage properties. In other words, the shear strength difference was more significant between saturated and unsaturated cases for small shear displacements. Consistent with its strength response, it should also be noted that saturation of the S40-5 soil mixture entirely changed its volumetric behavior under direct shear, as seen in Figure 6.26c. Specimens prepared at optimum moisture, and 95% of the standard Proctor dry density showed an initial contraction followed

by dilation in all tests. On the other hand, saturating the S40-5 soil mixture shifted specimens to a completely contractive soil response (Figure 6.26c).

For the S40-15 soil mixture (FC=40%, PI=15%), tests performed with unsaturated specimens and geogrids with and without drainage property showed a similar strength behavior. Tests with geogrids had approximately 26% lower peak shear strength value compared to the specimen's own peak shear strength (test without geogrid) (Figure 6.23b). Saturation of the specimens caused a decrease in strength response both in tests having geogrid with and without drainage property. However, while all other parameters were the same, saturation of the specimen decreased the peak and ultimate (residual) strength by 18% in tests with draining geogrid (DG), while it decreased by 29% in the geogrid without drainage property (G) for the test conditions in this study (Figure 6.23b).

As described in Section 3.3.6.2.2, excess pore water pressures measured with the pressure transducer during shear in three saturated tests of S20-5 and S40-15 are shown in Figure 6.24. After the saturation procedure, the pressure value measured with the transducer was recorded prior to the shear test. Excess pore water pressures generated during shear were calculated according to their change from this value.

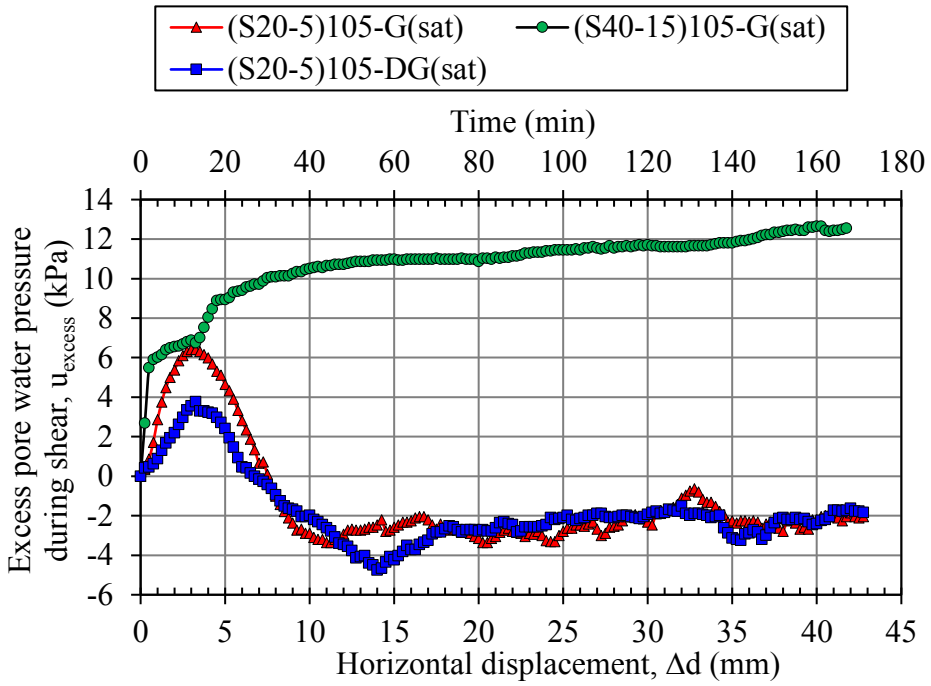


Figure 6.24. Excess pore water pressure with horizontal displacement during shear in saturated direct shear tests

Views of the piezometer pipe levels (previously de-aired and saturated) during shear for S20-5 and S40-15 specimens are presented in Figure 6.25. They helped confirm the observed trends of decrease or increase in excess pore water pressure measured with the transducer. For instance, the initial increase of pore water pressure and decrease thereafter to negative values were observed for the S20-5 soil mixture for both tests having geogrids with and without draining property (Figure 6.24). This trend was also observed in piezometer pipes in agreement with the transducer data. The initial rise in water level was observed in Figure 6.25b, and the water level decreased and became invisible, as shown in Figure 6.25c.

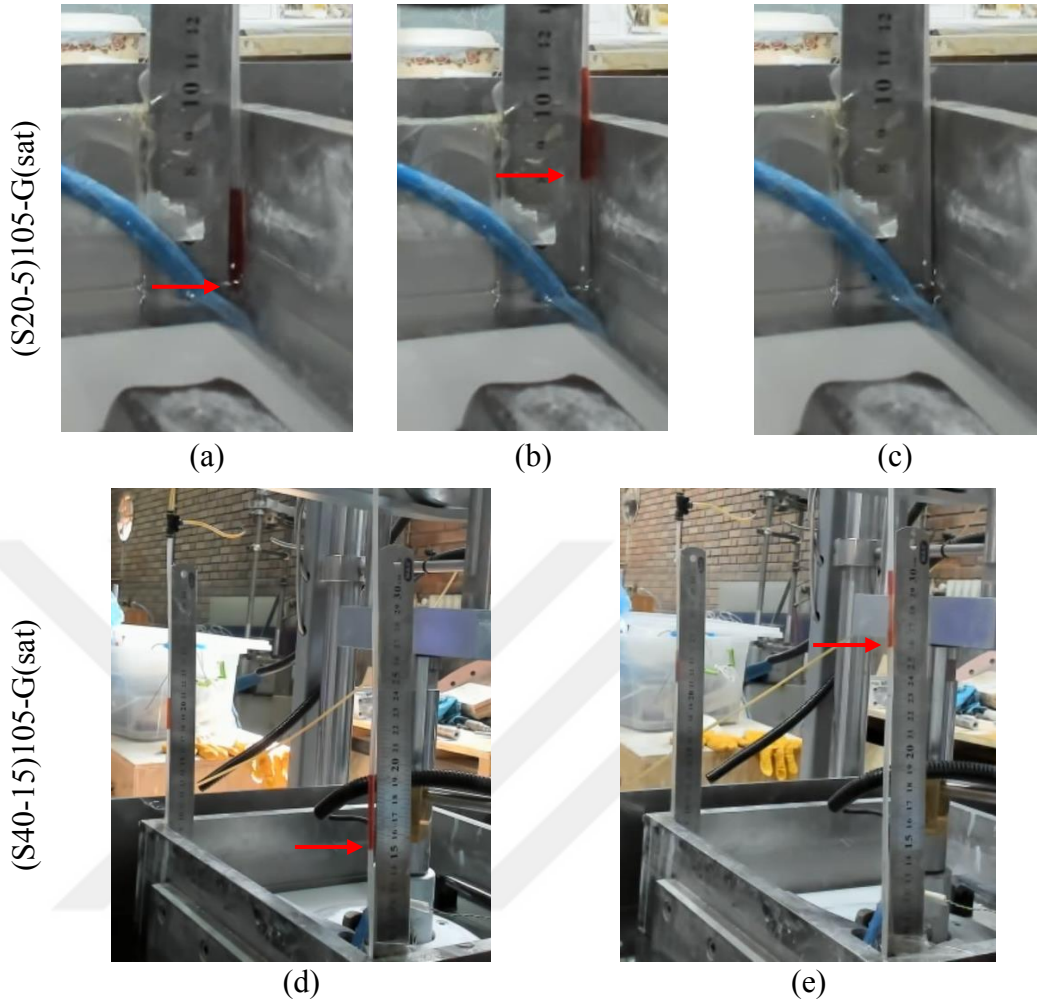


Figure 6.25. Views of the piezometer pipes during shear (a) initial level, (b) pore pressure increase, and (c) pore pressure decrease for S20-5 soil mixture. (d, e) Pore pressure increase in S40-15

A slightly lower initial excess pore pressure generation was observed in the S20-5 soil mixture with draining geogrid compared to geogrid without drainage (Figure 6.24). Afterwards, both tests resulted in negative pore water pressure generation for higher shear displacements. Measured pore pressure behavior was also compatible with the vertical displacements during shear observed for saturated S20-5 specimens (Figure 6.26a).

A continuous increase in excess pore water pressure during shear was observed for saturated S40-15 soil mixture and geogrid without draining property (Figure 6.24).

Pore pressure increase caused a significant reduction in strength value (Figure 6.23b), and led to a more contractive response, as seen in Figure 6.26d. As observed from piezometer pipes, the water level also rose in the test with the draining geogrid. However, the amount of rising was less than the test having geogrid without the draining property.

It was concluded that the drainage property in geogrids helps to reduce excess pore water pressure generation in the soil-geogrid interface for the saturated specimens. According to the results of this study, the contribution of the drainage was more critical in saturated soils of FC=40%, rather than FC=20% (both for PI=5% and PI=15%) in case soils were initially compacted to 95% of their standard Proctor dry densities (Figure 6.22, Figure 6.23).

According to the vertical displacement with horizontal displacement plots (Figure 6.26), saturating the specimens in all tests resulted in a more contractive soil response without exception. Saturating the S20-5 mixture increased the initial contraction; in other words, it shifted the graphs down; however, specimens still showed a dilatant response at higher displacements, although the amount of the dilation was reduced.

In specimens with PI=15% (both for FC=20% and FC=40%), all tests with and without geogrid showed contraction under 105 kPa initial normal stress. Although the resultant maximum vertical settlements were generally higher in S20-15 compared to S40-15, saturating the specimens increased the total amount of contraction by 23-30% for S20-15 and 61-104% for S40-15.

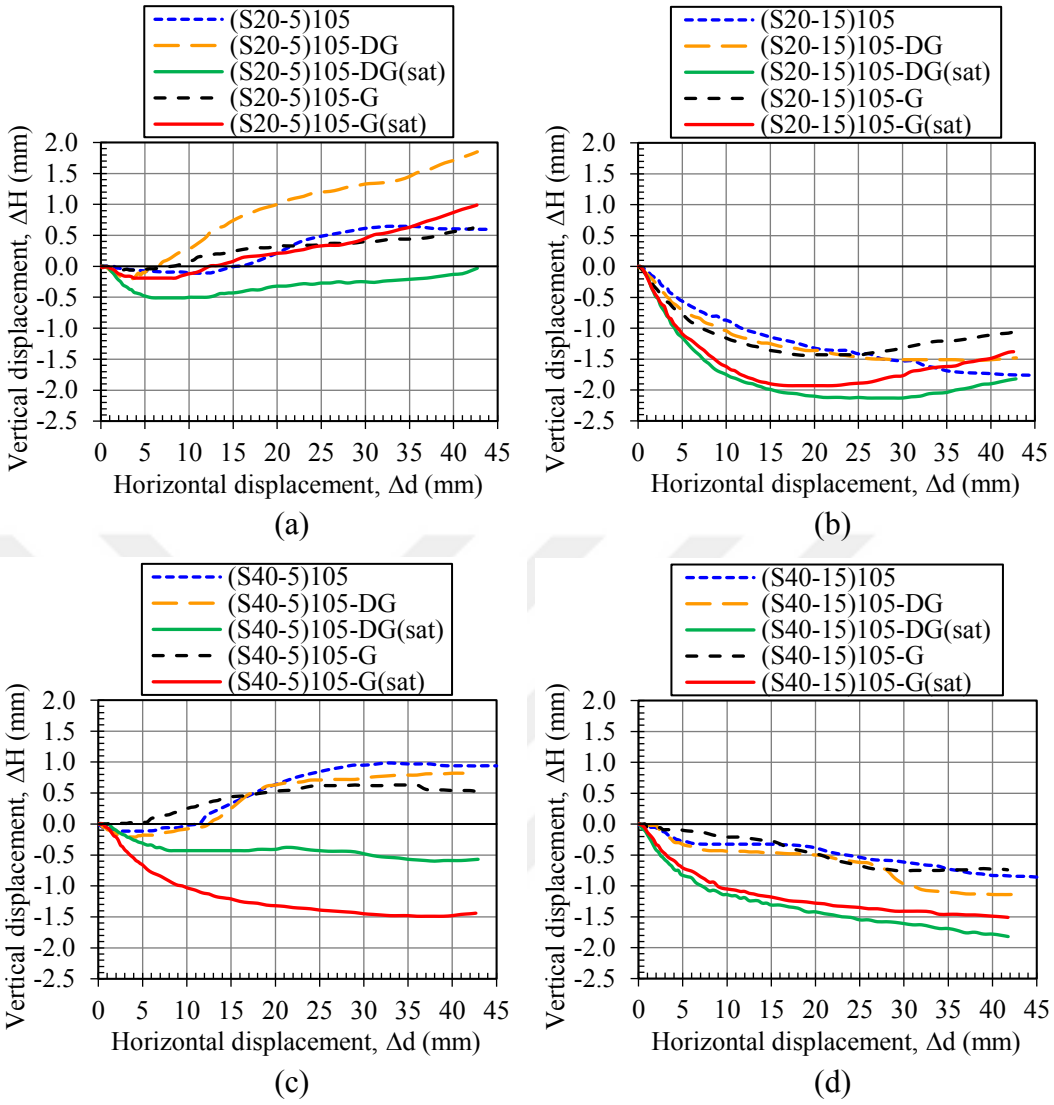


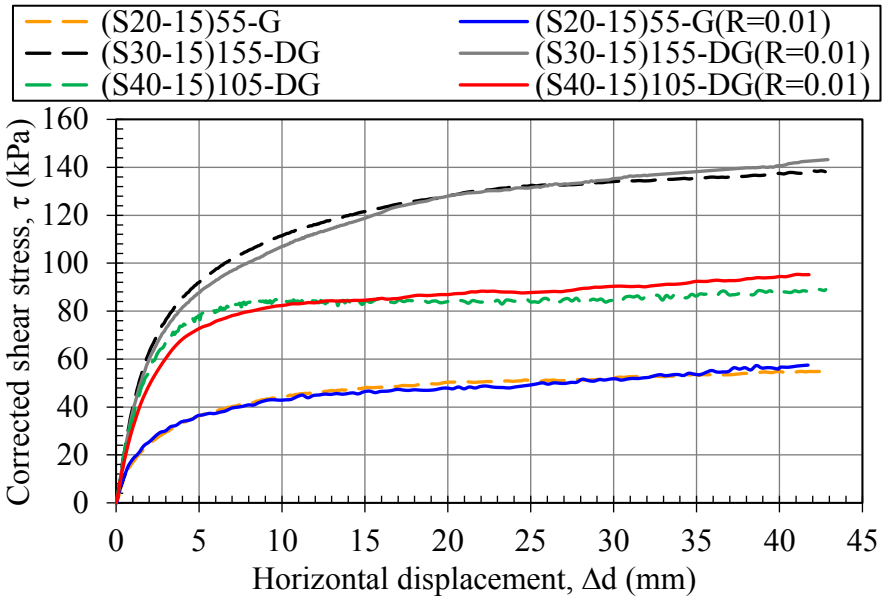
Figure 6.26. Comparison of the saturated tests' vertical displacement with horizontal displacement plots for (a) S20-5, (b) S20-15, (c) S40-5, and (d) S40-15

6.2.2.2 Discussion of Direct Shear Tests with a Shear Rate of 0.01 mm/min

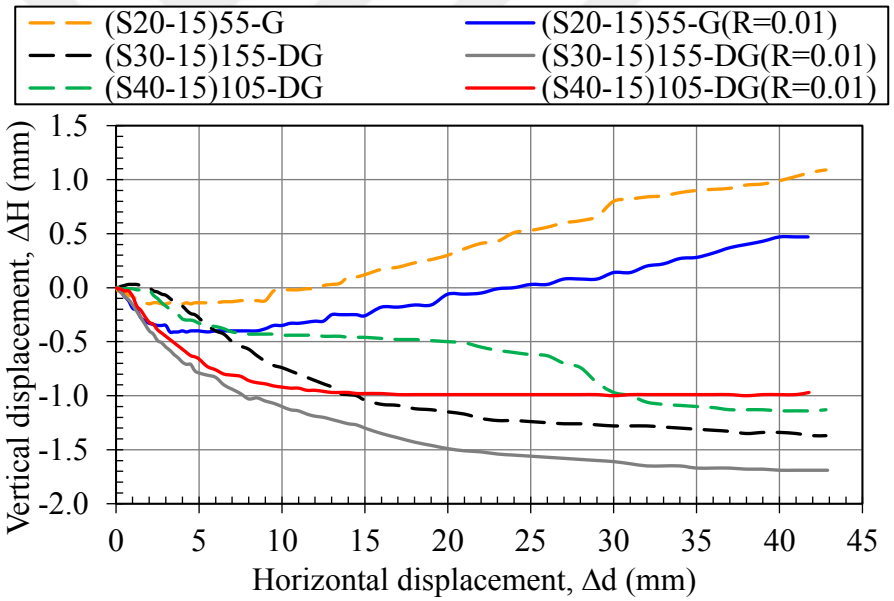
Direct shear tests were performed with a 0.25 mm/min shear rate in this study. Three tests were carried out with 0.01 mm/min to evaluate the effect of shear rate on strength response for specimens compacted at 95% of the standard Proctor dry density and optimum moisture content. One direct shear test approximately took 72 hours with this shear displacement rate. Recommendations of the ASTM D5321-14 were considered to determine the shear rate to ensure drained testing conditions even though specimens were not fully saturated. Specimens with a higher fines content and plasticity index (S20-15, S30-15, and S40-15) were tested with geogrids with and without drainage property under different normal stresses. While the other parameters were the same, test results at different shear rates are presented in Figure 6.27.

It was observed that strength response was not significantly affected by the rate of shear displacement for the tested specimens. Results indicated that peak and ultimate (residual) strength values did not vary more than 5%. It could be concluded that there was no significant excess pore pressure generation (or suction change) at the soil mixture-geogrid interface that reduces the strength response in tests with a shear rate of 0.25 mm/min in specimens prepared at optimum moisture content and 95% of the standard Proctor dry densities.

It was also observed in Figure 6.27b that behavioral trends for vertical displacement were similar at tests with different shear rates. A contraction followed by dilation was observed in the specimen with a fines content of 20% and plasticity index of 15% (S20-15) under 55 kPa initial normal stress, whereas other specimens showed a fully contractive response.



(a)



(b)

Figure 6.27. Comparison of the direct shear test results with 0.25 mm/min and 0.01 mm/min shear rates. (a) corrected shear stress-horizontal displacement plot, and (b) vertical displacement-horizontal displacement plot

CHAPTER 7

CONCLUSIONS

This study aimed to examine the behavioral thresholds of coarse-fine mixtures (CFM) or intermediate materials from different engineering aspects such as hydraulic, mechanical, and compressional responses. Parameter-controlled laboratory experiments were carried out to address the restrictions in the commonly used design guidelines for using intermediate materials as backfill soils in the design of mechanically stabilized earth walls (MSEW).

Ten different soil mixtures were prepared in the laboratory with carefully selected target properties for the particle size distribution, fines content (FC), and plasticity index (PI). In other words, the prepared mixtures were planned to have the characteristics near the sand-gravel, silt-clay material transition zones, or to have the dominant features of both groups. Instead of generating gap-graded binary mixtures, CFM were prepared by combining different proportions of commercially available soils (from fine gravel to clay-sized particles) to obtain mixtures whose coarse fraction was based on well-graded sand with gravel. Seven different soil products, fine gravel, coarse-, medium- and fine-graded sands, non-plastic silt, kaolin, and bentonite, were used to obtain ten different soil mixtures. Two of them were well-graded and poorly graded sands with gravel (SW, SP), and the other eight were CFM with predetermined index properties having FC of 12%, 20%, 30%, and 40%, and PI of 5% and 15%.

The geotechnical properties of laboratory-prepared CFM specimens were investigated in terms of the fines content and plasticity effect on soil classification, index properties, compressibility, hydraulic conductivity, and strength properties. In addition, CFM interaction with geogrid and interface friction coefficients in direct

shear failure mode was studied by conducting large direct shear tests (300 mm x 300 mm cross-section).

The CFM specimens in this study were prepared at 95% of the standard Proctor dry densities and optimum moisture contents (w_{opt}), similar to the criteria often recommended in design codes for the MSEW.

7.1 Conclusions on Index and Hydraulic Properties

Index characteristics of CFM and their relationship were investigated after their preparation in the laboratory. Mechanical (dry) and wet sieve analysis, hydrometer tests, specific gravity determination, standard Proctor compaction tests, Atterberg limits determination, minimum and maximum density tests (for coarse/cohesionless soils) were executed within this scope.

Soil mixtures were classified according to widely used soil classification systems and the Revised Soil Classification System of Park and Santamarina (2017). Variances in the definition of the same mixture for different systems and shortcomings for mixed soils were evaluated.

The methylene blue (MB) spot test method was used to determine the specific surface area (SSA) of the coarse-fine mixtures' cohesive fractions in this study. SSA of the coarse fractions was estimated by the particle shape and size properties, and the total SSA of the mixture was calculated according to the percent fractions of coarse/cohesionless and fine/cohesive portions. SSA of CFM was evaluated by associating the results with Atterberg limits and hydraulic conductivity test results.

Saturated hydraulic conductivities of CFM were determined with rigid wall and flexible wall hydraulic conductivity tests. During saturation, the volume change properties of CFM were examined.

Some of the important findings for the index and hydraulic properties of CFM, based on the experimental data in this study, are as follows:

1. In soil classification systems such as USCS, ESCS, and AASHTO, the engineering behavior of soils is predicted according to the predominance of fine or coarse particle fractions. The same soil can be defined and named differently due to the variations in material transition boundaries. In this study, it was observed that USCS, ESCS, and AASHTO soil classifications could not adequately represent the intermediate soils/CFM in terms of their dominant engineering behavior.

2. According to Park and Santamarina (2017)'s Revised Soil Classification System (RSCS), fines governed the flow characteristics of all CFM in this study. FC thresholds, controlling the hydraulic properties for soils having the same particle shape and plasticity characteristics as CFM in this study, could be observed from the classification charts prepared for each mixture. Accordingly, while the FC threshold governing flow was between 5% and 28% for mixtures with PI = 5%, it was between 2% and 12% for PI=15%, according to Park and Santamarina (2017). The FC threshold for mechanical behavior was between 20% and 30%. These results are in agreement with the past findings for the transitional thresholds. This study concludes that the RSCS of Park and Santamarina (2017) can represent the transitional properties of CFM in terms of mechanical and hydraulic behavior.

3. The results of the Proctor compaction test indicated that FC and maximum dry unit weights had a linear relationship for PI=15%. Compaction characteristics of CFM could be predicted according to their particle gradation and plasticity properties. It was observed that higher FC and PI led to an increase in optimum moisture contents and a decrease in maximum dry unit weights.

4. Liquid limits of samples passing through No. 40 and No. 200 sieves were significantly affected by the cohesionless fine sand having particle sizes between 0.425 mm and 0.075 mm. The effect of plasticity on CFM is better reflected when the Atterberg limits of CFM are determined by sieving the samples through No. 200 sieve. Therefore, this study recommends the determination of LL on the portion of the sample that is smaller than 0.075 mm (No. 200 sieve) for CFM.

5. The specific surface area (SSA) of the plastic portion passing a No. 200 sieve was directly proportional to the percent fraction (by dry weight) of plastic ingredients (such as kaolin and bentonite in this study). With this approach, SSA could be estimated in 90-120% of the measured data. This conclusion suggests that the total SSA of CFM can be calculated from the weighted average of the SSAs of the relevant fractions constituting CFM.

6. The SSA of the cohesive fraction for specimens passing through No. 40 and No. 200 sieves was estimated between 35% and 168% of the measured data with empirical correlations of Farrar and Coleman (1967) and Chapuis and Aubertin (2003). However, poor estimates were observed in this study for CFM with lower plasticity.

7. Results in this study indicated that comparing the intergranular void ratio with the maximum void ratio of the granular fraction is a practical indicator for evaluating the transition between fine or coarse-grained dominance rather than evaluating the global void ratio. In terms of particle packing for the CFM initially compacted to 95% of the standard Proctor dry density, this transition was observed to occur at 15% fines for PI=5%, while it was around 12% for PI=15%. Transitional FC decreased with the increase in plasticity index. However, it should be noted that factors such as relative sizes of particles, particle shape, and angularity also affect the threshold values. Therefore, soil-specific consideration is required if the transitional FC of the CFM is to be determined.

8. As FC and PI increased, the hydraulic conductivity of CFM decreased. There was a threshold of FC at which hydraulic conductivities decreased significantly, as appeared in the measurements of this study. It was between 12% and 20% for PI=5%, whereas around 30% for PI=15%.

9. The empirical correlations that developed for pure clays or pure granular materials were not able to accurately predict the measured hydraulic conductivities of the CFM in this study. However, some correlations made closer estimates than others. For instance, correlations of Hazen (1892, 1911) and Chapuis (2004) estimated the

measured hydraulic conductivity of CFM in this study within an order of magnitude except for the mixture having 40% fines and 15% plasticity index. In addition, equations of consolidation theory underestimated the hydraulic conductivity of CFM with PI=15% within an order of magnitude. On the other hand, hydraulic conductivities of CFM were underestimated by one to four orders of magnitude by Kozeny (1927) - Carman (1956) and other correlations relating SSA with hydraulic conductivity. This study indicates that there are some difficulties in estimating SSA and using prediction methods of hydraulic conductivities, especially for CFM.

10. The saturated hydraulic conductivity values of the CFM were in the range of $1x10^{-3}$ to $2.4x10^{-5}$ cm/s for PI=5% and $3.8x10^{-5}$ to $1.3x10^{-7}$ cm/s for PI=15%. The saturated hydraulic conductivity values were similar to clays for CFM with PI=15% and FC more than about 25%. The unsaturated hydraulic conductivity values of CFM will be smaller than the reported values here. This result may imply that, in MSEW, even if such CFM having PI=15% are used as compacted backfill, in a heavy rainfall event, or a pond of water accumulation, water infiltration into the CFM can be expected to be very slow.

7.2 Conclusions on Unconfined Compressive Strength, Shear Strength by Triaxial Tests, and Compressibility

Unconfined compressive strength (UCS) tests were performed to investigate coarse-fine mixtures' compressive strength properties, and isotropically consolidated undrained (ICU) triaxial strength tests were performed for the shear strength evaluation, in addition to large direct shear tests.

Compressibility properties were evaluated by the consolidation data of the saturated CFM specimens within the scope of triaxial tests and one-dimensional static large-scale compression tests.

Some of the important findings for the strength and compressibility response of the CFM, based on the experimental data presented in this study, are as follows:

1. Unconfined compressive strength (UCS) values of all CFM in this study were in the range of 79 to 161 kPa, except for the soil mixture with FC=12% and PI=5%, which had 23 kPa UCS. UCS values of CFM with PI=15% were always higher as compared to CFM with PI=5% having the same FC. If the UCS values are used to determine undrained shear strength values (as it is done for saturated clays), the undrained shear strength values in the range of 40 to 80 kPa would be obtained (except for the mixture with FC=12% and PI=5%). However, it should be kept in mind that the CFM specimens in the UCS tests in this study were unsaturated and that the "undrained" condition may not hold true.

2. More pronounced failure surfaces were observed with the increasing FC and PI according to the failed specimen appearances as a result of the UCS tests. In addition, more explicit bulging was detected in the middle of the specimens for CFM having fines content less than 20% for both PI=5% and PI=15%.

3. UCS values of CFM increased as FC and PI increased. For the CFM having PI=15%, the UCS value varied significantly between 20% and 30% fines content. In addition, higher axial strains at failure and a lower rate of decrease in compressive stress after reaching the peak value were observed with the increase in FC and PI. However, CFM with FC=20% and PI=15% had the highest axial strain at failure compared to other data as an outlier trend.

4. ICU triaxial compression tests on saturated CFM under up to 300 kPa confining pressures indicated that the effective cohesion intercept values ranged between 0 to 7 kPa and effective friction angle values were in the range of 27 to 40 degrees for all saturated CFM in this study. A general trend of decreasing effective friction angle with increasing FC was observed.

5. ICU triaxial tests indicated that higher FC and PI values decrease both undrained and effective internal friction angles. As a general trend, the effective friction angle of the mixture with PI=5% was 2° to 6° higher than PI=15% for a given FC. In addition, undrained friction angles did not considerably vary with fines content for PI=15%. The undrained friction angle for CFM with PI=5% was significantly higher

than PI=15% for the same FC up to 20% of fines content, after which the effect of PI decreased.

6. According to the stress paths resulting from triaxial tests, the variation of the stress ratio at critical state (M) with fines content had an approximately linear correlation for the same PI. A narrow range of M values was observed for PI=5% compared to PI=15%. For the same FC, the effect of PI on the variation of M values was larger for higher FC values.

7. Void ratio and mean effective stresses at critical state (p') under different initial consolidation pressures showed a linear correlation for the same CFM. Although the gradient (λ) of the critical state line in ν-lnp' space slightly increased with FC, the gradients (λ) of the CFM with PI=15% were almost twice the gradient values of PI=5% for the same FC.

8. The degree of initial contraction tendencies in triaxial tests was quantified using two normalized parameters. u_{excess}/σ'_c represents the initial increase in excess pore water pressure with respect to the consolidation pressure, whereas $(\sigma'_c-p'_{min})/\sigma'_c$ stands for the reduction in the mean effective stress relative to the consolidation pressure. This study confirms that both of these parameters can be used for the reasonable quantification of the initial contraction tendencies during undrained compression. It was observed that the degree of initial contraction tendency increased with the consolidation pressure in all mixtures.

9. According to the contractive/dilative tendencies of the mixtures observed during ICU triaxial tests, most of the CFM in this study showed an initial contraction followed by dilation. CFM in this study were categorized into three groups according to the similarities of their stress paths and normalized excess pore water pressure (u_{excess}/σ'_c) variation with axial strain. Mixtures with PI=15% were generally included in the group of specimens having relatively high initial contraction followed by dilation. For the PI=5%, on the other hand, FC=12% belonged to the group of specimens having relatively low initial contraction followed by dilation irrespective of the consolidation pressure. However, specimens with fines contents of 30% and

40% consolidated under 150 and 300 kPa effective stresses showed a fully contractive response accompanied by strain-softening. Contractive/dilative tendencies of the mixtures with PI=5% switched from dilation-dominated response to contraction-dominated response with the accompanied FC increase. FC=20% can be considered the transitional boundary, in which the volumetric tendencies of the mixtures with PI=5% changed.

10. Higher axial strains at failure (larger than 9%) were observed for mixtures with PI=15% compared to PI=5% independent from consolidation pressures in triaxial tests. For the PI=5%, on the other hand, FC=12% showed high axial strains at failure as the strain-hardening behavior was observed in this mixture at all consolidation pressures. Strain-softening response was observed for the mixtures with PI=5% and FC larger than 12%. Peak strengths were reached at axial strains lower than 5% for these mixtures.

11. The amount of strain-softening in mixtures with PI=5%, having fines content of 20%, 30%, and 40%, was expressed with Brittleness Index (I_B) as a measure of the reduction in the value of peak strength in triaxial tests. Brittleness indices ranged between 0.09 and 0.26 for the CFM in this study. A general trend of a slight increase in I_B was observed with fines content.

12. Skempton's pore pressure parameter at failure (A_f) was calculated for all CFM as a result of ICU triaxial compression tests in this study. CFM with PI=5%, having 12% and 20% fines, had A_f in between 0 and 0.5. According to Bishop and Henkel (1962), the A_f values for 0 and 0.5 corresponded to loose sand and alluvial sandy clays, respectively, whereas these ranges corresponded to lightly overconsolidated clays, according to Skempton (1954). On the other hand, fines content of 30% and 40% generally corresponded to A_f values of 0.5 and 1 as a general trend in this study. Skempton (1954) classified soils having A_f in between 0.5 and 1 as normally consolidated clays, whereas 0.25 and 0.75 as compacted sandy clays. In addition, it was also observed that the effect of PI on A_f was more dramatic at low FC values as 12% and 20%.

13. Compressibility properties of the saturated mixtures before triaxial compression tests were evaluated by the percent volumetric strains during consolidation. While a time-dependent volumetric discharge was observed for all CFM with PI=15% at all consolidation pressures and fines contents, a significant part of the volumetric strain occurred immediately after the application of consolidation pressures in CFM with PI=5%. In addition, fines contents between 30% and 40% for PI=15% can be considered the threshold at which normally-consolidated clay-like behavior begins to be observed based on the coefficient of consolidation (c_v) values for the saturated CFM in this study.

14. Variation of intergranular relative densities with different initial consolidation pressures indicated that the fines content threshold at which material switched to fine-grained to coarse-grained domination in terms of particle packing increases with the effective stress on the specimen. Transitional FC increased from 15% at saturated state to 16.5% at 300 kPa consolidation pressure for PI=5%, whereas it went from 12% at saturated state to approximately 14% at 300 kPa consolidation pressure for PI=15%. Changes in threshold FC and void ratios were relatively low in this study as the mixtures initially compacted at 95% of the standard Proctor densities. Variation in transitional FC in terms of particle packing can be expected to be more significant in soils with higher void ratios.

15. Specimens were prepared to have initial degrees of saturation ranging between 57% and 78% before the static large compression tests. This study indicated that submersion of the specimens in water for one week before compression tests increased the degrees of saturation to a range lower than 79% and 93%. In other words, water submersion over a period of one week did not provide complete saturation of the specimens. This may imply that if such CFM are used in MSEW, in a heavy rainfall event, when a pond of water remains on the ground surface for a week, it may not cause complete saturation of the CFM, although it will be expected to cause an increase in the degree of saturation of the CFM.

16. Fines content increase and submerging the specimens in water did not create a significant variance in the axial strain values observed in static large compression tests for PI=5%. Axial strains ranged between 1.0% and 2.1% at the loading stage, in which the maximum stress was applied (1280 kPa). On the other hand, a considerable increase was detected with FC for PI=15%. Axial strains at the maximum loading stage were in the range of 2.84%-6.17% and 2.62%-8.47% for unsubmerged and submerged tests, respectively. The variation of axial strain from FC=12% to FC=20% was more drastic than other fines contents for the CFM with PI=15%.

17. Compression indices (C_C) deduced from the e-logσ plots as a result of compression tests indicated that C_C values for PI=5% varied in a relatively smaller range (0.013 and 0.034) for unsubmerged and submerged tests. On the other hand, higher C_C values were observed for PI=15% and larger FC values. It varied between 0.055 and 0.182 for unsubmerged tests, whereas 0.049 and 0.117 for submerged tests for CFM with PI=15%. Similarly, higher rebound indices (C_s) were observed with higher FC and PI, while the most significant increase with FC was observed in PI=15% for submerged tests.

18. For the CFM in this study, secant constrained modulus (M_s) obtained from compression tests ranged between 22 and 127 MPa for PI=5%, whereas 4 and 49 MPa for PI=15%. A significant decrease of constrained modulus with PI was observed for the same FC and normal stress.

7.3 Conclusions on Large Direct Shear Response

Strength properties of CFM and their interaction with geogrids (having two different surfaces that one has in-plane drainage capability) were investigated through large direct shear tests (300 mm x 300 mm cross-section). Three normal stresses of 55, 105, and 155 kPa were applied to specimens initially prepared at optimum moisture content and 95% of the standard Proctor dry densities. A total of 90 large direct shear tests were carried out in the scope of this study.

Most direct shear tests in this study were performed by applying a 0.25 mm/min shear rate. Three tests were performed with 0.01 mm/min under different normal stresses to evaluate the effect of shear rate on specimens having FC of 20%, 30%, and 40% with 15% PI.

Eight tests were performed under 105 kPa initial normal stress to investigate the interaction of CFM with the geogrid in the saturated condition. Tests were carried out on specimens containing 20% and 40% fines with 5% and 15% plasticity indices. Specimens were saturated by a pressurized water supply (≈ 35 kPa) from the bottom and sides of the specimens after preparation and normal load application.

Some of the important findings for the large direct shear tests of soil mixtures, based on the experimental data presented in this study, are as follows:

1. Corrected shear stress and horizontal displacement plots of SW and SP soil mixtures (without geogrid) resembled the shear strength behavior of medium/dense sands. Under all initial normal stresses, stress increased up to a peak shear strength and reduced thereafter to an ultimate (residual) value for these soil mixtures. A small initial contraction followed by dilation was observed during shear. Similar to SW and SP, strength reduction after the peak was observed for CFM with PI=5% and PI=15% under 55 kPa initial normal stress. However, after the peak value was reached, the strength reduction of CFM was significantly reduced or became zero as the initial normal stress increased up to 155 kPa.

2. All tests performed under 55 kPa initial normal stress and all CFM with PI=5% showed an initial contraction followed by dilation in direct shear tests. However, the amount of initial contraction increased, and the following dilation decreased with normal stress. Low initial contraction followed by dominant dilatant response was observed when FC=12%, whereas the amount of contraction significantly increased with normal stress for further FC increases. In fact, CFM with PI=15% showed a fully contractive response for FC higher than 12% under initial normal stresses of 105 kPa or higher.

3. SW and SP soil mixtures (dry and no fines) had the highest internal friction angles, 49.3° and 46.2°, respectively. Friction angles of CFM were around 40° - 41° for FC=12%. For higher fines content, friction values decreased to around 38° for PI=5% and 35° for PI=15%. All CFM, in their compacted state and under a maximum of 155 kPa normal stress (correspond to an 8-m-high MSEW), had more than 34° effective friction angle, which is the minimum value required for backfill soils in MSEW according to FHWA (2009). CFM with PI=5% had a 1° to 4° higher internal friction angle than PI=15% for the same FC. Cohesion intercept of CFM increased with fines content and plasticity index. CFM with FC=12% and PI=5% had the lowest cohesion (7 kPa), whereas the other values ranged between 16.9 and 30.7 kPa.

4. Peak strengths were reached at smaller horizontal (shear) displacements in SW and SP soil mixtures compared to CFM. Horizontal displacements at the peak were directly proportional to the normal stress. Peak shear strengths of CFM were reached at shear displacements ranging between 5.4 mm and 38.7 mm. As a general trend up to FC=20%, CFM with PI=5% tended to reach peak strength earlier than CFM with PI=15%, which reversed after FC=20%.

5. The cohesion intercept decreased when soil mixtures interacted with geogrid in all CFM tested in this study. The amount of decrease was quantified by the efficiency on cohesion (E_c), which ranged between 5.5% and 73.6%.

6. The friction angle of the interface (δ) decreased to 42.2° from 49.3° for SW soil mixture and 43.1° from 46.2° for SP soil mixture. For CFM, on the other hand, slightly lower and higher friction values at the interface were observed compared to mixtures' own internal friction angles, although there was no significant variation in most of the tests. Efficiency on friction (E_ϕ) ranged between 76.5% and 111.3% for all CFM in this study.

7. Interface shear strength coefficients at peak strength (α_{peak}) varied between 0.65 and 1.01 for the soil mixtures in this study. Higher bond efficiencies in the range of 0-0.19 were observed in CFM with PI=5% compared to PI=15% when specimens

(95% of standard Proctor compaction at optimum moisture) interacted with geogrid. Although fluctuations in the value of α_{peak} were observed with fines content, maximum values were observed at FC=12%, and minimum values were observed at FC=40% as a general trend. The lowest α_{peak} values observed for FC=40% were between 0.73 and 0.83 in this study.

8. While other variables were the same, the interface shear strength coefficient increased between 0.04 and 0.22 when the initial normal stress increased from 55 kPa to 155 kPa. A similar amount of increase was observed for both mixtures, having PI=5% and PI=15%.

9. Interface shear strength coefficient observed at ultimate/residual strength (α_{res}) were between 0.72 and 1.05 for soil mixtures in this study. In most tests, α_{res} was higher than the α_{peak}, and both values were less than 1. In other words, geogrid presence had a more pronounced effect on peak strength reduction compared to residual values. In addition, the highest shear strength coefficients (values higher than 1) were observed at CFM having 12% and 20% fines and 5% plasticity index, rather than SW or SP soil mixtures which were dry and included no fines.

10. Test results performed with a 0.01 mm/min displacement rate indicated that shear strength and volumetric behavior during shear were not significantly changed as compared to tests performed at 0.25 mm/min for unsaturated specimens. It can be concluded that no significant excess pore water pressure that reduces the strength of the soil mixture-geogrid interface was generated in tests with a 0.25 mm/min shear rate (for specimens prepared at optimum moisture content and 95% of the standard Proctor dry density).

11. Test results with saturated specimens indicated that no significant variation in strength values was observed for the tests with draining geogrid and geogrid without drainage when the specimens had 20% fines. The initial increase of excess pore water pressure and decrease thereafter to negative values were measured for specimens with 20% fines and a 5% plasticity index. However, it was also observed that the initial increase of pore pressure was slightly lower in tests with draining geogrid

compared to geogrid without drainage. In accordance with the pore pressures, a contraction followed by a dilation was observed as vertical movement during shear. However, saturating the specimens increased the amount of initial contraction and decreased the following dilation significantly.

12. In the tests of CFM with 40% fines and 5% plasticity index and geogrid without drainage property, 8% peak strength reduction was observed in the saturated condition compared to the unsaturated case. On the other hand, no significant change in peak strength value was observed in tests with the draining geogrid. For small shear displacement levels, an explicit decrease in strength was observed in saturated tests compared to unsaturated ones for both types of geogrids. Saturating the specimens changed the unsaturated specimens' volumetric behavior under shear from an initial contraction followed by dilation to a complete contraction.

13. For the unsaturated specimens (at optimum moisture) of CFM having FC=40% and PI=15%, tests having geogrids with and without drainage property showed similar strength behavior. Saturating the specimens resulted in a significant strength reduction for both geogrid types as compared to the unsaturated condition. While the decrease in peak and ultimate (residual) strength values were 18% in the draining geogrid, it was approximately 29% in the geogrid without drainage. In addition, it was observed that the water level continuously rises during shear in the piezometer pipes placed within the specimens for both geogrids. However, the amount of rising was less in the draining geogrid. According to the results of this study, the contribution of the drainage was more critical for saturated soils when FC=40% rather than FC=20% (both for PI=5% and PI=15%), in case specimens were initially prepared at 95% of the standard Proctor dry density.

7.4 CFM usage in MSEW

This study indicates that there are different behavioral thresholds for the same soil for different engineering responses such as compressive strength or shear strength, compression, hydraulic properties, or in terms of coarse and fine particles' packing

in the soil matrix (i.e., the ability to stress transfer between coarse-grained particles). In addition, other than FC and PI, as generally indicated in the codes for the design of MSEW, other factors such as mineralogy, the relative particle sizes of coarse and fine fractions, particle shape, and angularity contribute to the diversification of the engineering behavior. Therefore, soil-specific analyses may still be required to estimate the expected in-situ material behavior accurately. Based on the coarse-fine mixtures (CFM) within the scope of this study, the results that can be associated with CFM usage as backfill in MSEW are as follows:

According to the large static compression test results for unsubmerged and water submerged specimens in this study, axial strains were between 0.5% and 0.9% for PI=5%, and 0.9% and 4.0% for PI=15% under 320 kPa vertical stress. It should be noted that because tests were applied on laterally constrained 1-D compression conditions, these values could not be directly associated with their expected end-of-construction settlement in the field. However, collecting intermediate materials' settlement data which is somewhere in between coarse and fine-grained settlement responses, can provide valuable information for the expected volume change behavior of CFM under MSEW service loads.

In this study, CU triaxial compression tests on saturated compacted CFM indicated the strain-hardening/softening behavior, contractive/dilative tendencies, and the variation of pore pressure parameters at failure co-dependently changed with fines content (FC) and plasticity index (PI). In addition, quantities of the intermediate soils' hydraulic conductivity and the thresholds at which the behavioral transitions occur significantly varied depending on again the FC and PI relationship, according to the results of this study. Therefore, as the databases for the intermediate soils, having the potential to be used as backfill, are improved, FC and PI criteria in the guidelines can be recommended as co-dependent parameters having the alternative ranges for different FC and PI pairs.

According to the direct shear test results, all CFM in this study, in a state compacted to 95% of the standard Proctor maximum dry densities at optimum moisture content,

satisfied the minimum design friction angle criterion (34 degrees) of FHWA (2009) for backfill materials. Again at optimum moisture, interface friction measured for all CFM (for the geogrids used in this study) was also above the interface friction recommended as a conservative design parameter (reduction of tanϕ by 2/3) by FHWA (2009).

According to the direct shear test results, differences in interface shear strength values (peak and ultimate/residual) between the tests with draining geogrid and geogrid without drainage varied up to 15% for the CFM compacted at 95% of the standard Proctor dry density and optimum moisture content. However, higher strength values were observed with draining geogrid in some tests and geogrid without drainage in others. In other words, the drainage component did not affect the interface strength in a particular trend for unsaturated specimens, while all other parameters were the same. In addition, while the specimens were at optimum moisture contents, the strength behavior of the tests with a shear rate of 0.01 mm/min and 0.25 mm/min were similar. In accordance with this conclusion, in the numerical study on the stability of geocomposites in different climate conditions by Nunes et al. (2022); they reported that the effectiveness of the drainage in geocomposites is significantly reduced for unsaturated soils. On the other hand, drainage effectiveness increases under near or fully saturated conditions to dissipate excess pore water pressure.

When the specimens were saturated, a significant decrease in shear strength of the soil-geogrid interface was observed due to the excess pore water pressure generation in CFM with FC=40% and PI=15% in this study. In addition, consolidation data from triaxial tests on saturated specimens indicated that fines content of 30% to 40% at PI=15% was the threshold at which the measured coefficient of consolidation values approximated the values associated with normally-consolidated clays, according to NAVFAC DM 7.1 (2022). For these reasons, consideration of effective drainage measures appears to be critical for saturated soils with high fines and plasticity, as shown in this study.

Specimens were submerged in a water bath for not less than seven days in the scope of large compression tests. Although this method increased the degrees of saturation, specimens could not be completely saturated. In the direct shear tests, on the other hand, specimens' degree of saturation was increased further by supplying pressurized water from the bottom and sides and by keeping the specimens submerged in water.

As mentioned above, the strength behavior of unsaturated/saturated CFM and the fact that saturation of the specimens could not be provided easily without a pressurized water supply highlight the importance of preventing water infiltration into the MSEW fill. As Koerner (2005) explicitly stated, water seepage from retained earth zone, as well as water infiltration from the front, top, and behind the reinforced zone, should be prevented by implementing an external drainage system if high fines are included in the backfill.

It should be noted that this study examined CFM materials with a maximum of 40% fines content and a maximum of 15% PI value. Therefore, at least 60% or more of the CFM in this study were made of granular (sandy-gravelly) soils. The trendlines and results of this study cannot be extrapolated to predict the behavior of soils with higher fines content or higher PI values. Furthermore, higher fines content and higher PI values are not recommended as a backfill soil in MSEW.

7.5 Recommendations for Future Research

This study focused on the geotechnical properties of coarse-fine mixtures (CFM) compacted at relatively dense states (95% of standard Proctor densities). CFM interaction with geogrid and intermediate/transitional soils that can be used in the design of MSEW were investigated. An increase in the number of experimental studies with intermediate materials (according to their suitability for MSEW backfill) prepared with varying initial properties may help develop a library or a database. A clearer prediction of the intermediate material behavior on-site will enable the international specifications/codes to be updated. These varying material properties

may include different initial densities (or could be expressed as percentages of standard Proctor compactness) and the wet and dry parts of the optimum moisture contents. In addition, the performance of the intermediate soils having different particle gradations (such as gap-graded or uniform gradation) and shape could be investigated. Interactions of intermediate materials with geogrid can be diversified for different geogrid properties, such as extruded or biaxial types.

Determining the initial stress states, transmissivity, and soil-water characteristic curves could help more accurately predict the behavior of the unsaturated backfill material as it is prepared in situ. In addition, more studies focusing on expanding the MSEW design methodologies (that were mainly developed for clean granular fill materials) to include intermediate soils (predominantly granular soils with fine/cohesive soils) may be useful.

REFERENCES

AASHTO (2002). (American Association of State Highway and Transportation Officials). Standard specifications for highway bridges.

AASHTO M145-91 (2017). (American Association of State Highway and Transportation Officials). Standard specification for classification of soils and soil-aggregate mixtures for highway construction purposes.

Abdi, M. R., Sadrnejad, A., & Arjomand, M. A. (2009). Strength enhancement of clay by encapsulating geogrids in thin layers of sand. *Geotextiles and Geomembranes*, *27*, 447–455. https://doi.org/10.1016/j.geotexmem.2009.06.001

Abedi, M., & Yasrobi, S. S. (2010). Effects of plastic fines on the instability of sand. *Soil Dynamics and Earthquake Engineering*, *30*, 61–67. https://doi.org/10.1016/j.soildyn.2009.09.001

Abeele, W. V. (1986). The influence of bentonite on the permeability of sandy silts. *Nuclear and Chemical Waste Management*, *6*, 81–88. https://doi.org/10.1016/0191-815X(86)90091-4

Abu-Farsakh, M. Y., Farrag, K., Almoh'd, I., & Mohiuddin, A. (2004). Evaluation of interaction between geosynthetics and marginal cohesive soils from pullout tests. *Proceedings of Geo Jordan,* 299-310. https://doi.org/10.1061/40735(143)25

Abu-Farsakh, M., Coronel, J., & Tao, M. (2007). Effect of soil moisture content and dry density on cohesive soil – geosynthetic interactions using large direct shear tests. *Journal of Materials in Civil Engineering, 19*, 540–549. https://doi.org/10.1061/(ASCE)0899-1561(2007)19:7(540)

Acar, Y. B., & Olivieri, I. (1989). Pore fluid effects on the fabric and hydraulic conductivity of laboratory-compacted clay. *Transportation Research Record*, 144–159.

Al-Moadhen, M. M., Clarke, B. G., & Chen, X. (2018). The permeability of composite soils. *Environmental Geotechnics*, *2013*, 1–13. https://doi.org/10.1680/jenge.18.00030

Alakayleh, Z., Prabhakar Clement, T., & Fang, X. (2018). Understanding the changes in hydraulic conductivity values of coarse- and fine-grained porous media mixtures. *Water*, *10*(313), 1–13. https://doi.org/10.3390/w10030313

Alfaro, M. C., Miura, N., & Bergado, D. T. (1995). Soil-geogrid reinforcement interaction by pullout and direct shear tests. *Geotechnical Testing Journal, GTJODJ*, *18*(2), 157-167.

Almohd, I., Abu-Farsakh, M., Khalid, F., (2005). Geosynthetic reinforcement-cohesive soil interface during pullout. Proceedings of the 13th Great Lakes Geotechnical and Geoenvironmental Conference. https://doi.org/10.1061/40821(181)4

Alyamani, M. S., & Sen, Z. (1993). Determination of hydraulic conductivity from complete grain-size distribution curves. *Ground Water*, *31*(4), 551-555. https://doi.org/10.1111/j.1745-6584.1993.tb00587.x

Arab, P. B., Araújo, T. P., & Pejon, O. J. (2015). Identification of clay minerals in mixtures subjected to differential thermal and thermogravimetry analyses and methylene blue adsorption tests. *Applied Clay Science*, *114*, 133–140. https://doi.org/10.1016/j.clay.2015.05.020

ASTM C127-15 (2015). (American Society for Testing and Materials) Standard Test Method for Relative Density (Specific Gravity) and Absorption of Coarse Aggregate. https://doi.org/10.1520/C0127-15

ASTM C131-20 (2020). (American Society for Testing and Materials) Standard Test Method for Resistance to Degradation of Small-Size Coarse Aggregate by Abrasion and Impact in the Los Angeles Machine. https://doi.org/10.1520/C0131_C0131M-20

ASTM D698-12 (2012). (American Society for Testing and Materials) Standard Test Methods for Laboratory Compaction Characteristics of Soil Using Standard Effort (12,400 ft-lbf/ft^3 (600 kN-m/m^3)). https://doi.org/10.1520/D0698-12E01

ASTM D854-14 (2014). (American Society for Testing and Materials) Standard Test Methods for Specific Gravity of Soil Solids by Water Pycnometer. https://doi.org/10.1520/D0854-14

ASTM D1140-17 (2017). (American Society for Testing and Materials) Standard Test Methods for Determining the Amount of Material Finer than 75-µm (No. 200) Sieve in Soils by Washing. https://doi.org/10.1520/D1140-17

ASTM D2166-16 (2016). (American Society for Testing and Materials) Standard Test Method for Unconfined Compressive Strength of Cohesive Soil. https://doi.org/10.1520/D2166_D2166M-16

ASTM D2216-10 (2010). (American Society for Testing and Materials) Standard Test Methods for Laboratory Determination of Water (Moisture) Content of Soil and Rock by Mass. https://doi.org/10.1520/D2216-10

ASTM D2434-19 (2019). (American Society for Testing and Materials) Standard Test Method for Permeability of Granular Soils (Constant Head). https://doi.org/10.1520/D2434-19

ASTM D2487-17 (2017). (American Society for Testing and Materials) Standard Practice for Classification of Soils for Engineering Purposes (Unified Soil Classification System). https://doi.org/10.1520/D2487-17E01

ASTM D2488-09a (2009). (American Society for Testing and Materials) Standard Practice for Description and Identification of Soils (Visual-Manual Procedure). https://doi.org/10.1520/D2488-09A

ASTM D3080-04 (2004). (American Society for Testing and Materials) Direct Shear Test of Soils Under Consolidated Drained Conditions. https://doi.org/10.1520/D3080-04

ASTM D4253-16 (2016). (American Society for Testing and Materials) Standard Test Methods for Maximum Index Density and Unit Weight of Soils Using a Vibratory Table. https://doi.org/10.1520/D4253-16E01

ASTM D4318-17 (2017). (American Society for Testing and Materials) Standard Test Methods for Liquid Limit, Plastic Limit, and Plasticity Index of Soils. https://doi.org/10.1520/D4318-17E01

ASTM D4767-11 (2020). (American Society for Testing and Materials) Standard Test Method for Consolidated Undrained Triaxial Compression Test for Cohesive Soils. https://doi.org/10.1520/D4767-11R20

ASTM D5084-16 (2016). (American Society for Testing and Materials) Standard Test Methods for Measurement of Hydraulic Conductivity of Saturated Porous Materials Using a Flexible Wall Permeameter. https://doi.org/10.1520/D5084-16A

ASTM D5321-14 (2014). (American Society for Testing and Materials) Standard Test Method for Determining the Shear Strength of Soil-Geosynthetic and Geosynthetic-Geosynthetic Interfaces by Direct Shear. https://doi.org/10.1520/D5321_D5321M-14

ASTM D6637M-15 (2015). (American Society for Testing and Materials) Standard Test Method for Determining Tensile Properties of Geogrids by the Single or Multi-Rib Tensile Method. https://doi.org/10.1520/D6637_D6637M-15

ASTM D6913-17 (2017). (American Society for Testing and Materials) Standard Test Methods for Particle-Size Distribution (Gradation) of Soils Using Sieve Analysis. https://doi.org/10.1520/D6913_D6913M-17

ASTM D7928-21 (2021). (American Society for Testing and Materials) Standard Test Method for Particle-Size Distribution (Gradation) of Fine-Grained Soils Using the Sedimentation (Hydrometer) Analysis. https://doi.org/10.1520/D7928-21

Aubertin, M., Chapuis, R. P., & Mbonimpa, M. (2005). Discussion of "Goodbye, Hazen; Hello, Kozeny-Carman," by W. David Carrier III. *Journal of Geotechnical and Geoenvironmental Engineering, 131,* 1056-1057. https://doi.org/10.1061/(ASCE)1090-0241(2005)131:8(1056)

Balakrishnan, S., & Viswanadham, B. V. S. (2016). Performance evaluation of geogrid reinforced soil walls with marginal backfills through centrifuge model tests. *Geotextiles and Geomembranes*, *44*(1), 95–108. https://doi.org/10.1016/j.geotexmem.2015.06.002

Bauer, G. E., & Zhao, Y. (1993). Evaluation of shear strength and dilatancy behavior of reinforced soil from direct shear tests, *Geosynthetic soil Reinforcement Testinq Procedures, ASTM STP 1190,* S. C. Jonathan Cheng, Ed., American Society for Testing and Materials, Philadelphia, 138-151. https://doi.org/10.1520/STP24318S

Bayoglu, E. (1995). Shear Strength and Compressibility Behaviour of Sand – Clay Mixtures. Master of Science Thesis, Middle East Technical University.

Been, K., & Jefferies, M. G. (1985). A state parameter for sands. *Géotechnique*, *35*(2), 99–112. https://doi.org/10.1680/geot.1985.35.2.99

Been, K., & Jefferies, M. G., & Hachey, J. (1991). The critical state of sands. *Géotechnique*, *41*(3), 365–381. https://doi.org/10.1680/geot.1991.41.3.365

Benson, C. H., Zhai, H., & Wang, X. (1994). Estimating hydraulic conductivity of compacted clay liners. *Journal of Geotechnical Engineering*, *120*(2), 366–387. https://doi.org/10.1061/(ASCE)0733-9410(1994)120:2(366)

Bergado, D. T., Chai, J. C., Abiera, H. O., Alfaro, M. C., & Balasubramaniam, A. S. (1993). Interaction between cohesive-frictional soil and various grid reinforcements. *Geotextiles and Geomembranes, 12*(4), 327–349. https://doi.org/10.1016/0266-1144(93)90008-C

Bishop, A. W. (1967). Progressive failure-with special reference to mechanism causing it. *Proceedings of the Geotechnical Conference*, *2*, 142-150.

Bishop, A. W., & Henkel, D. J. (1962). The measurement of soil properties in the triaxial test. Edward Arnold (Publishers) Ltd. London.

Bowles, J. E. (1988). Foundation analysis and design, 5th Ed., McGraw Hill Book Co., Inc., Singapore.

Burwash, W. J. & Frost, J. D. (1991). Case history of a 9 m high geogrid reinforced retaining wall backfilled with cohesive soil. *Geosynthetics Conference, 2*, 485-493.

BS 1377 (1990). Methods of test for soils for civil engineering purposes. *British Standards Institution*, London.

BS 6031 (2009). Code of practice for earthworks. *British Standards Institution*, London.

BS 8006 (1995). Code of practice for strengthened/reinforced soils and other fills. *British Standards Institution*, London.

BS 8006-1 (2010). Code of practice for strengthened/reinforced soils and other fills. *British Standards Institution*, London.

Cabalar, A. F. (2010). Applications of the oedometer, triaxial and resonant column tests to the study of micaceous sands. *Engineering Geology*, *112*, 21–28. https://doi.org/10.1016/j.enggeo.2010.01.004

Cabalar, A. F. (2011). The effects of fines on the behaviour of a sand mixture. *Geotechnical and Geological Engineering*, *29*, 91–100. https://doi.org/10.1007/s10706-010-9355-z

Cabalar, A. F., Khalaf, M. M., & Isik, H. (2020). A comparative study on the undrained shear strength results of fall cone and vane shear tests in sand–clay mixtures. *Arabian Journal of Geosciences*, *13*(395), 1-11. https://doi.org/10.1007/s12517-020-05351-5

Cabalar, A. F., & Mustafa, W. S. (2015a). Fall cone tests on clay-sand mixtures. *Engineering Geology*, *192*, 154–165. https://doi.org/10.1016/j.enggeo.2015.04.009

Cabalar, A. F., & Mustafa, W. S. (2015b). Behaviour of sand–clay mixtures for road pavement subgrade. *International Journal of Pavement Engineering*, *18*(8), 1–13. https://doi.org/10.1080/10298436.2015.1121782

Carman, P. C. (1956). Flow of gases through porous media. Butterworths Scientific Publications. London.

Carrier, W. D. (2003). Goodbye, Hazen; Hello, Kozeny-Carman. *Journal of Geotechnical and Geoenvironmental Engineering 129,* 1054-1056. https://doi.org/10.1061/(ASCE)1090-0241(2003)129:11(1054)

Casagrande, A., & Fadum, R. E. (1940). Notes on soil testing for engineering purposes: Harvard Soil Mechanics Series No. 8. Cambridge, MA, Harvard University.

Chang, C. S., Meidani, M., & Deng, Y. (2017). A compression model for sand–silt mixtures based on the concept of active and inactive voids. *Acta Geotechnica*, *12*(6), 1301–1317. https://doi.org/10.1007/s11440-017-0598-1

Chapuis, R. P. (1990). Sand-bentonite liners: predicting permeability from laboratory tests. *Canadian Geotechnical Journal*, *27*(1), 47–57. https://doi.org/10.1139/t90-005

Chapuis, R. P. (2004). Predicting the saturated hydraulic conductivity of sand and gravel using effective diameter and void ratio. *Canadian Geotechnical Journal*, *41*(5), 787–795. https://doi.org/10.1139/T04-022

Chapuis, R. P. (2012). Predicting the saturated hydraulic conductivity of soils: a review. *Bulletin of Engineering Geology and the Environment*, *71*(3), 401–434. https://doi.org/10.1007/s10064-012-0418-7

Chapuis, R. P., & Aubertin, M. (2003). On the use of the Kozeny-Carman equation to predict the hydraulic conductivity of soils. *Canadian Geotechnical Journal*, *40*(3), 616–628. https://doi.org/10.1139/t03-013

Chapuis, R. P., & Légaré, P-P. (1992). A simple method for determining the surface area of fine aggregates and fillers in bituminous mixtures. *ASTM Special Technical Publication,* 177-186.

Cho, G. C., Dodds, J., & Santamarina, J. C. (2006). Particle shape effects on packing density, stiffness, and strength: Natural and crushed sands. *Journal of Geotechnical and Geoenvironmental Engineering*, *132*(5), 591–602. https://doi.org/10.1061/(ASCE)1090-0241(2006)132:5(591)

Christopher, B. R., & Stulgis, R. P. (2005). Low permeable backfill soils in geosynthetic reinforced soil walls: State-of-the-practice in North America. *Proceedings of North American Geo-Synthetics Conference (NAGS 2005)*, 14–16.

Christopher, B. R., Zornberg, J. G., & Mitchell, J. K. (1998). Design guidance for reinforced soil structures with marginal soil backfills. *Proceedings of the Sixth International Conference on Geosynthetics, 2,* 797–804.

Chu, J., & Leong, W. K. (2002). Effect of fines on instability behaviour of loose sand. *Géotechnique*, *52*(10), 751–755. https://doi.org/10.1680/geot.2002.52.10.751

Chung, C.-K., Kim, J.-H., Kim, J., & Kim, T. (2018). Hydraulic conductivity variation of coarse-fine soil mixture upon mixing ratio. *Advances in Civil Engineering*, *2018*, 1–11. https://doi.org/10.1155/2018/6846584

Clancy, J. M., & Naughton, P. J. (2011). An experimental study of pullout resistance of a multifunctional geosynthetic in fine grained fills using an innovative pullout apparatus. *Geo-Frontiers,* 3609-3618. https://doi.org/10.1061/41165(397)369

Coop, M. R., & Lee, I. K. (1993). The behaviour of granular soils at elevated stress. *Predictive Soil Mechanics*. Thomas Telford, London, 186-198.

Cubrinovski, M., & Rees, S. (2008). Effects of fines on undrained behaviour of sands. *Geotechnical Earthquake Engineering and Soil Dynamics IV Congress, Geotechnical Special Publication*, *181*, 1–11. https://doi.org/10.1061/40975(318)91

Dafalla, M., Shaker, A. A., Elkady, T., Al-Shamrani, M., & Dhowian, A. (2015). Effects of confining pressure and effective stress on hydraulic conductivity of sand-clay mixtures. *Arabian Journal of Geosciences*, *8*(11), 9993–10001. https://doi.org/10.1007/s12517-015-1925-1

Dewhurst, D. N., Aplin, A. C., & Sarda, J. P. (1999). Influence of clay fraction on pore-scale properties and hydraulic conductivity of experimentally compacted mudstones. *Journal of Geophysical Research: Solid Earth*, *104*(B12), 29261–29274. https://doi.org/10.1029/1999jb900276

Dolinar, B. (2009). Predicting the hydraulic conductivity of saturated clays using plasticity-value correlations. *Applied Clay Science*, *45*, 90–94. https://doi.org/10.1016/j.clay.2009.04.001

Durukan, Z., & Tezcan, S. S. (1992). Cost analysis of reinforced soil walls. *Geotextiles and Geomembranes*, *11*(1), 29–43. https://doi.org/10.1016/0266-1144(92)90011-X

EBGEO (2011). Recommendations for design and analysis of earth structures using geosynthetic reinforcements, *German Geotechnical Society.*

Ekici, A., Huvaj, N., & Akgüner, C. (2019). Index properties and classification of marginal fills or coarse-fine mixtures. *Geo-Congress 2019,* 91–99. https://doi.org/10.1061/9780784482131.010

Ekici, A., Huvaj, N., & Akgüner, C. (2022). Effects of fines content and plasticity on index properties and hydraulic conductivity of coarse-fine mixtures. *Journal of Materials in Civil Engineering*, 34 (5). https://doi.org/10.1061/(ASCE)MT.1943-5533.0004149

EN ISO 14688-2. (2018). Geotechnical investigation and testing – Identification and classification of soil. Part 2: Principles for a classification. *Comité Européen de Normalisation*, Brussels.

Fabian, K., & Fourie, A. (1986). Performance of geotextile-reinforced clay samples in undrained triaxial tests. *Geotextiles and Geomembranes*, *4*, 53–63. https://doi.org/10.1016/0266-1144(86)90036-1

Farrar, D. M., & Coleman, J. D. (1967). The correlation of surface area with other properties of nineteen British clay soils. *Journal of Soil Science, 18*(1), 118-124. https://doi.org/10.1111/j.1365-2389.1967.tb01493.x

Ferreira, P. M. V., & Bica, A. V. D. (2006). Problems in identifying the effects of structure and critical state in a soil with a transitional behaviour. *Géotechnique*, *56*(7), 445–454. https://doi.org/10.1680/geot.2006.56.7.445

Ferreira, F. B., Carlos, D. M., Vieira, C. S., & Lopes, M. L. (2015a). Soil-geogrid interaction in pullout conditions: influence of soil moisture content and density. *Geotechnical Engineering for Infrastructure and Development,* 1421-1426. https://doi.org/10.1680/ecsmge.60678

Ferreira, F. B., Vieira, C. S., & Lopes, M. L. (2015b). Direct shear behaviour of residual soil–geosynthetic interfaces – influence of soil moisture content, soil density and geosynthetic type. *Geosynthetics International*, *22*(3), 257–272. https://doi.org/10.1680/gein.15.00011

FHWA (Federal Highway Administration) (2009). Design and construction of mechanically stabilized earth walls and reinforced soil slopes. *Geotechnical Engineering Circular No. 11,* Publication No. FHWA-NHI-10-024.

Gassner, F. W., & James, G. M. (1998). Failure of two fabric reinforced segmental block walls in South Africa. *Proceedings of the sixth International Conference on Geosynthetics*, 559–564.

Geoguide 6 (2017). Guide to reinforced fill structure and slope design, *Geotechnical Engineering Office*.

Georgiannou, V. N., Burland, J. B., & Hight, D. W. (1990). The undrained behaviour of clayey sands in triaxial compression and extension. *Géotechnique*, *40*(3), 431–449. https://doi.org/10.1680/geot.1990.40.3.431

Georgiannou, V. N., Hight, D. W., & Burland, J. B. (1991). Behaviour of clayey sands under undrained cyclic triaxial loading. *Géotechnique*, *41*(3), 383–393. https://doi.org/10.1680/geot.1991.41.3.383

Germaine, J. T., & Germaine, V. (2009). Geotechnical Laboratory Measurements for Engineers. 1-351. https://doi.org/10.1002/9780470548790

Gleason, M. H., Daniel, D. E., & Eykholt, G. R. (1997). Calcium and sodium bentonite for hydraulic containment applications. *Journal of Geotechnical*

Engineering, *123*(5), 438–445. https://doi.org/10.1061/(ASCE)1090-0241(1997)123:5(438)

Guler, E., & Ocbe, C. (2003). Centrifuge and full scale models of geotextile reinforced walls and several case studies of segmental retaining walls in Turkey. *Emirates Journal for Engineering Research*, *8*(1), 15–23.

HA 68/94 (1994). Design methods for the reinforcement of highway slopes by reinforced soil and soil nailing techniques. *Design Manual for Roads and Bridges*, Volume 4, Section 1, Part 4.

Hansen, D. (2004). Discussion of "On the use of the Kozeny-Carman equation to predict the hydraulic conductivity of soils." *Canadian Geotechnical Journal*, *41*(5), 990–993. https://doi.org/10.1139/T04-028

Hatami, K., & Bathurst, R. J. (2005). Parametric analysis of reinforced soil walls with different backfill material properties. *Proceedings of North American Geo-Synthetics Conference (NAGS 2005).*

Hazen, A. (1892). Some physical properties of sands and gravels, with special reference to their use in filtration. *State Sanitation*, 232-248. https://doi.org/10.4159/harvard.9780674600485.c25

Hazen, A. (1911). Discussion of "Dams on Sand Foundations" by A. C. Koenig. *Transactions of the American Society of Civil Engineers, 73*, 199-203.

Holtz, W. G., & Gibbs, H. J. (1956). Triaxial shear tests on pervious gravelly soils. *Journal of the Soil Mechanics and Foundation Division, 82*(1)*,* 1-22.

Holtz, R. D., & Kovacs, W. D. (1981). An Introduction to Geotechnical Engineering. Englewood Cliffs, NJ: Prentice Hall.

Hong, B., Li, X., Wang, L., Li, L., Xue, Q., & Meng, J. (2020). Using the effective void ratio and specific surface area in the Kozeny-Carman equation to predict the hydraulic conductivity of loess. *Water (Switzerland)*, *12*(1). https://doi.org/10.3390/w12010024

Indraratna, B., Karimullah Hussaini, S. & Vinod, J. S. (2012). On the shear behavior of ballast-geosynthetic interfaces. *Geotechnical Testing Journal, 35*(2), 305–312. https://doi.org/10.1520/GTJ103317

Ishihara, K., Tatsuoka, F., & Yasuda, S. (1975). Undrained deformation and liquefaction of sand under cyclic stresses. *Soils and Foundations*, *15*(1), 29–44. https://doi.org/10.3208/sandf1972.15.29

Jewell, R. A., Milligan, G. W. E., Sarsby, R. W., & Dubois, D. (1985). Interaction between soil and geogrids. *Polymer grid reinforcement, Thomas Telford Limited, London*, 18–30.

Kacprzak, G., Boutin, C., & Doanh, T. (2010). Permeability of sand-clay mixtures. *Archives of Civil Engineering*, *56*(4), 299–320. https://doi.org/10.2478/v.10169-010-0017-6

Kandhal, P. S., & Parker, F. (1998). Aggregate tests related to asphalt concrete performance in pavements. *NCHRP Final Report 405, Transportation Research Board,* National Academy Press.

Keller, G. R. (1995). Experiences with mechanically stabilized structures and native soil backfill. *Transportation Research Record*, *1474*, 30–38.

Kempton, G. T., Jones, C. J. F. P., Jewell, R. A., & Naughton, P. J. (2000). Construction of slopes using cohesive fills and a new innovative geosynthetic material. *EUROGEO 2000: Proceedings of the 2nd European Geosynthetics Conference, Environmental and Hydraulic Applications Workshops, 2*, 1–6.

Kenney, T. C. (1977). Residual strength of mineral mixture. *Proceedings of the 9th International Conference of Soil Mechanics and Foundation Engineering*, 155–160.

Kenney, T. C., van Veen, W. A., Swallow, M. A., & Sungaila, M. A. (1992). Hydraulic conductivity of compacted bentonite–sand mixtures. *Canadian Geotechnical Journal*, *29*(3), 364-374. https://doi.org/10.1139/t92-042

Kim, D., & Ha, S. (2014). Effects of particle size on the shear behavior of coarse grained soils reinforced with geogrid. *Materials*, *7*(2), 963–979. https://doi.org/10.3390/ma7020963

Kim, U., Kim, D., & Zhuang, L. (2016). Influence of fines content on the undrained cyclic shear strength of sand-clay mixtures. *Soil Dynamics and Earthquake Engineering*, *83*, 124–134. https://doi.org/10.1016/j.soildyn.2016.01.015

Kim, D., Nam, B. H., & Youn, H. (2018). Effect of clay content on the shear strength of clay–sand mixture. *International Journal of Geo-Engineering, 9*(19). https://doi.org/10.1186/s40703-018-0087-x

Koerner, R. M. (2005). Designing with Geosynthetics (Fifth Edit). New Jersey: Pearson Prentice Hall.

Koerner, R. M. (2012). Designing with geosynthetics-Vol. 1 (Sixth edit). Xlibris Corporation.

Koerner, R. M., & Koerner, G. R. (2013). A data base, statistics and recommendations regarding 171 failed geosynthetic reinforced mechanically stabilized earth (MSE) walls. *Geotextiles and Geomembranes*, *40*, 20–27. https://doi.org/10.1016/j.geotexmem.2013.06.001

Kozeny, J. (1927). Über kapillare Leitung des Wassers im Boden. *Sitzungsber Akad. Wiss. Wien. 136*, 271–306.

KTS (2013). Karayolu Teknik Şartnamesi. *Karayolları Genel Müdürlüğü,* Ankara.

Kuerbis, R. (1989). The Effect of Gradation and Fines Content on the Undrained Response of Sand. Master of Science Thesis, The University of British Columbia.

Kumar, G. V. (1996). Some Aspects of the Mechanical Behaviour of Mixtures of Kaolin and Coarse Sand. Doctor of Philosophy Thesis, University of Glasgow.

Kumar, G. V., & Muir Wood, D. (1999). Fall cone and compression tests on clay-gravel mixtures. *Géotechnique*, *49*(6), 727–739. https://doi.org/10.1680/geot.1999.49.6.727

Ladd, R. S. (1978). Preparing test specimens using undercompaction. *Geotechnical Testing Journal, GTJODJ, 1*(1), 16-23. https://doi.org/10.1520/GTJ10364J

Lade, P. V., Liggio Jr., C. D., & Yamamuro, J. A. (1998). Effects of non-plastic fines on minimum and maximum void ratios of sand. *Geotechnical Testing Journal, 21*(4), 336-347. https://doi.org/10.1520/GTJ11373J

Lambe, T. W. (1955). The permeability of fine-grained soils. *Symposium on Permeability of Soils,* 56–67. https://doi.org/10.1520/STP46165S.56–67

Lambe, T. W., & Whitman, V. R. (1969). Soil Mechanics. John Wiley and Sons. New York.

Lee, S., Kim, S., Kim, J., & Kim, T. (2016). Partial drainage characteristics of intermediate soils with low plasticity from Incheon, Korea. *Japanese Geotechnical Society Special Publication,* 604–609. https://doi.org/10.3208/jgssp.KOR-17

Li, Y. (2017). Residual Shear Behavior of Composite Soils. London: Taylor & Francis Group.

Liu, C., Ho, Y., & Huang, J. (2009a). Large scale direct shear tests of soil / PET-yarn geogrid interfaces. *Geotextiles and Geomembranes*, *27*(1), 19–30. https://doi.org/10.1016/j.geotexmem.2008.03.002

Liu, C.-N., Zornberg, J. G., Chen, T.-C., Ho, Y.-H., & Lin, B.-H. (2009b). Behavior of geogrid-sand interface in direct shear mode. *Journal of Geotechnical and Geoenvironmental Engineering*, *135*(12), 1863–1871. https://doi.org/10.1061/(asce)gt.1943-5606.0000150

Lopez, R. H., Kang, Y. H., & Zornberg, J. (2006). Poorly draining soil reinforced with geosynthetic with in plane drainage: Efficiency and pore pressure behavior. *COBRAMSEG 2006, XIII Congresso Brasileiro de Mecânica dos Solos e Engenharia Geotécnica,* 1–5.

Marr, W. A., & Stulgis, R. P. (2013). Selecting backfill materials for MSE retaining walls. *NCHRP Project 24-22/Final Report, Transportation Research Board of The National Academies,* October.

Martins, F. B., Bressani, L. A., Coop, M. R., & Bica, A. V. D. (2001). Some aspects of the compressibility behaviour of a clayey sand. *Canadian Geotechnical Journal*, *38*(6), 1177–1186. https://doi.org/10.1139/cgj-38-6-1177

Mbonimpa, M., Aubertin, M., Chapuis, R. P., & Bussière, B. (2002). Practical pedotransfer functions for estimating the saturated hydraulic conductivity. *Geotechnical and Geological Engineering*, *20*(3), 235–259. https://doi.org/10.1023/A:1016046214724

McGeary, R. K. (1961). Mechanical packing of spherical particles. *Journal of the American Ceramic Society*, *44*(10), 513–522. https://doi.org/10.1111/j.1151-2916.1961.tb13716.x

MCHW (2016). Manual of Contract Documents for Highway Works. Volume 1, *Specification for Highway Works*.

Mesri, G., & Olson, R. E. (1971). Mechanisms controlling the permeability of clays. *Clays and Clay Minerals*, *19*(3), 151–158. https://doi.org/10.1346/CCMN.1971.0190303

Mesri, G., & Vardhanabhuti, B. (2009). Compression of granular materials. *Canadian Geotechnical Journal,* *46*(4), 369–392. https://doi.org/10.1139/T08-123

Mitchell. J. K. (1976). Fundamentals of soil behaviour. New York: Wiley.

Mitchell, J. K. (1981). Soil improvement – State of the art report. *Proceedings 10th International Conference on Soil Mechanics and Foundation Engineering*, 509-521.

Mitchell, J. K., & Zornberg, J. G. (1995). Reinforced soil structures with poorly draining backfills Part II: Case histories and applications. *Geosynthetics International*, *2*(1), 265–307. https://doi.org/10.1680/gein.2.0011

Mitchell, J. K., Seed, R. B., & Seed, H. B. (1990). Kettleman hills waste landfill slope failure. I: Liner-system properties. *Journal of Geotechnical Engineering*, *116*(4), 647–668. https://doi.org/10.1061/(ASCE)0733-9410(1990)116:4(647)

Mitchell, J. K., & Soga, K. (2005). Fundamentals of soil behavior. 3rd edition, John Wiley & Sons, Hoboken.

Mollins, L. H., Stewart, D. I., & Cousens, T. W. (1996). Predicting the properties of bentonite-sand mixtures. *Clay Minerals, 31*(2), 243-252. https://doi.org/10.1180/claymin.1996.031.2.10

Monkul, M. M., & Ozden, G. (2005). Effect of intergranular void ratio on one-dimensional compression behavior. *Proceedings of International Conference on Problematic Soils*.

Monkul, M. M., & Ozden, G. (2007). Compressional behavior of clayey sand and transition fines content. *Engineering Geology, 89*, 195–205. https://doi.org/10.1016/j.enggeo.2006.10.001

Muir Wood, D., & Kumar, G. V. (2000). Experimental observations of behaviour of heterogeneous soils. *Mechanics of Cohesive-Frictional Materials*, *5*, 373–398.https://doi.org/10.1002/1099-1484(200007)5:5<373::AID-CFM100>3.0.CO;2-D

Naeini, S. A., & Baziar, M. H. (2004). Effect of fines content on steady-state strength of mixed and layered samples of a sand. *Soil Dynamics and Earthquake Engineering*, *24*, 181–187. https://doi.org/10.1016/j.soildyn.2003.11.003

Nagaraj, H. B. (2016). Influence of gradation and proportion of sand on stress–strain behavior of clay–sand mixtures. *International Journal of Geo-Engineering, 7*(19). https://doi.org/10.1186/s40703-016-0033-8

Nagaraj, T. S., Pandian, N. S., & Narasimha Raju, P. S. R. (1993). Stress-state-permeability relationships for fine-grained soils. *Géotechnique*, *43*(2), 333–336. https://doi.org/10.1680/geot.1993.43.2.333

Nagaraj, T. S., Pandian, N. S., & Narasimha Raju, P. S. R. (1994). Stress-state-permeability relations for overconsolidated clays. *Géotechnique*, *44*(2), 349–352. https://doi.org/10.1680/geot.1994.44.2.349

Nakase, A., Katsuno, M., & Kobayashi, M. (1972). Unconfined compression strength of soils of intermediate grading between sand and clay, *Report of Port and Harbour Research Institute, 11*(4), 83-102 (in Japanese).

Naughton, P. J., Jewell, R. A., & Kempton, G. T. (2001). The design of steep slopes constructed from cohesive fills and a geogrid. *Proceeding of the International Symposium on Soil Reinforcement*.

Naughton, P. J., Giroud, J. P., Rimoldi, P., Scotto, M., & Crowther, D. (2015). The design of steep slopes using low-permeability fill and draining geogrids. *Geotechnical Engineering for Infrastructure and Development,* 2055-2060. https://doi.org/10.1680/ecsmge.60678

NAVFAC DM 7.1 (2022). Unified Facilities Criteria, Soil Mechanics Design Manual 7.1. Naval Facilities Engineering Systems Command.

NCMA (The National Concrete Masonry Association) Manual (2007). State-of-the-practice design of segmental retaining walls: NCMA's third edition manual, 1–15. https://doi.org/10.1061/40909(228)7

Ni, Q., Tan, T. S., Dasari, G. R., & Hight, D. W. (2004). Contribution of fines to the compressive strength of mixed soils. *Géotechnique*, *54*(9), 561–569. https://doi.org/10.1680/geot.54.9.561.56936

Nocilla, A., Coop, M. R., & Colleselli, F. (2006). The mechanics of an Italian silt: An example of "transitional" behaviour. *Géotechnique*, *56*(4), 261–271. https://doi.org/10.1680/geot.2006.56.4.261

NORDIC (2005). Nordic guidelines for reinforced soils and fills. *Nordic Geosynthetic Group,* Retrieved from www.sgf.net

Novais-Ferreira, H. (1971). The clay content and the shear strength in sand-clay mixtures. *Proc. 5th African Reg. Conf. Soil Mech. Found. Engrng*, Luanda, *1*, 3-9.

Nunes, G. B., Portelinha, F. H. M., Futai, M. M., & Yoo, C. (2022). Numerical study of the impact of climate conditions on stability of geocomposite and geogrid reinforced soil walls. *Geotextiles and Geomembranes*, 50(4), 807-824, https://doi.org/10.1016/j.geotexmem.2022.04.004

O'Kelly, B. C., & Naughton, P. J. (2008). Enhancement in the interface shear resistance achieved by a novel geogrid with in-plane drainage. *GeoCongress* 2008, 740–747. https://doi.org/10.1061/40971(310)92

Olmez, M. S., & Ergun, M. U. (2008). Kil-kum karışımlarının kayma dayanımı özellikleri. *Zemin Mekaniği ve Temel Mühendisliği Onikinci Ulusal Kongresi*, 303–312.

Olson, R. (1989). Lecture notes on direct shear test, https://www.cyut.edu.tw/~jrlai/CE7334/Unit3.pdf

Ovando-Shelley, E., & Pérez, B. E. (1997). Undrained behaviour of clayey sands in load controlled triaxial tests. *Géotechnique, 47*(1), 97–111. https://doi.org/10.1680/geot.1997.47.1.97

Palmeira, E. M. (2009). Soil-geosynthetic interaction: Modelling and analysis. *Geotextiles and Geomembranes*, *27*(5), 368–390. https://doi.org/10.1016/j.geotexmem.2009.03.003

Papadopoulou, A. I., & Tika, T. M. (2016). The effect of fines plasticity on monotonic undrained shear strength and liquefaction resistance of sands. *Soil Dynamics and Earthquake Engineering, 88*, 191–206. https://doi.org/10.1016/j.soildyn.2016.04.015

Park, J., & Santamarina, J. C. (2017). Revised soil classification system for coarse-fine mixtures. *Journal of Geotechnical and Geoenvironmental Engineering*, *143*(8), 1–13. https://doi.org/10.1061/(ASCE)GT.1943-5606.0001705

Phanikumar, B. R., Amshumalini, C., & Karthika, R. (2010). Swell–consolidation characteristics of artificial sand clay mixes. *Indian Geotechnical Conference,* 325-326.

Pitman, T. D., Robertson, P. K., & Sego, D. C. (1994). Influence of fines on the collapse of loose sands. *Canadian Geotechnical Journal*, *31*, 728–739. https://doi.org/10.1139/t94-084

Polito, C. P., & Martin, J. R. (2001). Effects of nonplastic fines on the liquefaction resistance of sands. *Journal of Geotechnical and Geoenvironmental Engineering*, *127*(5), 408–415. https://doi.org/10.1061/(ASCE)1090-0241(2001)127:5(408)

Poulos, S. J. (1981). The steady state of deformation. *Journal of Geotechnical and Geoenvironmental Engineering*, *107*(5), 553-562.

Rahman, M. M., & Lo, S. R. (2008). The prediction of equivalent granular steady state line of loose sand with fines. *Geomechanics and Geoengineering*, *3*(3), 179–190. https://doi.org/10.1080/17486020802206867

Rahman, M. M., Lo, S. R., & Gnanendran, C. T. (2008). On equivalent granular void ratio and steady state behaviour of loose sand with fines. *Canadian Geotechnical Journal*, 45(10), 1439-1456. https://doi.org/10.1139/T08-064

Rahman, M. M., & Lo, S-C. R. (2011). Effects of fines and fines type on undrained behaviour of sandy soils under critical state soil mechanics framework. *Geotechnical Engineering for Disaster Mitigation and Rehabilitation and Highway Engineering*, 403–408. https://doi.org/10.1142/9789814365161_0050

Rahman, M. M., Lo, S. R. & Baki, M. A. L. (2011). Equivalent granular state parameter and undrained behaviour of sand–fines mixtures. *Acta Geotechnica*, 6, 183–194. https://doi.org/10.1007/s11440-011-0145-4

Raja, J., Dixon, N., Frost, M., Fraser, I., & Fowmes, G. (2012). Designing with marginal fills: Understanding and practice. *EuroGeo5: the 5th European Geosynthetics Congress.*

Ren, X. W., & Santamarina, J. C. (2018). The hydraulic conductivity of sediments: A pore size perspective. *Engineering Geology*, *233*, 48–54. https://doi.org/10.1016/j.enggeo.2017.11.022

Revil, A., Grauls, D., & Brévart, O. (2002). Mechanical compaction of sand/clay mixtures. *Journal of Geophysical Research, 107*(B11), 1-15. https://doi.org/10.1029/2001jb000318

Roscoe, K. H., Schofield, A. N., & Wroth, C. P. (1958). On the yielding of soils. *Géotechnique, 8*(1), 22-53. https://doi.org/10.1680/geot.1958.8.1.22

Sandri, D. (2005). Drainage recommendations for MSE walls constructed with marginal fills. *NAGS / GRI-19 Cooperative Conference Proceedings.*

Sandri, D. B., Silver, G., & Trazo, R. (2000). Design, construction, and monitoring of a 14.9M high geosynthetic reinforced segmental retaining wall in a seismically active region. *Proceedings of the Advances in Transportation and Geoenvironmental Systems Using Geosynthetics,* 244-256. https://doi.org/10.1061/40515(291)16

Santamarina, J. C., Klein, K. A., Wang, Y. H., & Prencke, E. (2002). Specific surface: determination and relevance. *Canadian Geotechnical Journal*, *39*, 233–241. https://doi.org/10.1139/t01-077

Santucci De Magistris, F., Silvestri, F., & Vinale, F. (1998). The influence of compaction on the mechanical behaviour of a silty sand. *Soils and Foundations*, *38*(4), 41-56. https://doi.org/10.3208/sandf.38.4_41

Sanzeni, A., Colleselli, F., & Grazioli, D. (2013). Specific surface and hydraulic conductivity of fine-grained soils. *Journal of Geotechnical and Geoenvironmental Engineering*, *139*(10), 1828–1832. https://doi.org/10.1061/(ASCE)GT.1943-5606.0000892

Scarborough, J. A. (2005). A tale of two walls: Case histories of failed MSE walls. *Geo-Frontiers Congress 2005*, 1-12. https://doi.org/10.1061/40787(166)12

Shakoor, A., & Cook, B. D. (1990). The effect of stone content, size, and shape on the engineering properties of a compacted silty clay. *Bulletin of the*

Association of Engineering Geologists, 27(2), 245-253. https://doi.org/10.2113/gseegeosci.xxvii.2.245

Shelley, T. L., & Daniel, D. E. (1993). Effect of gravel on hydraulic conductivity of compacted soil liners. *Journal of Geotechnical Engineering, 119*(1), 54–68. https://doi.org/10.1061/(ASCE)0733-9410(1993)119:1(54)

Shi, X. S., & Yin, J. (2018). Consolidation behavior for saturated sand-marine clay mixtures considering the intergranular structure evolution. *Journal of Engineering Mechanics*, *144*(2), 1–11. https://doi.org/10.1061/(ASCE)EM.1943-7889.0001391

Shi, X. S., & Zhao, J. (2020). Practical estimation of compression behavior of clayey/silty sands using equivalent void-ratio concept. *Journal of Geotechnical and Geoenvironmental Engineering*, *146*(6). https://doi.org/10.1061/(ASCE)GT.1943-5606.0002267

Shin, H., & Santamarina, J. C. (2013). Role of particle angularity on the mechanical behavior of granular mixtures. *Journal of Geotechnical and Geoenvironmental Engineering*, *139*(2), 353–355. https://doi.org/10.1061/(asce)gt.1943-5606.0000768

Shipton, B. (2010). The Mechanics of Transitional Soils. Doctor of Philosophy Thesis, Imperial College, London.

Shipton, B., & Coop, M. R. (2012). On the compression behaviour of reconstituted soils. *Soils and Foundations*, *52*(4), 668–681. https://doi.org/10.1016/j.sandf.2012.07.008

Shipton, B., & Coop, M. R. (2015). Transitional behaviour in sands with plastic and non-plastic fines. *Soils and Foundations*, *55*(1), 1–16. https://doi.org/10.1016/j.sandf.2014.12.001

Shire, T., O'Sullivan, C., & Hanley, K. J. (2016). The influence of fines content and size-ratio on the micro-scale properties of dense bimodal materials. *Granular Matter*, *18*(52), 1–10. https://doi.org/10.1007/s10035-016-0654-9

Simons, M. J., & Cameron, N. (2012). Use of an innovative geocomposite to reinforce marginal fill soils in Southern Ontario. *Proceedings, Annual Conference - Canadian Society for Civil Engineering*, 1-10.

Simpson, D. C., & Evans, T. M. (2015). Behavioral thresholds in mixtures of sand and kaolinite clay. *Journal of Geotechnical and Geoenvironmental Engineering*, *142*(2). https://doi.org/10.1061/(ASCE)GT.1943-5606.0001391

Sivapullaiah, P. V., Sridharan, A., & Stalin, V. K. (2000). Hydraulic conductivity of bentonite-sand mixtures. *Canadian Geotechnical Journal, 37*(2), 406-413. https://doi.org/10.1139/t99-120

Skempton, A. W. (1954). The pore-pressure coefficients A and B. *Geotechnique*, *4*(4), 143–147. https://doi.org/10.1680/geot.1954.4.4.143

Stark, T. D., & Hussain, M. (2013). Empirical correlations: Drained shear strength for slope stability analyses. *Journal of Geotechnical and Geoenvironmental Engineering*, *139*(6), 853–862. https://doi.org/10.1061/(ASCE)GT.1943-5606.0000824

Stark, T. D., Choi, H., & McCone, S. (2005). Drained shear strength parameters for analysis of landslides. *Journal of Geotechnical and Geoenvironmental Engineering*, *131*(5), 575–588. https://doi.org/10.1061/(ASCE)1090-0241(2005)131:5(575)

Tanaka, H., Tanaka, M., & Shiwakoti, D. R. (2001). Characteristics of soils with low plasticity: Intermediate soil from Ishinomaki, Japan and lean clay from Drammen, Norway. *Soils and Foundations, 41*(1), 83-96. https://doi.org/10.3208/sandf.41.83

Tatsuoka, F., & Yamauchi, H. (1986). A reinforcing method for steep clay slopes using a non-woven geotextile. *Geotextiles and Geomembranes*, *4*(3–4), 241–268. https://doi.org/10.1016/0266-1144(86)90044-0

Tavenas, F., Jean, P., Leblond, P., & Leroueil, S. (1983). The permeability of natural soft clays. Part II: Permeability characteristics. *Canadian Geotechnical Journal*, *20*(4), 645–660. https://doi.org/10.1139/t83-073

Taylor, D. W. (1948). Fundamentals of soil mechanics. *Jonh Wiley & Sons*, New York.

Terzaghi, K. (1925). Principles of soil mechanics, III - Determination of the permeability of clay. *Engineering News-Record, 95*, 832-836.

Terzaghi, K. (1943). Theoretical soil mechanics. *John Wiley,* New York.

Terzaghi, K., Peck, R. B., & Mesri, G. (1996). Soil Mechanics in Engineering Practice. 3rd Edition, John Wiley and Sons, Inc., New York.

Thevanayagam, S. (1998). Effect of fines and confining stress on undrained shear strength of silty sands. *Journal of Geotechnical and Geoenvironmental Engineering*, *124*(6), 479-491. https://doi.org/10.1061/(ASCE)1090-0241(1998)124:6(479)

Thevanayagam, S., Fiorillo, M., & Liang, J. (2000). Effect of non-plastic fines on undrained cyclic strength of silty sands. *Soil Dynamics and Liquefaction,* 77–91. https://doi.org/10.1061/40520(295)6

Thevanayagam, S., & Mohan, S. (2000). Intergranular state variables and stress-strain behaviour of silty sands. *Géotechnique*, *50*(1), 1–23. https://doi.org/10.1680/geot.2000.50.1.1

Thevanayagam, S., Shenthan, T., Mohan, S. and Liang, J. (2002). Undrained fragility of clean sands, silty sands, and sandy silts. *Journal of Geotechnical and Geoenvironmental Engineering*, 128(10), 849–859. https://doi.org/10.1061/(ASCE)1090-0241(2002)128:10(849)

Toumpanou, I. C., Pantazopoulos, I. A., Markou, I. N., & Atmatzidis, D. K. (2021). Predicted and measured hydraulic conductivity of sand-sized crushed limestone. *Bulletin of Engineering Geology and the Environment*, *80*(2), 1875–1890. https://doi.org/10.1007/s10064-020-02032-1

Tsuchida, T., Kitade, K., Tanaka, M., Kang, G.-o., & Kaya, K. (2020). Evaluation of design shear strength of intermediate soil for construction of breakwater at Port of Sakai. *Soils and Foundations*, *60*(1), 239–256. https://doi.org/10.1016/j.sandf.2019.11.011

UNEP GEAS (United Nations Environment Program Global Environmental Alert System) (2014). Sand, rarer than one thinks, 1-15. Retrieved from https://wedocs.unep.org/bitstream/handle/20.500.11822/8665/GEAS_Mar2014_Sand_Mining.pdf?sequence=3&isAllowed=y

Uyeturk, E. (2019). Geotechnical Characterization of Soils Prone to Rainfall-Induced Landslides in Rize (Northern Turkey). Master of Science Thesis, METU, Ankara

Vallejo, L. E. (2001). Interpretation of the limits in shear strength in binary granular mixtures. *Canadian Geotechnical Journal*, *38*(5), 1097–1104. https://doi.org/10.1139/cgj-38-5-1097

Wasti, Y., & Alyanak, I. (1968). Kil muhtevasının zeminin davranışına tesiri. *İnşaat Mühendisleri Odası, Türkiye İnşaat Mühendisliği 4. Teknik Kongresi,* Ankara.

Xenaki, V. C., & Athanasopoulos, G. A. (2003). Liquefaction resistance of sand-silt mixtures: an experimental investigation of the effect of fines. *Soil Dynamics and Earthquake Engineering*, *23*, 183–194. https://doi.org/10.1016/S0267-7261(02)00210-5

Xu, Y., Williams, D. J., Serati, M., & Vangsness, T. (2018). Effects of scalping on direct shear strength of crusher run and crusher run / geogrid interface.

Journal of Materials in Civil Engineering, 30(9), 1–12. https://doi.org/10.1061/(ASCE)MT.1943-5533.0002411

Yamamuro, J. A., & Lade, P. V. (1998). Steady-state concepts and static liquefaction of silty sands. *Journal of Geotechnical and Geoenvironmental Engineering*, *124*(9), 868–877. https://doi.org/10.1061/(ASCE)1090-0241(1998)124:9(868)

Yamamuro, J. A., & Wood, F. M. (2004). Effect of depositional method on the undrained behavior and microstructure of sand with silt. *Soil Dynamics and Earthquake Engineering*, *24*, 751–760. https://doi.org/10.1016/j.soildyn.2004.06.004

Yang, S., Lacasse, S., & Sandven, R. (2006a). Determination of the transitional fines content of mixtures of sand and non-plastic fines. *Geotechnical Testing Journal*, *29*(2), 102–107. https://doi.org/10.1520/gtj14010

Yang, S. L., Sandven, R., & Grande, L. (2006b). Instability of sand-silt mixtures. *Soil Dynamics and Earthquake Engineering-11th International Conference on Soil Dynamics and Earthquake Engineering (ICSDEE):* Part II, 26(2–4): 183–190. https://doi.org/10.1016/j.soildyn.2004.11.027

Yang, G., Liu, H., Lv, P., & Zhang, B. (2012). Geogrid-reinforced lime-treated cohesive soil retaining wall: Case study and implications. *Geotextiles and Geomembranes*, *35*, 112–118. https://doi.org/10.1016/j.geotexmem.2012.09.001

Yang, K. H., Thuo, J. N., Chen, J. W., & Liu, C. N. (2018). Failure investigation of a geosynthetic-reinforced soil slope subjected to rainfall. *Geosynthetics International*, *26*(1), 42–65. https://doi.org/10.1680/jgein.18.00035

Yin, J. H. (1999). Properties and behaviour of Hong Kong marine deposits with different clay contents. *Canadian Geotechnical Journal, 36*, 1085–1095. https://doi.org/10.1139/t99-068

Yukselen, Y., & Kaya, A. (2008). Suitability of the methylene blue test for surface area, cation exchange capacity and swell potential determination of clayey soils. *Engineering Geology*, *102*, 38–45. https://doi.org/10.1016/j.enggeo.2008.07.002

Zlatović, S., & Ishihara, K. (1995). On the influence of nonplastic fines on residual strength. *Earthquake Geotechnical Engineering*, 239–244.

Zornberg, J. G., & Kang, Y. (2005). Pullout of geosynthetic reinforcement with in-plane drainage capability. *Geo-Frontiers Congress 2005.* https://doi.org/10.1061/40782(161)33

Zornberg, J. G., & Mitchell, J. K. (1994). Reinforced soil structures with poorly draining backfills. Part I: Reinforcement interactions and functions. *Geosynthetics International*, *1*(2), 103-148. https://doi.org/10.1680/gein.1.0006

Zuo, L., & Baudet, B. A. (2015). Determination of the transitional fines content of sand-non plastic fines mixtures. *Soils and Foundations*, *55*(1), 213–219. https://doi.org/10.1016/j.sandf.2014.12.017

APPENDICES

A. Large Direct Shear Test Results

Results of the large direct shear tests conducted within the scope of this study are reported in Appendix A. Properties of the soil mixtures are presented in Section 3.1, direct shear specimen preparation procedure in Section 3.3.6.2, and notations for tests in Figure A.1 to Figure A.15 are described in Section 3.3.6.4.

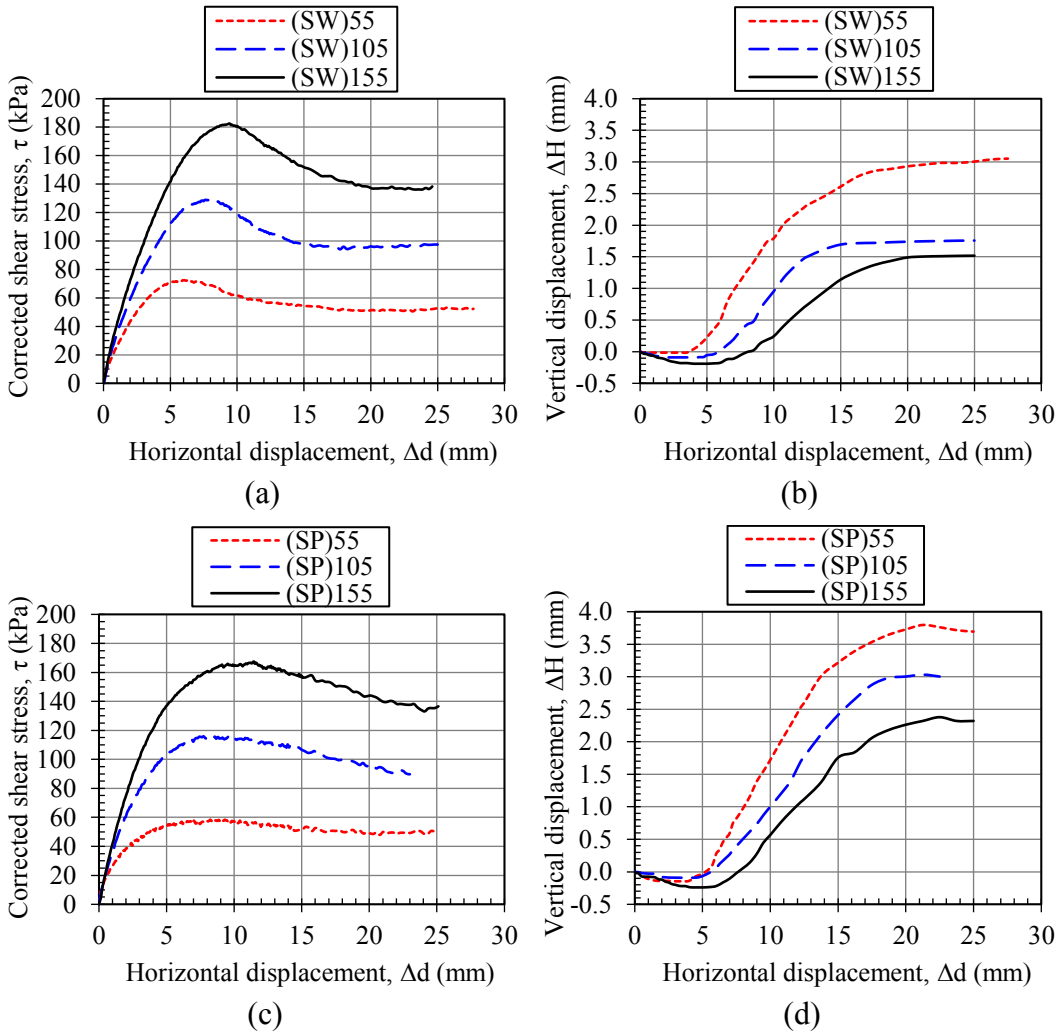


Figure A.1. SW (a, b) and SP (c, d) soil mixtures

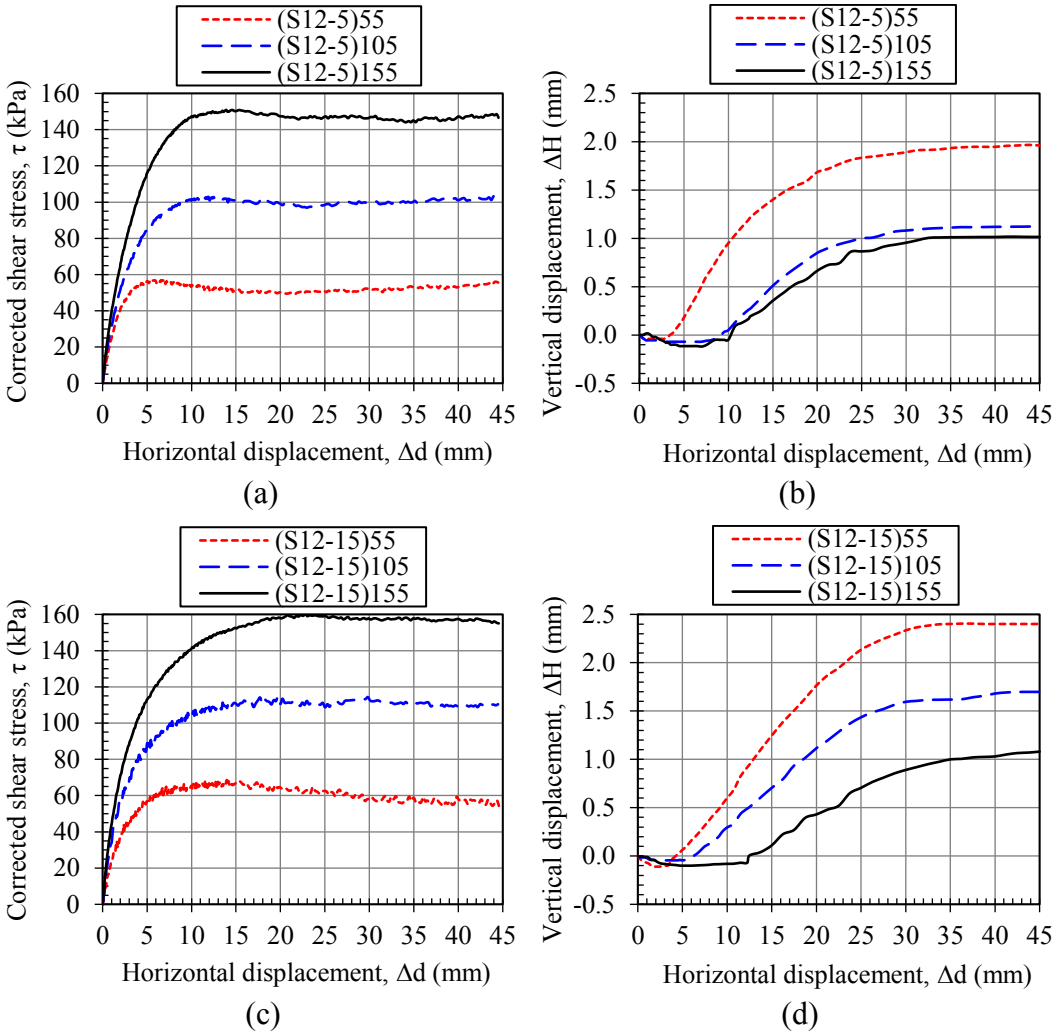


Figure A.2. S12-5 (a, b) and S12-15 (c, d) soil mixtures

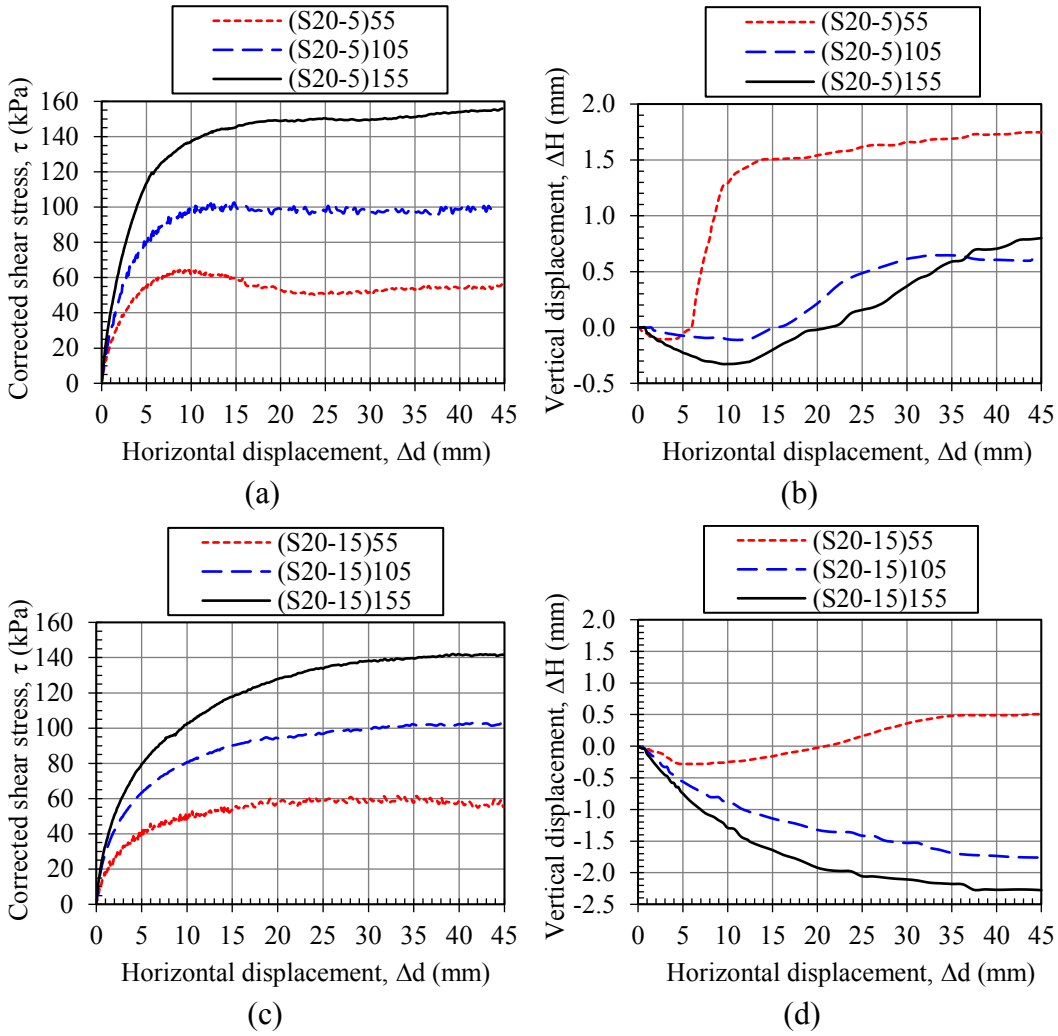


Figure A.3. S20-5 (a, b) and S20-15 (c, d) soil mixtures

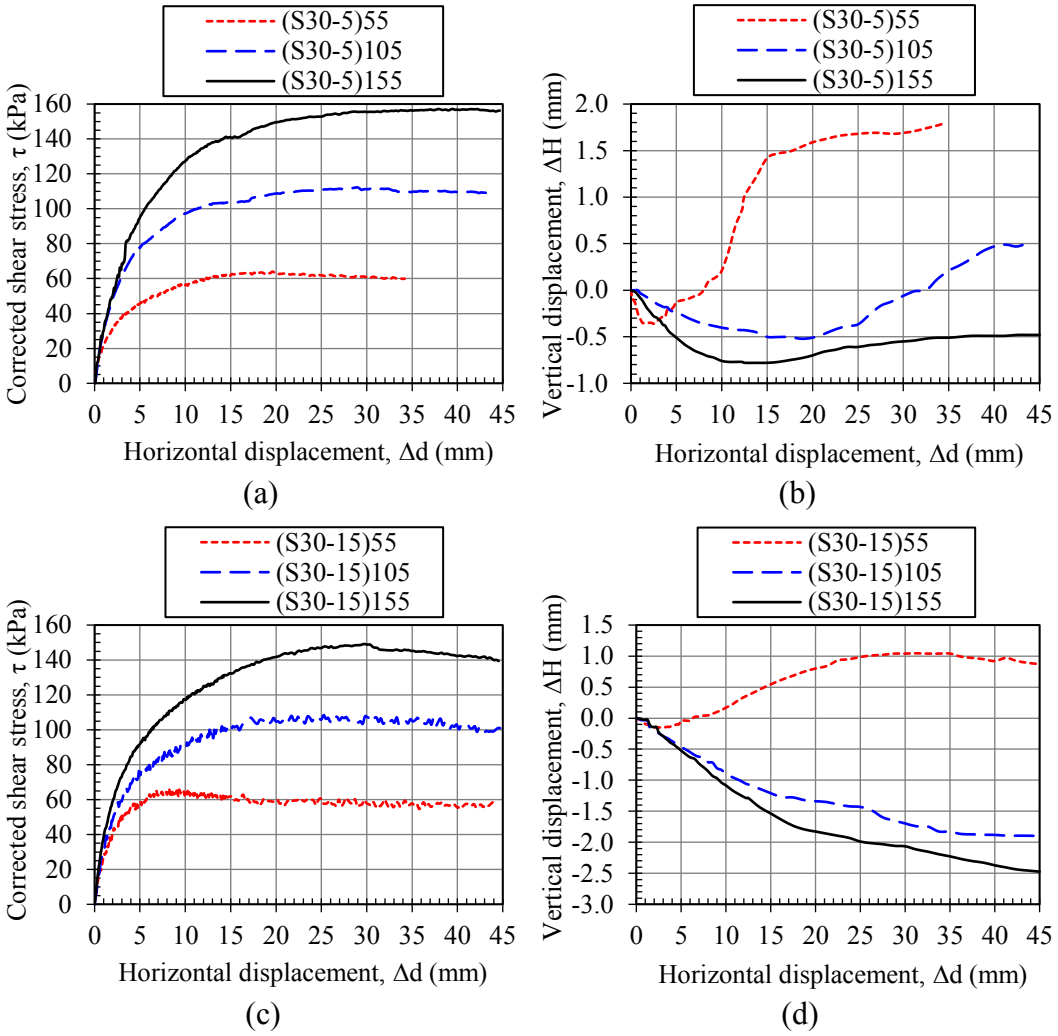


Figure A.4. S30-5 (a, b) and S30-15 (c, d) soil mixtures

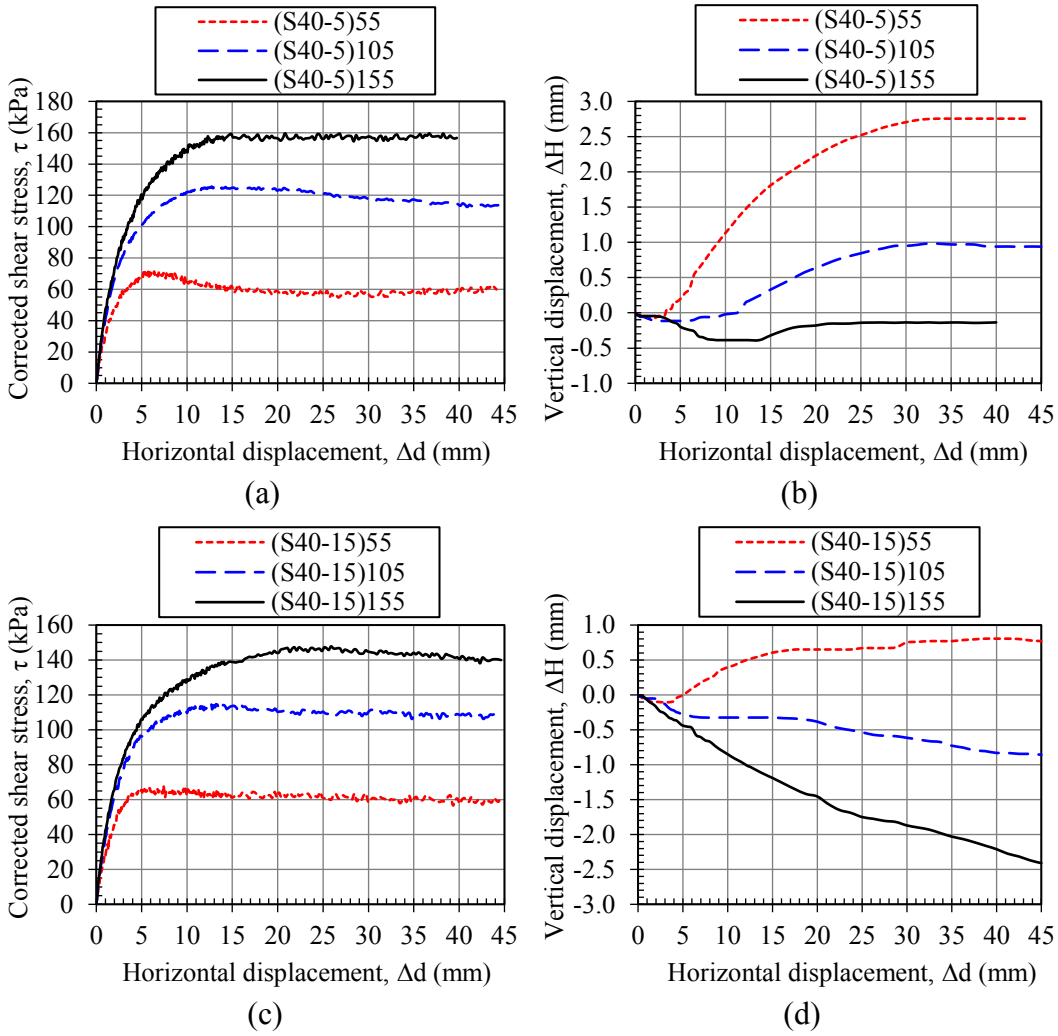


Figure A.5. S40-5 (a, b) and S40-15 (c, d) soil mixtures

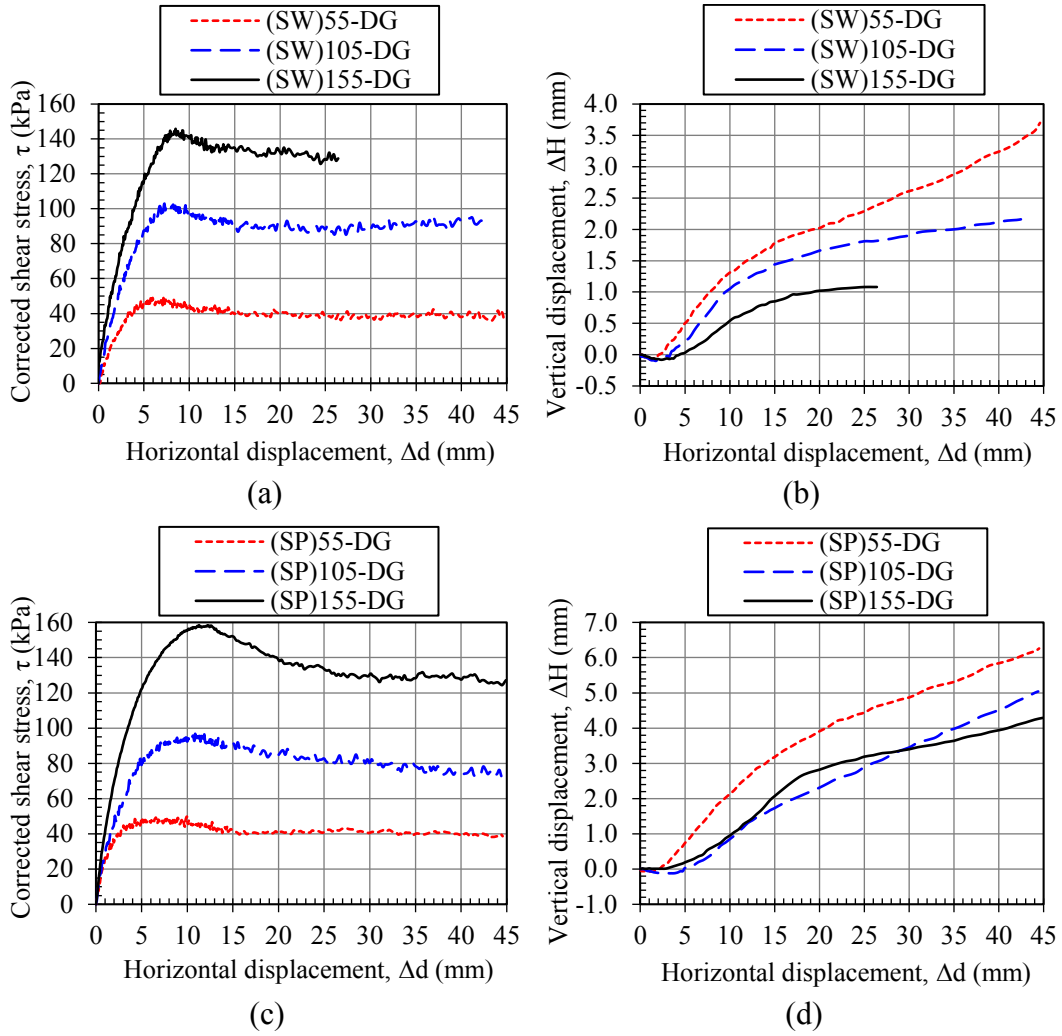


Figure A.6. SW (a, b) and SP (c, d) soil mixtures with geogrid having draining property (DG)

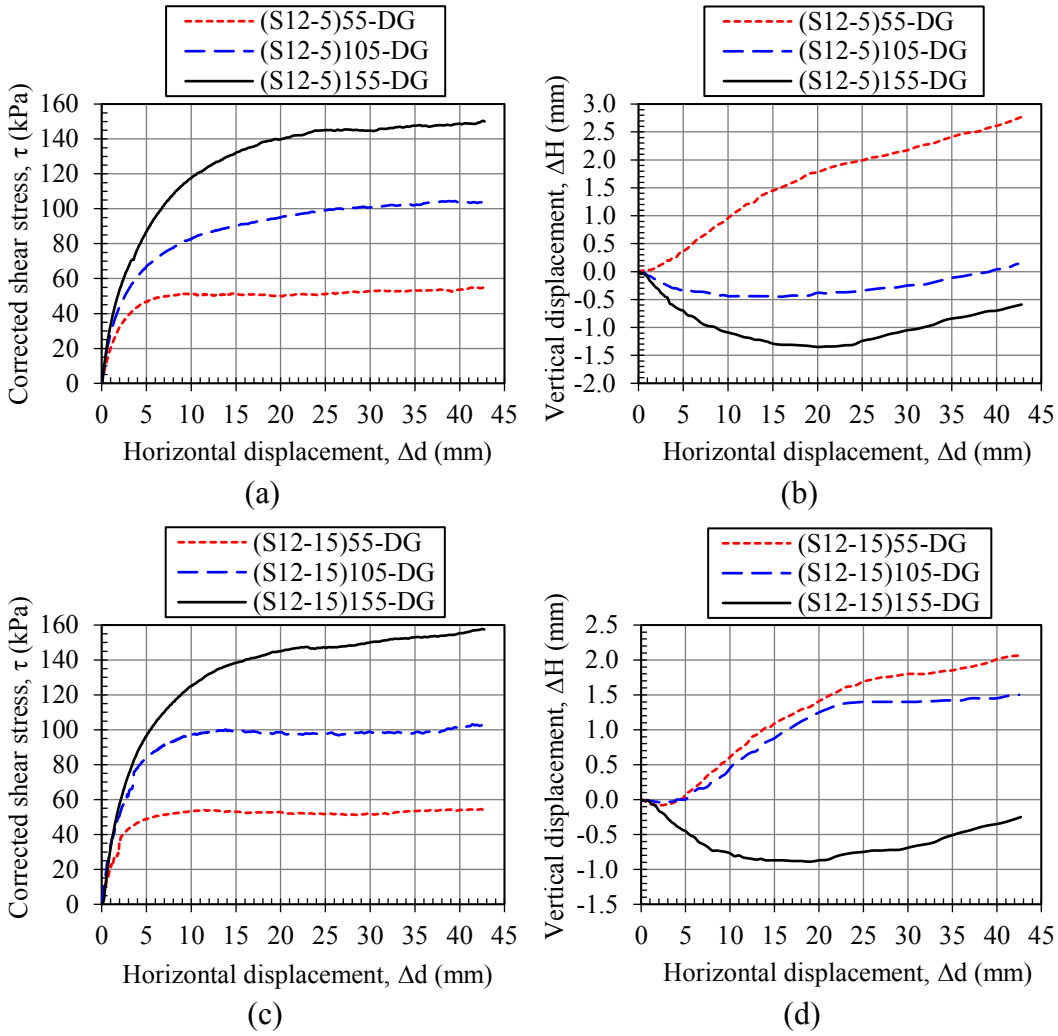


Figure A.7. S12-5 (a, b) and S12-15 (c, d) soil mixtures with geogrid having draining property (DG)

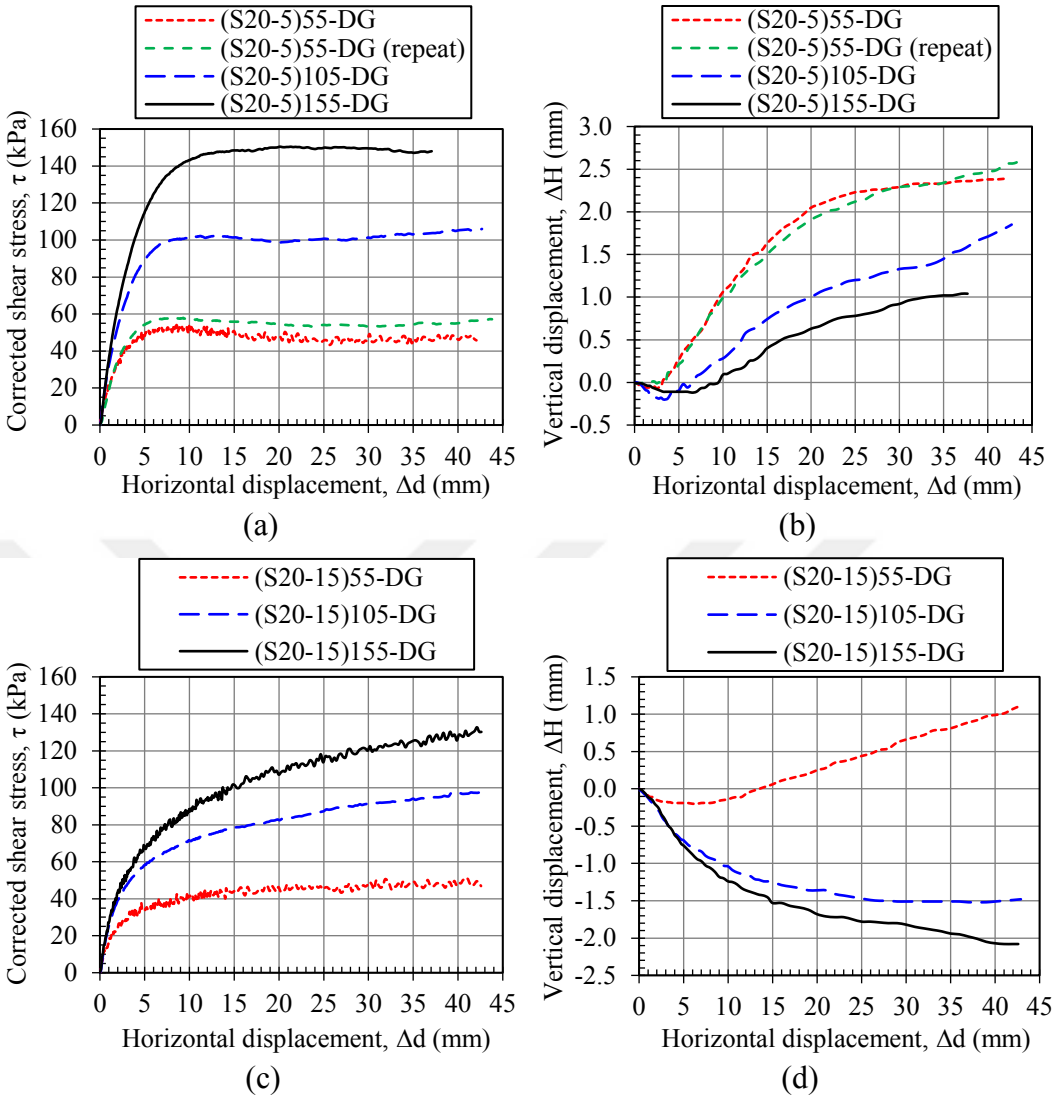


Figure A.8. S20-5 (a, b) and S20-15 (c, d) soil mixtures with geogrid having draining property (DG)

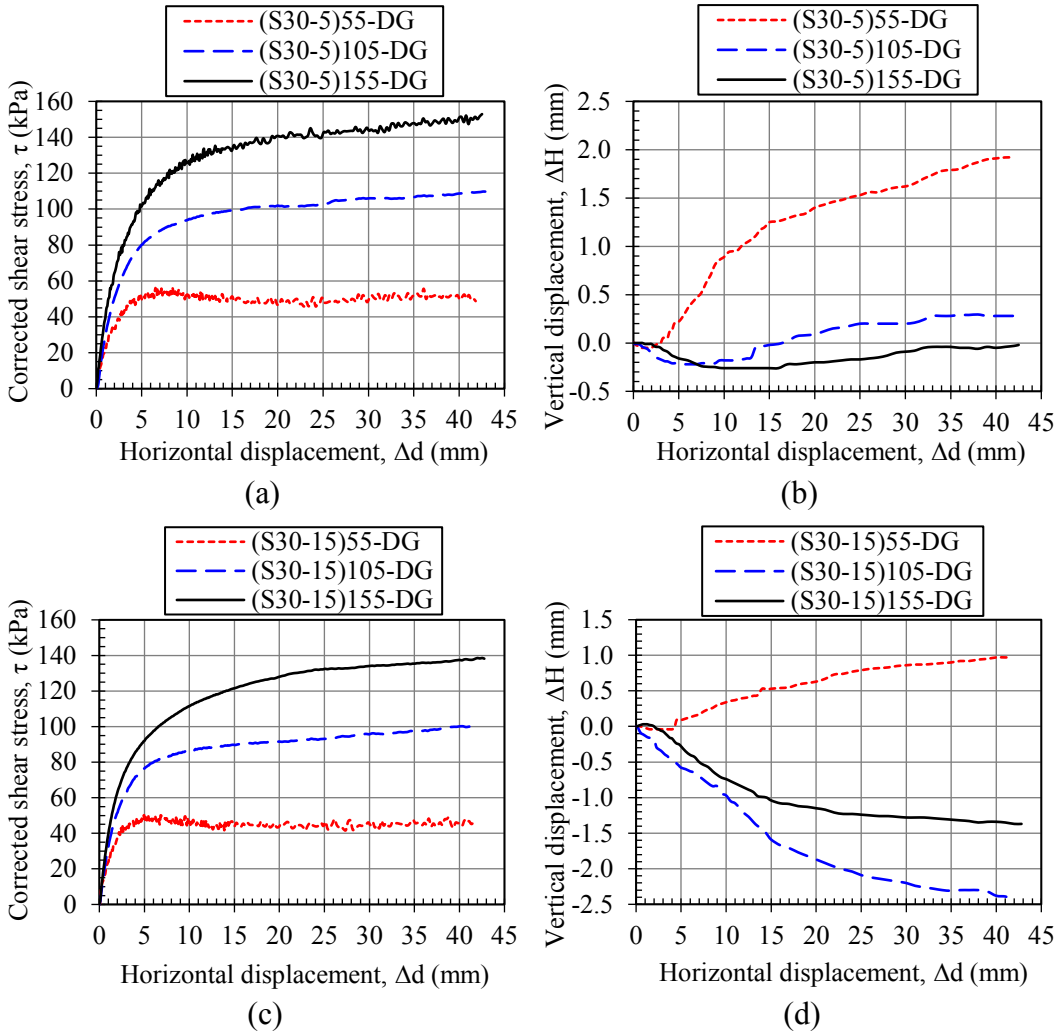


Figure A.9. S30-5 (a, b) and S30-15 (c, d) soil mixtures with geogrid having draining property (DG)

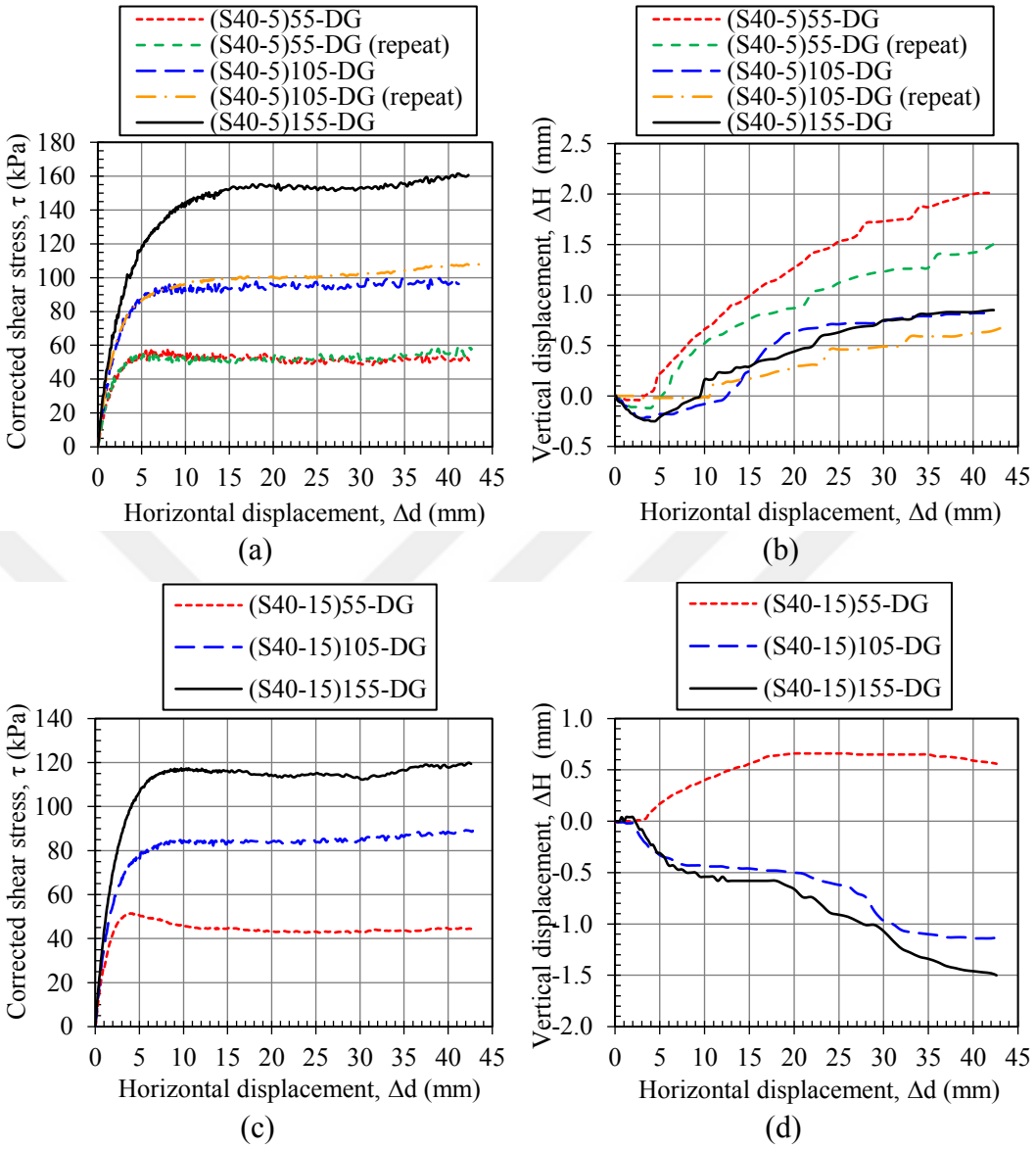


Figure A.10. S40-5 (a, b) and S40-15 (c, d) soil mixtures with geogrid having draining property (DG)

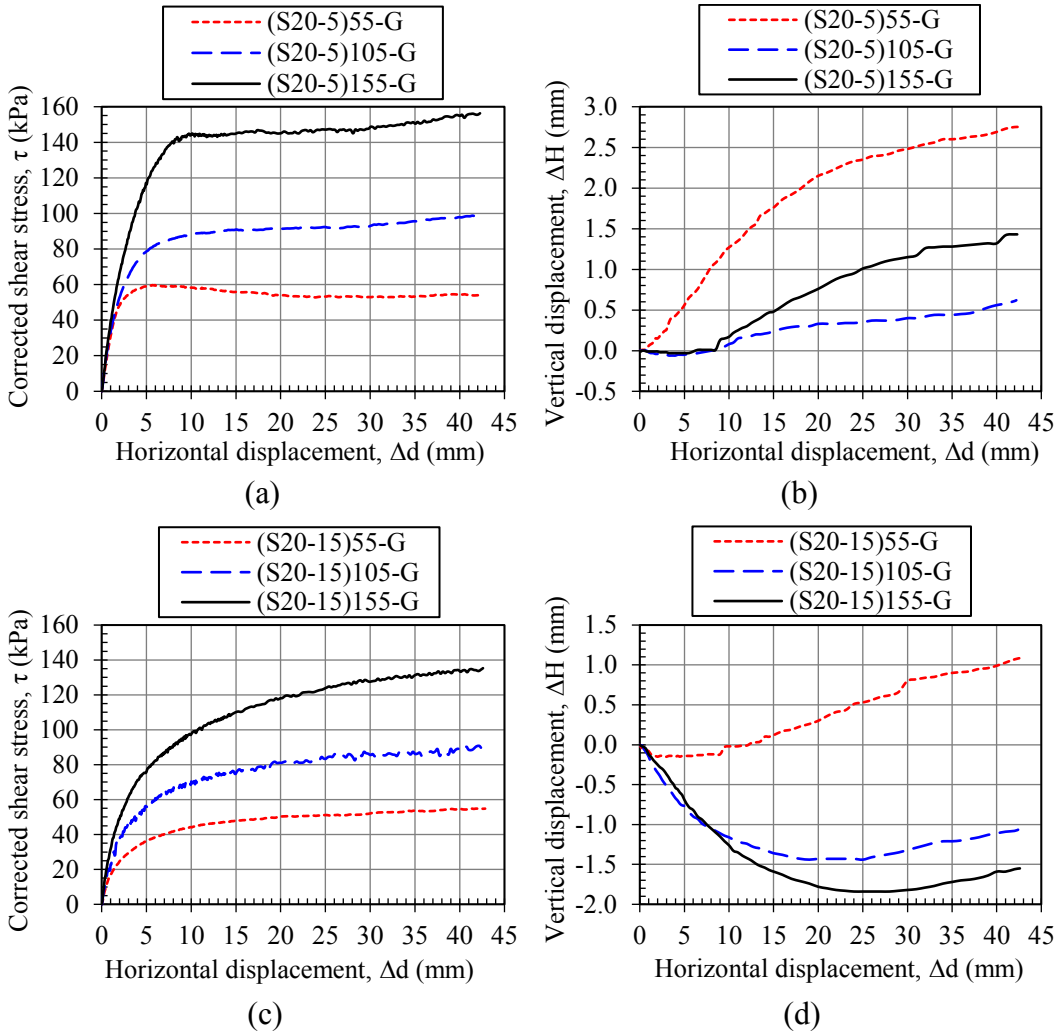


Figure A.11. S20-5 (a, b) and S20-15 (c, d) soil mixtures and geogrid without draining property (G)

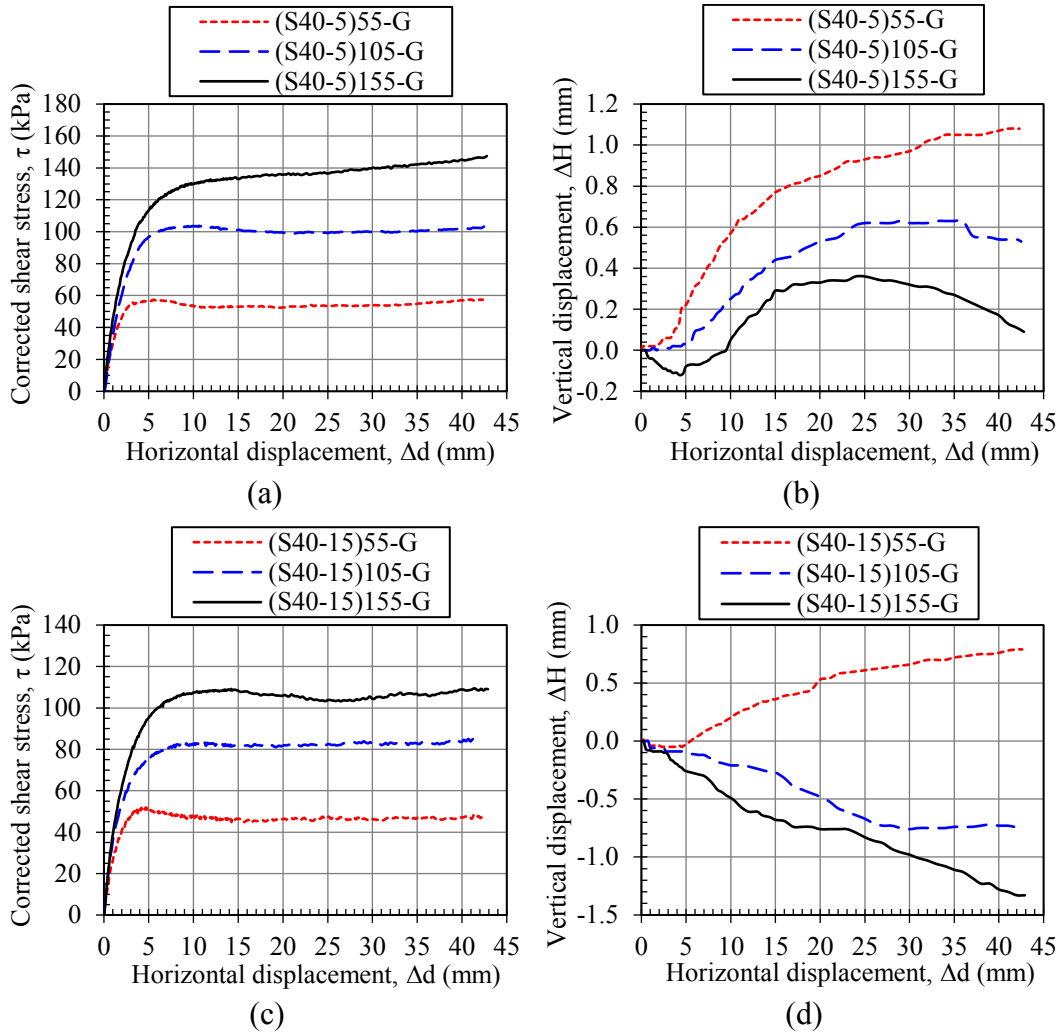


Figure A.12. S40-5 (a, b) and S40-15 (c, d) soil mixtures and geogrid without draining property (G)

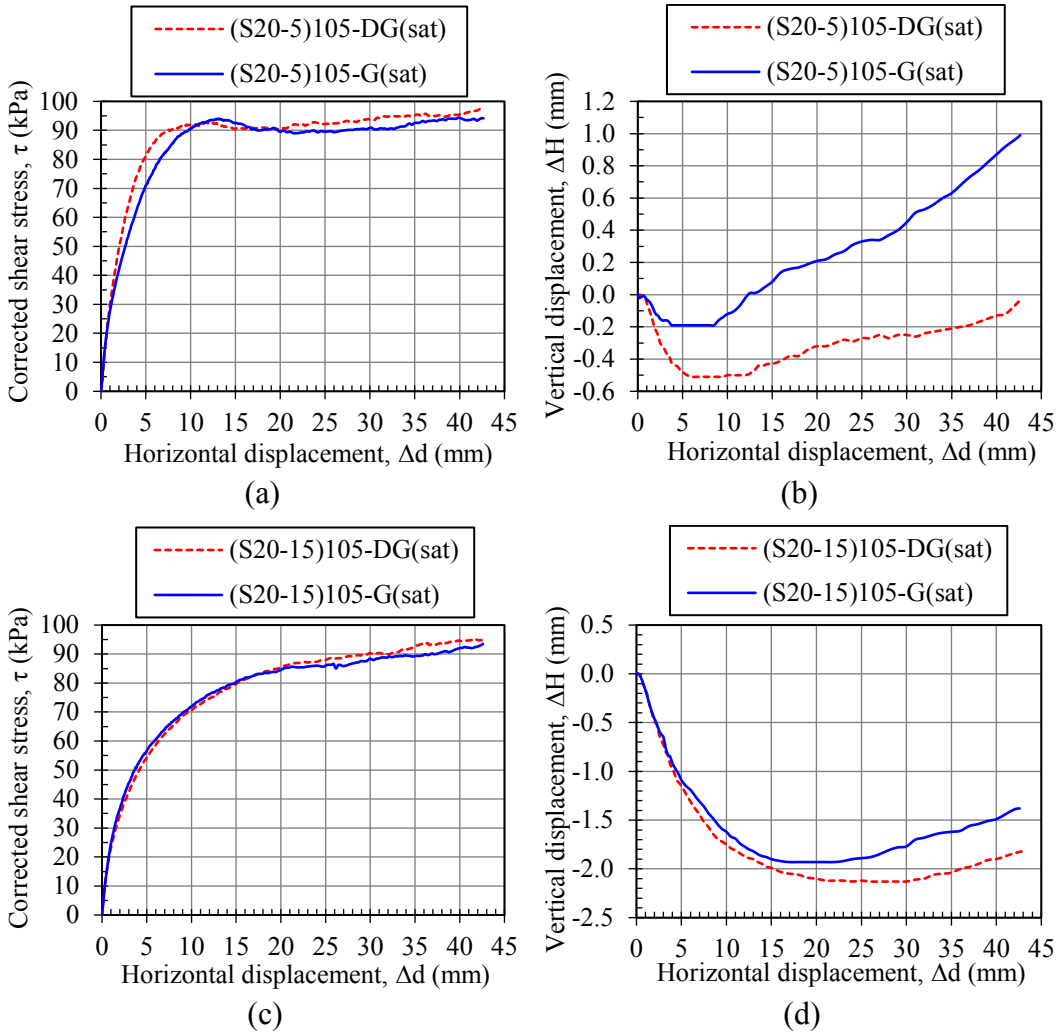


Figure A.13. Saturated S20-5 (a, b) and S20-15 (c, d) soil mixtures with geogrids

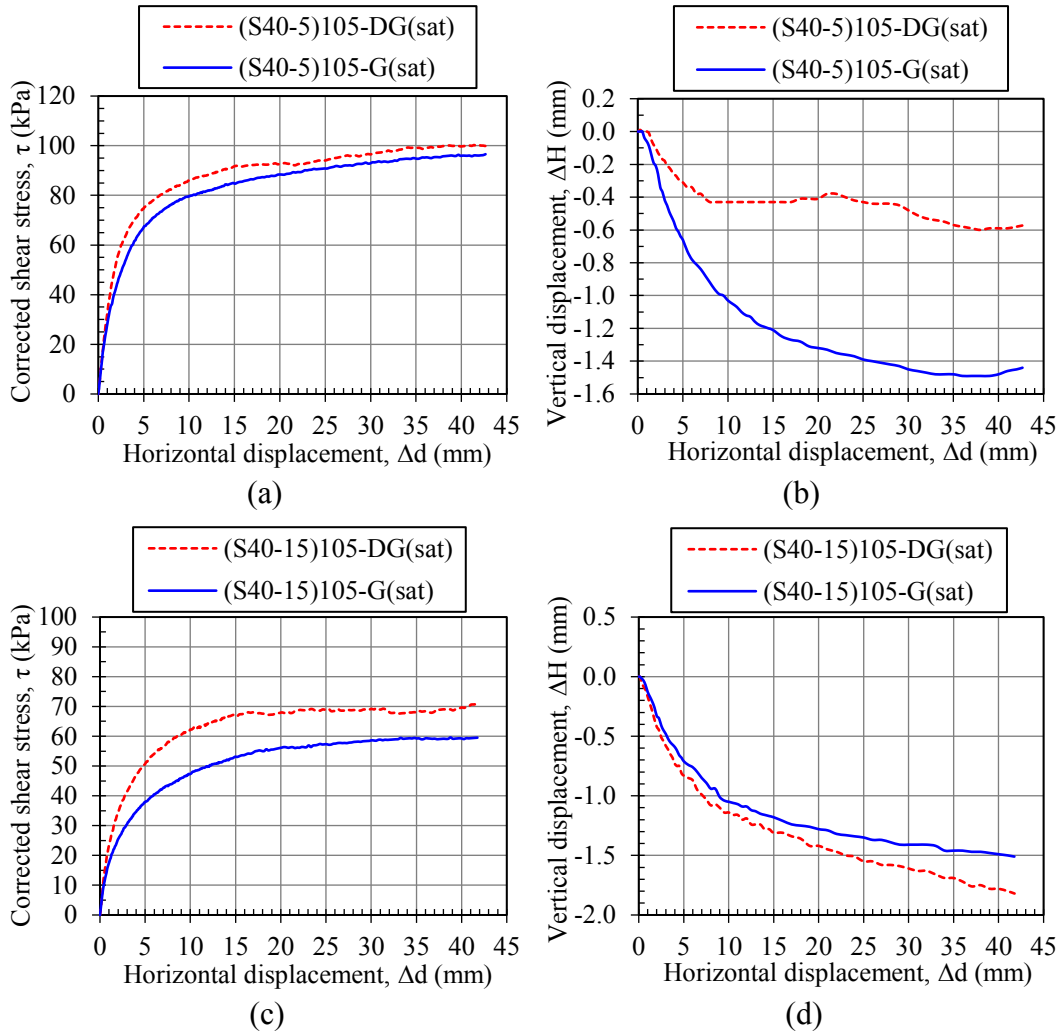


Figure A.14. Saturated S40-5 (a, b) and S40-15 (c, d) soil mixtures with geogrids

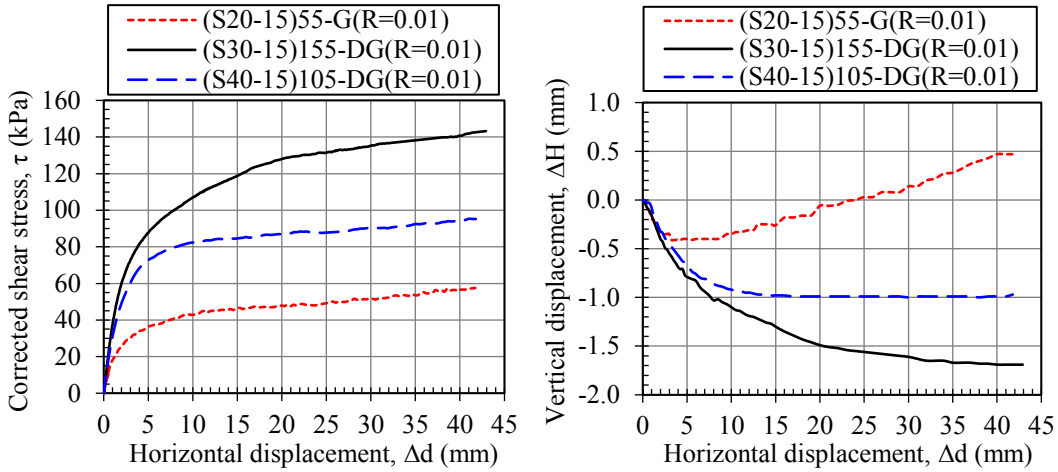


Figure A.15. Soil mixtures tested with a shear rate of 0.01 mm/min

B. Equipment Specifications

Properties of the equipment used in large compression tests and large direct shear tests are presented in Appendix B.

Large Compression Tests

One-dimensional static large-scale compression tests were conducted by a setup instrumented with one load cell and two displacement gages (Figure 3.25). Data were collected and recorded by a data acquisition system.

Data acquisition system: TESTBOX1001 (TDG Scientific Measuring Systems Ltd.)

- 16-Bit analogue digital converters (ADC)
- 8 channels
- ±10 V input range
- Independent adjustable gain for each channel (8 levels from x1 to x890)
- The sampling rate of 8 sample/second

Displacement gages: SLPIS linear potentiometer (Opkon Optic Electronic Inc.)

- 100 mm measurement capacity
- Infinite resolution
- Linearity: ±0.2%

Load cells: BM3 stainless steel S-type load cell (Zemic Europe)

- Maximum capacity of 5 tons
- Output sensitivity of 2.0 ± 0.004 mV/V
- Recommended excitation voltage of 5 ~ 12 V

Large Direct Shear Tests

Tests were carried out with the large direct shear setup designed by the author and manufactured by the Alfa Testing Equipment. A displacement-controlled electric

drive motor provides the shear displacement. The apparatus includes a load cell (for shear load) and displacement gages (horizontal and vertical).

Electric motor: R88M AC servo motor (Omron Industrial Automation)

- 0.75 kW rated output
- 3000 rpm rated speed
- 2.4 Nm rated torque
- 7.05 Nm peak torque

Displacement gages: SLPIS linear potentiometer (Opkon Optic Electronic Inc.)

- 50 mm measurement capacity
- Infinite resolution
- Linearity: ±0.5%

CURRICULUM VITAE